JET SHAPES IN CHARM PHOTOPRODUCTION AND DEEPLY INELASTIC SCATTERING AT HERA

Dissertation zur Erlangung des Doktorgrades
des Department Physik der Universität Hamburg

von

BRIAN ROSENVOLD GRELL
aus Medelby

Hamburg 2010

Gutachter der Dissertation: Prof. Dr. Robert Klanner
Dr. Benno List

Gutachter der Disputation: Dr. Benno List
Prof. Dr. Dieter Horns

Datum der Disputation: 21. September 2010

Vorsitzender des Prüfungsausschusses: Dr. Georg Steinbrück

Vorsitzender des Promotionsausschusses: Prof. Dr. Joachim Bartels

Dekan der MIN Fakultät: Prof. Dr. Heinrich Graener

Leiter des Department Physik: Prof. Dr. Daniela Pfannkuche

Abstract

This analysis investigates charm production processes in photoproduction and deeply inelastic scattering. The analysed data was collected with the H1 detector at the HERA accelerator in the years 1999-2000 for photoproduction and 2004-2007 for deeply inelastic scattering, corresponding to integrated luminosities of 83 pb^{-1}, respectively 348 pb^{-1}. Dijet events are selected with jet transverse momenta of at least 5 GeV, respectively 4 GeV, in the central rapidity region. One jet is tagged by a D^* meson to be initiated by a charm quark. The other is studied with respect to its mean integrated jet shape in order to deduce to which fraction it is initiated by a quark or a gluon. The jet shape is described by the fraction $\psi(r)$ of the jet energy inside a cone of radius r around the jet axis; it is found that for $r = 0.6$, $\psi(r)$ is most sensitive to differences between charm and light quark or gluon jets. The shape is measured as a function of various kinematic variables such as the jet energy and pseudorapidity, photon virtuality and x_γ^{obs}, the fraction of the photon momentum entering the hard interaction. The photoproduction data is compared to Pythia, the DIS data to RapGap Monte Carlo simulations. In the Monte Carlo calculation, direct and resolved photon processes are simulated separately to compare samples with an enriched fraction of quark, respectively gluon initiated jets. Deviations at low x_γ^{obs} are observed for higher values of Q^2, where direct and resolved expectations are nearly identical, hinting at an overestimation of gluon initiated jets. In most regions of phase space though, the resolution of the measurement excels the difference between direct and resolved predictions, allowing a distinction of such event samples.

Kurzzusammenfassung

Ziel dieser Analyse ist die Untersuchung der Charm-Produktionsprozesse in Photoproduktion und tief-inelastischer Streuung. Die hierfür vewendeten Daten wurden mit dem H1-Experiment am *ep*-Speicherring HERA in den Jahren 1999-2000 für Photoproduktion und in den Jahren 2004-2007 für tief-inelastische Streuung gesammelt. Dies entspricht integrierten Luminositäten von 83 pb^{-1} bzw. 348 pb^{-1}. Es wurden Zwei-Jet-Ereignisse mit transversalen Jet-Energien von mindestens 5 GeV und 4 GeV im zentralen Rapiditätsbereich ausgewählt. Ein Jet wird durch Rekonstruktion und Zuordnung eines D^*-Mesons als Charm-Jet identifiziert, der andere wird auf seine integrierte Jet Shape hin untersucht. Der Mittelwert dieser gibt Aufschluss über den Anteil der durch Quarks bzw. Gluonen ausgelösten Jets in der betrachteten Menge von Ereignissen. Die Jet Shape wird beschrieben durch den Bruchteil $\psi(r)$ der Jet-Energie innerhalb eines Kegels mit Radius r um die Jet-Achse; es zeigt sich, dass bei einem Radius $r = 0,6$ die grösste Sensitivität auf Unterschiede zwischen Charm- und leichten Quark- sowie Gluon-Jets erreicht wird. Die mittlere integrierte Jet Shape wird in Abhängigkeit unterschiedlicher kinematischer Variablen, wie etwa der Jet-Energie und -Pseudorapidität, der Photon-Virtualität und x_γ^{obs}, des Bruchteils des Photon-Impulses, der in die harte Wechselwirkung eingeht, gemessen. Die Photoproduktions-Daten werden mit der Pythia, die Daten aus tief-inelastischer Streuung mit der RapGap Monte Carlo-Simulation verglichen. In den Monte Carlo-Rechnungen werden die direkten und die aufgelösten-Photon-Prozesse separat simuliert, um Ereignis-Mengen mit angereichertem Anteil an quark- bzw. gluoninduzierten Jets zu studieren. Für hohe Photon-Virtualitäten werden bei kleinen x_γ^{obs} Abweichungen zur Monte Carlo-Erwartung beobachtet. Dies deutet auf eine Überschätzung von durch Gluonen initierten Jets in diesem Bereich des Phasenraums hin. In den meisten Bereichen des Phasenraums ist die Auflösung der Messung besser als die Differenz zwischen den direkten und den aufgelösten Erwartungen, was eine Unterscheidung zwischen solchen Ereignismengen erlaubt.

Overblik

Målet med denne analyse er, at undersóge mekanismerne bag produktionen af charm quarks. Hertil bliver der udnyttet data, der blev vundet ved H1 eksperimentet i ep-acceleratoren HERA i årene 1999-2000 m.h.t photoproduktion og i årene 2004-2007 m.h.t. dyb inelastisk stódning. Dette svarer til integrerede luminositeter på 83 pb^{-1} henholdsvis 348 pb^{-1}. Begivenheder med to jets med transversale impulser af mindst 5 GeV og 4 GeV i det centrale rapiditetsområde blev udvalgt. En jet bliver identificeret som charm jet ved at rekonstuere en D^* meson. Den anden undersóges m.h.t. dens jet shape. Middelværdien af disse giver udtryk for, til hvilken del disse jets blev udlóst af en kvark eller en gluon. Herved er jet shape $\psi(r)$ den del af jetenergien indenfor en kegle med radius r omkring jetaksen. Det viser sig, at $\psi(r)$ er mest sensitiv for forskelle mellem kvark- og gluonjets ved $r = 0,6$. Denne shape bliver bestemt som fuktion af flere kinematiske variabler som jetenergien og -pseudorapiditeten, fotonvirtualiteten og x_γ^{obs}, den del af fotonens impuls, der medvirker i den hårde vekselvirkning. Photoproduktionsdata bliver sammenlignet med Pythia, data fra dyb inelastisk stódning med RapGap Monte Carlo simulationer. I Monte Carlo beregningerne bliver de direkte og de oplóste foton processer simuleret separat, for at sammenligne próver med en forhójet andel af kvark- henholdsvis gluoninitierede jets. Ved stórre værdier af fotonvirtualiteten kan afvigninger ved små x_γ^{obs} iagttages, hvilket hentyder på en overvurdering af gluoninitierede jets. I de fleste områder af faserummet er det dog muligt at skelne mellem próver, der er dominerede af direkte henholdsvis oplóste processer.

Contents

Introduction

Elementary particle physics explores the smallest constituents of matter and their interactions. Present experimental data is very successfully described by the Standard Model where matter is built of six quarks and six leptons. These particles interact via the electroweak and strong forces, both of which are described in terms of quantum field theories. The theory of the strong interaction between quarks, mediated by gluons, is called Quantum Chromodynamics (QCD). Calculation of production cross sections in QCD are performed in perturbation theory with the strong coupling constant α_s as expansion parameter. The convergence of the perturbation series is ensured by the presence of a hard scale, at which α_s is small. In heavy quark production this hard scale can be provided by the mass of the heavy quark. QCD calculations can thus be tested by studying heavy quark production.

In *ep* collisions at HERA the dominant charm (c) production mechanism is the boson-gluon fusion process. In addition to the $c\bar{c}$-pair production in the direct process, processes where the photon exhibits a substructure, so-called resolved photon processes, provide a significant contribution. Here the photon acts as a source of quarks and gluons that participate in the hard interaction. In photoproduction where the exchanged photon is quasi-real this contribution is expected to be of additional importance.

In the investigation of charm production the step beyond the measurement of cross sections is the separation of the contributions from different processes to the cross section. In particular this means to what extent charm production can be attributed to the excitation process, where a quark from the photon participates in the hard interaction. It is this process which in leading order perturbative QCD produces a hard gluon in addition to a hard charm quark, while the direct and the remaining resolved processes lead to the production of two quarks as outgoing partons of the hard subprocess. This raises the experimental question whether a hard gluon can be observed as byproduct to charm production.

The direct observation of quarks and gluons is rendered impossible by colour confinement, however; the partons fragment into colour neutral hadrons which form jets. At low energies where non-perturbative behaviour dominates, the created hadrons are distibuted isotropically in space. At higher energies jet-like structures are observed that give clear experimental evidence of the partons coming from the hard interaction. In this context the study of e^+e^- collisions at PETRA in last centuries late seventies revealed three-jet events to be initiated by two quarks and an additional radiated gluon. This allows to refine the above question: Is it possible to deduce the type of initiating parton from the jet and so constrain the contributing physics process?

Jets are formed by a chain of elementary splitting processes of the initial quark or gluon. The relative strengths of these splitting processes are determined by the QCD colour factors and differ between quarks and gluons. Consequently the structure of jets initiated by quarks, respectively gluons, is different. When considering jets of equal energy, gluon jets are broader and contain more particles with a generally softer p_t spectrum. The study of the internal jet structure thus promises to be a means to distinguish the initial partons.

The present analysis' aim is the distinction of events with a charm quark pair from those with a charm quark and a gluon as final state partons from the hard scattering process. To this end dijet events are studied where one jet is tagged as being initiated by a charm quark while the shape of the other jet is analysed. The well established variable 'mean integrated jet shape' is used as the tool to achieve this goal. The tagging of the charm initiated jet is performed by the reconstruction of a D^* meson in the golden decay channel. The analysis is performed in photoproduction for data from the HERA 1 running period where the scattered electron has been detected in one of the two 'electron taggers' at $z = -33$ m, respectively $z = -44$ m, along the electron beam direction, corresponding to two different inelasticity regions. Further the regime of deeply inelastic scattering has been studied for HERA 2 data. The integrated luminosity for for the HERA 1 sample amounts to 51 pb^{-1}, respectively 32 pb^{-1}. The HERA 2 data sample has an integrated luminosity of 348 pb^{-1}.

The outline of this these is as follows: First an overview of the theoretical background is given. Emphasis here is put on heavy quark production mechanisms as well as quark and gluon jet properties. The second chapter focuses on the H1 detector and the components relevant for this analysis. The strategy for the analysis is presented in chapter three. The fourth chapter is dedicated to the reconstruction of the analysis objects. This includes the hadronic final state, jets, the D^* meson as well as the kinematic variables. The selection of the dijet data samples in photoproduction and deeply inelastic scattering is discussed in chapter five. Chapter six contains the details concerning the measurement of the jet shape. The results are presented in chapter seven. Finally in chapter eight the results are summarised and discussed, before an outlook closes the thesis.

Chapter 1

Heavy Flavour Production Mechanisms

1.1 Quantum Chromodynamics

The interaction between electrically charged particles is precisely described by Quantum Electrodynamics (QED) with the photon as gauge boson. Analogously Quantum Chromodynamics (QCD) is the quantum field theoretical description of the strong interaction between colour charged particles. It is based on the non-Abelian colour symmetry group $SU(3)$[1] and different from QED the QCD gauge bosons, the gluons, interact with each other as these carry colour charge themselves [1]. Hence gluon exchange involves a change of colour charge between the involved quarks. The coupling constant of the strong interaction α_s reflects the self-interaction of its gauge bosons by a behaviour opposite to the behaviour of the electromagnetic fine structure constant: At small distances (high momentum transfers) the coupling is very small while it increases towards larger distances (small momentum transfers). This *running coupling* leads to *asymptotic freedom* at small distances; the partons become quasi-free particles. The large value of α_s at low momentum transfers on the other hand results in so-called *confinement*: The quarks are bound in colour neutral states called hadrons.

Cross sections for particle interactions are calculated in perturbative QCD (pQCD) as a power series in α_s. Beyond leading order (LO) diagrams with additional gluons or quarks can yield large contributions due to the large value of the strong coupling constant. These contibutions are determined by integration of all particle momenta in the loop. Beyond LO also loop diagrams appear in the perturbation series which cause divergencies that make renormalisation necessary. As a consequence a renormalisation scale μ_r appears which sets the scale for α_s. The renormalisation scale μ_r with the dimension of an energy has to be large enough so that the power series converges, i.e. $\mu_r >> \Lambda_{QCD}$. Here Λ_{QCD} denotes the scale at which α_s gets very large causing divergencies in the perturbation series, it is of the order of 200 MeV. If μ_r fulfills this requirement it is referred to as a *hard scale.* All physical observables have to be independent of the choice of this scale.

In the production of heavy quarks the high quark mass $m_{c,b,t}$ provides a hard scale, and thus it is an ideal testing ground for pQCD. In this case, though, the presence of other large scales like the virtuality of the exchanged gauge boson Q^2 or the transverse momenta p_t of the quarks cause

---

[1] QED is based on the Abelian gauge group $U(1)$

the calculation to be more intricate. This *multi-scale problem* is treated according to the relative magnitudes of the involved scales [2].

1.2 Kinematics of Electron Proton Scattering

The interaction between electron and proton is in first order QED perturbation theory described as an exchange of a virtual gauge boson. This is depicted in figure 1.1. If the exchanged boson is a charged $W^{\pm}$ boson the electron becomes an uncharged neutrino at the electron vertex. In the case of neutral gauge boson, γ or Z^0, the electron as a particle is conserved. $\mathbf{k}$ and $\mathbf{k}'$ denote the momenta of the incoming, repectively outgoing lepton, $\mathbf{p}$ the momentum of the incoming proton. The negative square four momentum $-\mathbf{q}^2$ of the exchanged gauge boson is referred to as Q^2:

$$Q^2 = -\mathbf{q}^2 = -(\mathbf{k} - \mathbf{k}')^2. \tag{1.1}$$

The contributions to the cross section caused by $W^{\pm}$ or Z^0 exchange are supressed in relation to photon exchange by a factor of C,

$$C = \left(\frac{Q^2}{Q^2 + M^2_{Z^0,W^{\pm}}} \right)^2 . \tag{1.2}$$

Due to the high masses of $W^{\pm} \approx 80$ GeV and $Z^0 \approx 91$ GeV these contributions can be neglected for $Q^2 < 1000$ GeV^2 in the neutral current case. In the Breit frame[2] the negative four momentum transfer squared Q^2 can be regarded in terms of the wave length of the virtual photon $\lambda \approx 1/Q$, hence the resolution power of the photon for the exploration of the proton structure is given by Q.

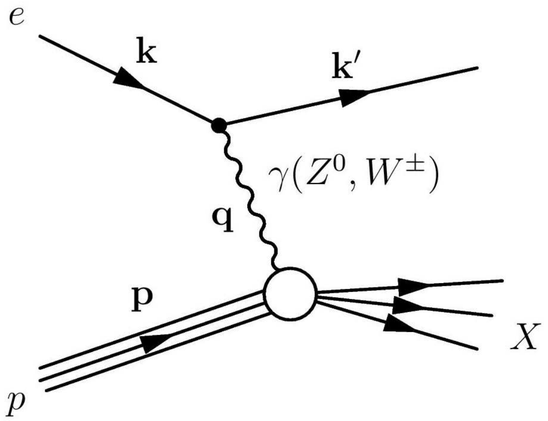

Figure 1.1: Schematical diagram of *ep* scattering including particle momenta.

From the four momenta of the particles entering in the electron proton scattering the following Lorentz-invariant quantities can be deducted:

---

[2] The Breit frame is defined as the frame of reference where the exchanged boson is fully spacelike [3].

The squared centre-of-mass energy s of the electron proton system:

$$s = (\mathbf{k} + \mathbf{p})^2. \tag{1.3}$$

In the quark parton model (cf. section 1.3) the Bjorken variable x is the momentum fraction of the struck parton in the proton:

$$x = \frac{Q^2}{2\mathbf{p} \cdot \mathbf{q}}. \tag{1.4}$$

The inelasticity is the energy fraction of the electron carried by the photon in the proton frame of reference:

$$y = \frac{\mathbf{p} \cdot \mathbf{q}}{\mathbf{p} \cdot \mathbf{k}}. \tag{1.5}$$

The energy squared in the photon-proton frame of reference is given by

$$W^2_{\gamma p} = (\mathbf{q} + \mathbf{p})^2. \tag{1.6}$$

When neglecting electron and proton rest masses the following relations can be derived for the above quantities:

$$Q^2 = sxy \tag{1.7}$$

$$W^2_{\gamma p} = ys - Q^2. \tag{1.8}$$

The above equations describe the full kinematics of the interaction. They consist of only three independent quantities. The kinematic region with a photon virtuality of $Q^2 \approx 0$ (i.e. the photon is quasi-real) is called photoproduction, the region of $Q^2 \gtrsim 2$ GeV^2 is referred to as deeply inelastic scattering (DIS).

1.3 Quark Parton Model

The *Quark Parton Model* describes the constituents of the nucleon as pointlike, non-interacting particles [4, 5]. These constituents were identified with quarks by J. Bjorken and E. Paschos [6]. In *ep* scattering a virtual photon is exchanged between the incoming photon and one of the quarks of the proton. The momentum fraction x carried by the struck quark (cf. equation 1.4) can be reconstructed by measured quantities of the electron. Figure 1.2 shows the Feynman diagram of the scattering of the electron off a quark of the incoming proton in the quark parton model. In leading order QCD gluon emissions and exchanges during the collision can be ignored. In this assumption the cross section for *ep* scattering can be determined by the cross section for quasi-elastic electron quark scattering at a given x and the probability $f_i(x)dx$ to find a quark i at that x. It is not possible to calculate these probability functions by pQCD, thus they have to be determined experimentally. The probability functions $f_i(x)dx$ are referred to as *Parton Density Functions* (PDF). The proton structure is parametrised by the proton structure functions $F_1(x, Q^2)$, $F_2(x, Q^2)$ and $F_3(x, Q^2)$ with $F_3(x, Q^2) = 0$ if Z^0 exchange is negligible, which is assumed here. The double differential cross section as a function of x and Q^2 yields

$$\frac{d^2\sigma}{dQ^2dx} = \frac{4\pi\alpha^2}{xQ^4}\left(xy^2F_1(x,Q^2) + (1-y)\,F_2(x,Q^2)\right). \tag{1.9}$$

In the quark parton model for free quarks the Callan-Gross [7] relation relates $F_1(x,Q^2)$ and $F_2(x,Q^2)$ if the interacting parton from the proton is a spin-1/2 Dirac particle:

$$F_2(x,Q^2) = 2xF_1(x,Q^2). \tag{1.10}$$

The proton structure function $F_2(x,Q^2)$ in the QPM is related to the PDF by

$$F_2(x,Q^2) = x\sum_i e_i^2 f_i(x,) \tag{1.11}$$

with the charge e_i of the quark i. J. Bjorken predicted the structure function to be independent of the momentum transfer Q^2 [4]. This effect is known as *scaling*. In that case the increase of Q^2 will not disclose new details of the quasi-free partons in the proton once these partons are resolved. A scaling behaviour was experimentally observed at $x \approx 0.1$, in good approximation confirming the quark parton model [8]. This scaling behaviour is interpreted as scattering off the valence quarks. Figure 1.3 shows experimental results by H1, ZEUS and various fixed target experiments of F_2 as function of Q^2 for different values of x. At low values of x, however, F_2 rises sharply with increasing Q^2, indicating *scaling violations.* These measurements along with other experiments reveal that only 50% of the proton momentum is carried by the charged valence quarks which gives rise to the conclusion that the quark parton model does not describe the full proton content.

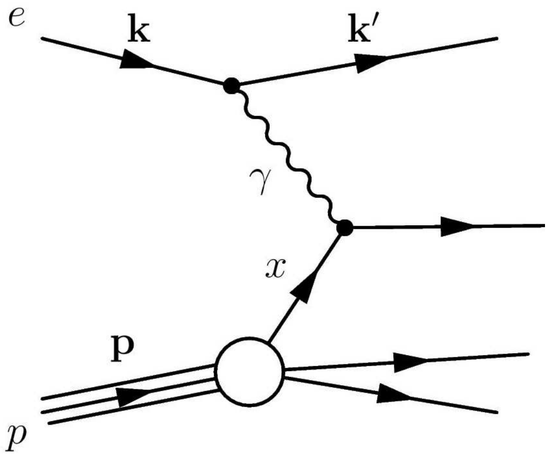

Figure 1.2: Feynman diagram of deeply inelastic scattering off a quark from the incoming proton in the quark parton model.

The momentum transfer Q^2 is associated with the Compton wavelength governing the resolution. With increasing Q^2 the Compton wavelength decreases and finer structures of the proton are resolved. The Q^2 dependence of F_2 at low x is hence interpreted as an increase of gluons and gluon-induced quark-antiquark pairs (so-called 'sea quarks'), which are visible due to the better resolution. As a consequence the ep cross section rises towards higher Q^2, as does F_2. For a succesful description of the proton content accounting for the gluon contributions the quark parton model has to be extended by means of pQCD. In this context the proton structure function F_2 in equation 1.11 can be viewed as the term of order zero in the expansion of F_2 as a power series in α_s.

1.4 Factorisation

By means of pQCD it is possible to calculate the hard subprocess on parton level for ep scattering. Ultraviolet divergencies are treated by introducing a renormalisation scale μ_r. The choice of this non-physical parameter should have no impact on the outcome of the calculation. Variation of μ_r can thus be used as a test for the validity of the perturbation series.

The inclusive cross section for ep scattering under consideration of processes within the proton can be computed by means of a factorisation ansatz. The *factorisation theorem* [9] can be seen as the field theoretical realisation of the quark parton model. Here a separation is made between the hard and soft subprocesses. The hard processes correspond to the short distance part and are computable in pQCD. They describe the interaction of high energy partons. The low energy interactions (long distance part) correspond to the soft processes. In figure 1.4 the factorisation ansatz and the separation of hard and soft processes is depicted. The factorisation scale μ_f differentiates between the pQCD computable hard matrix element and the soft processes of the parton within the proton before the hard interaction. These soft processes are included into the PDFs and are not calculated together with the hard matrix element. A problem with these processes is the radiation of soft gluons collinear with the quark, leading to divergent logarithmical terms in the perturbation series. In terms of factorisation the cross section can be expressed as

$$\sigma(ep \to eX) = \sum_i \int_{\xi=x}^{1} d\xi f_i(\xi, \mu_f^2) \hat{\sigma}_i \left(\hat{s}, \alpha_s\left(\mu_r\right), \mu_f\right). \tag{1.12}$$

Here $\hat{\sigma}$ is the 'hard cross section' on parton level calculated in pQCD. It is a function of the centre-of-mass energy $\sqrt{\hat{s}}$ in the parton system after the evolution, the renormalisation scale μ_r and the factorisation scale μ_f. The theorem allows to write the relation between the structure function F_2 and the proton PDF as follows:

$$F_2(x, Q^2) = \sum_i \int_{\xi=x}^{1} d\xi C_i \left(\frac{\xi}{x}, \frac{Q^2}{\mu_r^2}, \frac{\mu_f^2}{\mu_r^2}, \alpha_s(\mu_r^2) \right) f_i(\xi, \mu_f, \mu_r^2). \tag{1.13}$$

The sum again runs over the partons in the proton, the coefficient functions C_i can be calculated in pQCD.

Though the factorisation theorem is only proven in DIS it is applicable in photoproduction as well [10]. The PDF $f_{i/h}(x, \mu_f^2)$ is independent of the investigated hard scattering process, it depends only on the type of hadron h and parton i. The separation between hard and soft subprocesses is ambiguous, it is defined by the choice of factorisation scheme. The most important of these are the DIS scheme and the minimal subtraction scheme. In the case of inclusive processes a typical choice for renormalisation and factorisation scales is $\mu_f^2 = \mu_r^2 = Q^2$ [11]. In the DIS scheme , equation 1.11 holds in all orders of perturbation theory.

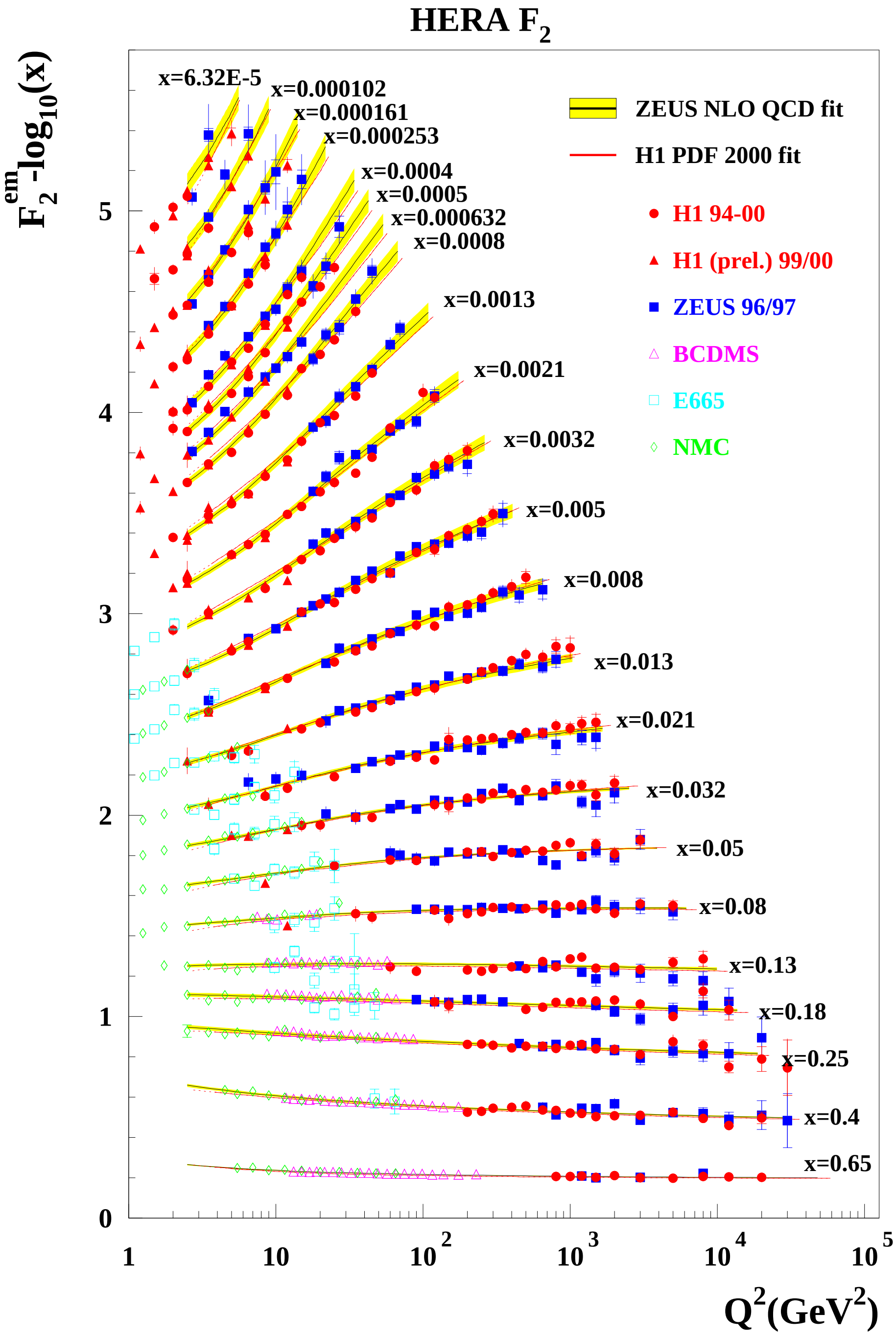

Figure 1.3: Proton structure function F_2 as function of Q^2 for different values of the Bjorken variable x. The data points are measured by H1, ZEUS and three fixed target experiments. The fits used by H1 and ZEUS are based on the DGLAP equations. The points and fit curves are offset by $-\log x$ to enhance the readability.

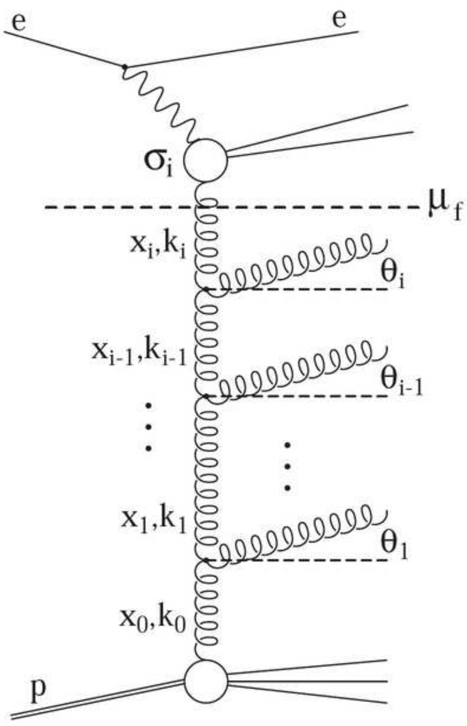

Figure 1.4: Schematical view of the factorisation ansatz, separating the hard interaction $\hat{\sigma}_i$ from the parton evolution.

1.5 Parton Evolution Models

The PDF describes the probability to find a quark or gluon in the proton with a momentum fraction x at a given Q^2. As these PDF cannot be calculated by pQCD they are determined experimentally. To this end the structure functions are parametrised at an initial scale μ_0 and fitted to the experimental data after evolution to the appropriate scale and calculation of the structure functions. The evolution equations used for this purpose account for gluon radiation from the quark as well as gluon splitting into quark or gluon pairs prior to the hard subprocess. Such radiations can occur more than once causing a parton ladder as depicted in figure 1.4 for gluons. All these radiative contributions are summed up, the succession depending on the evolution ansatz. The contributions are ordered according to the longitudinal momentum x_i, the transverse momentum $k_{t,i}$ or the angle θ_i of the radiated parton. The different approximations lead to different evolution schemes that also require different PDF input distributions. The three most important parton evolution schemes are presented in the following.

- The **DGLAP**[3] approach [12, 13, 14, 15] is the most used evolution scheme. In first order of α_s it uses four splitting functions $P_{ab}(z)$ that describe the probability of b radiating a new

---

[3] Dokshitzer, Gribov, Lipatov, Altarelli, Parisi

parton a with momentum fraction z. Assuming an initial scale Q_0^2 it is possible to calculate the parton distribution within the proton at another scale $\mu_f^2 > Q_0^2$. The proton structure at the initial scale is not predicted by the scheme and has to be determined experimentally. As the momentum fraction of the radiated parton is smaller than the momentum of the radiating parton, the integration of the evolution equation does not start at $\xi = 0$ but at $\xi = x$. One assumption of the DGLAP approach is that the transverse momenta $k_{t,i}$ of the radiated gluons are ordered along the gluon ladder according to $k_{t,i}^2 \gg k_{t,i-1}^2$. Additionally the longitudinal momenta x_i have to be large relative to the transverse momentum, i.e. the gluons must be radiated largely collinear. Hence the factorisation in this evolution is referred to as *collinear factorisation.* This condition is fulfilled for adequatetely large x. The DGLAP ansatz is expected to lose its viability for very small x.

- In the **BFKL**[4] approximation [16, 17] the evolution is performed in x, the leading $\alpha_s \ln(1/x)$ terms are resummed. This leads to strongly ordered longitudinal momenta $z_i = x_i/x_{i-1}$. BFKL evolution is expected to be valid for medium Q^2 and small x.
- The **CCFM**[5] approach [18, 19, 20, 21] is another way of evolving the PDF from the initial to a new scale. Here only gluons are used in the evolution and the gluon ladder is ordered with respect to the increasing angle of the emitted gluon: $\theta_i > \theta_{i+1}$. Emission under small angles and not too small x leads to the same sequence as in the DGLAP evolution as the transverse momentum q of the emitted gluon is $q_i > z_{i-1}q_{i-1}$ and $z_i = x_i/x_{i-1} \approx 1$. For small x the CCFM description approaches the BFKL model and accelerates the increase of the parton density towards small x. CCFM requires the unintegrated gluon density distribution $A(x_g, k_t^2, \mu_f^2)$, which depends on x and also on the transverse momentum k_t and the factorisation scale μ_f. Contrary to DGLAP the partons have an intrinsic transverse momentum before entering the hard subprocess.

HERA measurements of F_2 are very well described by the DGLAP approach all the way to the smallest accessible $x \approx 10^{-4}$ [22, 23]. Indication towards a better description by CCFM were found in forward jet production [24]. The inclusive proton structure function F_2 contains a large charm contribution through events with charm quarks in the final state. The measurement of this contribution, called $F_2^{c\bar{c}}$, hints towards a better description by CCFM at small x [25].

1.6 Charm Production

Charm and beauty quarks are also referred to as heavy flavours as their masses of $m_c \approx 1.5$ GeV and $m_b \approx 4.5$ GeV are far above the scale of QCD, Λ_{QCD}. HERA energies do not allow for top pair production and the single top production process has an extremely low cross section.

Because of the high charm quark mass, charm is produced predominantly in boson-gluon fusion (BGF), while gluons splitting to a charm anti-charm pair $g \to c\bar{c}$ as well as the production of charm quarks in hadronisation processes is supressed. Figure 1.5 shows the BGF processes. In the direct process (figure 1.5(1)) the incoming electron emits a photon. The photon interacts with a gluon from the proton, and a heavy quark pair is produced.

The photon is point-like and colour neutral. It can, however, fluctuate into a quark anti-quark pair plus gluons and thus indirectly participate in strong interactions. These hadronic constituents

---

[4] Balitsky, Fadin, Kuraev, Lipatov

[5] Ciafaloni, Catani, Fiorani, Marchesini

of the photon lead to so-called *resolved photon* events. In the *normal resolved* process (figure 1.5(2)) a parton from the photon interacts with a parton from the proton. In another possible resolved process a heavy quark from the photon takes part in the hard interaction (figure 1.5(3)-(5)). These processes are refered to as *charm excitation* processes. Especially in photoproduction where the exchanged photon is almost real, resolved processes dominate. However, the picture of direct and resolved processes gets ambiguous beyond LO.

The BGF cross section for direct processes in leading order can be expressed as [26]

$$\sigma_{\gamma g \to Q\bar{Q}}(s, m_Q^2) = \frac{\pi e_Q^2 \alpha \alpha_s}{s} \left(\left(2 + 2\omega - \omega^2\right) \ln \frac{1+\chi}{1-\chi} - 2\chi\left(1+\chi\right) \right) \tag{1.14}$$

with $\omega = 4m_Q^2/s$ and $\chi = \sqrt{1-\omega^2}$. The terms containing χ represent the threshold behaviour of heavy quark production; the kinematic region close to the charm production threshold is strongly favoured resulting in generally small charm quark transverse momenta. The larger mass and smaller charge of the beauty quark cause a supression of beauty production by a factor of roughly 200 with respect to charm.

The charm quark mass provides a sufficient hard scale making charm production a good testing ground for pQCD calculations, even in the absence of other hard scales. In addition charm production serves to probe the parton content of the photon and the proton. Here especially the gluon structure can be investigated, as the cross section is expected to be dominated by gluon-induced processes. The parton and hadron levels are closely related due to the hard fragmentation of the heavy quarks (cf. section 1.7).

In this analysis open charm production is explored. Here the partons from the produced $c\bar{c}$ pair fragment independently and form jets.

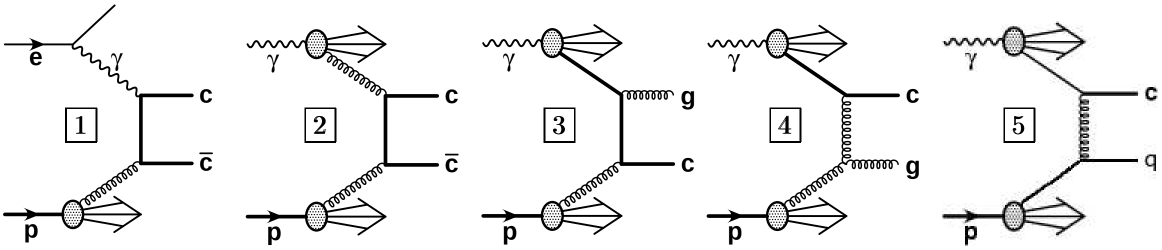

Figure 1.5: Charm production by boson-gluon fusion in leading order pQCD. (1) shows the direct process, (2) - (5) the resolved processes. (2) is the 'normal' resolved process, (3) - (5) are charm excitation processes.

1.7 Hadronisation

The colour charged quarks do not appear as free particles as a consequence of confinement. Hence the strongly interacting particles are bound in colourless states. The process of colour charged quarks forming colour neutral states, known as hadrons, is called *fragmentation* or *hadronisation*. In the case of BGF in the Monte Carlo simulation two partons are produced in the hard process. These partons produce a parton shower according to the evolution schemes discussed in section 1.5 as a sequence of particle branchings. Beyond a certain threshold, α_s becomes so large that pQCD is no longer applicable. Hence to describe the fragmentation process, phenomenological models are used. Two important models are presented in the following.

- **String fragmentation** (Lund model) [27, 28, 29] is based on the concept that after an interaction the two particles from a $q\bar{q}$ pair move away from each other. The colour field between them is confined in a narrow tube, the so-called string. At larger distances the QCD potential is proportional to the distance. As soon as sufficient energy is stored within the string, it breaks up and a new $q\bar{q}$ pair is produced. When the energy no longer suffices to produce further pairs the process stops and the created string fragments combine into hadrons. Gluons create kinks in the strings which influence the angular distribution of the produced hadrons. Figure 1.6 shows the formation of strings and the creation of new $q\bar{q}$ pairs.

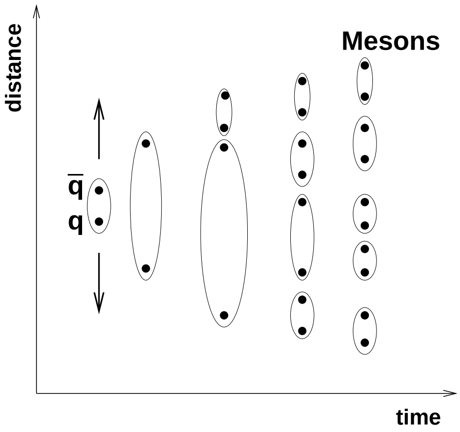

Figure 1.6: String fragmentation model showing the creation of mesons.

- **Independent fragmentation** is implemented in e.g. the Peterson and the Bowler model. Here the transition from a quark Q to a hadron H is fully characterised by the momenta of the quark and the hadron.

  A bound state $Q\bar{q}$ is formed by creating a light quark anti-quark pair $q\bar{q}$ from the vacuum where the remaining quark q continues hadronisation on its own. Because of the large difference in mass the heavy quark Q loses only a small fraction of its energy. Thus the energy of the heavy quark approximately equals the energy of the hadron containing the heavy quark.

- **Cluster fragmentation** exploits the property of so-called pre-confinement [30]: At the end of the perturbative phase, colour-connected partons tend be closely arranged in phase-space, leading to local colour compensation. The quarks are merged into colour-singlet clusters. Prior to this, though, each gluon is forced to split into a quark-antiquark pair. Clusters typically have masses of few GeV and decay independently into hadrons. Too heavy clusters split into two clusters. Too light clusters decay into a hadron under a slight rearrangement of energy and momentum with neighbouring clusters. The cluster's decay channel is based on the phase space probability.

In the above models the fragmentation can be parametrised in several ways. The Peterson parametrisation [31] implies that the probability for the fragmentation of a heavy quark solely depends on the energy transfer between initial and final state $\Delta E = E_H + E_q - E_Q$, with the energies E_H of the created hadron, E_q of the light quark and E_Q of the initial heavy quark. The probability $D_{Q\rightarrow H}$ of a heavy quark to fragment into a hadron containing the heavy quark is then inversely proportional to the square of the energy difference ΔE. Considering an additional factor for the longitudinal phase space the fragmentation function is parametrised

$$D_{Q\rightarrow H} = \frac{N}{z\left(1 - \frac{1}{z} - \frac{\epsilon_c}{1-z}\right)^2}. \tag{1.15}$$

Here z denotes the fraction of the longitudinal momentum transfered from the heavy quark to the hadron. The parameter N is for normalisation while ϵ_Q characterises how hard the fragmentation is; heavy quarks are expected to fragment harder. It is proportional to the relation of the quark masses squared $\epsilon_Q \propto M_q^2/M_Q^2$ but is usually left as a free parameter as the quark masses are not exactly known. A typical choice derived from e^+e^- data for the charm quark is $\epsilon_c \approx 0.058$ [32].

Another way to parametrise the fragmentation is the Bowler fragmentation function [28]:

$$D_{Q\rightarrow H} = N\frac{1}{z^{1+bm_Q^2}}\left(1-z\right)^a \exp\left(\frac{bm_t^2}{z}\right). \tag{1.16}$$

The parameters a and b must be determined through measurement.The transverse mass is given by $m_t = \sqrt{p_t^2 + m_Q^2}$ with mass m_Q and transverse momentum p_t of the heavy quark.

The fragmentation variable z cannot be measured directly. The inelasticity of a D^* meson (cf. section 4.4) the charm quark fragments to, however, is accessible as the fraction of the photon energy transfered to the D^* meson in the proton frame of reference:

$$z_{D^*} = \frac{\mathbf{p}\cdot\mathbf{p}_{D^*}}{\mathbf{p}\cdot\mathbf{q}} = \frac{(E-p_z)_{D^*}}{2yE_e} \tag{1.17}$$

with the four momentum $\mathbf{p}_{D^*}$ of the D^* meson. $(E-p_z)_{D^*}$ is the difference between energy and longitudinal momentum of the D^* meson and E_e is the energy of the incoming electron. It is expected that the D^* meson carries a very large energy fraction of the total event, and indeed most D^* mesons are observed at high z_{D^*} [33].

1.8 Jet Structure

Jets are the result of a chain of elementary splitting processes, i.e. parton branchings. Each branching is characterised by the virtuality Q^2 in the particular branching. As the parton shower develops, Q^2 decreases in the consecutive branching processes, hence α_s gets larger. The processes can thus be described by pQCD only up to a given cut-off value of parton virtuality. Beyond that fragmentation (cf. section 1.7) takes over. The factorisation scale μ_f marks this boundary in the Monte Carlo simulation. The internal jet structure is sensitive to hard as well as soft contributions from QCD, consequentially it can be used to probe both regimes.

The internal structure of the jet is supposed to depend mainly on the primary parton initiating the jet, less on the particular hard scattering process itself. The differences between quark and gluon jets arise from the $SU(3)$ group structure of QCD (cf section 1.1). Relative strengths of different parton branchings lead to differing splitting probabilities for quarks and gluons. Figure

1.7 shows the possible branching processes of quarks and gluons. The strength of the splittings are given by the QCD colour factors[6]

$$C_A = N_c = 3 \tag{1.22}$$

$$C_F = \frac{N_c^2 - 1}{2N_c} = \frac{4}{3} \tag{1.23}$$

$$T_R = \frac{1}{2} \tag{1.24}$$

with the number of colours N_c. As a result jets initiated by quarks exhibit different properties than jets induced by gluons. These differences are explored in terms of multiplicity of particles within the jet and angular jet size.

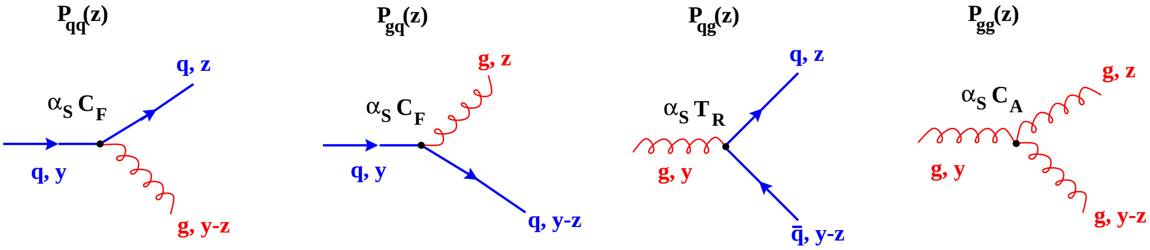

Figure 1.7: Quark and gluon splitting processes relevant for the jet development up to order α_s [35].

- **Particle multiplicity** within the jet can be calculated in pQCD as the average number of hadrons of type h in a jet initiated by a parton i at scale t [36] by

$$\langle n_h(t) \rangle_i = \int_0^1 dx D_i^h(x,t) \tag{1.25}$$

---

[6] The colour factors are manifestations of the group structure underlying QCD. The dynamics of a gauge group are completely defined by commutation relations between its generators T^i:

$$[T^i, T^j] = i \sum_k f^{ijk} T^k \tag{1.18}$$

with the structure constants f^{ijk}. Summation over all possible colour configurations in the initial, respectively final states leads to the appearance of combinatorial factors C_A, C_F and T_R, where

$$\sum_{j,k} f^{jkm} f^{jkn} = \delta^{mn} C_A \tag{1.19}$$

$$\sum_{k,\eta} T^k_{\alpha\eta} T^k_{\eta\beta} = \delta_{\alpha\beta} C_F \tag{1.20}$$

$$\sum_{\alpha,\beta} T^m_{\alpha\beta} T^n_{\beta\alpha} = \delta^{mn} T_R. \tag{1.21}$$

C_A, C_F and T_R are called QCD colour factors [34].

with the hadron energy fraction $x = E_h/E_{jet}$. The probability of a parton i to form a jet that contains the hadron h with the longitudinal momentum $p_l^h = xp_l^i$ is given by the fragmentation function $D_i^h(x,t)$. Since it describes a non-perturbative process it cannot be calculated by pQCD. However, as with the PDF the evolution with a scale t can be computed. When $t \to t + dt$ the function $D_i^h(x,t)$ can only change via the splitting of a parton i in this interval. Hence $D_i^h(x,t)$ satisfies the evolution equation

$$t\frac{\partial}{\partial t}D_i^h(x,t) = \sum_j \int_x^1 \frac{dz}{z}\frac{\alpha_s}{2\pi}P_{ij}(z,\alpha_s(t))D_j^h(x/z,t_0). \tag{1.26}$$

The evolution equation enables the prediction of $D_i^h(x,t)$ at an arbitrary scale t once it is parametrised at some scale t_0. The splitting functions $P_{ij}(z,\alpha_s(t_0))$ provide the probability of an initial parton i to emit a parton j with momentum $p_j = zp_i$. In figure 1.7 the fundamental splitting processes up to order α_s are depicted. In leading order the splitting functions yield

$$P_{qq}(z) = C_F\left(\frac{1+z^2}{1-z} + \frac{3}{2}\delta(1-z)\right) \tag{1.27}$$

$$P_{gq}(z) = C_F\left(\frac{1+(1-z)^2}{z}\right) \tag{1.28}$$

$$P_{qg}(z) = T_R\left(z^2 + (1-z)^2\right) \tag{1.29}$$

$$P_{gg}(z) = 2C_A\left(\frac{z}{1-z} + \frac{1-z}{z} + z\,(1-z)\right) + \delta(1-z)\frac{11C_A - 4N_fT_R}{6} \tag{1.30}$$

illustrating the proportionality between the branching probability and the QCD colour factors. Already the magnitude of the colour factors with T_R being the smallest hints at the fact that gluons splitting to quarks contribute least to the jet formation processes. With $C_A/C_F = 9/4$ most branchings are expected for jets initiated by gluons, these are thus on average broader than quark initiated jets at the same p_t.

Solving the DGLAP equations results in a relation between mean multiplicities [36]:

$$\langle n_h(t)\rangle_q \propto \frac{C_F}{C_A}\langle n_h(t)\rangle_g \tag{1.31}$$

valid for scales $t \gg t_0$. The difference arises from the greater effective colour charge of the gluon, proportional to $\sqrt{C_A}$, compared to $\sqrt{C_F}$ for the quark.

In terms of a model the difference becomes descriptive: The dominant asymptotic contribution to the multiplicity of a quark jet originates in the emission of a highly virtual gluon by the initial quark. The gluon forms a gluon jet with lower energy than the original quark jet. Hence one factor of C_A is replaced by C_F resulting in a reduction of the average multiplicity by a factor of C_A/C_F. This scenario is depicted in figure 1.8 [36]. This asymptotic behaviour, however, holds true only at very large scales [37].

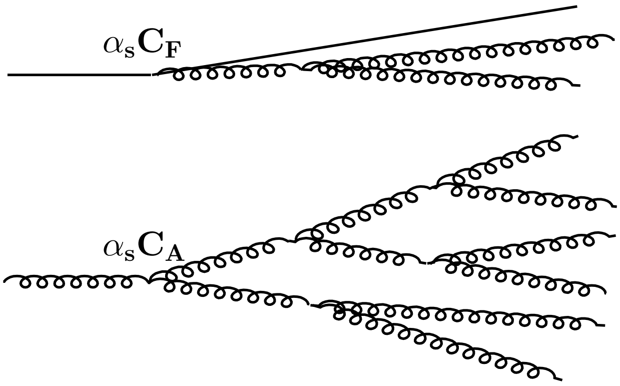

Figure 1.8: The structure of jets initiated by a quark, respectively gluon. Gluon jets in general are broader and contain more particles than quark jets. Typically a quark emits a gluon that develops into a gluon subjet at a lower energy than a jet originally initiated by gluon.

- In order to determine an **angular jet size** an event is classified as two-jet event if all but a fraction ϵ of the total energy is contained within a pair of cones of half-angle δ. According to this definition the angular size of a quark, respectively gluon, induced jet for a given small ϵ in lowest order yields

$$\delta_q \propto \exp \frac{\pi(1-f_2)}{4C_F\alpha_s(s)|\ln\epsilon|} \tag{1.32}$$

$$\delta_g \propto \exp \frac{\pi(1-f_2)}{4C_A\alpha_s(s)|\ln\epsilon|} \tag{1.33}$$

  with $f_2 = \sigma_{2jet}/\sigma_{total}$ [38]. As a consequence the relation between the angular sizes of quark and gluon jets can be expressed as

$$\delta_g \propto \delta_q^{C_F/C_A}. \tag{1.34}$$

  as $C_F/C_A = 4/9$ the angular jet size of gluon jets is larger than that of quark jets, i.e. gluon jets are broader than quark jets.

If jets of equal energy produced under the same circumstances are initiated by either a quark or a gluon the average multiplicity of the jets' constituents (i.e. hadrons, after the fragmentation) is predicted by QCD to be larger for gluon jets. Consequently the particle spectrum is softer and the jet energy is distributed at larger mean angles with respect to the jet axis. Further the fragmentation function of a gluon jet is softer.

Experiments at LEP have confirmed the differences between light quark and gluon jets predicted by QCD [37, 39, 40]. Mean charged multiplicity results of the e^+e^- collider were found to be consistent with HERA measurements [41].

This analysis investigates the jet structure as a means to find the contributions of gluon and quark jets to the hadronic final state and in this way to discriminate the charm production processes.

1.9 Monte Carlo Event Generators

A Monte Carlo event generator is a computer program to model high energy interactions between the incoming particles. The theoretical predictions implemented in this simulation is an integral component of a high energy physics experiment. The defined goal is the description of the complete process from the initial state to the final state consisting of stable hadrons. Random number generators are used to create events according to their theoretical probability. Afterwards a detailed simulation of the detector response is performed. In this way the acceptance and efficiency of the detector for a certain physical process can be studied by reconstructing simulated events analogously to data events.

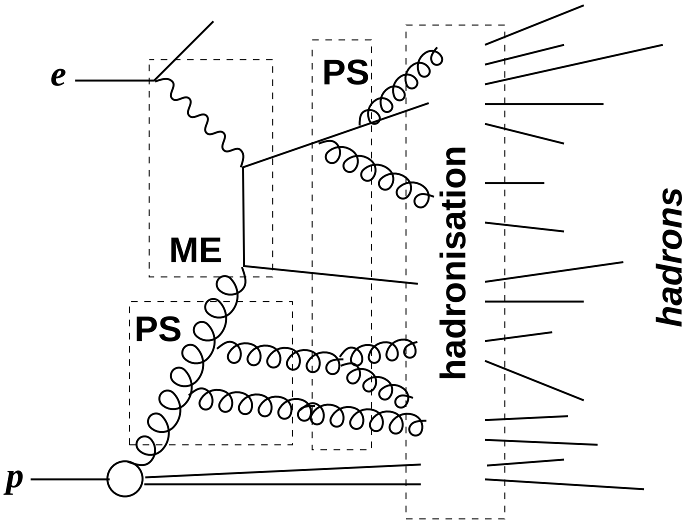

Figure 1.9: Consecutive steps for simulating physics events within a Monte Carlo generator featuring initial and final state parton showers (PS), the hard matrix element (ME) and hadronisation.

Generation of physics events falls into three categories coinciding with the QCD factorisation ansatz. The procedure for the initial state consists of generating parton showers, here particularly emission of gluons. Subsequently the hard matrix element is calculated in leading order perturbation theory. The final state is formed by parton showers and finally hadronisation. This state of the generation consists only of stable particles with lifetimes greater than 10^{-8} s. Later decays are treated in the detector simulation. Figure 1.9 shows the event generation procedure. In this analysis three different Monte Carlo event generators are used. In the following these are briefly introduced.

- The **Pythia** Monte Carlo generator employs DGLAP evolution with on-shell matrix elements. In the current analysis the parton density functions CTEQ5L [42] are used. As renormalisation scale $\mu_r = p_t^2 + (P_1^2 + P_1^2 + m_q^2 + m_{\bar{q}}^2)/2$ with P_1^2 and P_2^2 as the virtualities of the incoming particles is used. It is designed for the photoproduction regime and in this analysis is it used in version 6.1 as a comparison for the photoproduction data. Further it serves to determine reconstruction efficiency, purity and stability in this domain. Eventually the detector correction in photoproduction has been peformed on the base of the Pythia simulation.

- The **RapGap** Monte Carlo generator [43] is based on the DGLAP evolution equations. For the parametrisation of the proton PDF the fit CTEQ6L [44] is implemented and the renormalisation scale $\mu_r^2 = Q^2$ is chosen. In the DIS domain the RapGap Monte Carlo in version 3.1 is compared to the data and the reconstruction is studied in the same way as in photoproduction with the Pythia simulation.
- The **Cascade** Monte Carlo generator [45] applies the k_t factorisation for the initial parton cascade and utilises the CCFM evolution where only gluons are considered. J2003 [46] is employed as parametrisation of the unintegrated gluon density. The renormalisation scale is chosen as $\mu_r = 4m_q^2 + p_t^2$. The Cascade program is applicable to photoproduction as well as DIS. Here it is used in version 1.2 as a cross check comparison with the data. Additionally it is utilised to estimate the systematic uncertainty of the detector correction. In Cascade the hadronic photon component is included in the k_t factorisation, hence no explicit distinction is made between direct and resolved processes.

In addition to the above charm Monte Carlo samples, smaller light quark and beauty samples were studied in order to compare charm jet shapes with those of uds and b.

Chapter 2

HERA and the H1 Experiment

This chapter gives an overview of the HERA accelerator and the properties of the electron and proton beams. Furthermore the H1 detector and its subsystems are presented where special emphasis is put on the systems relevant for this analysis. These include the central tracking detectors, the liquid argon and backward calorimeters as well as the electron taggers and the trigger system.

2.1 The HERA Storage Ring

The **H**adron-**E**lektron-**R**ing-**A**nlage HERA has a circumference of 6336 m and consists of two separate rings for the electrons (respectively positrons) and the protons. Shown in figure 2.1 is the HERA collider and its pre-accelerators. Located in the middle of the four straight accelerator segments are the interaction points where the beams can collide. Two of the four experiments used only one beam. In the HERMES experiment the electron beam was collided with a polarised gas target to investigate amongst others the spin structure of the proton. The HERA-B experiment created nucleon-proton interactions on up to eight wire targets with the aim to verify CP violation within the B system. The two multi-purpose experiments H1 and ZEUS analyse the collision of the proton and the electron beam.

The filling scheme of HERA is defined by 220 high frequency sections, so-called bunches, displaced by 96 ns. Not all of these bunches are filled with particles, however, as a time gap is needed for the extraction of the beams.

The protons are accelerated in three steps before they are injected from PETRA[1] into HERA at 40 GeV. Three of these PETRA trains consisting of 60 bunches each can be filled into HERA. Once inside HERA the protons are accelerated with a high frequency voltage at 52 MHz up to an energy of 920 GeV. The high frequency voltage is superimposed with a 208 MHz system to compress the bunch length. This yields a typical bunch length of 1 ns [2] though also satellite bunches in a distance of 4.8 ns before and after the main bunch are created.

The electrons are accelerated by three pre-accelerators and are injected from PETRA into HERA at 12 GeV where they are further accelerated to 27.6 GeV. The beam profile in flight direction is gaussian and the bunches are short enough to make further compressing dispensable.

---

[1] **P**ositron **E**lektron **T**andem **R**ing **A**nlage

[2] Full width at half maximum

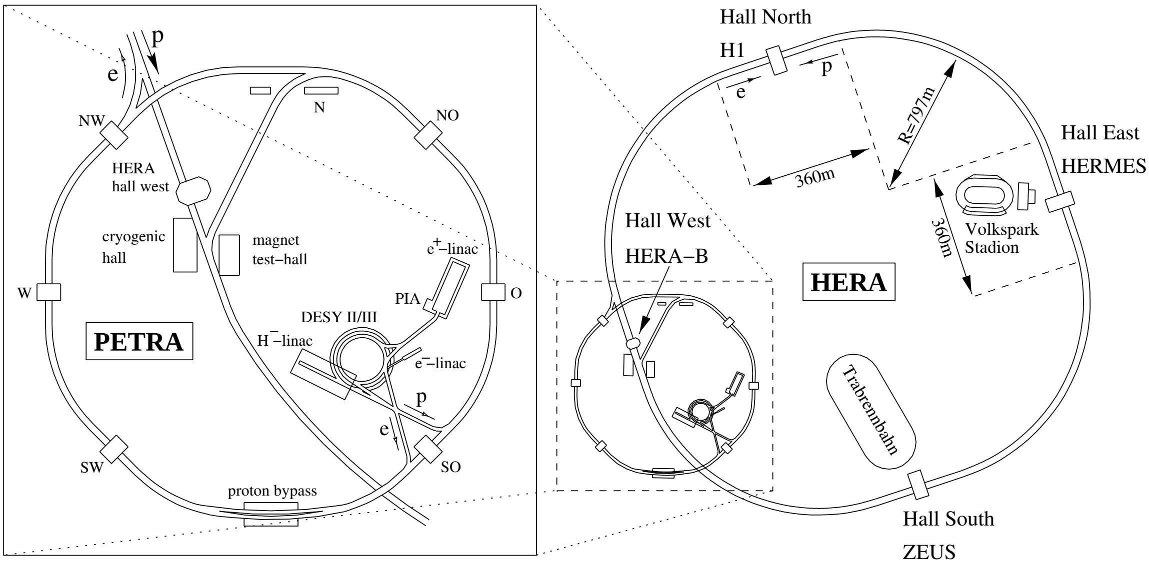

Figure 2.1: The HERA collider and its pre-accelerators.

Located at the beginning and at the end of the PETRA trains are the proton, respectively electron pilot bunches. These do not have a collision partner and are used in the determination of the beam induced background which is important for the measurement of the luminosity.

After successful data taking through the years 1992-2000 (HERA 1) the collider has been upgraded to achieve higher specific luminosity. For this the cross sections of both beams have been reduced by a factor of three to $\sigma_x \times \sigma_y = 118\ \mu\text{m} \times 32\ \mu\text{m}$ while maintaining the beam currents. This required amongst others the installation of super conducting magnets within the H1 and ZEUS detectors resulting in the need to reconstruct the innermost detector regions.

In the beginning of 2004 data taking at H1 was resumed although high background rates in the starting period compromised data taking so beam currents and the number of filled bunches had to be reduced for that time. According to schedule HERA was shut down in June 2007. For the measurement of the longitudinal proton structure function F_L, HERA was operated at lowered proton beam energies during the last months of operation. Figure 2.2 shows the integrated luminosity H1 was able to take during all of the HERA running time.

2.2 The H1 Detector

The H1 detector shown in figure 2.3 is a multi-purpose detector built to investigate the electron proton interaction. Protons run through the experiment in z direction electrons in $-z$ direction, they collide at the interaction point in the middle of the detector. The experiment is constructed to cover as much as possible of the entire solid angle of 4π around the interaction point. It is built asymmetrical with more instrumentation in the forward proton direction to take into account the asymmetrical beam energies.

The following coordinate system is used: The flight direction of the protons defines the positive

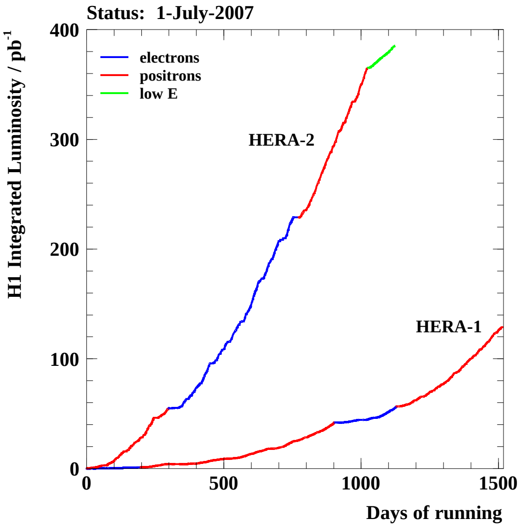

Figure 2.2: Integrated luminosity before (HERA 1) and after (HERA 2) the luminosity upgrade. The slope i.e. specific luminosity has increased drastically since high background rates in the beginning of HERA 2 were reduced and full beam currents were viable.

z direction. Perpendicular the xy plane is spanned by the x axis pointing to the center of the HERA ring and the y axis pointing upwards. The nominal interaction point lies in the origin of the coordinate system. The polar angle θ is defined relative to the z axis, ϕ is the azimuthal angle in the xy plane where $\phi = 0$ corresponds to the x axis.

The H1 detector is built in a shell structure beginning innermost with tracking detectors and followed by the electromagnetic and hadronic calorimeters. The super conducting solenoid generates a magnetic field, uniform in the central tracking region, of 1.15 T. The coil is located outside the calorimeters to avoid adverse effects on the energy measurement of the scattered electron in particular. The iron return yoke for the magnetic flux is instrumented and is used as a muon detector. Table 3.1 shows a list of the detector components of H1.

Throughout the years 2001 to 2003 the H1 detector particularly the tracking detector in forward direction and the trigger systems for the increased interaction rate have been upgraded. One of these projects was the fast track trigger FTT that enables to select events online based on their track signature [47, 48].

The detector components important for this analysis are presented in the following sections. An in-depth description can be found elsewhere [49].

2.3 Tracking

The innermost part of the H1 detector consists of tracking chambers to measure the path of flight of charged particles, i.e. tracks and the event vertex. The magnetic field causes tracks to be curved, the curvature of the tracks allows the determination of the momentum and sign of charge of the particles. Figure 2.4 shows the central tracking system of H1 in the $r\phi$ plane. The following detector

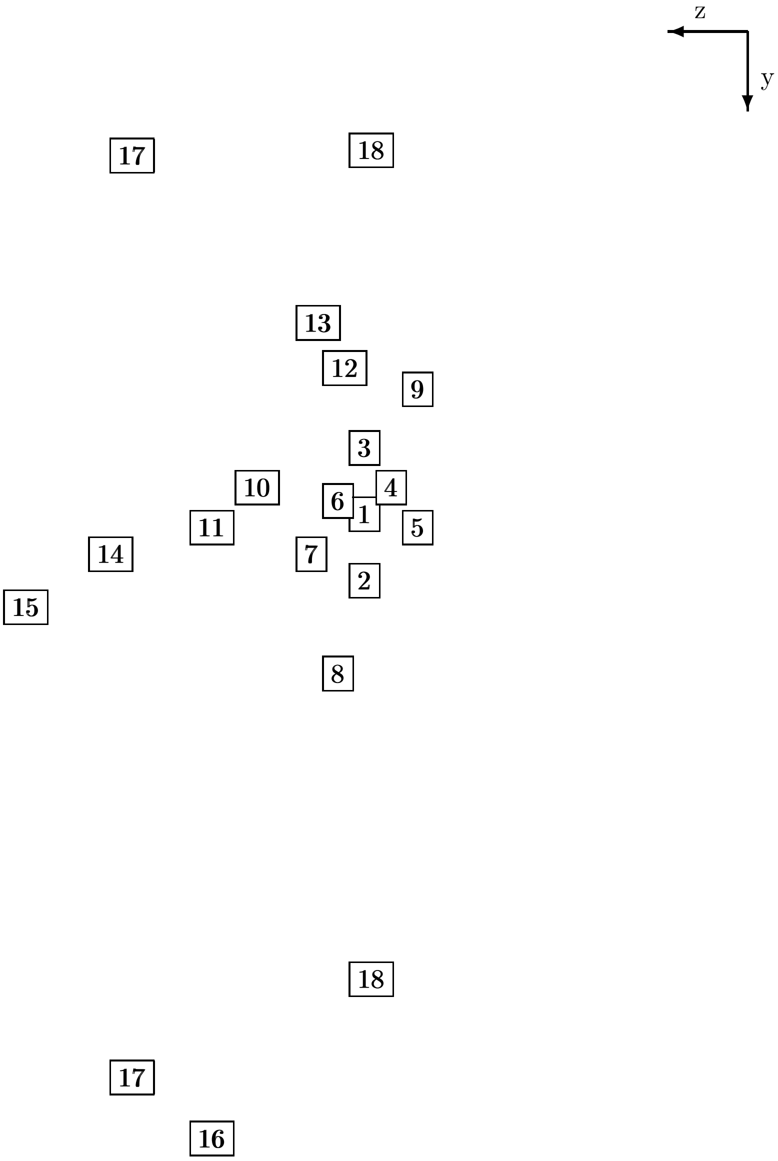

Figure 2.3: Longitudinal drawing of the H1 detector. In table 2.1 the numbered detector components are specified.

Number	Detector Component	Acronym
	Tracking Systems	
1	Central Silicon Tracker	CST
2	Forward Silicon Tracker	FST
3	Backward Silicon Tracker	BST
4	Central Inner Proportional Chamber	CIP
5	Central Outer Z Chamber	COZ
6	Inner Central Jet Chamber	CJC1
7	Outer Central Jet Chamber	CJC2
8	Forward Tracking Detector	FTD
9	Backward Proportional Chamber	BPC
	Calorimetry Systems	
10	Electromagnetic Liquid Argon Calorimeter	LAr em
11	Hadronic Liquid Argon Calorimeter	LAr had
12	Backward Electromagnetic Calorimeter	SpaCal em
13	Backward Hadronic Calorimeter	SpaCal had
	Further Systems	
14	Super Conducting Solenoid	
15	Instrumented Iron Return Yoke/ Central Muon Detector	CMD
16	Forward Muon Detector	FMD
17	Time of Flight System	TOF
18	Super Conducting Focusing Magnets	

Table 2.1: List of the Main H1 Detector Components, cf. figure 2.3

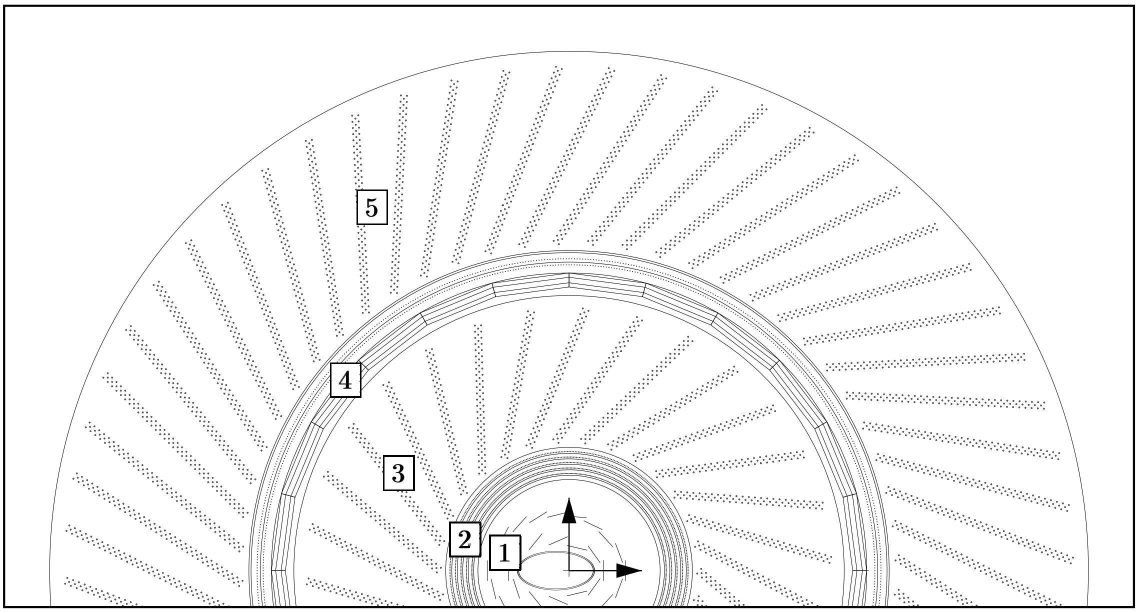

Figure 2.4: Radial view of the central tracking chambers of the H1 detector. From the innermost CST(1) going outwards the CIP(2), CJC1(3), COZ(4) and CJC2(5) are shown. The signal wires in CJC1 and CJC2 are aligned in beam direction and depicted as dots.

components, beginning from the beam pipe and moving outwards, form the H1 tracking system: The central silicon tracker (CST) is supplemented in forward and backward direction by the other two silicon detectors FST and BST, respectively. The central inner proportional chamber (CIP) is used for online event selection through determination of the origin of tracks in z direction. Next are the two concentrical central jet chambers (CJC1 and CJC2). These measure tracks with high resolution in $r\phi$ and moderate resolution in z direction. To compensate for this the central outer z chamber (COZ) is built in betwen CJC1 and CJC2 to determine the position in z more precisely. In backward direction another proportional chamber (BPC) is installed to measure the angle of the scattered electron.

In the following an overview of the detector components mentioned above is given. Excluded in this overview are the FST and BST systems as these were not used in this analysis (and were not even installed for parts of the HERA 2 data taking period). The forward tracking detector (FTD) figure 2.3 was not used either and will not be mentioned further.

2.3.1 Central Silicon Tracker

The CST [50] performs precision measurements of tracks from charged particles near the interaction point and extracts exact vertex and track information. It consists of two layers attached to the beam pipe in radii of 5 cm and 10 cm, respectively and it is adjusted to the beam pipe's elliptical cross section. As it has only two layers it cannot reconstruct tracks on its own but is used to enhance tracks reconstructed by CJC1 and CJC2. It has double sided sensors that contribute track points in $r\phi$ and z. With the p-doted side the position in the $r\phi$ plane is measured. Together with the CJC the CST reaches a track resolution to the vertex of ~ 40 μm. With the n-doted side the z position is determined in this case with a resolution of ~ 70 μm.

2.3.2 Central Inner Proportional Chamber

The CIP [51, 52] was installed in the course of the HERA 2 upgrade and consists of five active detector layers. As a multi-wire proportional chamber with pad readout its wires are aligned parallel to the beam direction. It encloses the CST as a cylinder with radii from 15.7 cm to 19.3 cm. In z direction it covers an area from $z = -112.7$ cm to $z = 104.3$ cm which corresponds to an angular range in θ from 11° to 169°. With a fast response time of ~ 75 ns the chamber is able to determine the time of the primary interaction t_0 of the event and is used for online event selection. By using masks tracks are reconstructed and their z vertex position is used for the trigger decision.

2.3.3 Central Jet Chamber

The main component of the H1 tracking system is the CJC [54]. It consists of two separate chambers: the inner CJC1 and the outer CJC2. Both chambers have an overall lenght in z from -112.5 cm to 107.5 cm. The CJC enloses the CIP concentrically with an inner radius of 20.3 cm and an outer radius of 84.4 cm. Requiring that the track is fully confined to at least CJC1 a coverage in θ of $20^\circ - 160^\circ$ is reached. CJC1 (2) is subdivided into 30 (60) cells each of which contains 24 (32) signal wires in the center. These cells are tilted by 30° to account for the Lorentz angle. As a consequence, the tracks, curved by the magnetic field, cross at least one cell border and can thus be measured in at least two cells. To reconstruct the location of a hit drifting times of the charges from that location to the signal wires are analysed. With knowledge of the position of the wires, drift times and drift velocities the exact point in space of a hit is computed. A priori it is unknown from which side charges drift towards the wire. This leads to a right-left ambiguity. Thus for each hit a so-called mirror hit is reconstructed. However this ambiguity can be resolved for most tracks because the wires are slightly staggered.

Through the curvature of tracks caused by the magnetic field the transverse momentum of the particle can be determined from the reconstruction of the track in the $r\phi$ plane. Here the CJC has a resolution of $\sigma_{p_\mathrm{t}}/p_\mathrm{t} = 0.005 p_\mathrm{t}\ \mathrm{GeV}^{-1} \oplus 0.015$ [53].

2.3.4 Central Outer Z Chamber

The cylindrical COZ is positioned between CJC1 and CJC2. Its active length is 2160 mm and its inner and outer radii are 920 mm and 970 mm, respectively. This corresponds to a θ coverage of $25^\circ - 155^\circ$. While the CJC has a high resolution in $r\phi$, measurement of z by charge division has a resolution of only $\sigma_z \approx 22$ mm per single hit. Like the CJC the COZ is a drift chamber, but here the signal wires are perpendicular to the z axis so the z position can be determined exactly by measuring the drifting times.

The chamber consists of 24 identical rings each measuring 9 cm. Each ring is subdiveded in ϕ by the supporting bars into 24 drifting cells. Three pairs of potential wires and four signal wires are located within each cell totalling 96 signal wires. The z resolution of the chamber is $\sigma_z \approx 350\ \mu m$ [54].

The thickness of the COZ is 1.5 % of a radiation length X_0 for particles passing perpendicular through the chamber which causes interaction of these particles (energy loss, conversion, multiple scattering) between CJC1 and CJC2. This fact has to be considered when fitting tracks passing through CJC1 as well as CJC2.

2.3.5 Backward Proportional Chamber

The BPC is located in backward direction at $z = -146$ cm directly in front of the backward calorimeter (SpaCal). It has the shape of a hexagon with a hole in the center for the beam pipe. The radius of this hole is about 140 mm the outer diameter is about 1600 mm. The BPC is divided into an upper and a lower part divided by a horizontal non-sensitive strip with a width of 80 mm. The six layers of wires are arranged in three groups rotated by 60° each. The chamber is 136 mm thick which equals 0.116 radiation lenghts X_0.

The BPC supports the SpaCal in the measurement of the scattering angle θ of the electron. It has a resolution of $\sigma_\theta = 0.5$ mrad. Its alignment uncertainty causes a systematic error of $\sigma_\theta^{\text{syst.}} = 0.8$ mrad [55].

2.3.6 Track Reconstruction

Within the solenoid field of the H1 detector charged particles follow a circular path in the $r\phi$ plane by the magnetic field applied in z direction. Thus tracks are described by a helix with the five parameters $\kappa, d_{CA}, \phi, \theta, z_0$. κ is the curvature of the track and a measure of the transverse momentum p_t following the relation

$$p_\text{t} = -Q \cdot 0.29979 B_z[\text{T}] \cdot \frac{1}{\kappa[\text{m}^{-1}]}$$

where $B_z[\text{T}]$ is the magnetic field in z direction and Q is the charge of the particle. The distance of closest approach (d_{CA}) is the smallest distance in the $r\phi$ plane from the origin of the coordinate system. Instead of d_{CA} it is common to use the smallest distance d'_{CA} from the track to the primary event vertex. The azimuth angle ϕ is the angle of the track in the $r\phi$ plane at the d_{CA}. The polar angle θ is the angle between the track and the z axis. z_0 denotes the distance in z from the event vertex to the d_{CA}.

These parameters can be determined by a circle fit in the $r\phi$ plane and a linear match in rz to the hits in the tracking detectors. Simplified the method first assigns the hits to a track [56, 57]. Initially this assignment is performed for CJC hits in the $r\phi$ plane. After this provisional fit hits from the other tracking systems are successively added and the track fit is repeated. This yields tracks without the constraint of a common origin i.e. the event vertex.

Based on these tracks the event vertex can be pinpointed in the $r\phi$ plane. The tracks originating from the event vertex in the $r\phi$ plane are then used to compute the z position of the event vertex (z vertex). The vertex position in the $r\phi$ plane only varies by a few 100 μm because the beams' radial extension is very limited. The z vertex position however varies up to ±35 cm. Generally the primary event vertex can be determined with a very high resolution as information of many tracks are combined. For tracks compatible with this event vertex, the fit is repeated with the vertex as additional node in $r\phi$ and rz.

This leads to two different kinds of tracks: Vertex fitted tracks have an additional precice point of reference combining information from several tracks. Non vertex fitted tracks do not use this supplemental information.

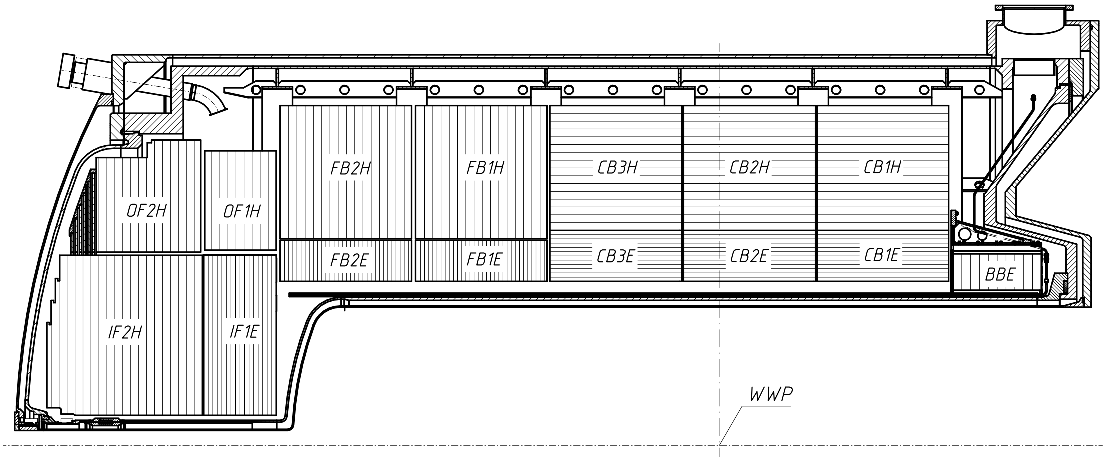

Figure 2.5: Side view of the liquid argon calorimeter. Visible is the separation into particular wheels. 'E' denotes the electromagnetic, 'H' the hadronic sections.

2.4 Liquid Argon Calorimeter

The liquid argon calorimeter (LAr) covers the central and forward region of the H1 detector in the angular range of $4° < \theta < 153°$. It is divided into two sections, the electromagnetic and the hadronic one. The electromagnetic section is the innermost, i.e. closer to the interaction point, part and it measures the energy of photons and electrons. The energy of hadrons is determined by the electromagnetic and the outer hadronic section.

The LAr calorimeter is a sampling calorimeter with active layers of liquid argon and absorbers of lead in the electromagnetic and of stainless steel in the hadronic section. The thickness of the elecromagnetic part is equal to about 20-30 radiation lengths while the hadronic part's is equal to 4.7-7 interaction lengths. Both parts merge continuously, i.e. there is no dead material between them. The calorimeter is divided into eight wheels in z-direction each of which consists of eight identical octants. The absorber plates are always aligned such that particles originating from the interaction point impact with an angle larger than 45°. To keep the argon in a liquid state the entire calorimeter is located within a cryostate.

The LAr is a non-compensating calorimeter, it has on average a larger response for electromagnetic compared to hadronic energy depositions. A software weighting algorithm is applied to correct for the electromagnetic shower fraction of energy depositions caused by hadrons, examining shower shapes. Since the shape of low energetic hadronic depositions is irregular, for energy depositions below $\sim 7-10$ GeV in a specific cone weighting factors are applied without detailed analysis of the shower shape.

The high granularity of all in all roughly 45000 channels ensures a reasonable separation of electrons and pions as well as a high angular resolution. The electromagnetic section reaches an energy resolution of $\sigma_E/E \approx 11\%\sqrt{E/\mathrm{GeV}} \oplus 1\%$. The hadronic section reaches $\sigma_E/E \approx 50\%\sqrt{E/\mathrm{GeV}} \oplus 2\%$ [58]. Despite the long time a full signal takes to be collected and the large number of channels trigger signals for the online event selection can be generated within the latency time of 2.3 μs of the first trigger level (see trigger section), e.g. high local energy deposition is a

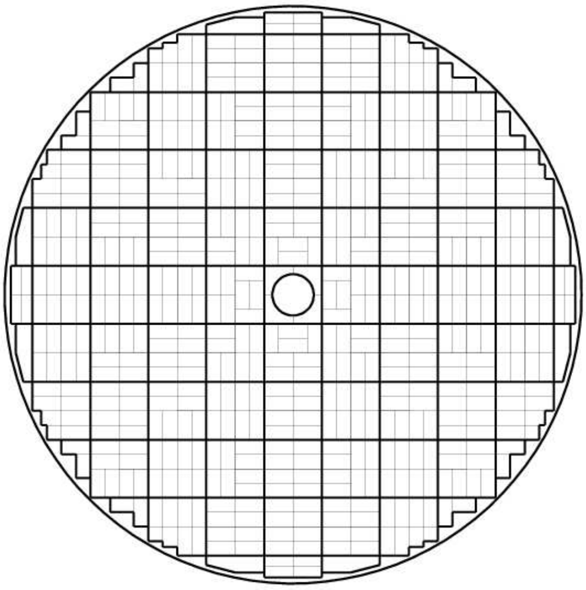

Figure 2.6: Drawing of the SpaCal (electromagnetic section). The thin lines represent the division into submodules. Eight submodules are combined into a module (strong lines).

typical trigger condition.

2.5 SpaCal

The spaghetti calorimeter (SpaCal) is located in the backward region of the H1 detector. It is a sampling calorimeter as the LAr and it uses lead as absorbing and scintillating fibres as active materials [59]. It is located behind the backward proportional chamber (BPC) at $z = -1.6$ m. Its diameter is 160 cm. Like the LAr the SpaCal consists of an electromagnetic and a hadronic section. Shown in figure 2.6 is an $r\phi$ view of the electromagnetic part.

The electromagnetic section consists of roughly 1150 quadratic cells with side length of 40.5 mm and a depth of 250 mm. This depth amounts to a thickness of 27.47 X_0, i.e. electrons deposit their entire energy within the electromagnetic part of the SpaCal. Pairs of cells are grouped into submodules, a group of eight submodules forms a module.

Scintillating fibres are embedded in into the lead absorber in z direction. With a diameter of 0.5 mm, a ratio of 2.27 between absorbing material and fibres and a Moliere radius of 25 mm the electromagnetic shower mostly covers several cells which considerably improves the resolution of the cluster position. The fibres direct the light out the backward end of the detector where the fibres of each single cell are bundled on a light mixer in front of a photomultiplier. The photomultiplier transforms the light into an electric pulse which is also amplified. A mesh type photomultiplier which can be operated in large magnetic fields is used [60].

The energy resolution amounts to $\sigma_E/E \approx 7\%\sqrt{E/\mathrm{GeV}} \oplus 1\%$ [61] and the scattering angle of

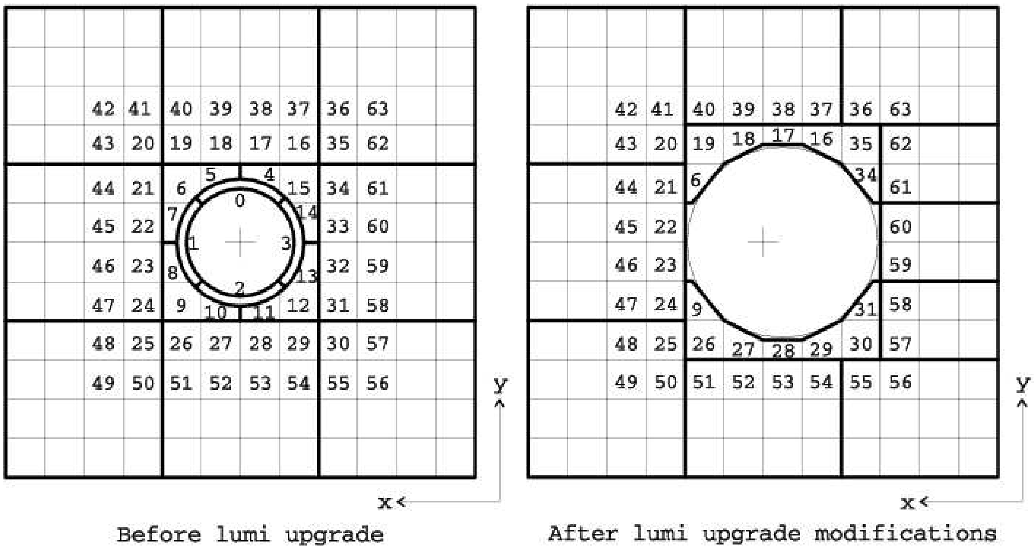

Figure 2.7: The cells of the inner region of the SpaCal before and after reconstruction due to the luminosity upgrade including their numbering. The origin of the coordinate system is illustratd by a cross within the central region.

the electron can be measured with a resolution of ∼ 2 mrad. The time resolution is about 1 ns which predestines the SpaCal to trigger on the scattered electron. It is furthermore possible to supress beam induced background not originating from the interaction point based on time information from the SpaCal.

The hadronic section of the SpaCal is constructed in a similar way as the electromagnetic part. The side length of the cells is about four times the length of the cells in the electromagnetic section and the ratio between absorber and scintillator is 3.4. The depth is as in the electromagntic part 250 mm. This corresponds to only one hadronic interaction length. The main purpose of the hadronic section is to veto hadrons in the process of identifying electrons.

In the course of the luminosity upgrade at HERA the new superconducting GG magnet was installed which caused the necessity to modify the innermost part of the SpaCal. In case of the hadronic section only some of the inner cells were removed. For the electromagnetic part the so-called insert, the structure directly adjacent to the beam pipe, was remodeled. This considerably increased the inner radius. Figure 2.7 shows the electromagnetic section before and after the reconstruction. Within the HERA 2 data taking period only electron scattering angles of $\theta > 174.5^\circ$ [62] can be measured i.e. only photon virtualities $Q^2 > 4$ GeV^2 can be reached. The center of the SpaCal is no longer identical to the origin of the xy coordinate system so the Q^2 acceptance is asymmetrical in ϕ.

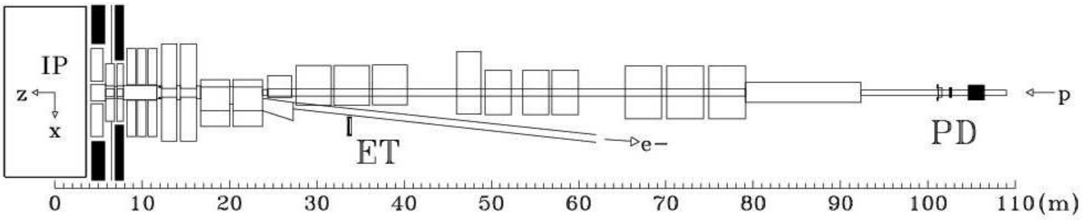

Figure 2.8: The H1 Luminosity system consisting of the electron tagger ET33 at $z = -33.4$ m and the photon detector at $z = -103.1$ m. Not shown here is the second electrn tagger ET44 at $z = -43.2$ m.

2.6 Electron Taggers and Luminosity System

In the years 1999-2000 several systems to detect the scattered electron in photoproduction events (i.e. $Q^2 < 0.01$ GeV^2) were installed at H1. These systems consisted of TlCl/TlBr crystal Cerenkov calorimeters. As the scattering angle for electrons in photoproduction events is too small for them to be detected in the SpaCal these devices were placed close to the beam pipe at $z = -33.4$ m and $z = -43.2$ m and called ET33 and ET44, respectively. Electrons in events with an inelasticity of $0.2 < y < 0.7$ could reach ET33 while the acceptance for ET44 was $0.03 < y < 0.3$. A third electron tagger was installed at $z = -8.0$ m but as its acceptance is poorly understood it is not included in this analysis.

During the luminosity upgrade prior to HERA 2 running (2004-2007) several magnets were added for beam collimation and focusing. For this the electron taggers had to be removed. Though other taggers were installed for periods, namely ET6 at $z = -5.4$ m and in 2006 another tagger at $z = -30$ m, problems with low event yield and little overall data taking, respectively, have kept them from entering this analysis. As a consequence the investigated photoproduction events are limited to HERA 1 running time.

At H1 luminosity is determined by measuring the rate of the Bethe-Heitler process [63]. As the Bethe-Heitler process $ep \rightarrow ep\gamma$ is calculatable in Quantum Electro Dynamics to a precision better than 0.5%, it is well suited for the task. In conjunction with ET33 for HERA 1 and ET6 for HERA 2, respectively, a system to detect the photon formed the H1 luminosity system. This photon detector (PD) was of similar type as the electron taggers and located at $z = -102.9$ m for HERA 1. In HERA 2 the PD was replaced by a sampling calorimeter made of quartz fibres with a tungsten absorber [64] at $z = -101.8$ m. In front of the detector a beryllium filter is placed for background supression as well as a water Cerenkov counter [65].

The electron taggers are only used in the online determination of luminosity and as a crosscheck. Offline only the photon rate in the PD is used for luminosity calculation. A precision better than 1.5% is reached for determination of luminosity in this analysis for HERA 1. For HERA 2 the precision amounts to 2.5% - 5.0%.

2.7 Trigger

At HERA electron and proton bunches collide every 96 ns. This leads to a nominal rate of bunch crossings of 10.4 MHz. The rate of expected electron proton scattering events is several kHz. Background events produce a rate three orders of magnitude higher than sought after physics events. Reading out the H1 detector after an event takes about 1.4 ms during which the detector is unable to register new events. To reach a dead time of less than 10%, the maximum read out rate of the detector is limited to 50 Hz [66]. Thus an effective trigger system must be able to supress background as well as to select only those physics events of interest for later analysis.

To accomplish these goals the trigger system in H1 consists of four levels. On each level the event rate is gradually reduced while the time available to analyse the remaining events increases. Thus on higher trigger levels more complex investigations can be made and more detector information can be considered in the decision to keep or reject an event. Level four finally selects events after the complete detector has been read out. In total the input rate decreases from 10 MHz at level 1 (L1) to 50 Hz at level 4 (L4). The maximum output rate at L4 is 10 Hz to 50 Hz which is the rate at which events are permanently stored. The functuality of the H1 trigger levels is as follows [67]:

L1: At trigger level one a decision is made based on special trigger signals from various detector components. Such a trigger signal, e.g. energy deposition in the liquid argon calorimeter, forms one of the 256 so-called trigger elements. Logical combinations of trigger elements are called subtriggers and an event is kept if at least one subtrigger gives a positive decision. All subdetectors store their data in a 2.3 μs pipeline i.e. the data of 24 bunch crossings are stored in this pipeline simultaneously. Within this time the L1 decision to keep an event has to be taken. If this is the case the pipeline is stopped. The time until the pipeline is restarted is the so-called deadtime in which no further data can be collected.

To reduce the rate of a particular subtrigger it can be scaled down by a specific factor n (prescale). In this case only every nth positive decision of this subtrigger is considered in the further chain of data taking basically reducing the integrated luminosity felt by this subtrigger.

The L1 output rate should not be significantly above 1 kHz, otherwise latency time of L2 would contribute significantly to the overall dead time.

L2: After a positive L1 decision the second trigger level begins its calculation. Data from level one are at the disposal of the L2 trigger systems. The topological triggers and neural networks combine information of different subsystems. Since the year 2005 also the so-called fast track trigger refines its L1 decision on L2. These three systems transmit their decision as up to 96 trigger elements which again are combined to subtriggers. Usually one L2 subtrigger validates exactly one corresponding L1 subtrigger though not every L1 subtrigger has an associated L2 condition. The L2 decision whether to reject an event or to start the full detector readout has to be made within 20 μs. Since in HERA 1 trigger level three was not active the L2 output rate had to be below 50 Hz. In HERA 2 the rate could be up to 200 Hz.

L3: Activated within the scope of the commissioning of the fast track trigger in 2005 trigger level three uses information from level 2 track trigger and other trigger systems. It consists of 16 circuit boards that analyse the data and validates the L1 and L2 decisions. Should all boards make a negative decision data read out is aborted. The level three decision has to be taken within 100 μs.

L4: After complete read out of the detector all data from the event are sent to a computer farm. Here a complete reconstruction of the event is performed. Afterwards the event is classified into an L4 event class. It is judged by this classification whether an event is rejected or kept. If they belong to a physics event class, e.g. specific final state finders select them or a scattered electron with sufficient high Q^2 has been identified, they are kept. For crosschecking also a small fraction of the events not classified into a physics class is kept with an according weight factor, the so called L4 weight.

The maximum decision time on L4 is 100 ms.

Even with the above trigger setup it is not always possible to maintain the required rate reduction. The prescale factor mentioned in the L1 description is the only viable solution to exploit the largest possible part of the total bandwidth. As the rates however are strongly dependent upon the instantaneous luminosity and the current background conditions the prescale factors are dynamically adjusted to ensure a virtually constant L4 input rate. By means of weight factors determining priority it is possible to automatically divide the available L4 input rate onto the particular subtriggers.

Chapter 3

Analysis Strategy

In this analysis the production mechanisms involved in charm production at HERA in photoproduction and deeply inelastic scattering are explored. These are in leading order QCD represented by direct, resolved and excitation processes (cf. chapter 1). In the direct processes ($\gamma g \to c\bar{c}$) and in the 'normal resolved' processes ($gg \to c\bar{c}$) a charm quark pair is produced in the hard interaction. By contrast in the excitation processes ($qg \to cg$ and $gg \to cq$) that are supposed to represent the largest fraction of the resolved photon processes [69] the products of the hard interaction are a charm quark and a gluon.

A charm enriched event sample is studied consisting of dijet events where one jet is tagged by a $D^{*\pm}$ meson in the so-called golden decay channel $D^{*\pm} \to D^0\pi_s^\pm \to K^\mp\pi^\pm\pi_s^\pm$ (cf. section 4.4) to originate from a charm quark. The origin of the second jet is investigated by exploiting its internal structure. The structure of this 'analysed jet' is expected to depend mainly on the type of the primary parton. It can originate from a charm quark, a gluon or a light quark. Hence this approach is sensitive to differences between $c\bar{c}$ and cg types of events.

3.1 Experimental Signature of Resolved Processes

Direct and resolved processes differ in the way in which the photon participates in the hard interaction. In direct processes the photon enters the hard interaction directly while in resolved processes the photon interacts via hadronic states. The structure of the photon is resolved and only one parton takes part in the hard subprocess. The difference between these two types of photon interaction is reflected in the fraction of the photon momentum entering the hard inteaction. The variable x_γ^{obs} represents the fraction of the incoming photon energy which participates in the production of the two highest-p_t jets. In this analysis it is defined as

$$x_\gamma^{\mathrm{obs}} = \frac{\sum_{h\in\mathrm{Jet1}}(E-p_z) + \sum_{h\in\mathrm{Jet2}}(E-p_z)}{\sum_h (E-p_z)}. \tag{3.1}$$

where the sums in the numerator run over the particles associated with the two jets and the one in the denominator over all detected hadronic final state particles. The method for reconstructing the variable x_γ^{obs} is discussed in detail in section 4.6.

Direct and resolved events tend to populate different regions in the x_γ^{obs} distribution. For direct processes x_γ^{obs} approaches the value one because the hadronic final state consists of only the two hard jets and the proton remnant in the forward region which contributes little to $\sum_{h\in\mathrm{h}}(E-p_z)$. In resolved processes, x_γ^{obs} can obtain values much closer to zero.

In this analysis the jet structure in direct enriched and resolved enriched event samples is studied. These samples are defined by $x_\gamma^{obs} > 0.75$ and $x_\gamma^{obs} \leq 0.75$, respectively. This enables to study separately direct and resolved processes.

3.2 Jet Shape Analysis

The basic aspect of this analysis is to distinguish processes using the difference in the jet structure of quark, respectively gluon initiated jets. The most common way of resolving the internal jet structure is to measure the energy distribution perpendicular to the jet axis direction, inspired by the cone-type algorithms. The physical observable used for this purpose is the integrated jet shape $\psi(r)$ [70]. It is defined as the fraction of the transverse momentum of the jet deposited within a cone of radius r around the jet axis with respect to the jet transverse momentum within a cone with larger radius $R = 1$,

$$\psi(r) = \frac{\sum_{i,r_i<r} P_{t,i}}{\sum_{i,r_i<R} P_{t,i}} \tag{3.2}$$

with the sums running over the objects in the hadronic final state. The distance between particle and jet axis r_i is measured in the $\eta\phi$-plane according to

$$r_i = \sqrt{\Delta\eta_i^2 + \Delta\phi_i^2}. \tag{3.3}$$

Here $\Delta\eta_i$ and $\Delta\phi_i$ are the distances of the hadronic final state particle to the jet axis in pseudorapidity η and azimuthal angle ϕ, respectively. The choice of $R = 1$ is motivated by the jet algorithm (cf. section 4.2) and it is supposed that an investigated jet is fully contained within a cone of this radius. The measurement of the the integrated jet shape is indicated in figure 3.1.

The mean over all jets studied within a selected data sample is determined via

$$\langle\psi(r)\rangle = \frac{1}{N_{events}} \sum_{events} \psi(r). \tag{3.4}$$

This mean integrated jet shape is considered separately for the tagged charm initiated jet and the remaining jet with this second jet in the focus of the analysis. For more details on charm selection and jet reconstruction cf. sections 4.2 and 4.4.

As discussed in section 1.8 gluon jets are expected to be broader, contain more particles and exhibit a softer p_t spectrum when compared to quark initiated jets. In terms of the mean integrated jet shape

$$\langle\psi(r)\rangle_{gluon} < \langle\psi(r)\rangle_{quark} \tag{3.5}$$

for all $r < R$. The fraction of the total transverse momentum of the particles within a radius r rises slower for broader jets, i.e. the value at a given radius is smaller.

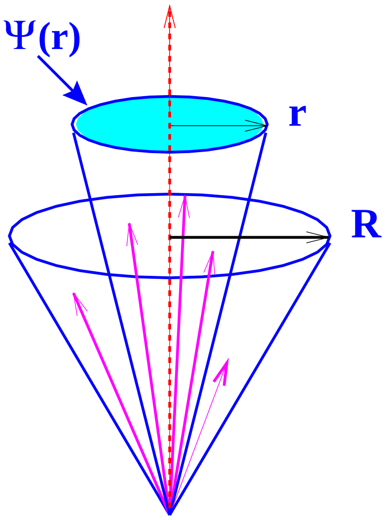

Figure 3.1: Visual suggestion of the integrated jet shape.

3.3 Other Experiments

The concept of jet shape measurement has been realised by several experiments. Selected results are briefly presented in the following.

- At the OPAL experiment at the e^+e^- collider LEP the mean integrated jet shape of light quark, beauty and gluon initiated jets was measured for high jet energies [40]. In figure 3.2 the mean integrated jet shape of gluon jets is compared to uds, respectively beauty jets. The gluon jets exhibit a much broader shape than the uds jets but were found to be similar in shape to beauty jets. All three comply reasonably with pQCD predictions. The analysed charm quark initiated jets in this analysis are expected to more or less resemble light quark jets due to the smaller mass difference between the charm and the strange quark, while the large mass difference between charm and beauty quarks causes a different behaviour in the respective jet shapes.
- At the H1 experiment the mean integrated jet shape was measured for a flavour inclusive dijet sample in DIS [71], shown in figure 3.3 The Monte Carlo model LEPTO predicts a fraction of roughly 80% photon-gluon fusion events with two quarks in the partonic final state, and reasonably describes the measurement. This confirms the expectation of jets in DIS being predominantly initiated by quarks.
- In photoproduction the jet shape of a flavour inclusive sample was measured at the ZEUS experiment [72]. The mean integrated jet shape at the fixed cone radius $r = 0.5$ is shown in figure 3.4 as a function of the jet pseudorapidity. With increasing η_{jet} the jets broaden which is consistent with the increasing fraction of gluon jets. The Pythia description fails to predict the strong broadening in the direction of forward pseudorapidities.
- Another ZEUS measurement was performed on a D^*-tagged photoproduction dijet sample [73, 74]. Figure 3.5 shows the mean integrated jet shape at $r = 0.3$ as a function of η_{jet}. In

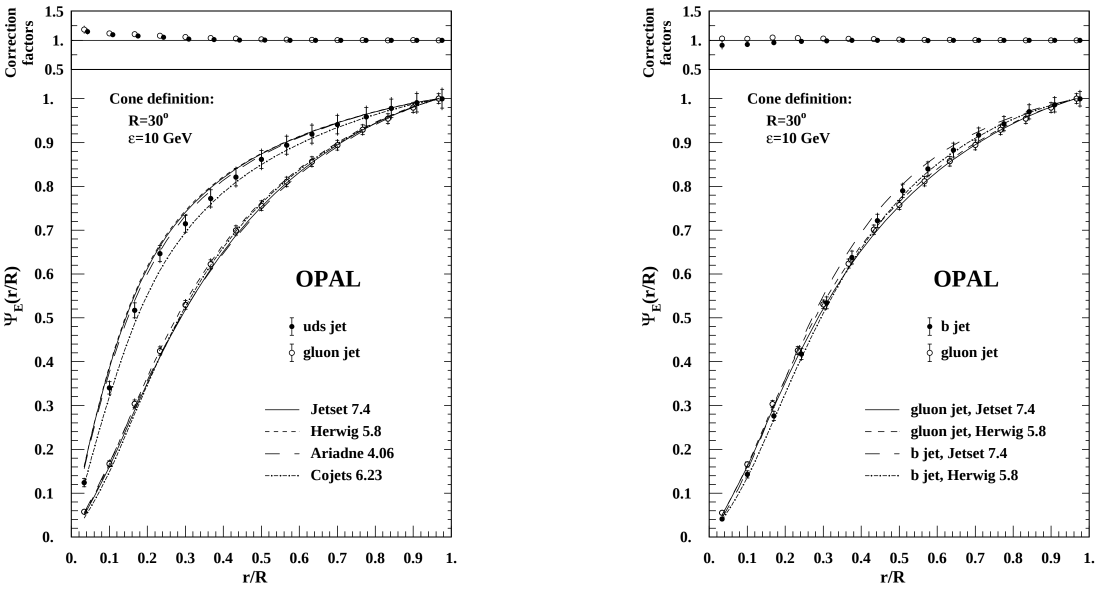

Figure 3.2: Mean integrated jet shape for gluon jets compared to light quark jets (left) and beauty jets (right) as measured by the OPAL experiment.

the most forward η_{jet} bin the total and the direct-enriched samples differ, here the Monte Carlo prediction fails to describe the direct-enriched data.

- In photoproduction a flavour inclusive and a charm-enriched dijet sample was studied at the H1 experiment [35, 75]. The charm tagging is performed by selecting a muon jet, the untagged jet is studied. In figure 3.6 the mean integrated jet shape for two regions of x_γ^{obs} is shown. The lower x_γ^{obs} region is not described by the Monte Carlo simulation, instead the data is compatible with a pure direct sample.

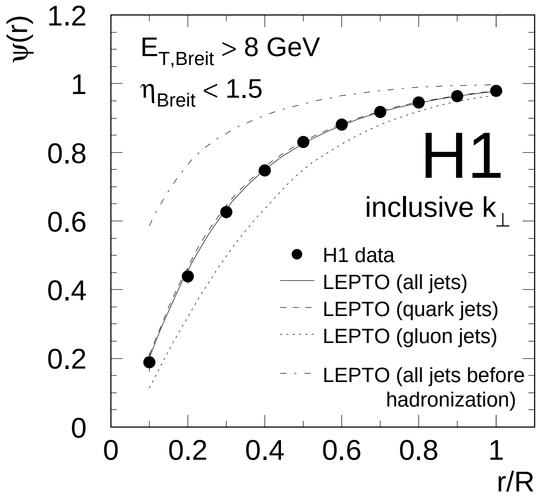

Figure 3.3: Mean integrated jet shape of jets with 10 GeV^2 $< Q^2 \leq$ 120 GeV^2 as measured by the H1 experiment compared to the LEPTO Monte Carlo model.

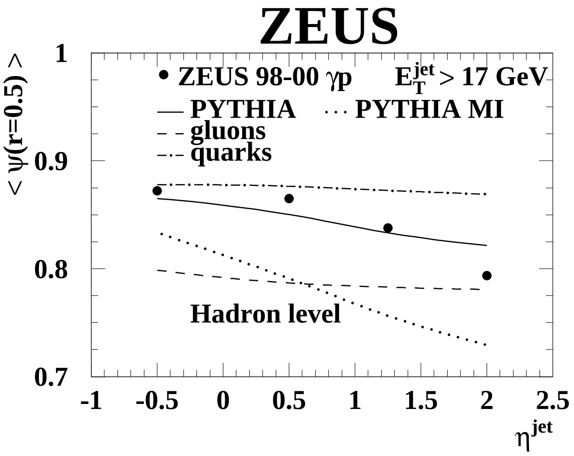

Figure 3.4: Mean integrated jet shape at fixed cone radius $r = 0.5$ as function of η_{jet} in photoproduction as measured by the ZEUS experiment.

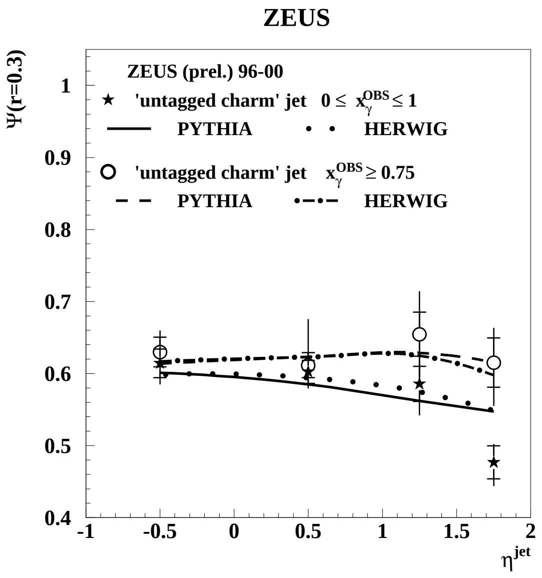

Figure 3.5: Mean integrated jet shape at fixed cone radius $r = 0.3$ as function of η_{jet} in photoproduction as measured by the ZEUS experiment. Shown are the total and direct-enriched dijet samples for $p_{t,jet} > 7(6)$ GeV.

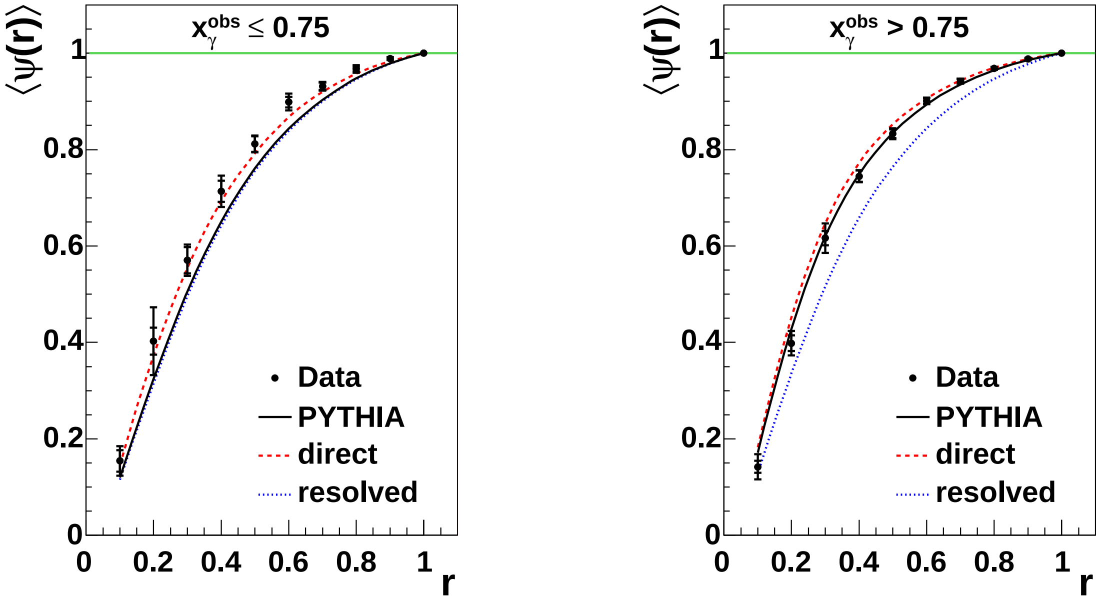

Figure 3.6: Mean integrated jet shape of the untagged jet in the charm-enriched sample for photoproduction. Shown are two different x_γ^{obs} regions and the total Pythia Monte Carlo prediction as well as separate direct and resolved expectations.

Chapter 4

Reconstruction of the Analysis Objects

This chapter describes the reconstruction of different entities essential for this analysis. First the reconstruction of the hadronic final state objects using the Hadroo2 algorithm will be elucidated. These objects serve as input for the jet algorithm necessary to define the jets studied in the analysis. Another important factor is the identification of a charm quark as initiator of a jet. To this end the decay of D^* mesons in the *golden channel* as charm tag is discussed. Finally the determination of the variable x_γ^{obs} as a means to possibly distinguish between direct and resolved processes is discussed.

4.1 Reconstruction of the Hadronic Final State

The particles produced in *ep* scattering can be measured as tracks within the tracking system or as energy depositions in the calorimeters. In the area covered by the CJC tracks can be measured precisely for a transverse momentum up to $p_t = 25$ GeV. The uncertainty of the measurement increases with increasing p_t as discussed in section 2.3.3 whereas the precision of the calorimeter increases (cf. section 2.4). A limiting factor for the track measurement is the fact that only charged particles can be detected within the tracking system, on average roughly one third of the particles are missed by the trackers. The calorimeter detects charged as well as neutral particles except neutrinos. To optimise the use of the full energy and momentum range information from calorimeter and tracking system is combined.

For the identification and measurement of hadronic final state (HFS) objects the Hadroo2 algorithm [76] is used. One of the main features of this algoritm is the choice of the source of information used for the reconstruction of a particle. This choice is based on a comparison of the energy resolution of a track with the corresponding calorimeter cluster. This leads to an important condition for the algorithm: the avoidance of double counting the energy. The problem of double counting appears for particles detected as tracks in the tracking system as well as clusters in the calorimeter. In the case of this scenario the information with the smallest uncertainty in the energy resolution is used.

The HFS objects defined by the Hadroo2 algorithm can consist of appropriate combinations of track and cluster energy information or of only track or only cluster information. The algorithm decides if the HFS objects are determined from the four-vector defined by the transverse momentum of the track or by the cluster energy.

The algorithm starts out with selecting the input information, the tracks and the clusters. The tracks this algoritm uses are from either the central region ($20^\circ \leq \theta \leq 160^\circ$), so-called central tracks, or from the forward region ($6^\circ \leq \theta \leq 25^\circ$), so-called forward tracks. A third class, so-called combined tracks, consists of linked segments from the central as well as the forward region in the range $6^\circ \leq \theta \leq 40^\circ$. The tracks may origin either from the primary or a secondary vertex. The preference of assigning the different classes of tracks to be identified as a HFS or to be combined with a cluster is ordered in the following way: central track, combined track, forward track. The detailed track selection criteria for HFS objects can be found in [76]. In this analysis the pseudorapidity of the HFS objects is limited to the central region thus only central tracks are allowed.

Before the Hadroo2 algorithm is executed the scattered electron is searched for by the electron finder and the track and cluster of this candidate are locked and not used by Hadroo2.

The geometrical position of the CJC with respect to the SpaCal and LAr is taken into account when the cluster position is matched. This is important in order to ensure that the track extrapolation to the calorimeter surface points to the corresponding cluster. Only the LAr and the SpaCal are considered in the calometric measurement while e.g. the energy measured in the instrumented iron from the CMD (tail catcher) is disregarded due to insufficient energy resolution and non-negligible contribution of noise.

As a first particle hypothesis the pion mass is asumed for the tracks. The energy of a track is given by

$$E_{track}^2 = p_{track}^2 + m_\pi^2 = \frac{p_{t,track}^2}{\sin^2\theta} + m_\pi^2. \tag{4.1}$$

with an uncerainty $\sigma_{E_{track}}$ obtained from standard error propagation of

$$\frac{\sigma_{E_{track}}}{E_{track}} = \frac{1}{E_{track}} \sqrt{\sigma_\theta^2 \frac{p_{t,track}^2}{\sin^4\theta}\cos^2\theta + \frac{\sigma_{p_t}^2}{\sin^2\theta}} \tag{4.2}$$

where σ_θ and σ_{p_t} are the errors of θ and p_t of the track while neglecting their correlations. The error of the energy measurement in the case the particle is detected in the calorimeter is estimated to

$$\left(\frac{\sigma_E}{E}\right)_{LAr,expect.} = \frac{\sigma_{E,LAr,expect.}}{E_{track}} = \frac{0.5}{\sqrt{E_{track}}}. \tag{4.3}$$

The uncertainties of equations 4.2 and 4.3 are then compared to decide if tracker or calorimeter provides the superior measurement. The track is considered to be of *good quality* if

$$\frac{\sigma_{E_{track}}}{E_{track}} < \frac{\sigma_{E,LAr,expect.}}{E_{track}}. \tag{4.4}$$

In the central region this is the case for energies up to 25 GeV (12 GeV, resp. 13 GeV for forward and combined tracks). In figure 4.1 the extrapolation of a track as a helix to the surface of the calorimeter is illustrated. Inside the calorimeter the track is extrapolated as a straight line. The calorimetric energy $E_{cone-cyl.}$ is calculated as the sum of all cluster energies for clusters overlapping with the volume of a cone with opening angle $\alpha = 67.5^\circ$ and a cylinder with a radius of 25 cm for the electromagnetic part and 50 cm for the hadronic part.

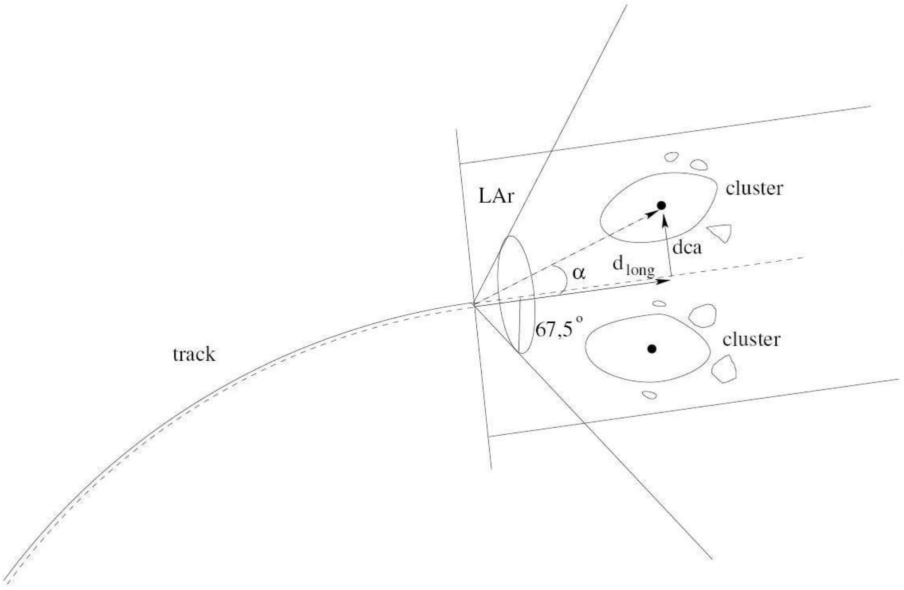

Figure 4.1: Scematic of the combination algorithm. The axis of the cone as well as the cylinder is a straight line extrapolation of the particle trajectory into the calorimeter. The distance of closest approach *dca* of a cluster is defined with respect to this line. This figure was taken from [76].

The energies of the track E_{track} and its associated cluster $E_{cone-cyl.}$ including fluctuations of both measurements within their standard deviations are compared. If

$$E_{cone-cyl.} < E_{track} \cdot \left(1 + 1.96 \sqrt{\left(\frac{\sigma_{E_{track}}}{E_{track}}\right)^2 + \left(\frac{\sigma_E}{E}\right)^2_{LAr,expect.}} \right) \tag{4.5}$$

the track is used to define the HFS object and the corresponding clusters are discarded. For $E_{cone-cyl.} > E_{track}$ it is postulated that one of the clusters originates from the charged particle track and a second from a neutral particle or another track extrapolated into the same calorimetric volume. The energy difference is considered further in the algorithm as a new cluster.

If the track does not fulfill the requirement of being a *good track* (cf. equation 4.4) and

$$E_{cone-cyl.} - 1.96\sigma_{E_{cone-cyl.}} < E_{track} < E_{cone-cyl.} + 1.96\sigma_{E_{cone-cyl.}} \tag{4.6}$$

with $\sigma_{E_{cone-cyl.}} = 0.5\sqrt{E_{cone-cyl.}/\mathrm{GeV}}$ (GeV), the track energy is considered to be compatible with the calorimetric energy deposition. In this case the cluster energy is used to compute the four-vector that defines the HFS object.

After all tracks are extrapolated the remaining clusters are used to form the neutral HFS objects. If more than 95% of the cluster energy are deposited in the electromagnetic part and more than 50% in the first two layers of the calorimeter the energy deposition ocurred most likely due to a photon. In this case the electromagnetic energy scale is used for the cluster energy, otherwise the hadronic energy scale is applied.

Charm events presented in this analysis are well reconstructed by the Hadroo2 algorithm as the HFS particles are dominated by relatively low energies. A typical control distribution for the HFS reconstruction algorithm is the ratio of the transverse momenta p_t of the HFS objects and the scattered electron, called the p_t balance distribution. Figure 4.2 shows the p_t balance distribution of the DIS data presented in section 5.3 and RAPGAP Monte Carlo simulation. The peak position is at a value of one which means the transverse momentum of the hadronic final state is predominantly reconstructed balancing the transverse momentum of the scattered electron.

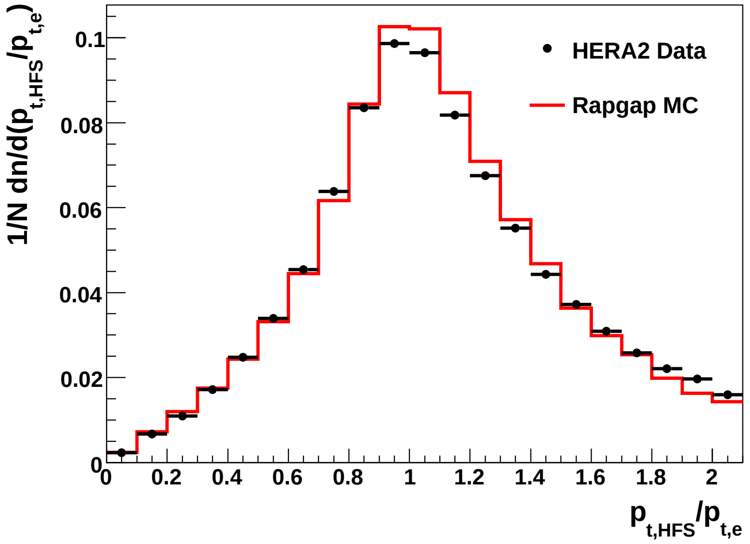

Figure 4.2: p_t balance distribution at reconstruction level. The distinctive peak at the value 1 indicates sensible reconstruction of the hadronic final state. The Monte Carlo model describes the data reasonably well. For further details an the p_t balance see also section 4.3 on jet energy calibration.

4.2 Jet Reconstruction

Quarks do not appear as free particles due to their colour. The quarks produced in the hard interaction, e.g. the BGF process, are fragmenting into hadrons. Due to the limited transverse momenta they produce so-called jets of particles. These jets keep some of the kinematical characteristics of the corresponding quark or gluon though relatively smeared. The reconstruction of these jets of hadrons is performed using jet algoritms. The resulting jets have to be well correlated in momentum and angle with the quarks or gluons which produced them.

One very important requirement for a jet algorithm is that it should be as insensitive as possible to the effects of hadronisation. Furthermore it is of importance that it is collinear and infrared safe: In perturbative QCD divergencies occur whenever two massless partons are parallel (i.e. collinear) or one massless parton has a vanishingly small (i.e. infrared) energy. Both divergencies are cancelled in the total cross section by virtual contributions. For this cancellation also in the jet calculation the treatment of two parallel particles must be identical to the treatment of a single particle with their combined momentum. Similarly the jet must not be affected by the addition of a soft particle. Experimentally the algoritm must be independent of the resolution of the detector.

The jet finder algorithm used in this analysis is the inclusive k_t jet algorithm [77]. Beyond fulfilling the above requirements this algorithm has other advantages like the fact that the cone algorithm problem with overlapping jets[1] is absent [78].

As in any jet finder the used input is a list of partons, hadrons or particle candidates at detector level. The k_t algorithm is defined by separation variable d_{ij} which decides whether the parton or particle i and j are combined or not using the relative transverse momentum and a recombination procedure. This procedure defines how partons or particles are to be combined. In this analysis the algoritm is applied in the laboratory frame using a p_t weighted recombination scheme with the distance parameter $R_0 = 1$, for more details cf. e.g. [79]. The iterative procedure of the algorithm runs through the following steps:

1. The separation variable is defined for every pair of particles:

$$di,j = \min\left(p_{t,i}^2, p_{t,j}^2\right) R_{i,j}^2 / R_0 \tag{4.7}$$

where the distance $R_{i,j}$ in the $\eta\phi$ plane is defined as

$$R_{i,j} = \sqrt{(\eta_i - \eta_j)^2 + (\phi_i - \phi_j)^2}. \tag{4.8}$$

2. A similar quantity as the separation variable is defined for every particle with respect to the beam axis:

$$d_i = p_{t,i}^2, \tag{4.9}$$

$p_{t,i}$ denoting the transverse momentum of particle i.

3. The minimum between the distance of each pair of particles and the distance of every single object with respect to the beam

$$d_{min} = \min(d_i, d_{i,j}) \tag{4.10}$$

is determined.

4. If d_{min} is a single particle distance d_i, the object i is considered a complete protojet and added to the output list. The object i is then deleted from the list of particles to be considered further.

---

[1] The cone-type algorithms are based on finding a jet axis for which the amount of energy inside a cone (axis coincides with the jet axis) with fixed radius has a maximum. A known problem is the overlapping of two jets when the distance in $\eta\phi$ falls below a certain value: In the case of a hard parton splitting into another two partons, at hadron level two jets may be found while there is only one at parton level. Vice versa with two hard partons at the parton level and only identified jet at hadron level.

5. If d_{min} is the distance between two particles $d_{i,j}$, the two objects i and j are merged into a new pseudoparticle κ which is described by the following variables:

$$\begin{aligned} p_{t,\kappa} &= p_{t,i} + p_{t,j}, && (4.11)\\ \eta_\kappa &= \frac{p_{t,i}\eta_i + p_{t,j}\eta_j}{p_{t,\kappa}}, && (4.12)\\ \phi_\kappa &= \frac{p_{t,i}\phi_i + p_{t,j}\phi_j}{p_{t,\kappa}}. && (4.13)\end{aligned}$$

The k_t algorithm then returns to the first step now considering the already formed pseudoparticles and the remaining particles. The iteration of the five steps stops when only protojets are left. The protojets are massless and ardered according to decreasing p_t in the output list. Those protojets with a transverse energy beyond a certain threshold are defined as jets.

In the Monte Carlo simulation jets can be reconstructed on the parton level using partons produced in the hard scattering process after the parton shower. It is also possible to apply the algorithm on hadron level using the hadrons of the Monte Carlo events. On detector level the jet algorithm is run on input from the final state particles in the reconstructed Monte Carlo simulation as well as on data.

In order to compare theory and experimental data both need to be given on the same level. In the present analysis this comparison is done on hadron level. The correction of the data for detector properties is discussed in section 6.5.

4.3 Jet Energy Calibration

The predominant fraction of analysed events is characterised by relatively low values of four momentum transfer squared Q^2 and total transverse momentum p_t of the jets ($p_t \leq 10$ GeV). To improve the absolute scale of the HFS and jet energy measurement in this regime the *Low P_t HFS and Jet Energy Calibration* has been developed by [80]. This calibration has been applied in this analysis and a short overview will be presented below.

The energy measurement of hadronic showers suffers from the limited visible energy, i.e. the measurable energy fraction of the shower. This leads to a poor energy resolution and a systematic deviation resulting in the measured energy being significantly smaller than the energy carried by the hadron that initiated the shower. The energy measurement has to be corrected for these losses in order to reconstruct the energy of the initial hadron.

As electrons and protons in HERA are colliding head-on the total transverse momentum of the initial state is zero, and due to momentum conservation the final state transverse momentum has to be zero as well. This is utilised by balancing the transverse momentum of the HFS against the scattered electron: The electron transverse momentum is determined with high resolution by the reconstruction from the energy and polar angle measured with the backward calorimeter. This information is used to reevaluate the energy deposition of particles in the calorimeter (LAr and SpaCal). Tracks are unaffected by the calibration as these are considered to be well measured.

In order to achieve an accurate calibration the segmentation of the calorimeters is taken into account. This means that different calibration constants are assigned to different parts of the calorimeters. Each part of the calorimeters has its own calibration constant which is applied to all energy clusters measured there. Electromagnetic and hadronic parts of each calorimeter wheel are calibrated separately as the H1 calorimeter is not compensating.

The calibration constants are derived by means of an iterative procedure. For each wheel j of the calorimeter the calibration constants are denoted $\alpha^{it}_{em,j}$ for the electromagnetic and $\alpha^{it}_{had,j}$ for the hadronic calorimeter sections, where it is the iteration step. The initial calibration constants $\alpha^{it=0}_{em,j}$ and $\alpha^{it=0}_{had,j}$ are set to zero. The transverse momentum balance is defined as

$$P^{bal}_t = \frac{P_{t,h}}{P_{t,e}} \tag{4.14}$$

with the transverse component of the HFS four-momentum $p_{t,h}$ and the transverse momentum of the scattered electron $p_{t,e}$. The deviation of p^{bal}_t from unity determines corrections to calibration constants in every iteration step. The following iteration steps are performed:

1. In every iteration a loop over all events in a specially selected calibration sample is performed. For each event total four-momentum of all HFS particles in every calorimeter wheel is calculated as a sum of the three components referring to tracks (which are not further calibrated), electromagnetic and hadronic clusters in the calorimeter:

$$\vec{P}^{it}_j = \vec{P}_{track,j} + \vec{P}^{it}_{em,j} + \vec{P}^{it}_{had,j}. \tag{4.15}$$

2. Calibration constants are applied to the electromagnetic and hadronic clusters and evolve throughout the iteration. Hence the momenta of clusters are modified during the steps:

$$\vec{P}^{it}_{j,em} = \left(1 + \alpha^{it}_{em,j}\right) \vec{P}_{em,j} \tag{4.16}$$

$$\vec{P}^{it}_{j,had} = \left(1 + \alpha^{it}_{had,j}\right) \vec{P}_{had,j}. \tag{4.17}$$

The total four-momentum of the HFS is then the sum of four-momenta in all wheels:

$$\vec{P}^{it} = \sum_{j \in wheels} \vec{P}^{it}_j. \tag{4.18}$$

3. The new calibration constants for each wheel are calculated with the equations

$$\left(1 + \alpha^{it+1}_{em,j}\right) = \frac{\left(1 + \alpha^{it}_{em,j}\right)}{\langle P^{it}_{t,h}/P_{t,e}\rangle_{W^{it}_{em,j}}} \tag{4.19}$$

$$\left(1 + \alpha^{it+1}_{had,j}\right) = \frac{\left(1 + \alpha^{it}_{had,j}\right)}{\langle P^{it}_{t,h}/P_{t,e}\rangle_{W^{it}_{had,j}}}. \tag{4.20}$$

where $\langle P^{it}_{t,h}/P_{t,e}\rangle_{W^{it}_{em,j}}$ and $\langle P^{it}_{t,h}/P_{t,e}\rangle_{W^{it}_{had,j}}$ are the mean values of the $P^{it}_{t,h}/P_{t,e}$ and $P^{it}_{t,h}/P_{t,e}$ distributions weighted by the weights $W^{it}_{had,j}$ and $W^{it}_{em,j}$, respectively. Only the weights differ among the particular wheels in the calibration procedure, all other quantities remain static. These weights are set in every event for all electromagnetic and hadronic calorimeter wheels and depend on the contribution of HFS particles in these wheels to the total P_t balance of the event.

4. Deviations of $\langle P^{it}_{t,h}/P_{t,e}\rangle_{W^{it}_{em,j}}$ and $\langle P^{it}_{t,h}/P_{t,e}\rangle_{W^{it}_{had,j}}$ from unity supply a measure of how well the HFS is calibrated in each iteration step. Convergence of the iteration can be tracked by the quantity η defined as

$$\eta = \sum_{j\in wheels} \left(\left(\langle P^{it}_{t,h}/P_{t,e}\rangle_{W^{it}_{em,j}} - 1 \right)^2 + \left(\langle P^{it}_{t,h}/P_{t,e}\rangle_{W^{it}_{had,j}} \right)^2 \right). \tag{4.21}$$

The calibration procedure is stopped when η reaches zero within a required accuracy.

The weights $W^{it}_{em,j}$ and $W^{it}_{had,j}$ used in equations 4.19 and 4.20 are determined using a P_t-projection weighting scheme. This scheme is sensitive not only to the total transverse momentum, but also to the direction of the momentum vector in the transverse plane. The transverse momentum of the HFS particles in the wheel can then be projected to the direction of the scattered electron and thus obtain the real contribution of these particles to the total transverse momentum in the event (projecting in the direction of the scattered electron is the same as projecting in the direction of the total HFS momentum vector since these are back-to-back). The P_t^{bal} distribution is weighted with $W^{it}_{em,j}$ for the electromagnetic wheels and $W^{it}_{had,j}$ for the hadronic wheels with weights defined in the following way:

$$\begin{aligned} W^{it}_{em,j} &= \left(1+\alpha^{it}_{em,j}\right) \frac{(P_{em,j})_{proj}}{P_t^{ref}} && (4.22)\\ W^{it}_{em,j} &= \left(1+\alpha^{it}_{had,j}\right) \frac{(P_{had,j})_{proj}}{P_t^{ref}} && (4.23) \end{aligned}$$

where

$$\begin{aligned} (P_{em,j})_{proj} &= \left|(P_{em,j})_t \cos\phi_{em,j}\right| && (4.24)\\ \phi_{em,j} &= \arctan\left((P_{em,j})_y \,/\, (P_{em,j})_x \right) - \phi_e && (4.25)\\ (P_{had,j})_{proj} &= \left|(P_{had,j})_t \cos\phi_{had,j}\right| && (4.26)\\ \phi_{had,j} &= \arctan\left((P_{had,j})_y \,/\, (P_{had,j})_x \right) - \phi_e && (4.27) \end{aligned}$$

and ϕ_e is the azimuthal angle of the scattered electron. $\phi_{em,j}$ and $\phi_{had,j}$ is the difference between the azimuthal angle of the total momentum of the uncalibrated particles in the electromagnetic, respectively the hadronic, part of the wheel and the azimuthal angle of the scattered electron. $(P_{em,j})_{proj}$, respectively $(P_{had,j})_{proj}$, is then the transverse momentum $(P_{em,j})_t$, respectively $(P_{had,j})_t$, in the wheel projected in the direction of the scattered electron. The reference variable of the transverse momentum P_t^{ref} can be chosen to be either $P_{t,e}$ or $P_{t,h}$. Here $P_t^{ref} = P_{t,e}$ is chosen as the evolving variable $P_{t,h}$ turns out to lead to divergencies during the iteration process.

The iterative calibration method is successful in calibrating the hadronic final state and achieves to enhance the systematic uncertainty of the absolute energy scale down to 2% [80].

4.4 Charm Selection

In this analysis due to their good experimental signature D^* mesons are used to tag charm production processes. The D^{*+} (D^{*-}) meson is an excited $c\bar{d}$ ($\bar{c}d$) state with a mass of $m_{D^*} =$ 2010.0 MeV ± 0.5 MeV [81]. A charm quark hadronises with a probability of $f(c \rightarrow D^{*+}) = 0.235 \pm 0.0099$ into a D^{*+} meson [82]. The D^* meson decays via the strong interaction and thus has a very short lifetime. In 67.7% of the cases it decays into a D^0 meson and a charged pion. The mass of the D^* meson is only marginally above the mass of the D^0-π system resulting in a very low momentum of the decay particles in the D^* rest frame. Hence this pion is referred to as 'slow' pion, denoted π_s. The D^0 decays via the weak interaction. For the present analysis the decay channel into another charged pion (with the same charge as the slow pion) and an oppositely charged kaon will be studied. This channel

$$D^{*\pm} \rightarrow D^0\pi_s^\pm \rightarrow K^\mp\pi^\pm\pi_s^\pm \tag{4.28}$$

is also called the 'golden' decay channel due to its good experimental signature and the small mass difference between the $K\pi_s$ and the $K\pi\pi_s$ system which will be discussed in the following. The total branching ratio for D^* mesons decaying via the golden channel is $\mathcal{BR}(D^* \rightarrow K\pi\pi_s) = (2.57 \pm 0.06)\%$.

4.4.1 D* Reconstruction

To reconstruct a D^* meson in the golden channel first a decay of a D^0 meson into a kaon and an oppositely charged pion has to be found. To this end the invariant mass of all possible combinations of two tracks in the event are computed using the mass hypothesis of a kaon, respectively pion. If this invariant mass corresponds to the D^0 mass of $m_{D^0} = 1864.5$ MeV ± 0.4 MeV [81] within a window of 400 MeV the track of the slow pion will be searched among the remaining tracks. For this for each of the remaining tracks the pion mass is asumed and the invariant mass of the three particle combination $K\pi\pi_s$ is computed. Instead of cutting on this observable the mass difference between the three particle system and the two particle system

$$\Delta m = m_{K\pi\pi_s} - m_{K\pi} \tag{4.29}$$

is computed. To allow a fit of the background the upper boundary for a D^* candidate is $\Delta m = 0.170$ GeV. The variable Δm is very convenient as several uncertainties concerning the measurement cancel. As a consequence the resolution in the measurement of Δm is mainly governed by the measurement of the slow pion. The nominal value is given as $\Delta m = 145.421$ MeV ± 0.010 MeV [81].

Within this analysis an additional cut on the D^0 mass is performed beyond the initial cut to select D^* candidates. This narrow cut of ±80 MeV around the nominal D^0 mass which correponds to about 2.5 standard deviations drastically reduces the background. Through this it becomes possible to fit the Δm distribution and extract the number of D^* mesons. For the $m_{K\pi}$ distribution no such

D^* Candidate Selection

D^*	Δm	$<$	0.170 GeV
	p_{t,D^*}	$\geq$	2.0 GeV
	$\lvert\eta_{D^*}\rvert$	$<$	1.5
D^0	$\lvert m_{K\pi} - m_{D^0}\rvert$	$<$	80 MeV

Additional Selection for Decay Particles

K, π	$r_{end} - r_{start}$	$>$	17 cm
	p_t	$>$	300 MeV
	$p_{t,K} + p_{t,\pi}$	$\geq$	2.0 GeV
	θ	$>$	20°
	θ	$<$	160°
π_s	$r_{end} - r_{start}$	$>$	11 cm
	p_t	$>$	120 MeV
	θ	$>$	20°
	θ	$<$	160°

Table 4.1: Selection criteria for the D^* candidates and for the tracks considered decay products of the D^* meson. The radii r_{start} and r_{end} denote the first and the last CJC hit of the track.

cut is made, instead the Δm distribution is cut around ±4 MeV around the nominal value. This spectrum serves only as a control distribution.

To efficiently measure tracks in the H1 tracking chambers these tracks need a certain transverse momentum. To this end cuts in p_t are imposed on the D^* candidate and its decay particles. In addition background can be supressed as particles not originating from the decay of a heavy meson tend to have smaller transverse momentum. This particularly reduces the possible tracks for the reconstruction of the slow pion.

As the kaon and the pion carry the additional momentum from the decay of the D^0 meson combinatorial background can be further supressed by cutting on the sum of the transverse momenta from pion and kaon $p_{t,\pi} + p_{t,K}$.

It is furthermore necessary to limit the measurement of the tracks from the decay particles to areas where these tracks can be efficiently reconstructed. Hence it is required for the tracks of kaon, pion and slow pion to be measured within a polar angle θ between 20° and 160° and to have a minimum radial length of 17 cm for kaon as well as pion and 11 cm for the slow pion. The direction of the D^* meson is tightly correlated to the direction of the slow pion but also to the directions of the kaon and the pion accordingly the polar angle θ of the D^* meson needs to constrained. A more common notation is in form of the pseudorapidity $\eta = -\ln(\tan(\theta/2))$. To secure adequate quality of reconstructed tracks the D^* candidate needs to be detected within $|\eta_{D^*}| < 1.5$. Table 4.1 summarises the cuts concerning the D^* reconstruction.

4.4.2 Wrong Charge Combinations

As a means to handle the shape of the background distribution so-called wrong charge D^* candidates are studied. Instead of combining a negatively and a positively charged track to form the D^0 candidate two like sign tracks are merged and combined with a third, oppositely charged track as the slow pion. This means now the three particle system $K^{\pm}\pi^{\pm}\pi_s^{\mp}$ is regarded. This excludes the selection of a real D^0 meson while the wrongly charged background exhibits the same combinatorics and functional form in Δm as the combinatorial background in the signal data sample.

In this analysis the shape of the wrong charge background provides a further constraint in the fit of the Δm distribution. Moreover this background distribution is essential in the statistical subtraction to obtain corrected values for the jet shape in the signal region of the Δm spectrum.

4.5 Reconstruction Methods for the Event Kinematics

The measurement of the event kinematics in tagged photoproduction (i.e. the scattered electron is measured in the luminosity detector) and DIS is overconstrained as it relies not only on the measured properties of the scattered electron. Measurement of the hadronic final state provides a redundant way to determine the independent quantities Q^2 and y. Hence reconstruction of the event kinematics can be based on either the lepton final state, the hadronic final state or a combination of both methods [88].

It is convenient to choose the reconstruction method providing the best precision over the entire kinematic range of interest. In the following the different methods will be discussed in the face of the kinematic regimes governing this analysis.

4.5.1 The Electron Method

In the reconstruction of the event kinematics using the electron method only the polar scattering angle $\theta_{e'}$ and the energy of the scattered electron $E_{e'}$ (E_e denotes the energy of the incoming electron) are required. The photon virtuality is reconstructed in the following way:

$$Q_e^2 = 2E_e E_{e'}\left(1+\cos\theta_{e'}\right). \tag{4.30}$$

The inelasticity is given by

$$y_e = 1 - \frac{E_{e'}}{2E_e}\left(1-\cos\theta_{e'}\right). \tag{4.31}$$

The Bjorken scaling variable x is connected with these two quantities via

$$x_e = \frac{Q_e}{y_e \cdot s} \tag{4.32}$$

where s is the square of the centre of mass energy.

In the range of $y_e > 0.1$ the electron method is very precise, in addition it is experimentally very simple. The resolution of this method is given by

$$\frac{\delta y_e}{y_e} = \frac{1-y_e}{y_e}\left(\frac{\delta E_{e'}}{E_{e'}} \oplus \frac{\delta\theta_{e'}}{\theta_{e'}}\right).^2 \tag{4.33}$$

For $y \to 0$ the resolution deteriorates drastically. By use of the electron method an increase of the phase space towards lower y in DIS is not possible. In photoproduction a large fraction of the data collected with the ETag44 is in the kinematic range below $y > 0.1$. Another problem occurs in the photoproduction sample: Etag33 and Etag44 are not included in the detector simulation

---

[2] $A \oplus B \equiv \sqrt{A^2+B^2}$

of the Monte Carlo calculation, rendering the reconstruction of y_e in the Monte Carlo simulation impossible. Hence this method is avoided in the photoproduction regime of this analysis.

4.5.2 The Hadron Method

The hadron method relies exclusively on the hadronic final state and was introduced by Jacquet and Blondel [89]. When using conservation of longitudinal momentum and energy,

$$\left(E_P^{in} - P_{z,P}^{in}\right) + \left(E_e - P_{z,e}\right) = 2E_e = E_{e'}\left(1 - \cos\theta_{e'}\right) + \sum_{h \in HFS} E_h\left(1 - \cos\theta_h\right), \tag{4.34}$$

with $h \in HFS$ denoting that the sum runs over all hadrons in the hadronic final state, the inelasticity can be expressed in terms of the hadronic final state as

$$y_h = \frac{2E_e - E_{e'}\left(1 - \cos\theta_e\right)}{2E_e} = \frac{\Sigma}{2E_e} \tag{4.35}$$

with $\Sigma = \sum_{h \in HFS} E_h\left(1 - \cos\theta_h\right)$. The sum is performed over all hadronic final state particles neglecting their masses.

The resolution of the inelasticity reconstructed with this method is governed by the hadronic energy resolution:

$$\frac{\delta y_h}{y_h} = \frac{\delta\Sigma}{\Sigma}. \tag{4.36}$$

As the resolution does not diverge for lower inelasticities this method can be used at low values of y.

Analoguosly to the above Q^2 is reconstructed as

$$Q_h^2 = 2E_e\left(2E_e - \Sigma\right). \tag{4.37}$$

Due to limited resolution of the energy in the ETag44 and both electron taggers not being included in the Monte Carlo simulation the hadron method is used in the photoproduction regime of this analysis, as it does mot require the measurement of the scattered electron. Furthermore a good resolution at low inelasticities is required as the photoproduction y-range extends to $y = 0.05$. Figure 4.3 shows the y distribution of Pythia Photoproduction Charm Monte Carlo reconstructed with the hadron method.

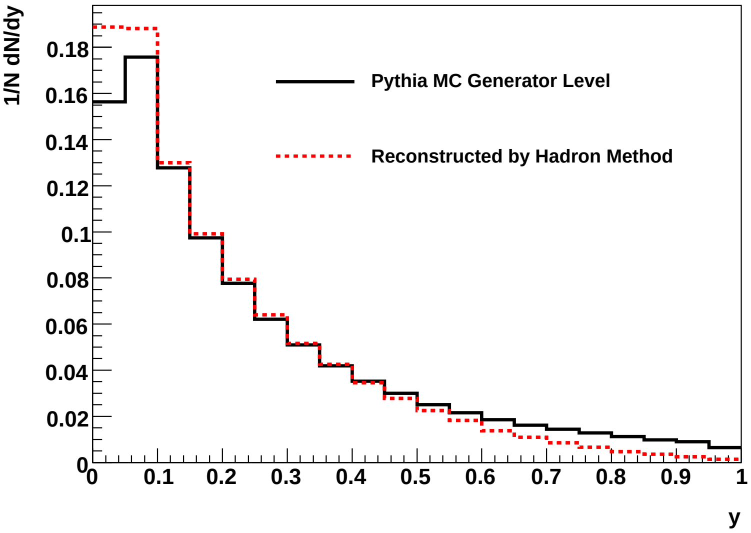

Figure 4.3: Distribution of the inelasticity y in photoproduction on generator level and reconstructed by the hadron method. Due to the Etag acceptances the y-range is limited to $0.05 < y < 0.65$. Within these boundaries the reconstruction method performs reasonably well.

4.5.3 The Σ Method

Emissions of collinear real photons from the incoming electron before the primary interaction with the proton (QED initial state radiation) lead to corrections as the initial electron energy in equation 4.35 is fixed to E_e. By replacing E_e with the initial electron energy deduced from the final state particles this problem is avoided. Using equation 4.34 and combining information from the hadronic final state and the scattered electron yields the Σ method [88]:

$$y_\Sigma = \frac{\Sigma}{\Sigma + E_{e'}\left(1 - \cos\theta_{e'}\right)}. \tag{4.38}$$

Again Σ denotes the difference between energies and longitudinal momenta of all hadronic final state particles $\Sigma = \sum_{h\in HFS}\left(E_h - p_{z,h}\right) = \sum_{h\in HFS} E_h\left(1 - \cos\theta_h\right)$ and is by construction insensitive to losses in forward direction. The resolution is superior to the hadron method and can be written as

$$\frac{\delta y_\Sigma}{y_\Sigma} = \left(1 - y_\Sigma\right)\left(\frac{\delta\Sigma}{\Sigma} \oplus \frac{\delta E_{e'}}{E_{e'}} \oplus \frac{\delta\theta_{e'}}{\tan(\theta_{e'}/2)}\right). \tag{4.39}$$

Within this method the photon virtuality Q^2 is given by

$$Q^2_\Sigma = \frac{E^2_{e'}\sin^2\theta_{e'}}{1 - y_\Sigma} \tag{4.40}$$

and the Bjorken scaling variable x by

$$x_\Sigma = \frac{E_{e'}^2 \sin^2\theta_{e'}}{s \cdot y_\Sigma \left(1 - y_\Sigma\right)}. \tag{4.41}$$

The Σ method archieves good resolutions especially at low inelasticities, the resolution of the photon virtuality is slightly inferior to the e method [90]. Figure 4.4 shows the Q^2 distribution generated by RAPGAP Monte Carlo and the reconstruction by e and Σ methods. While the reconstruction with both methods show good agreement with the generated Q^2 distribution, the e method exhibits slightly superior consistency.

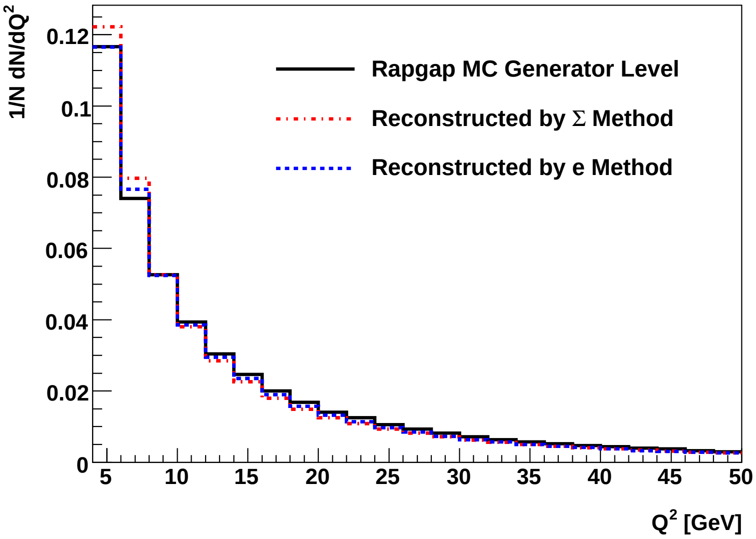

Figure 4.4: Q^2 distribution generated by RAPGAP Monte Carlo and reconstructed via Σ and e methods.

4.5.4 The $e\Sigma$ Method

The $e\Sigma$ method combines the advantages of the e method and the Σ method. At high inelasticities the e method is used while at low y it is reconstructed via the Σ method. The photon virtuality is reconstructed using the e method. The following equations define the $e\Sigma$ method:

$$Q_{e\Sigma}^2 = Q_e^2 \tag{4.42}$$

$$y_{e\Sigma} = \frac{2E_{e'}\Sigma}{\left(\Sigma + E_{e'}\left(1 - \cos\theta_{e'}\right)\right)^2} \tag{4.43}$$

$$x_{e\Sigma} = \frac{Q_e^2}{y_\Sigma \cdot s}. \tag{4.44}$$

In figure 4.5 the y distribution for DIS generated by RAPGAP Monte Carlo and reconstructed via the $e\Sigma$ method is shown. Ratio plots for y_h in photoproduction and for $y_{e\Sigma}$ and $Q_{e\Sigma}^2$ in DIS are shown in figures 4.6 and 4.7. The relative resolutions of the inelasticity y, the negative four momentum squared Q^2 as well as other kinematic quantities is discussed in further detail in section 6.1.2.

Analysis Regime	**Reconstruction Method**
HERA 1 Photoproduction	Hadron Method
HERA 2 DIS	$e\Sigma$ Method

Table 4.2: Summary of the applied reconstruction methods.

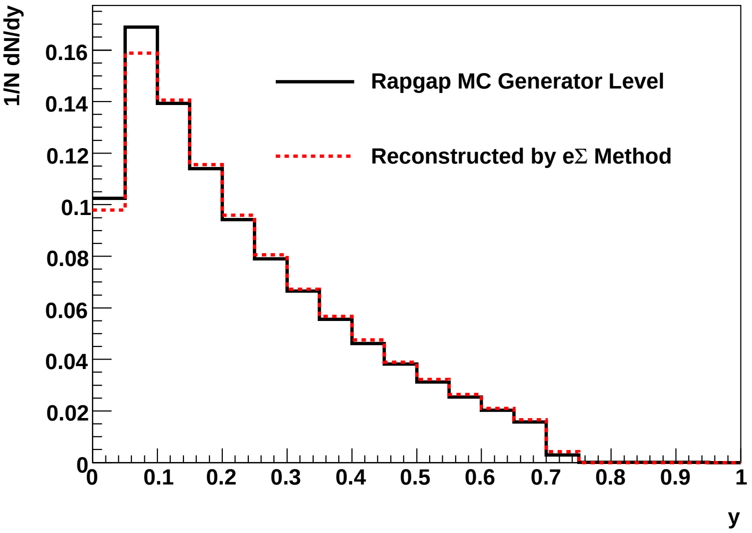

Figure 4.5: Distribution of the inelasticity in DIS on generator level and reconstructed by the $e\Sigma$ method. The polar angle $\theta_{e'}$ of the scattered electron in the Monte Carlo sample is limited to the backward calorimeter region causing a slump at $y = 0.7$ due to the geometrical acceptance of the calorimeter.

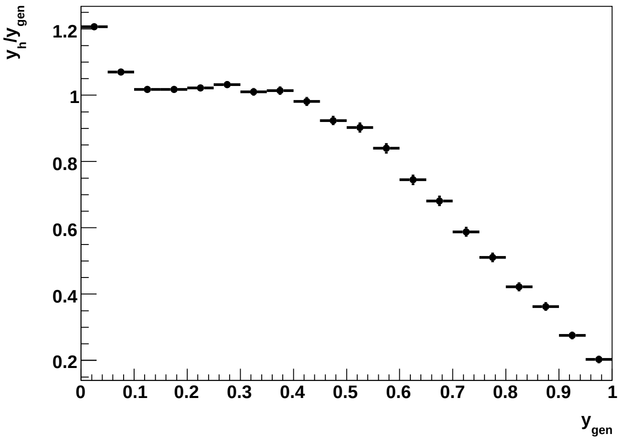

Figure 4.6: Ratio of y reconstructed with the hadron method to generated y with PYTHIA Monte Carlo in the photoproduction regime.

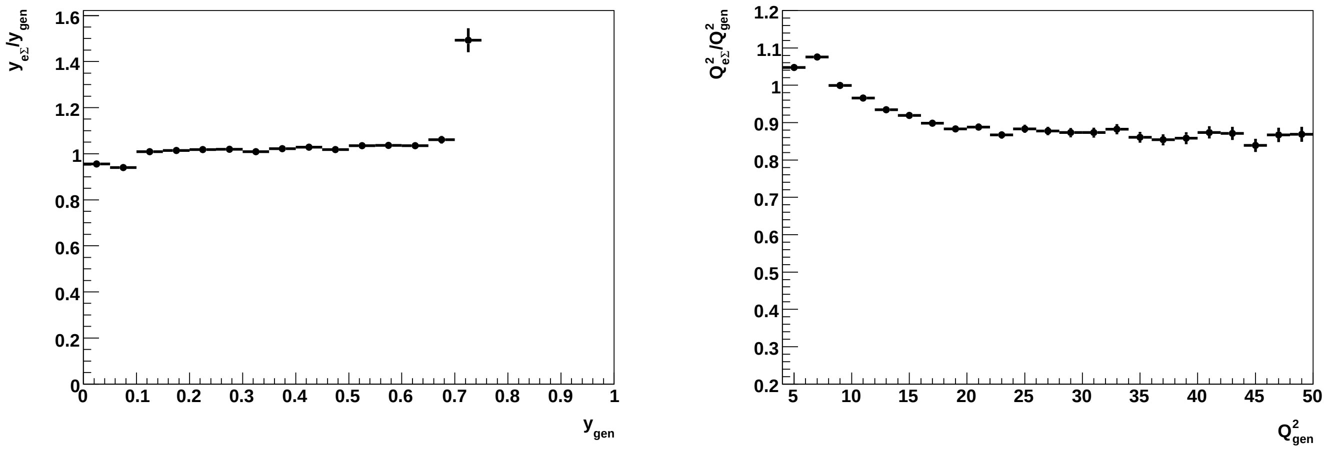

Figure 4.7: Ratio of reconstructed to generated values for y (left) and Q^2 (right) in DIS. Events generated with RAPGAP Monte Carlo, y and Q^2 reconstructed with the $e\Sigma$ method.

4.6 Reconstruction of $x_\gamma^{\mathbf{obs}}$

In analogy to the Bjorken variable x describing the momentum fraction of the struck quark within the proton the variable x_γ represents the fraction of the incoming photon energy which participates in the hard interaction. The momentum fraction carried by the incoming parton from the photon side is in leading order defined in the following way:

$$x_\gamma^{\mathrm{LO}} = \frac{p_{\mathrm{p}} \cdot p_{\mathrm{part}}}{p_p \cdot p_\gamma}. \tag{4.45}$$

Here p_{p}, p_γ and p_{part} denote the four momenta of the proton, the photon and the parton entering the hard interaction from the photon side, respectively. For direct processes equation 4.45 is exatly equal to one, for resolved processes it is smaller than one. In the colinear approximation, i.e. when the parton and the photon have the same direction, x_γ^{LO} can be written as

$$x_\gamma^{\mathrm{LO}} = \frac{E_{\mathrm{part}}}{E_\gamma} \tag{4.46}$$

where E_γ is the photon energy and E_{part} is the energy of the parton from the photon side participating in the hard interaction. In photoproduction E_γ is associated with the beam energy E_{e} via the inelasticity y as $E_\gamma = yE_{\mathrm{e}}$. Thus x_γ can be determined from the transverse energies $E_{\mathrm{t},j}$ and rapidities $\hat{y}_j$ of the outgoing hard partons:

$$x_\gamma^{\mathrm{LO}} = \frac{\sum_{j=\text{outgoing part.}} E_{\mathrm{t},j} e^{-\hat{y}_{\mathrm{j}}}}{2yE_{\mathrm{e}}} \tag{4.47}$$

with

$$\begin{aligned} E_{\mathrm{t},j} &= \sqrt{E_j^2 - p_{z,j}}, && (4.48)\\ \hat{y}_j &= \frac{1}{2}\ln\left(\frac{E_j + p_{z,j}}{E_j - p_{z,j}}\right) && (4.49) \end{aligned}$$

As it is not possible to measure partons directly it is necessary to rewrite equation 4.47 in terms of measurable quantities. To this end the sum over the outgoing partons is replaced by the sum over hadronic jets. In *ep* scattering with two outgoing particles as it is the case in boson-gluon fusion the variable x_γ^{obs} is defined as

$$x_\gamma^{\mathrm{obs}} = \frac{\sum_{\mathrm{jet}=1,2} E_{\mathrm{t,jet}} e^{-\hat{y}_{\mathrm{jet}}}}{2yE_{\mathrm{e}}} \tag{4.50}$$

where the sum in the numerator runs over the two jets with highest transverse momentum within the event. For massless jets $E_{\mathrm{t,jet}} e^{-\hat{y}_{\mathrm{jet}}} = (E - p_z)_{\mathrm{jet}}$. Thus follows

$$x_\gamma^{\mathrm{obs}} = \frac{\sum_{\mathrm{jet}=1,2} (E - p_z)_{\mathrm{jet}}}{2yE_{\mathrm{e}}}. \tag{4.51}$$

Within this analysis this definition will be used in a form that also holds true for deeply inelastic scattering:

$$x_\gamma^{\mathrm{obs}} = \frac{\sum_{h\in\mathrm{Jet1}} (E - p_z) + \sum_{h\in\mathrm{Jet2}} (E - p_z)}{\sum_h (E - p_z)}. \tag{4.52}$$

Here the sum in the numerator runs over all particles associated with the two highest transverse energy jets and the sum in the denominator runs over all detected hadronic final state particles. This is valid for the dijet sample. In the case of only one jet and an isolated D^* meson x_γ^{obs} is defined in the following way:

$$x_\gamma^{\text{obs}} = \frac{\sum_{h\in \text{D}^*}(E-p_z) + \sum_{h\in \text{Jet}}(E-p_z)}{\sum_h (E-p_z)} \tag{4.53}$$

where the first term in the numerator is the sum over the particles the D^* meson decays into, i.e. the kaon and two pions for the golden decay channel. The second term sums over the particles in the analysed jet.

In the above definition x_γ^{obs} is limited to the range $0 < x_\gamma^{\text{obs}} \leq 1$. Direct processes peak at $x_\gamma^{\text{obs}} = 1$ though a smearing is caused by parton showers and hadronisation effects so also values smaller than one are observable. Resolved processes populate the lower regions in the x_γ^{obs} spectrum. Though overlapping a clear separation is possible in photoproduction. For deeply inelastic scattering (DIS) the overlap increases considerably. Figure 4.8 shows charm MC PYTHIA for photoproduction and RAPGAP for DIS. In both cases direct and resolved processes are simulated at detector level, i.e. smearing effects are already included.

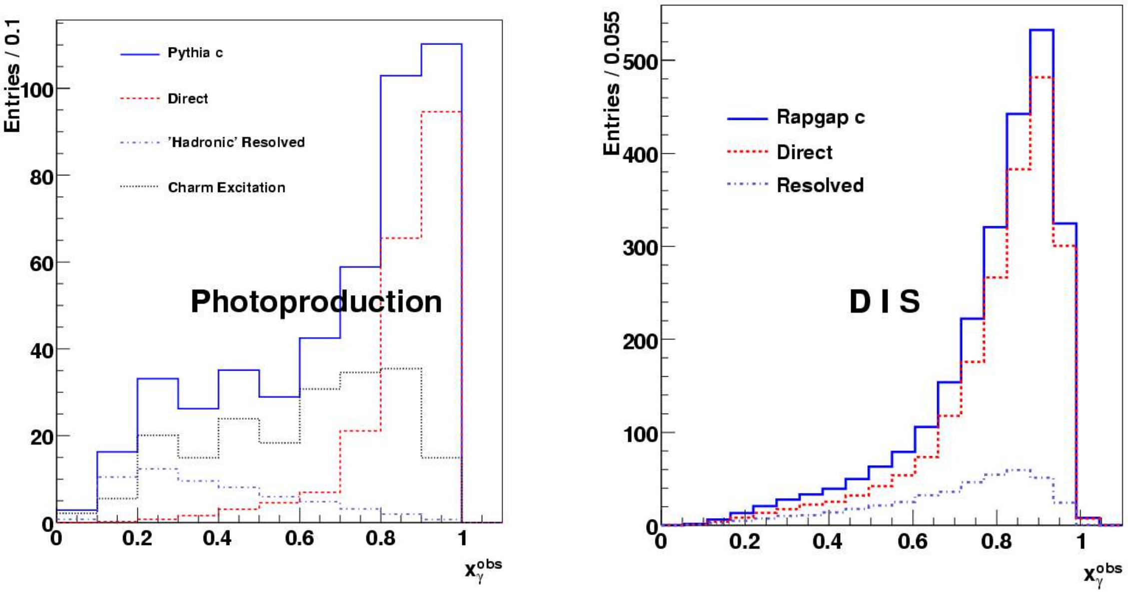

Figure 4.8: Simulated x_γ^{obs} distribution at detector level. Shown to the left is the photoproduction sample by the PYTHIA Monte Carlo Generator. To the right the DIS sample generated by RAPGAP is shown. Both show the samples after final data selection. The distributions are normalised to the integrated luminosity corresponding to the particular data taking period (i.e. HERA 1 Electron Tagger data for photoproduction and HERA 2 DIS data). In the PYTHIA sample the resolved contribution is further subdivided into the normal hadronic-like resolved component and charm excitation processes.

With higher photon virtuality the fraction of resolved events decreases rapidly, i.e. in DIS the fraction of direct events is much larger than in photoproduction which is clearly visible in the figure. By cutting the data sample into two regions of low and high values of x_γ^{obs}, respectively, a sample of resolved enriched events can be obtained at low values for x_γ^{obs}, though this is still dominated by direct events. As the fraction of resolved processes decreases with increasing four momentum transfer Q^2 a further enrichment can be reached by segmenting the sample into a low and a high Q^2 sample, see figure 4.9.

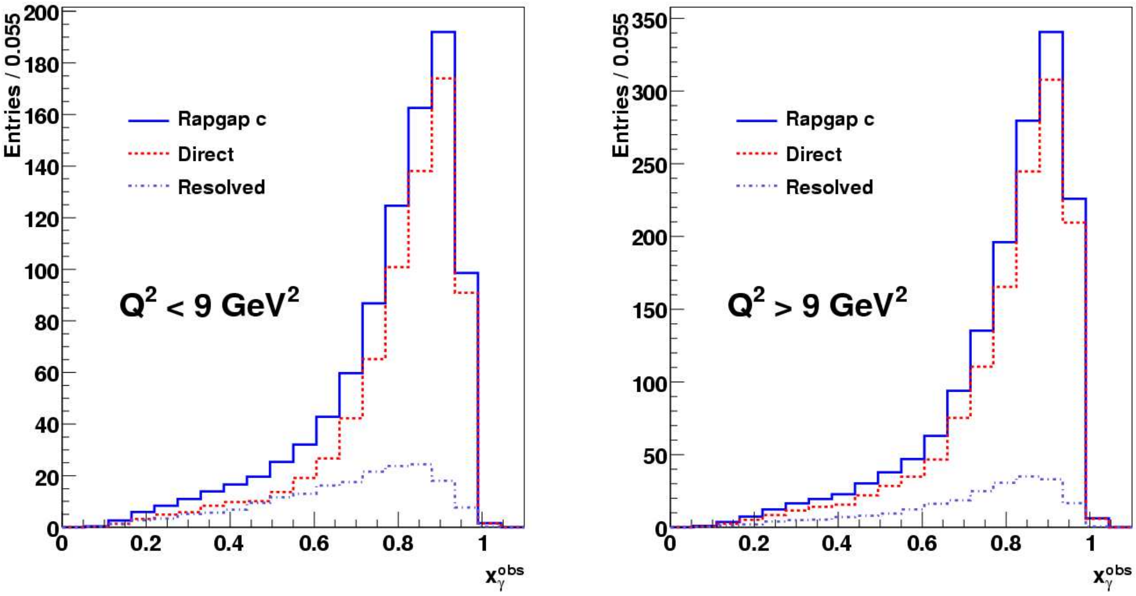

Figure 4.9: Simulated $x_\gamma^{\rm obs}$ distribution for the DIS sample divided into a low and a high Q^2 sample. For $Q^2 \leq 9$ GeV^2 the resolved fraction is nearly equal to the fraction of direct events at low $x_\gamma^{\rm obs}$. The right distribution shows events with $Q^2 > 9$ GeV^2 and is strongly dominated by direct processes.

Chapter 5

Data Selection

In this chapter the criteria for *ep*-events entering the analysis are discussed. The first section explores the general selection of charm jets, while the following sections cover the different data samples: Section 5.2 focuses on the HERA 1 photoproduction data collected by means of the electron taggers installed in the years 1999 and 2000. Section 5.3 covers the selection of the HERA 2 DIS data collected in the years 2004 through 2007. Table 5.5 summarises the final selection cuts.

5.1 Selection of Charm Initiated Jets

The reconstruction of jets and the energy calibration were described in detail in sections 4.2 and 4.3. In this analysis events with at least two jets are selected. While jets associated with charm production tend to have high transvese momenta, in particular higher than the D^* meson used for charm tagging, *uds* background events may show high jet multiplicities but generally have low total transverse momenta. A cut on the transverse momentum of $p_{t,jet1} > 5$ GeV for the highest-p_t jet and a cut of $p_{t,jet2} > 4$ GeV for the second-highest-p_t jet are applied. To ensure good reconstruction the selected jets are limited to a pseudorapidity range of $-1.9 < \eta_{jet} < 1.9$.

In section 4.4 the reconstruction of D^* mesons was discussed. In addition to the cuts defined there for the basic selection of D^* candidates more restricting cuts are applied in the final selection. To drastically suppress combinatorial background and thus enhance the signal-to-background ratio the transverse momentum of the D^* candidate is required to be $p_{t,D^*} \geq 2.6$ GeV. Analoguosly the cut on the sum of transverse momenta of the pion and the kaon is raised to $p_{t,\pi} + p_{t,kaon} \geq 2.4$ GeV. The figures 5.5 and 5.6 show the final Δm distribution and the fit to obtain the total number of D^* mesons for photoproduction. Figure 5.11 shows the same for DIS.

To associate a jet with a charm quark the jet containing a D^* meson is searched for by requiring agreement between the reconstructed direction of the D^* meson and the jet axis. For the jet to contain the D^* meson the deviation of its momentum vector from the jet axis must be smaller than $\Delta R = \sqrt{\Delta\eta^2 + \Delta\phi^2} < 1$[1], where $\Delta\eta$ and $\Delta\phi$ are the deviations in the η-ϕ plane. If this is fulfilled the jet is considered a D^* jet.

---

[1] This choice is motivated by the size of the distance parameter in the jet reconstruction algorithm cf. section 4.2, defining the maximum angular extent of a jet

The jet analysed for its jet shape properties is the highest-p_t jet not associated with a D^* meson. By means of this choice the analysed jet is free of any bias from the selection of the D^* candidate. To assure a clear separation no overlap between jets is allowed and the D^* candidate must fulfil a minimum distance requirement in the η-ϕ plane of $\Delta R > 1.5$ to the axis of the second jet.

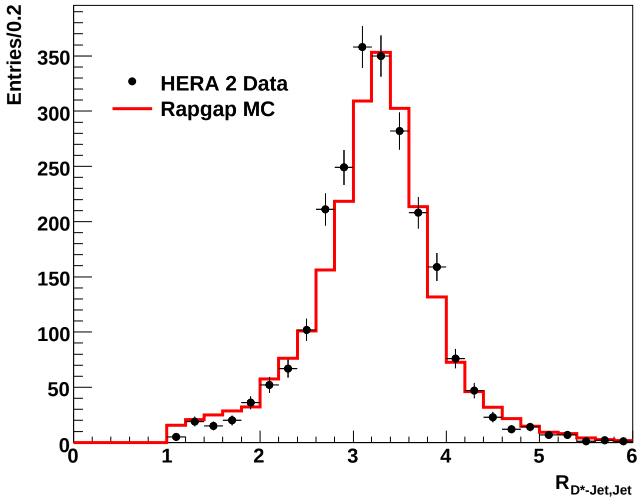

Figure 5.1: Distance in η-ϕ between the identified D^*-jet and the highest-remaining-p_t jet for HERA 2 signal events compared to the Monte Carlo simulation. The distinct peak around the value π visualises the back-to-back topology in ϕ.

The selection of jets is independent of the kinematic range and run periods relevant to this analysis. The selection criteria discussed above are valid in the HERA 1 photoproduction regime as well as in the HERA 2 deeply inelastic scattering regime.

5.2 Selection of Photoproduction Events

A photoproduction event is selected through the detection of the scattered electron in the electron tagger. For this analysis the tagger at $z = -33.4$ m (ET33) as well as the tagger at $z = -43.2$ m (ET44) have been used. This means that the electron is scattered by a very small angle of $\pi - \theta_{e'} <$ 5 mrad, constraining the value of the photon virtuality to $Q^2 < 0.01$ GeV^2 (Photoproduction implies that the photon entering the hard interaction is quasi real, i.e. $Q^2 \approx 0$ GeV^2). The selection of these events is detailed below.

5.2.1 Online Trigger Selection

The events are selected by the subtriggers S83 (electron in ET33) and S84 (electron in ET44). Both are combinations of level one (L1) trigger elements from the z-vertex trigger, the DCRPh trigger and the luminosity system without any level two (L2) conditions. In the following a description will be given of the triggers which provide the trigger elements for the subtriggers used.

- The **z-Vertex Trigger** is based on signals from the multiwire proportional chambers CIP, COP and FPC to provide rough information about the primary interaction vertex along the beam axis. Each of the above chambers consists of two independent layers. By building rays from the hits of the 16 ϕ-sectors of the chambers straight lines pointing to the z-axis are constructed. The intersections of these lines with the z-axis are filled into a histogram consisting of 16 bins in ϕ and 16 bins in z. Each ray contributes one entry to the z-vertex histogram. Rays originating from real particles end up in the same or adjacent bins whereas combinatorial background is randomly distributed. The process is illustrated in figure 5.2. The trigger element `zVtx_sig_1` fires if the histogram shows a significant peak. Both subtriggers S83 and S84 use this trigger element. More detailed information can be found in [83, 84].

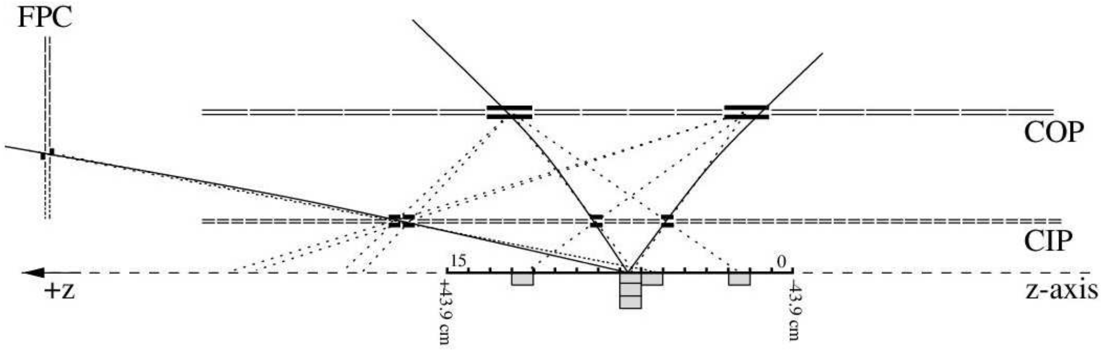

Figure 5.2: The z-vertex trigger: Particle trajectories (full lines) cause hits in the double layers of CIP, COP and FPC. Rays through the pads (dotted lines) are extrapolated to the z-axis. Only rays from particle trajectories form a significant peak in the z-vertex histogram.

- The **DCRPh Trigger** uses 10 out of the 56 wire layers of the CJC. A track can be parametrised in the r-ϕ plane by a curvature κ and an azimuthal angle ϕ at the distance of closest approach (dca') to the vertex, cf. section 2.3.6. The signals caused by measured tracks are compared to predefined masks in the two dimensional κ-ϕ space for small values of dca'. Tracks from cosmic muons and beam induced background events have a large dca'. The number of positive and negative tracks above two programmable transverse momentum thresholds is counted separately. Validation of a mask leads to a positive trigger decision. The subtriggers S83 and S84 require the trigger element `DCRPh_Tc` which fires if at least three track masks above 400 MeV are found. The DCRPh trigger is described in more detail in [85, 86].

- The **Luminosity System Trigger** provides the trigger elements `LU_ET`, `LU_ET_44` and `LU_PD_low`. The former two fire if an energy deposition above an adjustable threshold (6-9 GeV) is found in ET33, respectively ET44. The trigger element `LU_PD_low` functions in a similar way and fires if more than a given threshold (5-7 GeV) energy is deposited in the photon detector. This element is coupled via a logical *AND NOT* and serves as a veto against Bethe-Heitler processes.

Additionally both subtriggers contain trigger elements from the time-of-flight system (ToF) as a veto to supress background from beam-gas and beam-wall events from outside the interaction region.

S83 : `(zVtx_sig>1) && (DCRPh_Tc) && LU_ET && !LU_PD_low && !VETO`

S84 : `(zVtx_sig>1) && (DCRPh_Tc) && LU_ET_44 && !LU_PD_low && !VETO`

Trigger Element	**Description**
`zVtx_sig>1`	Significant maximum in the z-vertex histogram
`DCRPh_Tc`	At least three track masks above 450 MeV
`LU_ET`	Energy deposition in the ET33
`LU_ET_44`	Energy deposition in the ET44
`LU_PD_low`	Energy deposition in the Photon Detector
`VETO`	Veto from Veto Wall, Time-of-Flight detectors

Table 5.1: Trigger elements associated to the subtriggers S83 and S84, || denoting the logical *OR*, && denoting the logical *AND* and ! representing the logical *NOT*.

5.2.2 Offline Event Selection

In order to remove possible background due to proton beam gas interaction or cosmic showers contained in the online selected data sample a cut on the reconstructed value of the z-coordinate of the primary vertex of $|z_{vertex}| < 35$ cm is performed. The number of signal events decreases rapidly with increasing distance of the reconstructed primary vertex to the nominal interaction point as can be seen in figure 5.3. At high values of z_{vertex} the distribution approaches a plateau of background-only events which are discarded by the cut.

Due to geometry and beam optics the taggers ET33 and ET44 have a limited acceptance for electrons from photoproduction events. Besides the restriction of $Q^2 < 0.01$ GeV^2 due to the small scattering angle the acceptance is highly dependent on the inelasticity y. A parametrisation of the acceptance is available for the different run periods [87]. Due to different beam conditions the acceptance in the year 2000 has been slightly lower than in 1999 for the ET33. For the ET44 the acceptance has been shifted towards slightly lower inelasticities y in the year 2000 as compared to 1999. The acceptances of both taggers is shown in figure 5.4. To ensure an acceptance above 10% an inelasticity cut of $0.29 < y < 0.65$ is required for the ET33. For the ET44 the inelasticity is constrained to $0.05 < y < 0.15$. These cuts are illustrated in figure 5.4 by the dashed lines. These and all other cuts are summarised in table 5.5.

Neither of the taggers is included in the detector simulation of the Monte Carlo calculations. For comparison of data and Monte Carlo each Monte Carlo event is weighted by a factor corresponding to the acceptance determined by the above parametrisation.

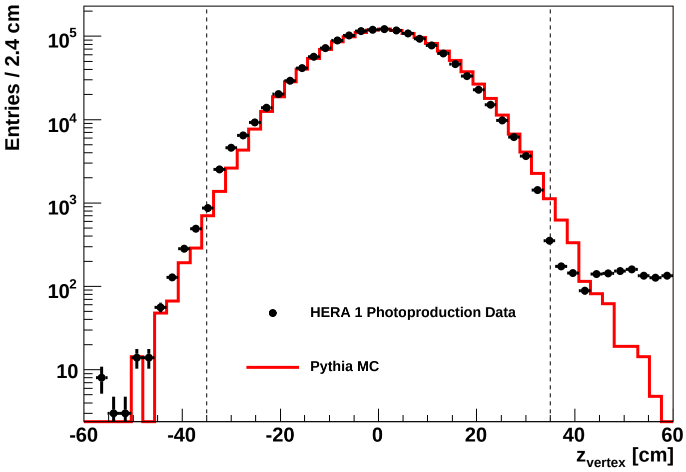

Figure 5.3: Distribution of the z-coordinate of the reconstructed primary vertex for photoproduction data. Also shown is the Monte Carlo distribution of signal events. The dashed lines indicate the cut at $|z_{vertex}| < 35$ cm.

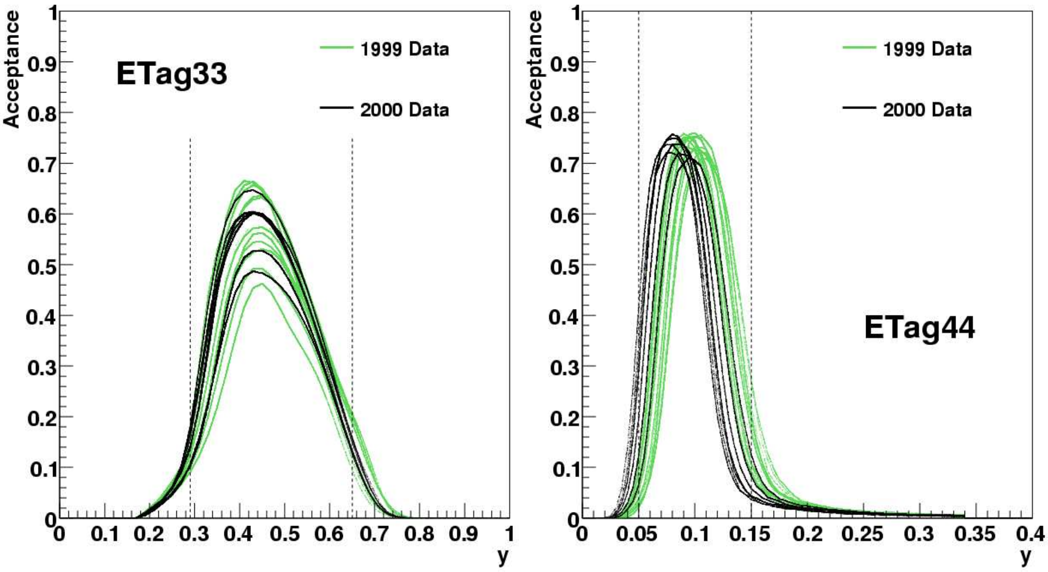

Figure 5.4: Acceptance of the ET33 (left) and ET44 (right) as function of the inelasticity y. The parametrisations also include inefficiencies due to the trigger requirements and due to cuts on the position of the energy deposition of the scattered electron within the tagger. Each year is subdivided into several periods during which the acceptance was constant. The vertical lines indicate the selected y-region to achieve acceptances of higher than 10%.

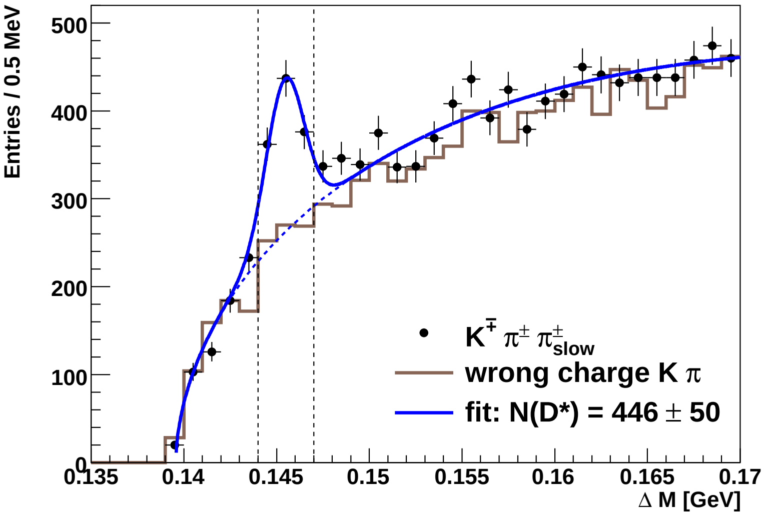

Figure 5.5: Distribution of the difference Δm between the invariant mass of the D* candidate and the D^0 candidate after photoproduction jet selection for the ET33 sample. The dotted lines indicate the signal region.

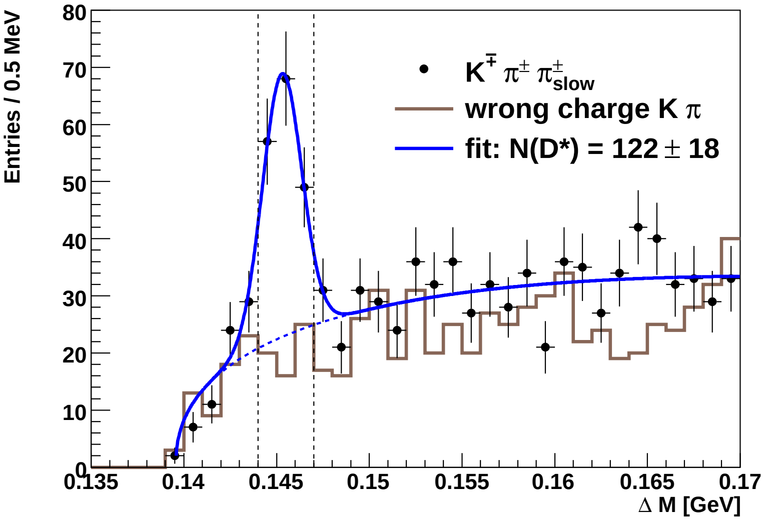

Figure 5.6: Distribution of the difference Δm between the invariant mass of the D* candidate and the D^0 candidate after photoproduction jet selection for the ET44 sample.

5.2.3 Integrated Luminosity

For the HERA 1 photoproduction selection only good and medium quality runs[2] were included. Furthermore trigger phase two or higher is requested, this means that high voltage is 100% on and the track triggers are active (see below). High voltage on the following subdetectors is requested: CJC1, CJC2, CIP, SpaCal, LAr, LUMI, ToF and VETO.

The total integrated luminosity collected with the subtrigger S83 is 59.3 pb^{-1}. However, due to high rates a prescale factor p has been applied to the subtrigger, i.e. only every p-th time the subtrigger has fired the event is accepted. The mean prescale factor for S83 in the analysed data is $\langle p \rangle = 1.16$. This is taken into account by downscaling the luminosity by this factor, leading to a corrected integrated luminosity for the subtrigger S83 of $\mathcal{L}_{S83} = 51.1\ \text{pb}^{-1}$. The subtrigger S84 is treated in a similar way yielding a corrected luminosity of $\mathcal{L}_{S84} = 31.8\ \text{pb}^{-1}$.

The figures 5.5 and 5.6 show the Δm distribution between the invariant mass of the D* candidate and the D^0 candidate as described in section 4.4. The number of D* mesons is determined through the fit of the peak and the background. The dotted lines indicate the signal region used for this analysis. The measurement of the jet shape variables is performed within this region and the integrals of the total fit function and the background function are considered in the determination of the fraction for the background subtraction. This is described in more detail in the following chapter.

Year	**Lepton Type**	$\mathcal{L}_{S83}$ $[\mathbf{pb}^{-1}]$	$\mathcal{L}_{S84}$ $[\mathbf{pb}^{-1}]$
1999	electron	6.9	4.3
1999	positron	17.8	11.1
2000	positron	26.4	16.4

Table 5.2: Lepton type and prescale corrected luminosity for the subtriggers S83 and S84 in the different HERA 1 data taking periods.

5.3 Selection of DIS Events

In a DIS event with $3.4\ \text{GeV}^2 \leq Q^2 \leq 100\ \text{GeV}^2$ the incoming electron is scattered into the backward calorimeter (SpaCal). Requiring the polar angle of the scattered electron $\theta_{e'}$ to be larger than 155° ensures a reconstruction by the SpaCal, furthermore the overlap region with the LAr calorimeter is avoided. This provides a measurement of the scattering angle $\theta_{e'}$ and the energy $E_{e'}$ of the electron with good resolution. The following section details the online and offline selection of the DIS events.

5.3.1 Online Trigger Selection

The 2-Jet D* DIS events in this analysis are collected by the subtrigger S61. S61 uses L1 conditions from the SpaCal and FTT triggers. These two triggers contributing trigger elements to S61 are presented below.

---

[2] To be of at least medium quality the CJCs, Calorimeters and Luminosity system must be fully operational.

- The **SpaCal Inclusive Electron Trigger** uses information from the electromagnetic section of the backward calorimeter (SpaCal) to identify the scattered electron. It is segmented into overlapping arrays of 4×4 cells each wherein energies are summed up for the trigger. The energy sum is compared to three different energy thresholds from 100 MeV to 20 GeV. The subtrigger S61 requires the element `SPCLe_IET>2` corresponding to an energy deposition of 9 GeV in the SpaCal to fire. Additional trigger elements are calculated separately for radii ($\leq$ 16 cm) close to the beam axis. The trigger element `SPCLe_IET_Cen_3` corresponds to an energy deposition of 9 GeV in the central SpaCal region. The subtrigger S61 combines both of these trigger elements by a logical *OR*.

- The **Fast Track Trigger (FTT)** digitises the analogue pulses from the CJC wires via a difference-of-sample algorithm and returns the charge Q measured at a time t on the respective CJC wire. The algorithm looks for hits by searching for charges Q exceeding the noise level. Time information can be extracted with a precision of 3 ns. Charge and time information is filled into shift registers which are then used in order to perform a parallel search for track segments in all trigger cells. Hereby also wires from neighbouring cells are taken into account to allow for tracks crossing cell boundaries. The track segments are then compared to predefined masks of possible track combinations.

  The trigger cells consist of four groups of three wires each (three in CJC1 and one in CJC2), i.e in total only 12 of the 56 wire layers in the CJCs are taken into account. This results in a very fast online track reconstruction allowing track information to be considered in the trigger decision. Offline the track reconstruction is refined. The subtrigger S61 requires the trigger element `FTT_mul_Td>0` which fires if at least one track with more than 900 MeV is found (in the beginning of FTT data taking the very similar condition `FTT_mul_Tc>1` requiring two tracks above 400 MeV was active instead). Figure 5.7 shows the division into trigger cells and the trigger layers in the CJCs.

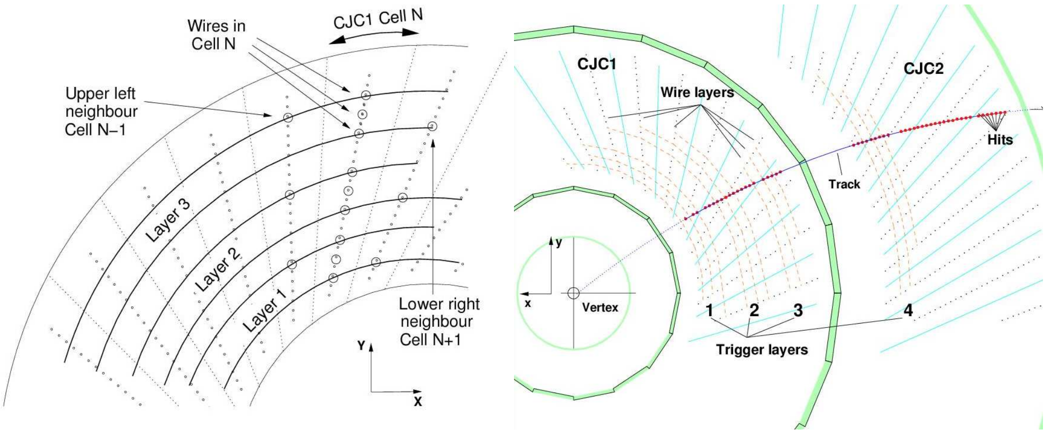

Figure 5.7: Radial view of the CJC. The left drawing shows the division into trigger cells and the wires from neigbouring cells taken into account for reconstruction of track segments. The right drawing gives an overview of both CJCs and the 4×3 wire layers used by the FTT.

The FTT was comissioned in the beginning of data taking in the year 2005. A minor fraction of the DIS data sample was collected prior to this in the year 2004. At this time the requirement of a track within the central tracking chambers was provided by the DCRPh trigger analogue to the description of the online selection of photoproduction events.

The subtrigger S61 consists of several additional trigger elements from the CIP, Veto Wall and Time-of-Flight Detectors to veto background events. A list of these elements is provided in table 5.3.

S61 : `(SPCLe_IET_Cen>2||SPCLe_IET_Cen_3) && (FTT_mul_Td>0) && !VETO && !CIPVETO`

Trigger Element	**Description**
`SPCLe_IET_Cen>2`	Energy deposition of > 9 GeV in SpaCal
`SPCLe_IET_Cen_3`	Energy deposition of > 9 GeV in central SpaCal region
`FTT_mul_Td>0`	Track in CJC with $p_t > 900$ MeV
`VETO`	Veto from Veto Wall, Time-of-Flight detectors
`CIPVETO:(CIP_mul>11)&&(CIP_sig==0)`	Veto from CIP

Table 5.3: Trigger elements associated to the subtrigger S61, || denoting the logical *OR* and && denoting the logical *AND* and ! representing the logical *NOT*.

5.3.2 Offline Event Selection

Equivalent to the selection of photoproduction events a cut on the z-coordinate of the primary event vertex of $|z_{vertex}| < 35$ cm is applied. The z_{vertex} distribution is displayed in figure 5.8.

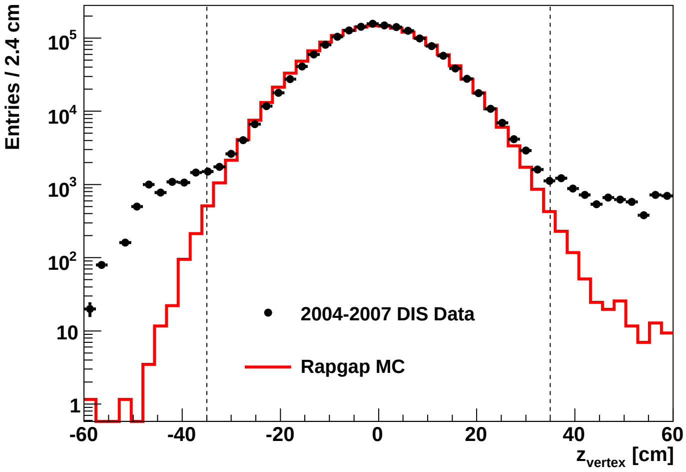

Figure 5.8: Distribution of the z-coordinate of the reconstructed primary vertex for DIS data. Also shown is the Monte Carlo distribution of signal events. The dashed lines indicate the cut at $|z_{vertex}| < 35$ cm.

The kinematic range of the DIS measurement is restricted to $3.4\ \mathrm{GeV}^2 \leq Q^2 \leq 100\ \mathrm{GeV}^2$, caused by the geometrical acceptance of the backward calorimeter. The Q^2 distribution for values of Q^2 from $1.5\ \mathrm{GeV}^2$ to $10\ \mathrm{GeV}^2$ is shown in figure 5.9. The cut at $Q^2 = 3.4\ \mathrm{GeV}^2$ ensures reasonable SpaCal acceptance. At lower values of Q^2 the electromagnetic shower is only partly contained in the backward calorimeter. The SpaCal acceptance furthermore limits the inelasticity to the region $0.02 < y < 0.7$.

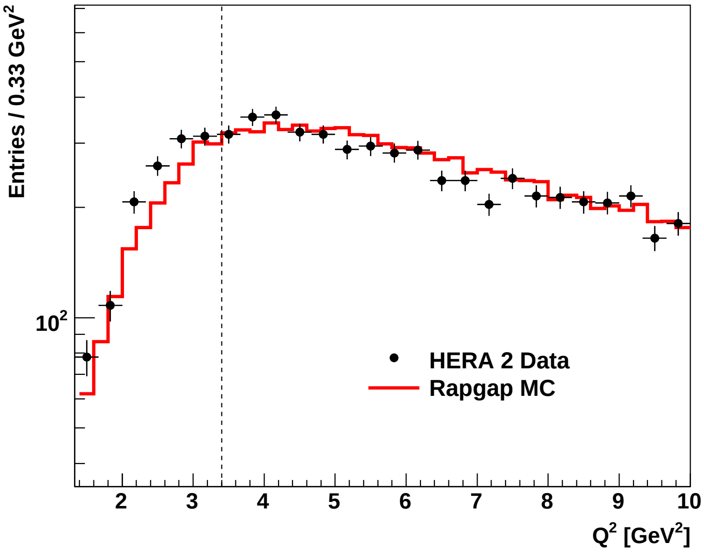

Figure 5.9: Distribution of the four momentum transfer squared Q^2 for signal events at low values of Q^2. The data is compared to the Monte Carlo simulation and the cut used for the analysis is indicated as a dashed line.

As the energy measurement towards the inner edge of the SpaCal becomes unreliable a further cut on the radial position of the cluster is applied. Only clusters with a minimum radial distance of 12 cm are accepted. This distance is determined with respect to the intersection of the electron beam with the plane of the backward calorimeter.

In general the electron beam has non-zero angle with respect to the z-axis of the coordinate system of the H1 detector. This circumstance is also referred to as *beam tilt*. The beam tilt is corrected for by recalculating the position of the cluster using corrected angular parameters of the scattered electron.

A fraction of the inner SpaCal region is hit by the synchrotron radiation fan of the electron beam. The corresponding cells are taken out of the trigger. To exclude these cells from the selection a box cut which covers the corresponding region of the backward calorimeter is applied. The radial cut as well as the box cut are illustrated in figure 5.10 which also shows the impact coordinates of the scattered electron in the SpaCal plane.

In addidition some cells do not provide trigger signals due to electronic problems, other cells with malfunctioning photomultipliers cannot be used for energy measurement. A detailed investigation of these problems was performed by [55, 91]. All these cells are excluded from the selection.

Table 5.5 gives a summary of all applied cuts.

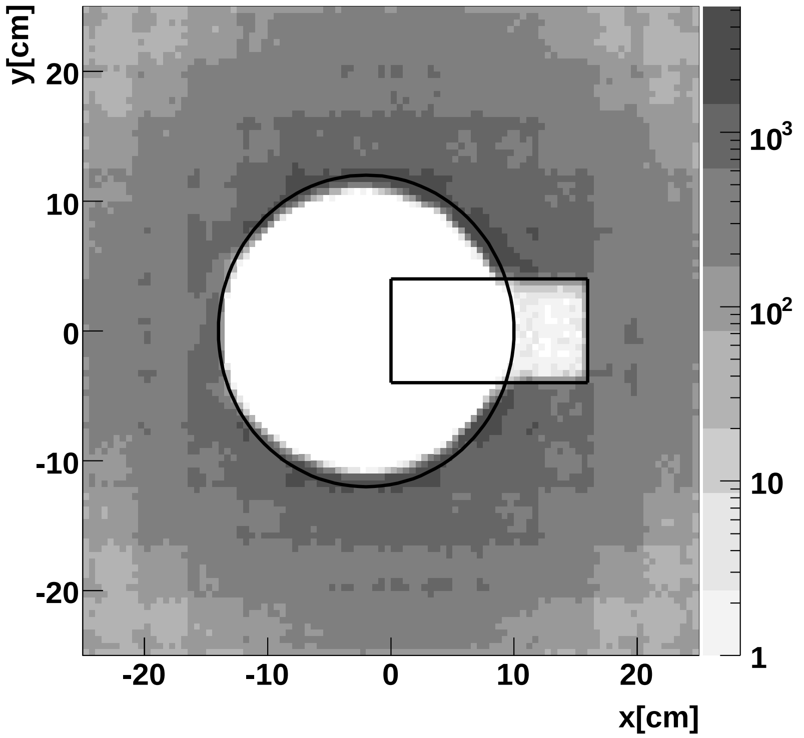

Figure 5.10: Inner SpaCal hitmap showing the distribution of the reconstructed impact positions of the scattered electrons in the backward calorimeter (HERA 2 data). No cuts are applied. The radial and box cuts are shown.

5.3.3 Integrated Luminosity

Also in the HERA 2 DIS part of this analysis only good and medium quality runs are included and trigger phase two or higher is requested (i.e. high voltage is 100% on and stable prescale settings are enabled). High voltage of the following subdetectors is requested: CJC1, CJC2, CIP, SpaCal, LAr, LUMI, VETO and ToF.

The prescale factor of the subtrigger S61 is kept very close to one. The integrated luminosity for the years 2004 through 2007 corrected for high voltage settings and prescale factors amounts to

$\mathcal{L} = 347.6\ \mathrm{pb}^{-1}$. Table 5.4 shows the integrated luminosities of the individual years, the colliding lepton type and the average prescale factor. Fig 5.11 shows the Δm distribution of the selected D* candidates.

Year	**Lepton Type**	**Avg. Prescale**	$\mathcal{L}$ $[\mathbf{pb}^{-1}]$
2004	positron	1.02	48.8
2005	electron	1.02	107.8
2006	electron	1.00	55.1
2006	positron	1.01	88.4
2007	positron	1.00	47.5

Table 5.4: Colliding lepton type and average prescale factors as well as the corrected integrated luminosity for the subtrigger S61 in the HERA 2 data taking period. Note that S61 is virtually prescale-free.

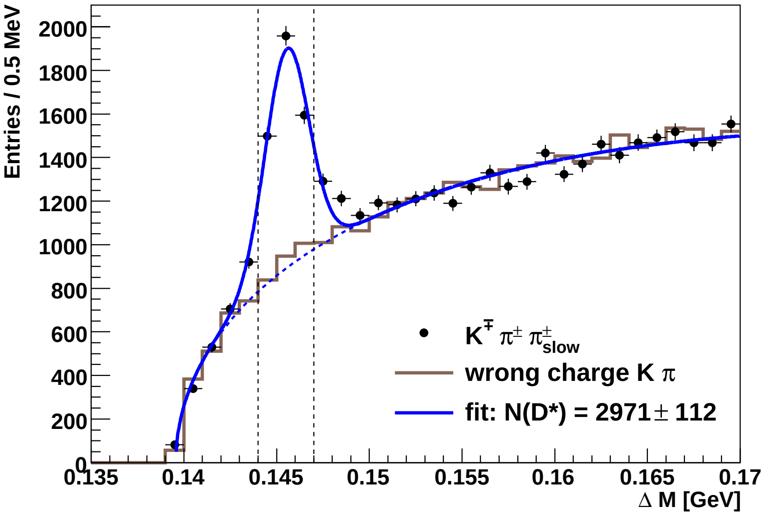

Figure 5.11: Distribution of the difference Δm between the invariant mass of the D* candidate and the D^0 candidate after jet selection for the DIS sample. The dotted lines indicate the signal region.

5.4 Selection Summary

In table 5.5 all cuts applied to select the photoproduction and DIS samples are shown. Figure 5.12 shows the event display of a two-jet DIS event with a reconstructed D* meson. The back-to-back topology in ϕ of the two jets is visible, as is the energy deposition of the scattered electron in the SpaCal. The detailed view on the lower right reveals a secondary vertex from the D^0 decay reconstructed with CST information. The primary decay particle was a D^{*-}. Note, however, that this event is chosen for demonstration; the D^* meson does not fulfil the angular requirement (cf. section 5.1) with respect to the jets.

Cut	**Photoproduction**	**Deeply Inelastic Scattering**
Subtrigger	S83,S84	S61
Scattered Electron	in ET33/ET44	in SpaCal
Q^2 [GeV]	< 0.01	3.4...100
y	0.05...0.15, 0.29...0.65	0.02...0.7
$\|z_{vtx}\|$ [cm]	< 35	< 35
Jets		
#	≥ 2	≥ 2
$p_{t,Jet1(2)}$ [GeV]	$\geq 5(4)$	$\geq 5(4)$
$\|\eta_{Jet}\|$	< 1.9	< 1.9
D*		
Δm [GeV]	< 0.17	< 0.17
$\|m_{K\pi} - m_{D^0}\|$ [GeV]	< 0.08	< 0.08
p_{t,D^*} [GeV]	≥ 2.6	≥ 2.6
$\|\eta_{D^*}\|$	< 1.5	< 1.5
$p_{t,K}$ [GeV]	> 0.3	> 0.3
$p_{t,\pi}$ [GeV]	> 0.3	> 0.3
$p_{t,K} + p_{t,\pi}$ [GeV]	≥ 2.4	≥ 2.4
p_{t,π_s} [GeV]	> 0.12	> 0.12
K, π Tracklength [cm]	> 17	> 17
π_s Tracklength [cm]	> 11	> 11
Signal Region		
Δm [GeV]	$0.144 \leq \Delta m \leq 0.147$	$0.144 \leq \Delta m \leq 0.147$
Integrated Luminosity $[\mathrm{pb}]^{-1}$	51.1 / 31.8	347.6

Table 5.5: Summary of all selection criteria for the photoproduction and DIS data samples. The cuts for the selection of a D* sample have already been discussed in section 4.4. After the initial D* selection these cuts are partially more restricting to improve the D* signal.

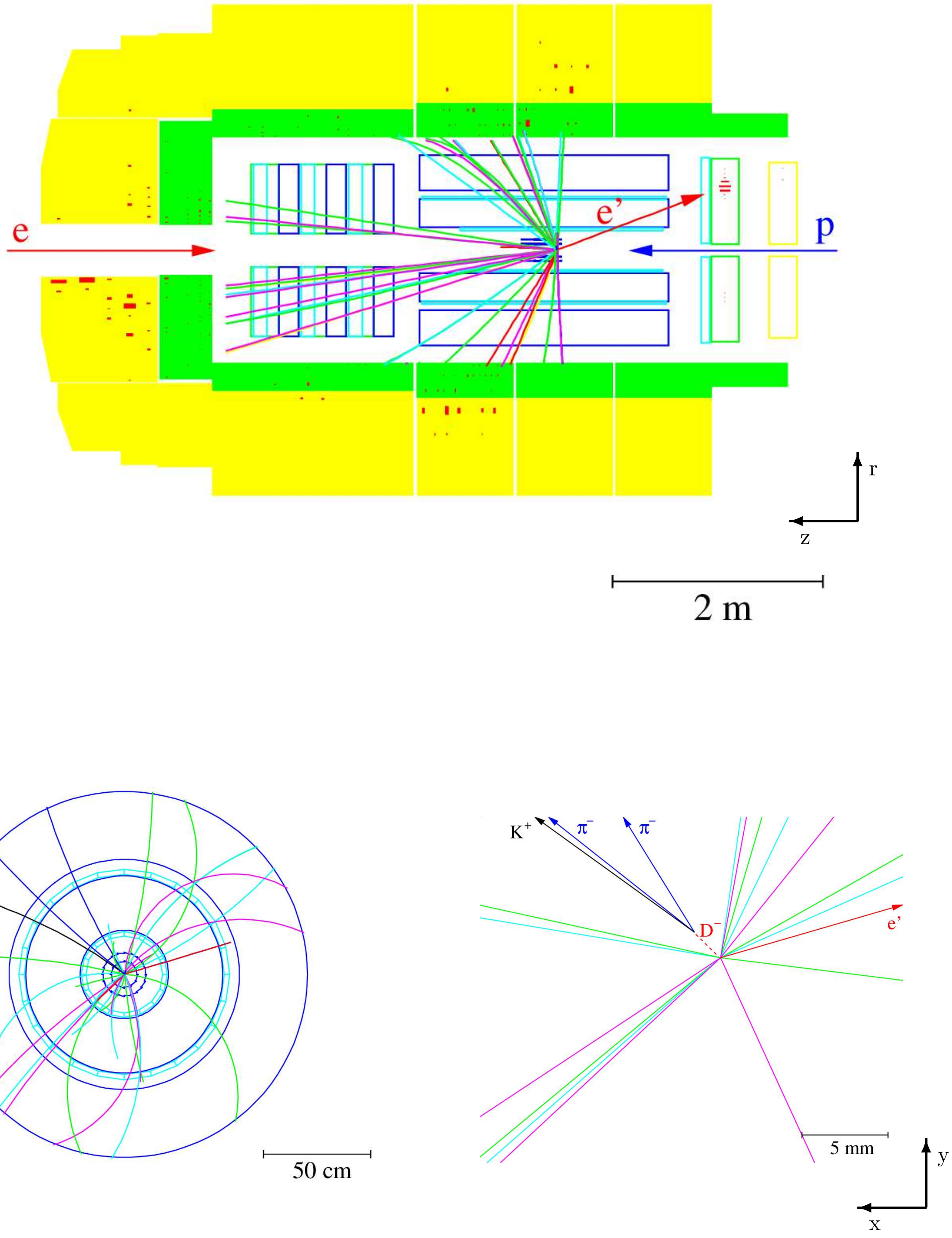

Figure 5.12: Event display of a dijet event with a reconstructed D* meson. The electron is scattered into the backward calorimeter tagging this as a DIS event, the proton remnant traverses the forward tracker. In the upper schematic the detector is shown in the rz plane. Below the central tracking system is shown in the $r\phi$ plane. On the right hand side a detailed view of the reconstructed tracks around the primary event vertex is given.

Chapter 6

Measurement of the Internal Structure of Charm Jets

This chapter focuses on all aspects of the jet structure measurement. First quality checks on the measured variables are performed. This includes a discussion on efficiency and the correlation between generated and reconstructed quantities. Next the background subtraction method is described and the determination of the statistical errors is shown. In order to be able to correct the data for detector effects by means of the Monte Carlo simulation it is necessary that the data are well described by the simulation. To confirm this the agreement between Monte Carlo and data is studied for several control distributions.

The mean integrated jet shape is presented at detector level subtracted for the aforementioned background. Finally the method for correcting the data for detector effects is discussed together with the systematic uncertainties.

6.1 Reconstruction Quality of the Kinematic Variables

In the measurement of the mean integrated jet shape (cf. chapter 3) efficiencies enter through the detector corrections described in section 6.5. These efficiencies are studied to ensure that the Pythia and RapGap Monte Carlo descriptions of the data are sufficient to make them applicable for the correction of the data to hadron level.

The fraction of events lost due to inefficiencies of the detector components and cuts from the event selection is given by $(1 - \epsilon_{tot})$. Here ϵ_{tot} is the total efficiency that factorises into

$$\epsilon_{tot} = \epsilon_{trig} \cdot \epsilon_{rec} \tag{6.1}$$

with the trigger efficiency ϵ_{trig} and the reconstruction efficiency ϵ_{rec}. The trigger efficiency is defined as the fraction of events satisfying the detector level selection cuts listed in table 5.5 that are actually triggered. The absolute magnitude of the trigger efficiency, however, is not important for this analysis.

The trigger efficiencies for the trigger elements composing the subtrigger S61 have been studied in detail by [55, 91], yielding efficiencies in the studied region above 98%.

The photoproduction subtriggers S83 and S84 are not included in the Monte Carlo simulation. This is accounted for by weighting the generated events by the respective electron tagger acceptance (as shown in figure 5.4). The mean electron tagger (ET33 or ET44) acceptance is calculated by averaging the acceptance function over the visible region using the Pythia Monte Carlo simulation [92]:

$$\mathcal{A}_{MC}^{ET} = \frac{\sum_i^{N_{rec}} a_{ET}(y_i, r_i)}{N_{rec}} \tag{6.2}$$

with the number of Monte Carlo events reconstructed in the visible region N_{rec}, the measured electron tagger acceptance a_{ET} parametrised as a function of the inelasticity y_i and the run period r_i of the reconstructed event. This acceptance already includes inefficiencies of the luminosity trigger elements. It amounts to about 40% for the respective electron tagger in the visible region and does not differ for direct and resolved events.

The other factor in determining the total efficiency, the reconstruction efficiency ϵ_{rec}, is discussed below.

6.1.1 Reconstruction Efficiency

The reconstruction efficiency includes the efficiency of all selection cuts, except of the trigger requirements, and the event reconstruction itself. It is determined with the Monte Carlo simulation and it is calculated as the fraction of the events reconstructed in the visible region after applying the selection cuts with respect to all generated events in the visible region:

$$\epsilon_{rec} = \frac{N(D^*_{rec})_{\text{rec\&vis cuts}}}{N(D^*)_{\text{gen,vis}}}. \tag{6.3}$$

The visible region is defined by the cuts in table 5.5 for detector level and in table 6.1 for hadron level. *Detector level* denotes the level at which particles are measured in the detector and *hadron level* means the level of decayed hadrons, i.e. in the Monte Carlo simulation the hadron level is the level before the generated, hadronised and then decayed particles are sent through the detector simulation.

Figure 6.1 shows the reconstruction efficiency for photoproduction events in bins of the analysed-jet quantities E_{jet}, η_{jet} and $p_{t,jet}$ as well as the event kinematics, y, x_γ^{obs} determined from the Pythia Monte Carlo simulation. No significant dependency on any of the studied variables is present and the behaviour is similar for direct and resolved events. The overall reconstruction efficiency amounts to about 50%.

For the DIS events the reconstruction efficiencies are shown in figure 6.2. These are determined from the RapGap Monte Carlo simulation. Here the overall reconstruction efficiency is about 70%. Also notable is a slighly higher reconstruction efficiency for resolved events.

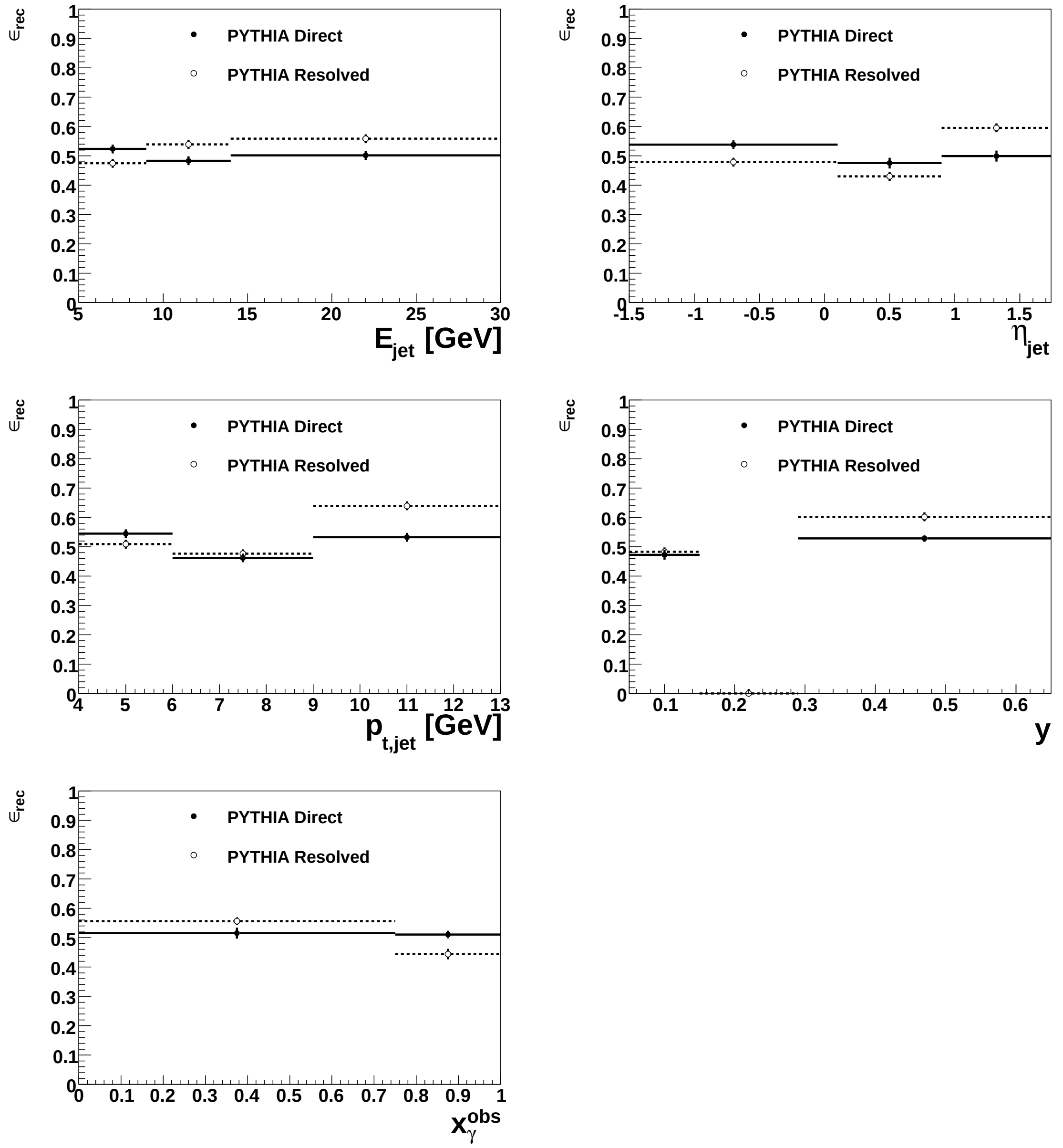

Figure 6.1: Reconstruction efficiency for direct and resolved photoproduction events as function of the variables E, η and p_t of the analysed jet as well as y and x_{γ}^{obs}. The efficiencies are calculated with the Pythia Monte Carlo simulation.

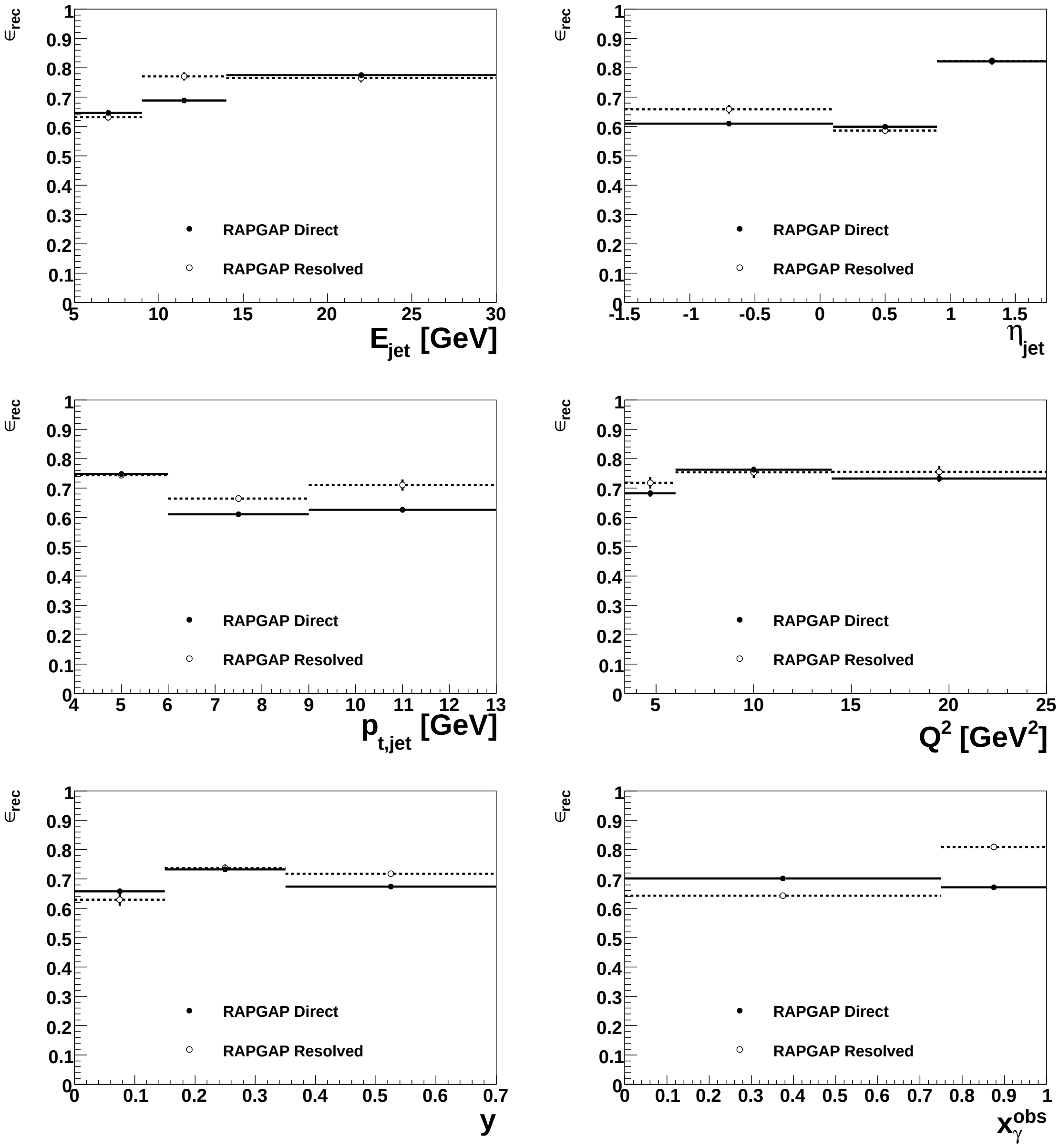

Figure 6.2: Reconstruction efficiency for direct and resolved DIS events as function of the variables E, η and p_t of the analysed jet as well as Q^2, y and x_γ^{obs}. The efficiencies are calculated with the RapGap Monte Carlo simulation.

Cut	**Photoproduction**	**Deeply Inelastic Scattering**
Q^2 [GeV^2]	< 0.01	3.4...100
y	0.05...0.15, 0.29...0.65	0.02...0.7
Jets		
#	≥ 2	≥ 2
$p_{t,Jet}$ [GeV]	$\geq 5(4)$	$\geq 5(4)$
$\lvert\eta_{Jet}\rvert$	< 1.9	< 1.9
D*		
p_{t,D^*} [GeV]	≥ 2.6	≥ 2.6
$\lvert\eta_{D^*}\rvert$	< 1.5	< 1.5

Table 6.1: Phase space selection cuts determining the visible region for the photoproduction and DIS Monte Carlo samples at hadron level.

6.1.2 Correlation between Generated and Reconstructed Variables

The relation between generated variables and their reconstruction as well as the resulting resolutions are studied in the Monte Carlo simulation to confirm that the widths of the analysis bins are adequate. This is done separately for direct and resolved events in photoproduction as well as in DIS.

Figures 6.3 and 6.4 show the correlations for photoproduction direct and resolved events using the Pythia Monte Carlo. The jet observables E_{jet}, η_{jet} and $p_{t,jet}$ are studied. Here the subscript *jet* denotes the analysed, i.e. the highest p_t not-D^* jet within $|\eta_{jet}| < 1.9$. Furthermore the correlation for the inelasticity y and the variable x_γ^{obs} are investigated. In the figures 6.5 and 6.6 these correlations and additionally the relationship between generated and reconstructed photon virtuality Q^2 are shown using the RapGap Monte Carlo simulation. Best correlations are observed in the variables η_{jet}, y and $W_{\gamma p}$. Overall the variables are well correlated and similar correlations are observed for direct and resolved events.

More quantitatively the difference between generated and reconstructed variables can be characterised by the relative deviation of the reconstructed variable from the generated one. For a variable v the relative resolution R can be expressed as

$$R(v) = \frac{v_{rec} - v_{gen}}{v_{gen}}. \tag{6.4}$$

The resolutions for the above variables are shown in figure 6.7 for photoproduction and in figure 6.8 for deeply inelastic scattering. Distributions for direct and resolved events are shown separately. The resolution is comparable for direct and resolved events for most of the variables, though the resolution for resolved events is slighly worse for the variable x_γ^{obs}. This is expected due to the different and more complex shape of resolved photon events.

The analysis bins chosen for the final differential jet shapes (cone radius is fixed and the above quantities are varied, cf. chapter 7) are broader than the full width at half maximum of the shown resolutions. The resolution of the jet axis measurement is taken into account in the determination of the systematic uncertainties. These are discussed in section 6.6.

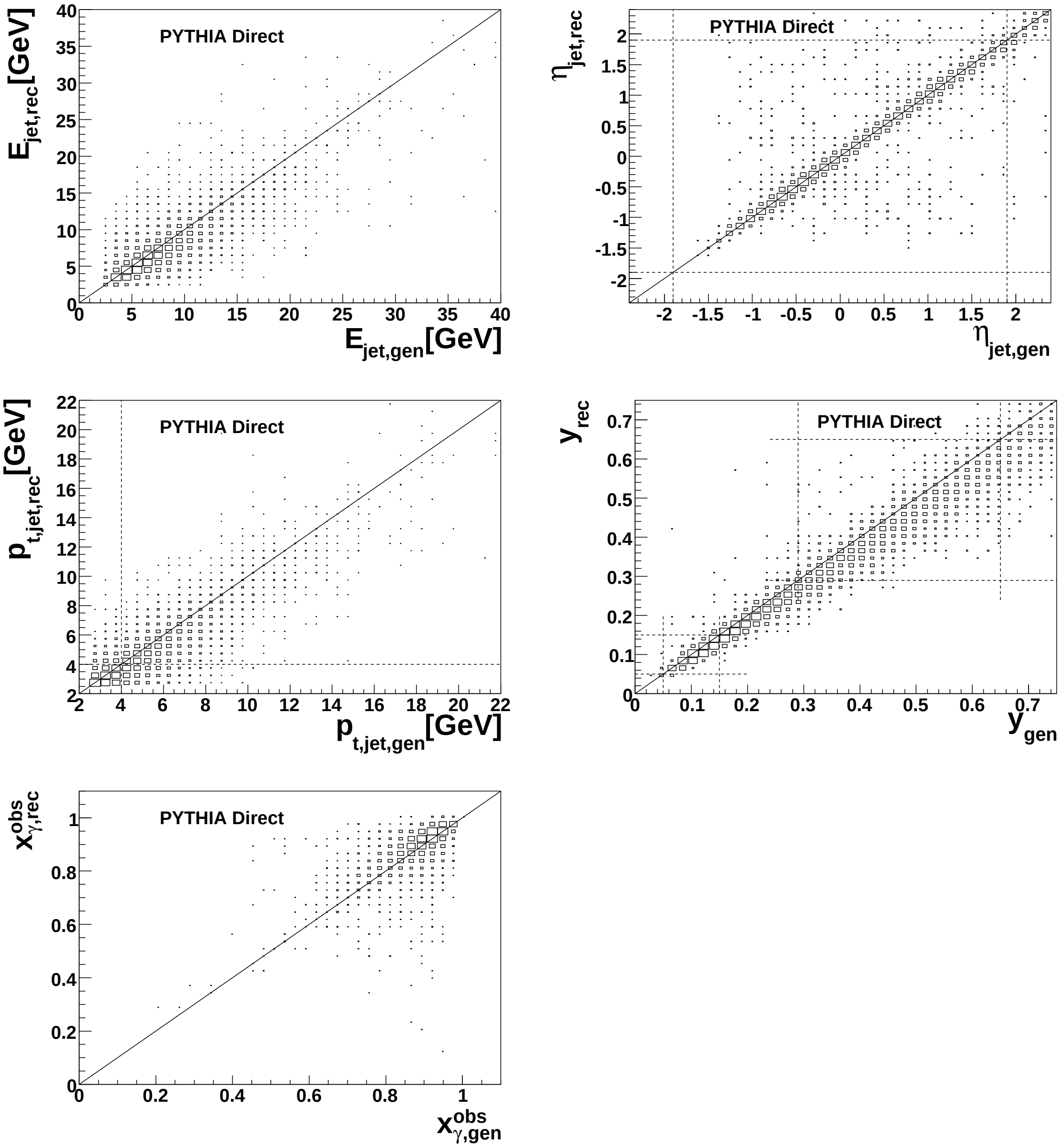

Figure 6.3: Reconstructed against generated variables for direct photoproduction events as simulated by the Pythia Monte Carlo. The index 'jet' denotes the analysed jet. The dashed lines indicate the applied cuts. The solid line serves as a reference to guide the eye.

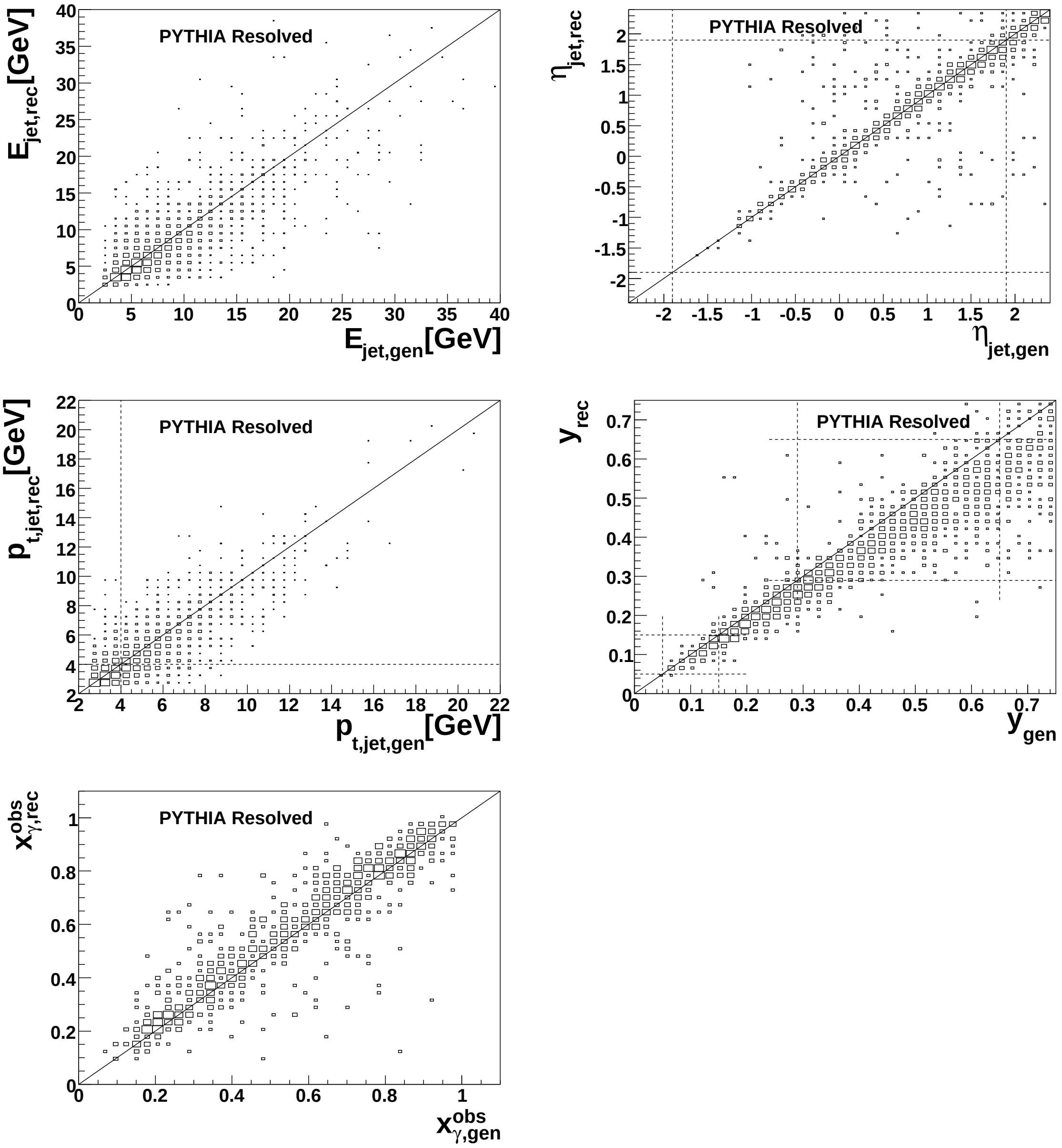

Figure 6.4: Reconstructed against generated variables for resolved photoproduction events as simulated by the Pyhia Monte Carlo. The index 'jet' denotes the analysed jet. The dashed lines indicate the applied cuts. The solid line serves as a reference to guide the eye.

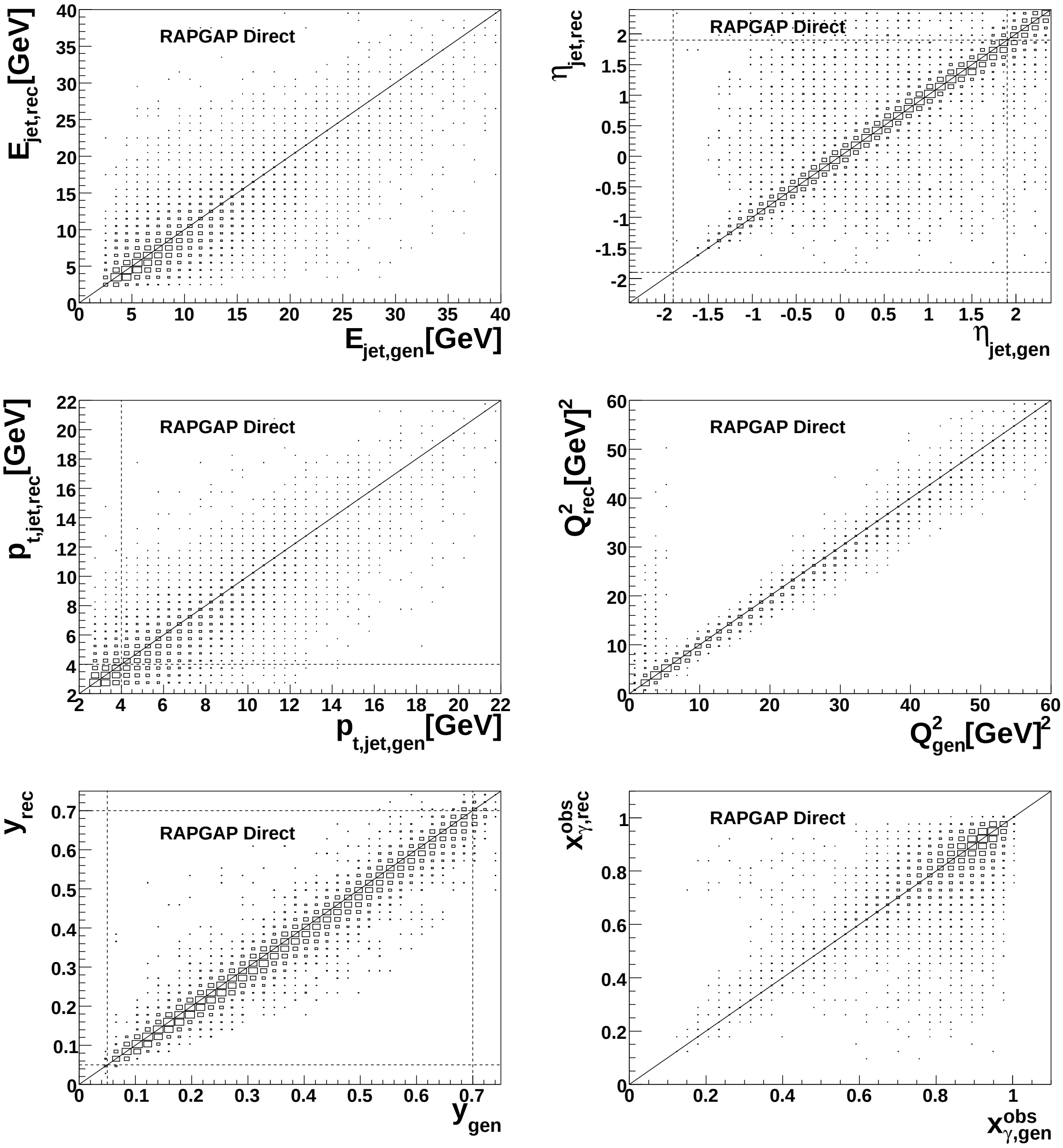

Figure 6.5: Reconstructed against generated variables for direct DIS events as simulated by the RapGap Monte Carlo. The index 'jet' denotes the analysed jet. The dashed lines indicate the applied cuts. The solid line serves as a reference to guide the eye.

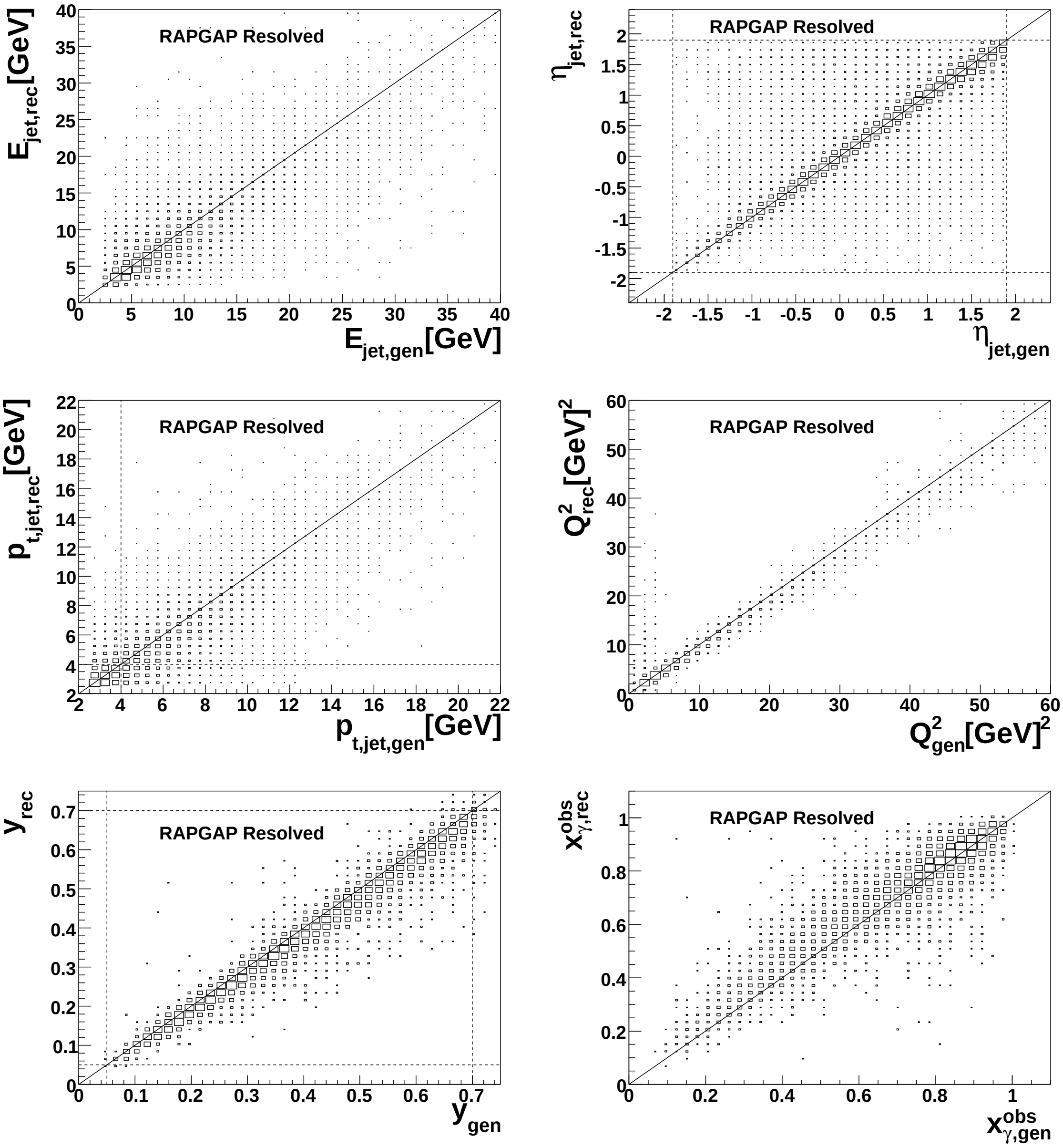

Figure 6.6: Reconstructed against generated variables for resolved DIS events as simulated by the RapGap Monte Carlo. The index 'jet' denotes the analysed jet. The dashed lines indicate the applied cuts. The solid line serves as a reference to guide the eye.

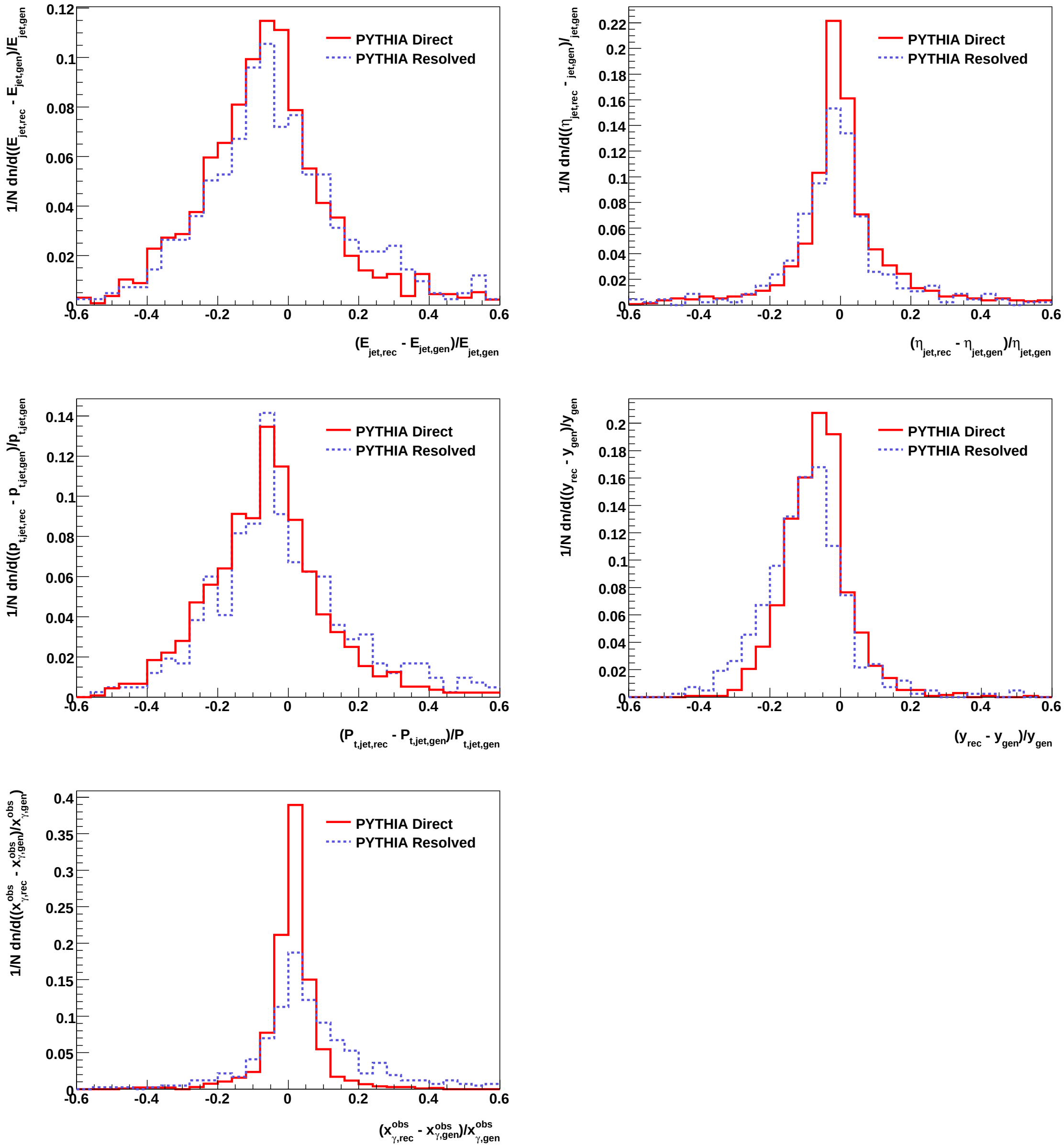

Figure 6.7: Relative resolution for photoproduction events in the jet variables E_{jet}, η_{jet} and $p_{t,jet}$ and in the event variables y and x_γ^{obs}. The distributions are simulated separately for direct and resolved events by the Pythia Monte Carlo. All distributions are normalised to unity.

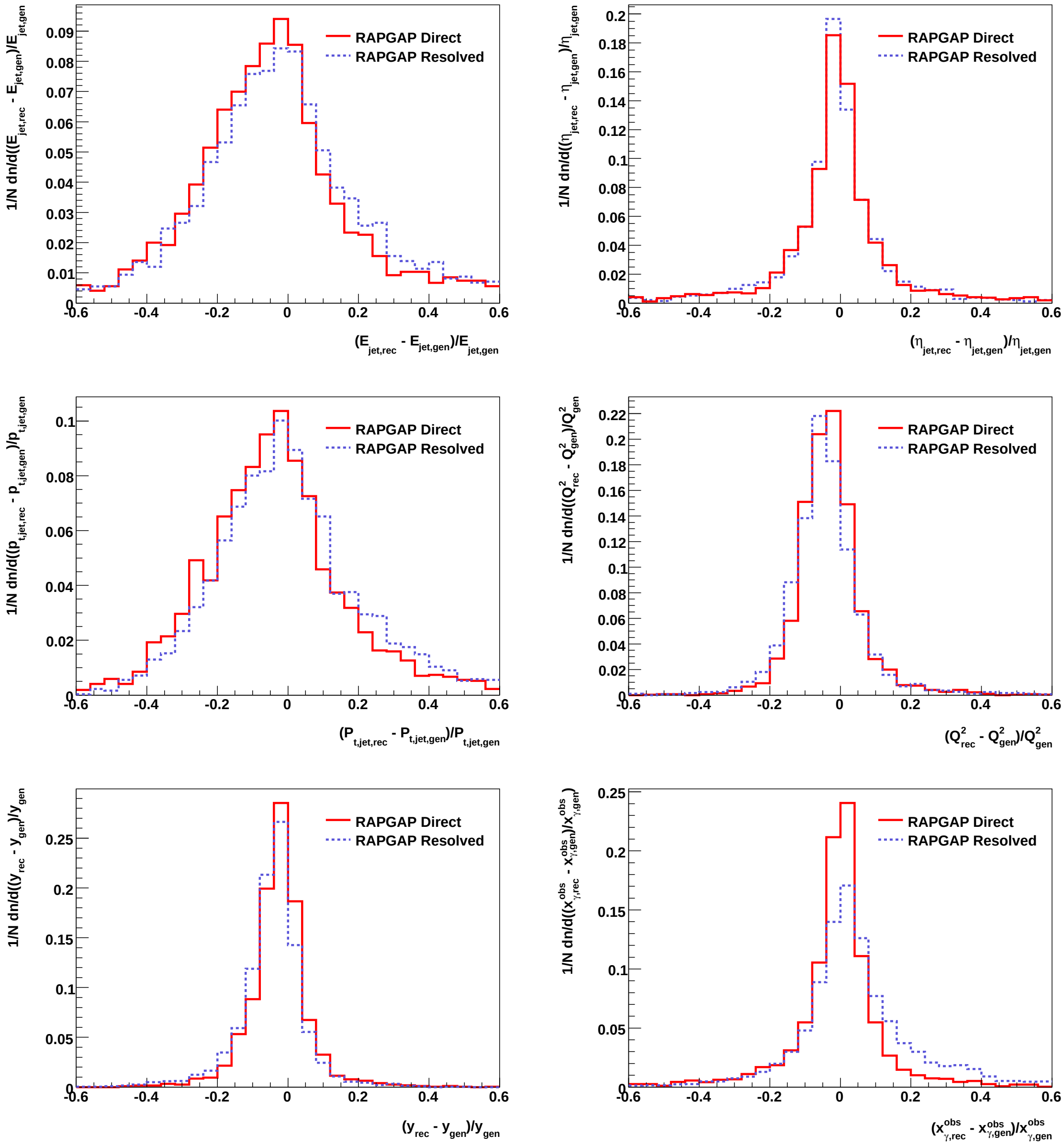

Figure 6.8: Relative resolution for DIS events in the jet variables E_{jet}, η_{jet} and $p_{t,jet}$ and in the event variables Q^2, y and x_γ^{obs}. The distributions are simulated separately for direct and resolved events by the RapGap Monte Carlo. All distributions are normalised to unity.

6.1.3 Purity and Stability

Migrations between bins are characterised by purity and stability. These two quantities are defined as the number of simulated events generated within a certain bin and reconstructed in the same bin, divided by the number of reconstructed events in that bin for purity, respectively divided by the number of generated events in the bin for stability. Purity P_i and stability S_i are given by

$$\begin{aligned} P_i &= \frac{N_{i,rec\&gen}}{N_{i,rec}}, & (6.5) \\ S_i &= \frac{N_{i,rec\&gen}}{N_{i,gen}} & (6.6) \end{aligned}$$

where the index i denotes the analysis bin and N_{rec}, respectively N_{gen}, the number of reconstructed, respectively generated, events in that bin. High values for purity and stability indicate a high resolution in the analysed quantity relative to the bin width, with infinite resolution corresponding to purities and stabilities equal to one. A common requirement is for purity and stability to be larger than 0.3.

Purities and stabilities are studied for the analysed quantities E_{jet}, $p_{t,jet}$, η_{jet}, y, x_γ^{obs}, for DIS also Q^2. For photoproduction these are shown in figures 6.9 and 6.10, respectively, for DIS in figures 6.11 and 6.12.

The Pythia charm Monte Carlo simulation is used for photoproduction. Results are shown separately for direct and resolved events. With the exception of the high x_γ^{obs} bin the purities for resolved events are slightly lower than those of direct events. All purities are above 0.3, the lowest being the lower p_t bin with a value slightly under 0.4. On average the purities in photoproduction are around 0.6. The stabilities follow the same trend as the purities but are altogether higher with an average value around 0.8.

In DIS the RapGap charm Monte Carlo is used to compute the purities and stabilities, also separating direct and resolved events. The purities in DIS are higher than in photoproduction, the lowest value is again obtained in the lowest p_t bin. The average is around 0.8, stabilities look similar.

6.2 Background Subtraction

The sample of D^* mesons obtained as described in the chapter concerning event selection is not a pure sample of charm hadrons. The background contribution to the measured quantities has to be statistically subtracted. The measured jet shapes are average values containing both signal and background from the total jet sample:

$$\psi^{\text{meas}} = \frac{1}{N} \sum_{i=1}^{N} \psi_i, \tag{6.7}$$

the sum running over number N of selected events. The statistical error of the measured jet shape is given as a standard deviation

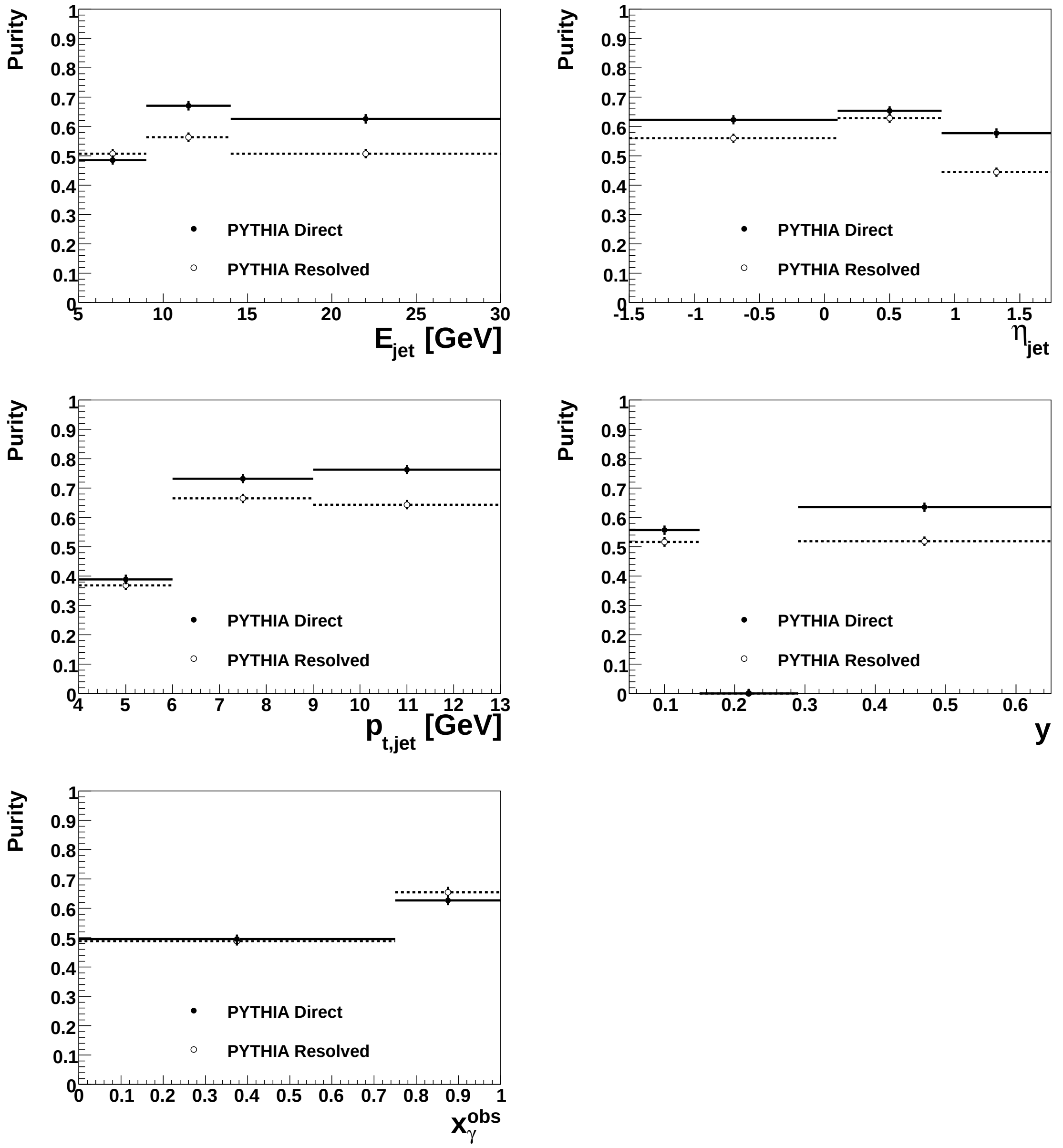

Figure 6.9: Purities of photoproduction events in the jet variables E_{jet}, η_{jet} and $p_{t,jet}$ and in the event variables y and x_{γ}^{obs}. The purities are calculated separately for direct and resolved events by the Pythia Monte Carlo.

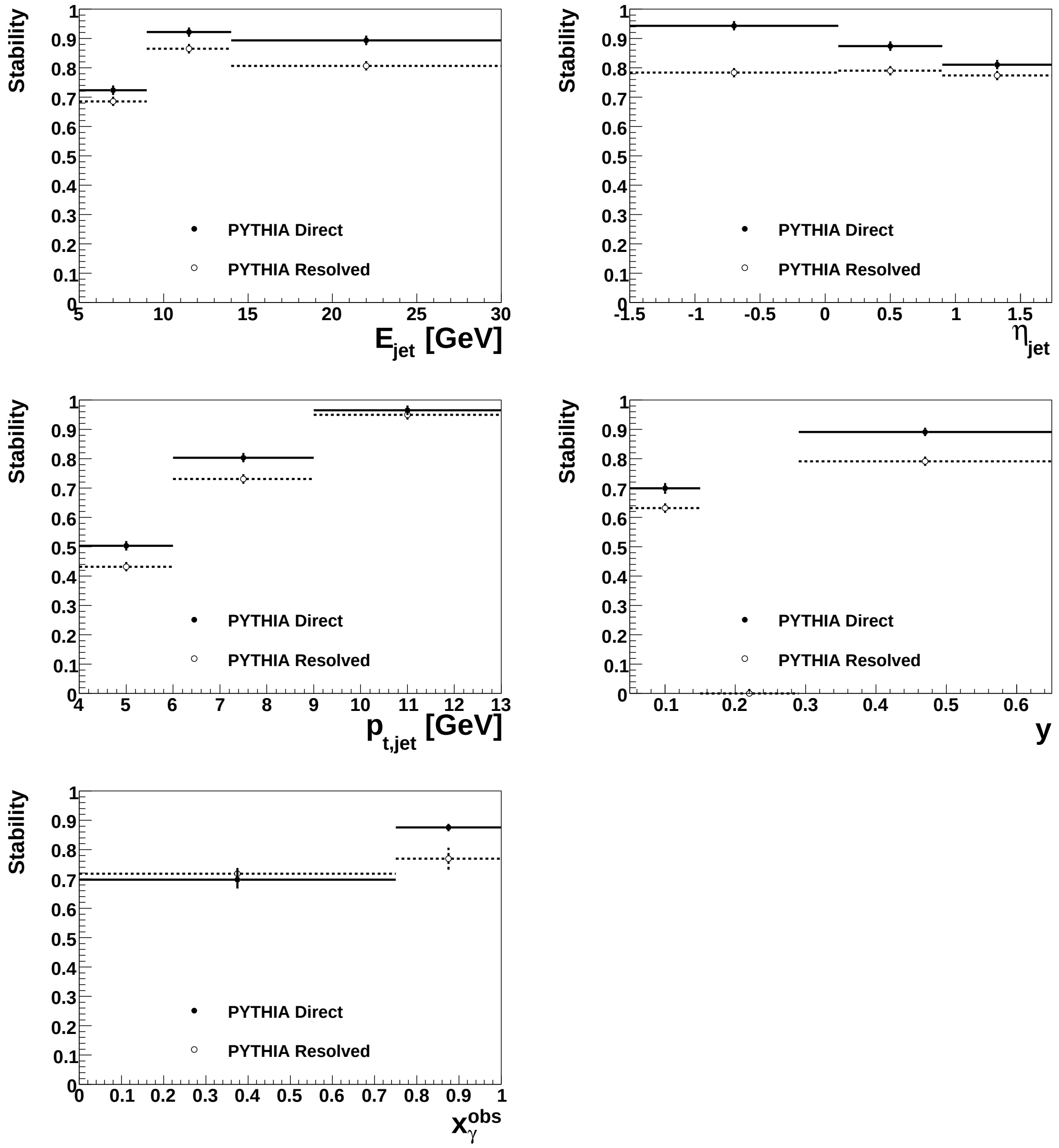

Figure 6.10: Stabilities of photoproduction events in the jet variables E_{jet}, η_{jet} and $p_{t,jet}$ and in the event variables y and x_{γ}^{obs}. The stabilities are calculated separately for direct and resolved events by the Pythia Monte Carlo.

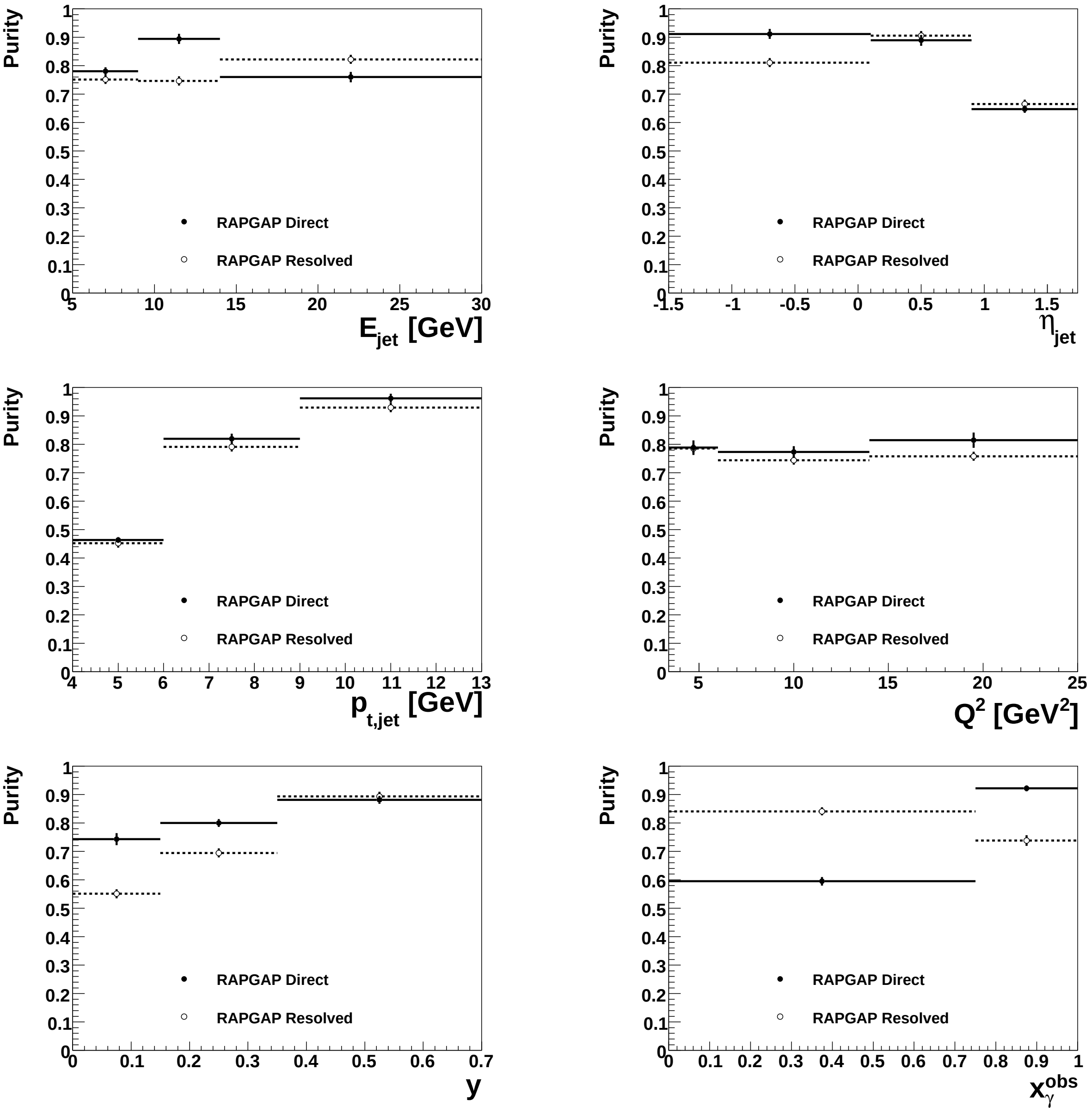

Figure 6.11: Purities of DIS events in the jet variables E_{jet}, η_{jet} and $p_{t,jet}$ and in the event variables Q^2, y and x_γ^{obs}. The purities are calculated separately for direct and resolved events by the RapGap Monte Carlo.

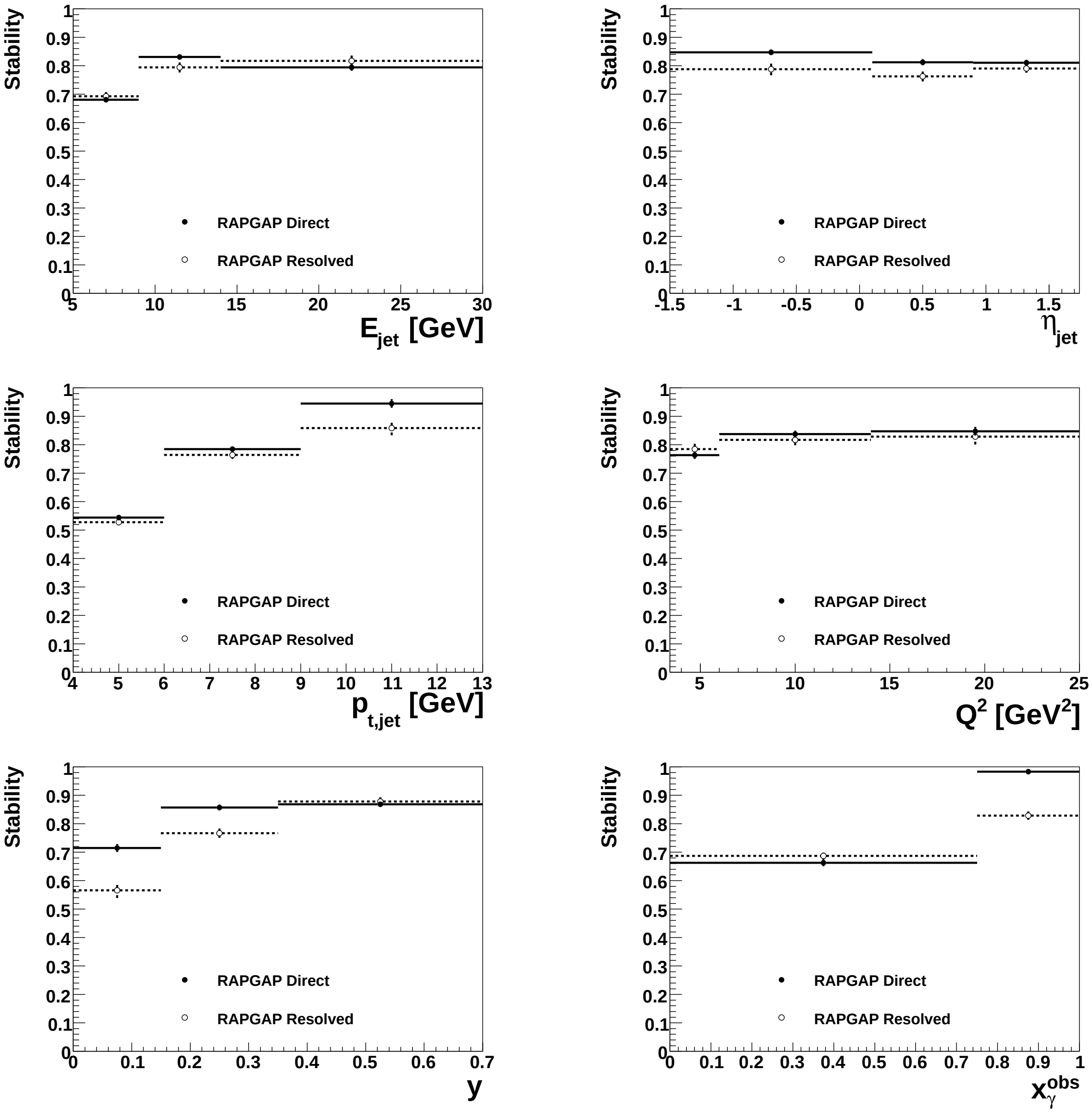

Figure 6.12: Stabilities of DIS events in the jet variables E_{jet}, η_{jet} and $p_{t,jet}$ and in the event variables Q^2, y and x_γ^{obs}. The stabilities are calculated separately for direct and resolved events by the RapGap Monte Carlo.

$$\sigma_{\text{stat}}(\psi^{\text{meas}}) = \sqrt{\frac{\sum_{i=1}^{N} \left(\psi(r)_i^{\text{meas}} - \langle \psi(r) \rangle^{\text{meas}}\right)^2}{N-1}}. \tag{6.8}$$

The measured jet shape can be expressed as composed of components originating from the signal and the background, respectively:

$$\psi^{\text{meas}} = (1 - f^{\text{back}}) \cdot \psi^{\text{sig}} + f^{\text{back}} \cdot \psi^{\text{back}} \tag{6.9}$$

where ψ^{sig} and ψ^{back} are the average values for the signal and the background jet sample, respectively, and f^{back} is the fraction of background jets in the total jet sample

$$f^{\text{back}} = \frac{N^{\text{back}}}{N^{\text{tot}}}. \tag{6.10}$$

This background fraction is determined by integrating the functions fitted to the D^* peak and the background within the signal region. The mean integrated jet shape for the background jet sample can be obtained by studying only wrong charge combinations of reconstructed D^* candidates (cf. section 4.4). The background subtracted signal yields

$$\psi^{\text{sig}} = \frac{\psi^{\text{meas}} - f^{\text{back}} \cdot \psi^{\text{back}}}{1 - f^{\text{back}}} \tag{6.11}$$

and has a statistical error of

$$\sigma_{\text{stat}}(\psi^{\text{sig}}) = \frac{1}{1 - f^{\text{back}}} \cdot \sqrt{\sigma^2_{\text{stat}}(\psi^{\text{meas}}) + \left(f^{\text{back}} \sigma^2_{\text{stat}}\,(\psi^{\text{back}})\right)^2 + \left(\frac{\psi^{\text{meas}} - \psi^{\text{back}}}{1 - f^{\text{back}}}\right)^2 \sigma^2_{\text{stat}}(f^{\text{back}})}. \tag{6.12}$$

In order to reduce the statistical error of the signal it is necessary to have a convenient signal-to-background ratio, i.e. a small value of f^{back}. This is ensured by the narrow cut on the signal region in the Δm distributions of $0.144\ \text{GeV} \leq \Delta m \leq 0.147\ \text{GeV}$ (cf. figures 5.5, 5.6 and 5.11). Depending on the kinematic region the value of f^{back} varies between 0.4 and 0.7.

In figure 6.13(a) right charge data (corresponding to ψ^{meas}) and wrong charge data (ψ^{back}) of the integrated jet shape at a cone radius of $r = 0.6$ are shown together with the RapGap charm Monte Carlo expectation. Also shown are the separate direct and resolved contributions. Figure 6.13(b) shows the background corrected distribution of the data (ψ^{sig}). The background subtracted data is in good agreement with the signal Monte Carlo. The shown distributions are from the DIS sample in the lowermost jet energy bin. The other bins in the analysis exhibit a similar behaviour.

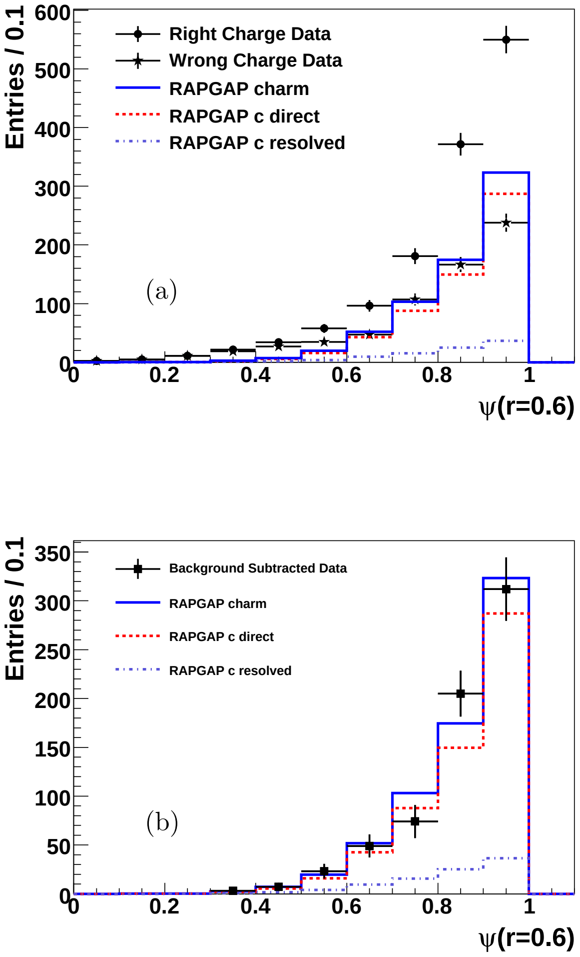

Figure 6.13: Integrated jet shape of the right charge ($\psi^{\text{meas}}(r = 0.6)$) and wrong charge data ($\psi^{\text{back}}(r = 0.6)$) together with the total RapGap charm Monte Carlo and its direct and resolved components on detector level (a). The Monte Carlo distribution is normalised to the integrated lumonisity of the data. In (b) the background subtracted data ($\psi^{\text{sig}}(r = 0.6)$) is shown with the same Monte Carlo.

In figure 6.14 the mean integrated jet shape is shown for right and wrong charge data as well as the background subtracted data. Also shown is the RapGap charm Monte Carlo expectation as well as RapGap uds Monte Carlo. The uds Monte Carlo agrees reasonably with the wrong charge distribution. The right charge data alone is not described. However, after subtraction of the background, the signal data is in good agreement with the charm Monte Carlo simulation.

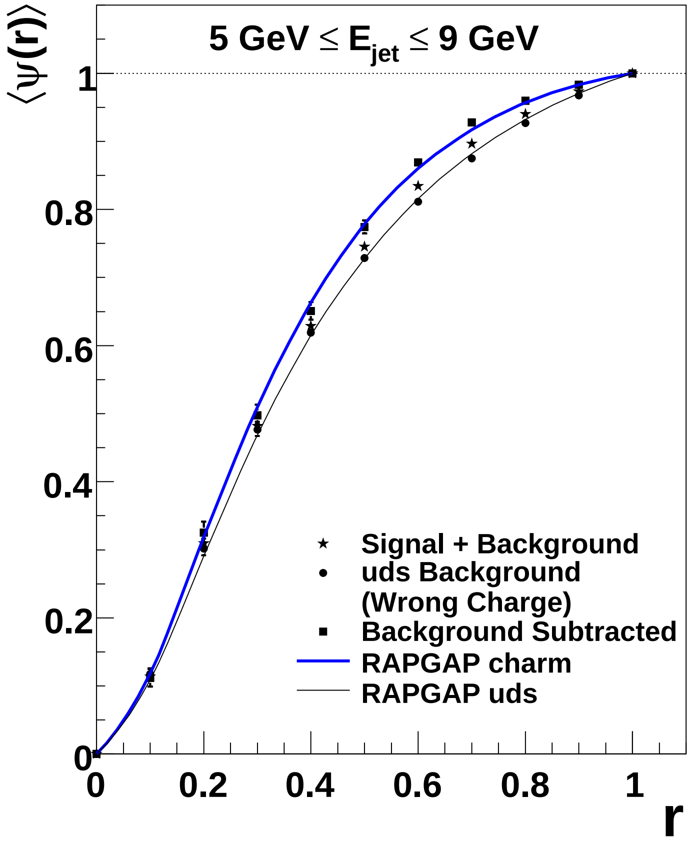

Figure 6.14: Mean integrated jet shape of right and wrong charge data as well as background subtracted data. Also shown are RapGap Monte Carlo expectations of charm and uds events on detector level.

6.3 Control Distributions

In section 6.1 the reconstruction quality, i.e. the correlation between detector level and generated hadron level has been explored as one necessary condition to enable the correction of the measured jet shapes at detector level to hadron level. Another condition that needs to be fulfilled is a reasonable description of the data by the Monte Carlo simulation at detector level. To this end the distributions of various variables are studied with respect to the agreement between data and the Monte Carlo simulation.

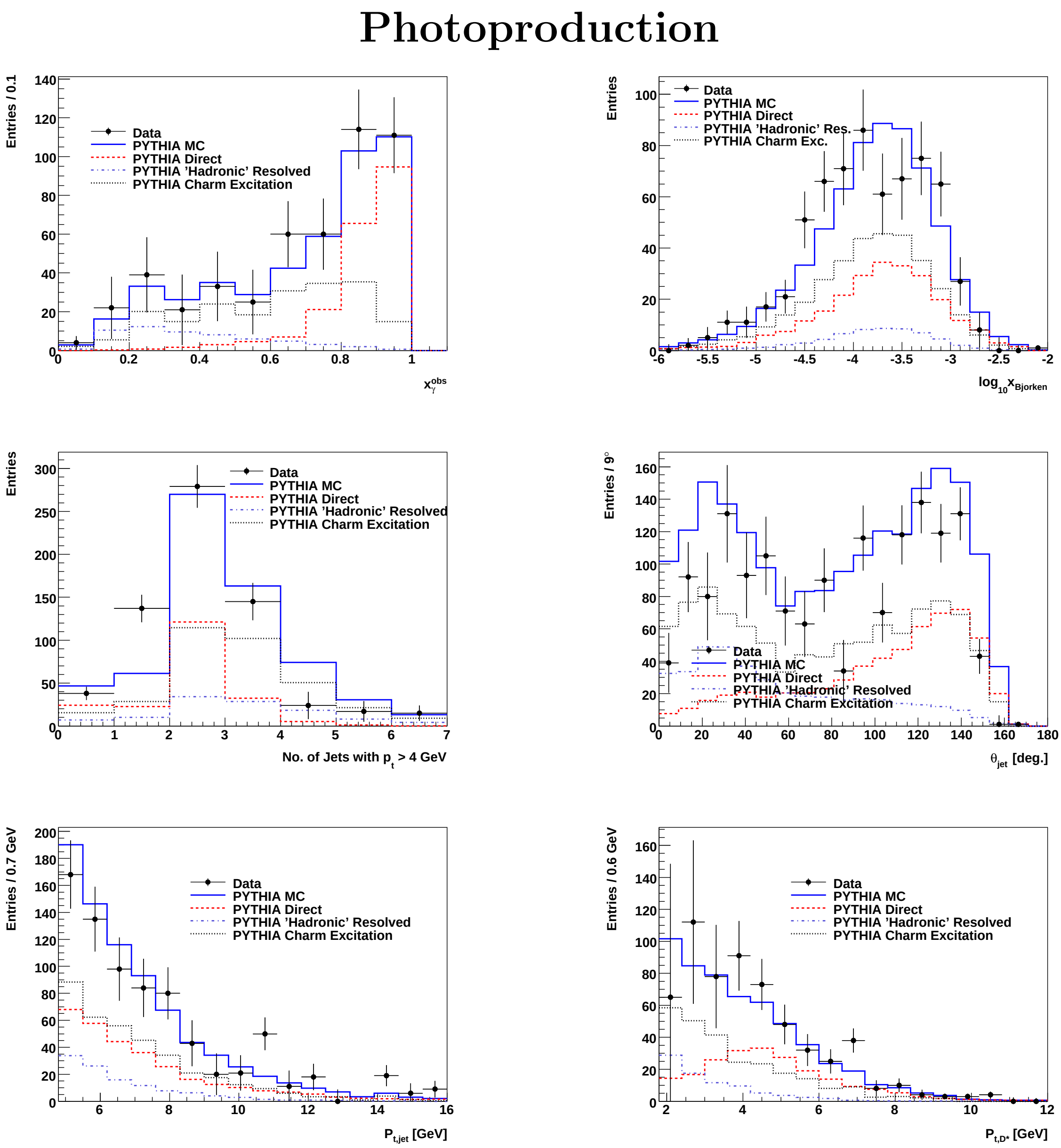

Figure 6.15: Distributions of x_γ^{obs}, $x_{Bjorken}$, the number of jets, the polar angle θ_{jet} and the transverse momentum $P_{t,jet}$ of the analysed jet as well as the transverse momentum P_{t,D^*} of the D^* meson. The measurement is performed in the signal region and the data points are corrected for wrong charge background. The data are compared to the Pythia Monte Carlo simulation. Direct and resolved expectations are shown separately. The Monte Carlo prediction is scaled to the integrated luminosity of the data.

DIS

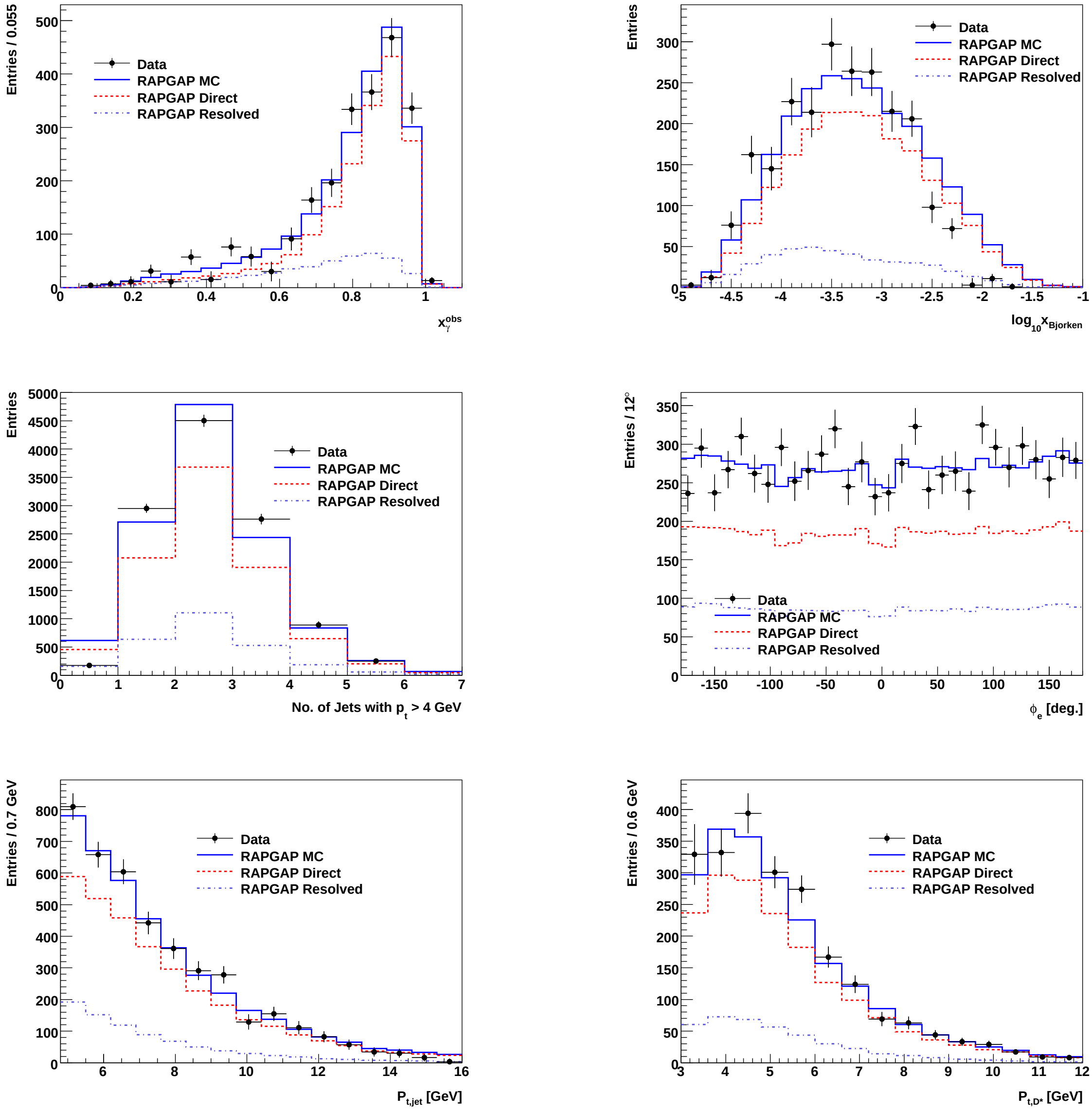

Figure 6.16: Distributions of x_γ^{obs}, $x_{Bjorken}$, the number of jets, the azimuthal angle ϕ_e of the scattered electron, the transverse momentum $P_{t,jet}$ of the analysed jet as well as the transverse momentum P_{t,D^*} of the D^* meson. The measurement is performed in the signal region and the data points are corrected for wrong charge background. The data are compared to the RapGap Monte Carlo simulation. Direct and resolved expectations are shown separately. The Monte Carlo prediction is scaled to the integrated luminosity of the data.

These control distributions for the photoproduction sample are shown in figure 6.15. Here the Pythia Monte Carlo simulation is compared to the data. The particular contributions of direct and resolved photon events (the further separation of the resolved events into charm excitation and hadron-like resolved events is depicted as well) is visualised. The variables x_γ^{obs} and $x_{Bjorken}$ are shown as well as jet and D^* variables (the number of jets, polar angle of the investigated jet as well as the transverse momentum of the jet and the D^* meson). The distributions are measured without cuts on the particular quantity, i.e. the distribution of the number of jets is plotted without a cut on the number of jets.

The data is overall well described by the Pythia Monte Carlo, though the simulation overestimates the number of few-jet (zero or one) events in relation to more-jet (two or three) events. The data distributions are corrected for background in a similar way as described in section 6.2.

For the DIS and RapGap Monte Carlo sample, control plots are shown in figure 6.16. Here also the distribution of the measured azimuthal angle ϕ_e of the scattered electron is displayed. As expected this distribution exhibits no dependency on ϕ_e (though a dent around zero degrees is observable, a remnant from the SpaCal geometry cut, cf. section 5.3.2). At large the Monte Carlo simulation is in good agreement with the data.

6.4 Mean Integrated Jet Shape at Detector Level

The core measurement of the present analysis is the mean integrated jet shape of charm initiated jets in photoproduction and DIS. The integrated jet shape is calculated according to equation 3.2. The mean values of these are determined by means of equation 3.4.

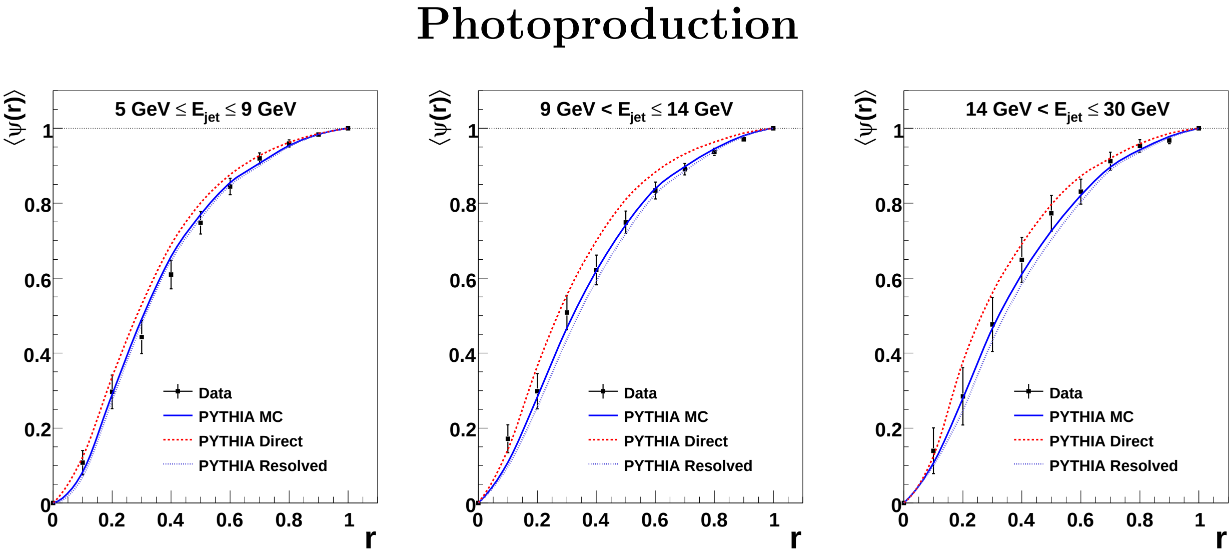

Figure 6.17: Mean integrated jet shape $\langle\psi(r)\rangle$ in photoproduction at detector level as function of the cone radius r for three different regions of the jet energy E_{jet}. Pythia charm Monte Carlo prediction is shown together with separate direct and resolved expectations. Only statistical errors of the data are shown. The statistical errors of the Monte Carlo simulation are negligible.

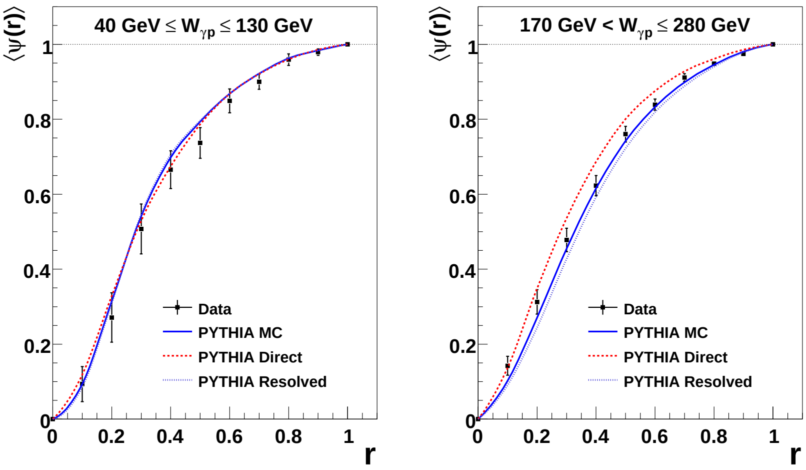

Figure 6.18: Mean integrated jet shape $\langle\psi(r)\rangle$ in photoproduction at detector level as function of the cone radius r for two different regions of $W_{\gamma p}$. Pythia charm Monte Carlo prediction is shown together with separate direct and resolved expectations. Only statistical errors of the data are shown. The statistical errors of the Monte Carlo simulation are negligible.

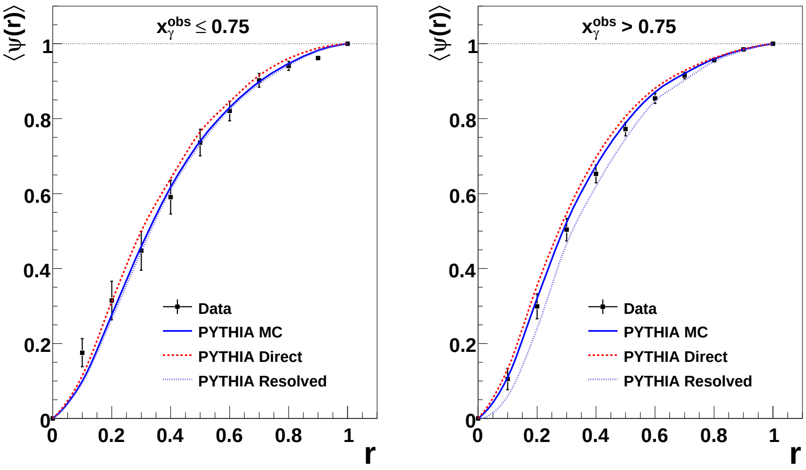

Figure 6.19: Mean integrated jet shape $\langle\psi(r)\rangle$ in photoproduction at detector level as function of the cone radius r for two different regions of x_{γ}^{obs}. Pythia charm Monte Carlo prediction is shown together with separate direct and resolved expectations. Only statistical errors of the data are shown. The statistical errors of the Monte Carlo simulation are negligible.

DIS

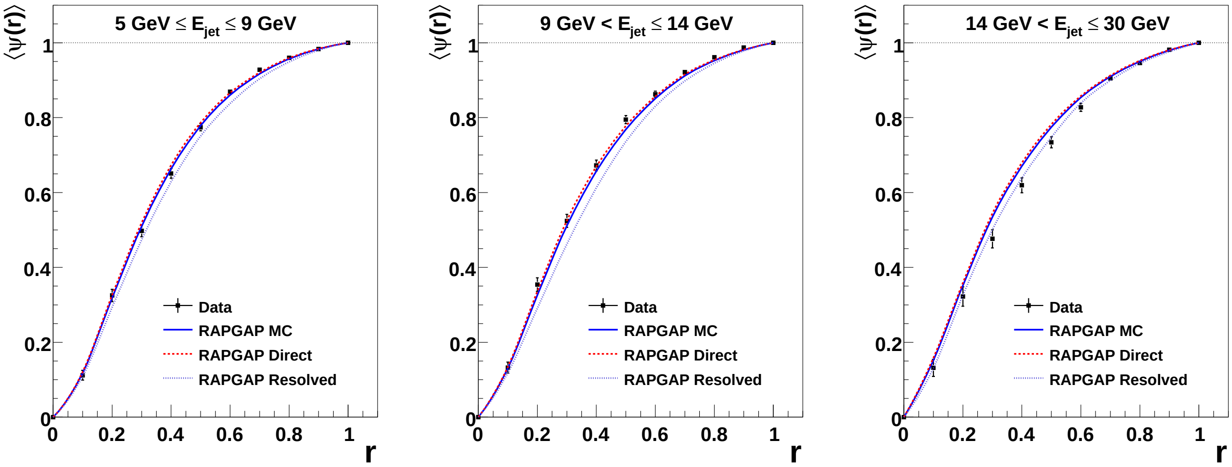

Figure 6.20: Mean integrated jet shape $\langle\psi(r)\rangle$ in DIS at detector level as function of the cone radius r for three different regions of the jet energy E_{jet}. RapGap charm Monte Carlo prediction is shown together with separate direct and resolved expectations. Only statistical errors of the data are shown. The statistical errors of the Monte Carlo simulation are negligible.

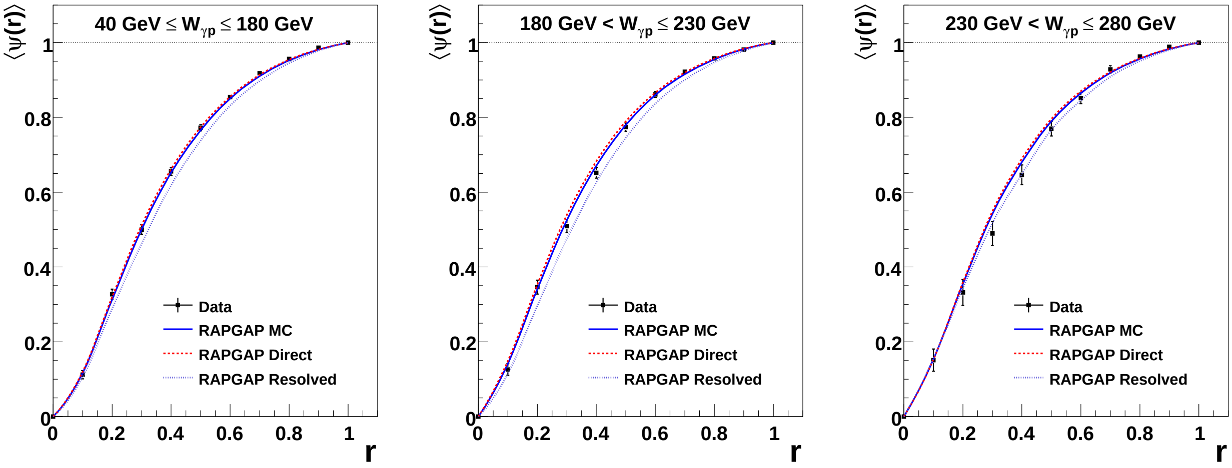

Figure 6.21: Mean integrated jet shape $\langle\psi(r)\rangle$ in DIS at detector level as function of the cone radius r for three different regions of $W_{\gamma p}$. RapGap charm Monte Carlo prediction is shown together with separate direct and resolved expectations. Only statistical errors of the data are shown. The statistical errors of the Monte Carlo simulation are negligible.

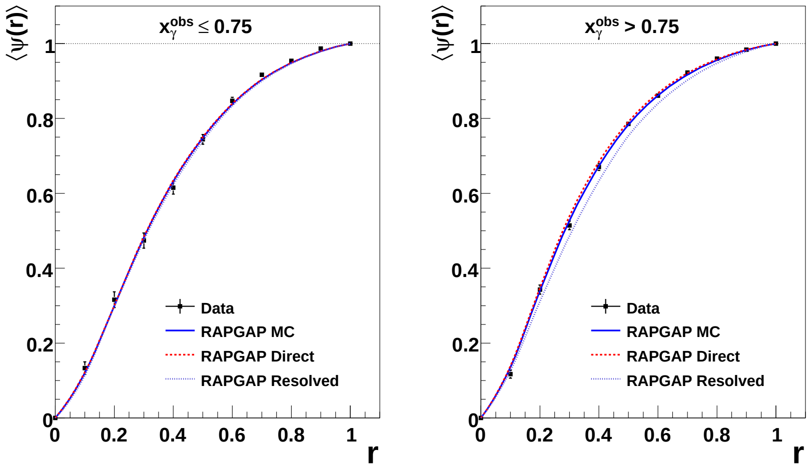

Figure 6.22: Mean integrated jet shape $\langle\psi(r)\rangle$ in DIS at detector level as function of the cone radius r for two different regions of x_γ^{obs}. RapGap charm Monte Carlo prediction is shown together with separate direct and resolved expectations. Only statistical errors of the data are shown. The statistical errors of the Monte Carlo simulation are negligible.

To study a jet sample unbiased by the selection of the D^* meson, the highest-P_t jet not associated with the D^* meson is analysed. The data are corrected for background as described in section 6.2. These measurements are compared to the Pythia Monte Carlo prediction in the photoproduction regime and to the RapGap Monte Carlo for DIS. Additionally, the prediction for direct and resolved events are shown separately. All Monte Carlo calculations have passed the detector simulation in order to be on the same reconstruction level as the data.

Figures 6.17 through 6.19 show the mean integrated jet shape $\langle\psi(r)\rangle$ in photoproduction as a function of the cone radius r in three regions of the E_{jet}, two regions of $W_{\gamma p}$ and two regions of x_γ^{obs}, respectively. The gap between the two $W_{\gamma p}$ regions is caused by the acceptances of the electron taggers ET33 and ET44 (cf. section 5.2.2). The lower x_γ^{obs} bin can be viewed as a resolved enriched sample, while the upper x_γ^{obs} bin is enriched in direct processes. The Pythia Mone Carlo predicts slightly more narrow jets at low jet energies and high values of x_γ^{obs}. The data suggest a slightly higher fraction of gluon jets in these bins. The overall description of the data by the Pythia Monte Carlo is good.

In the figures 6.20 through 6.22 the mean integrated jet shapes for DIS are shown in three bins of the jet energy E_{jet} and the energy in the photon-proton frame of reference $W_{\gamma p}$ (note the three consecutive $W_{\gamma p}$ bins as opposed to photoproduction) and in two bins of x_γ^{obs}. In DIS the difference between direct and resolved jet shapes as predicted by the RapGap Monte Carlo is much smaller than in photoproduction. The prediction is in good agreement with the data, though jets above 14 GeV are predicted slightly more narrow than the data suggest.

6.4.1 Jet Shape at Fixed Cone Radius

In order to visualise the mean integrated jet shape as a function of different physical variables a fixed cone radius of $r = 0.6$ is chosen.

Photoproduction

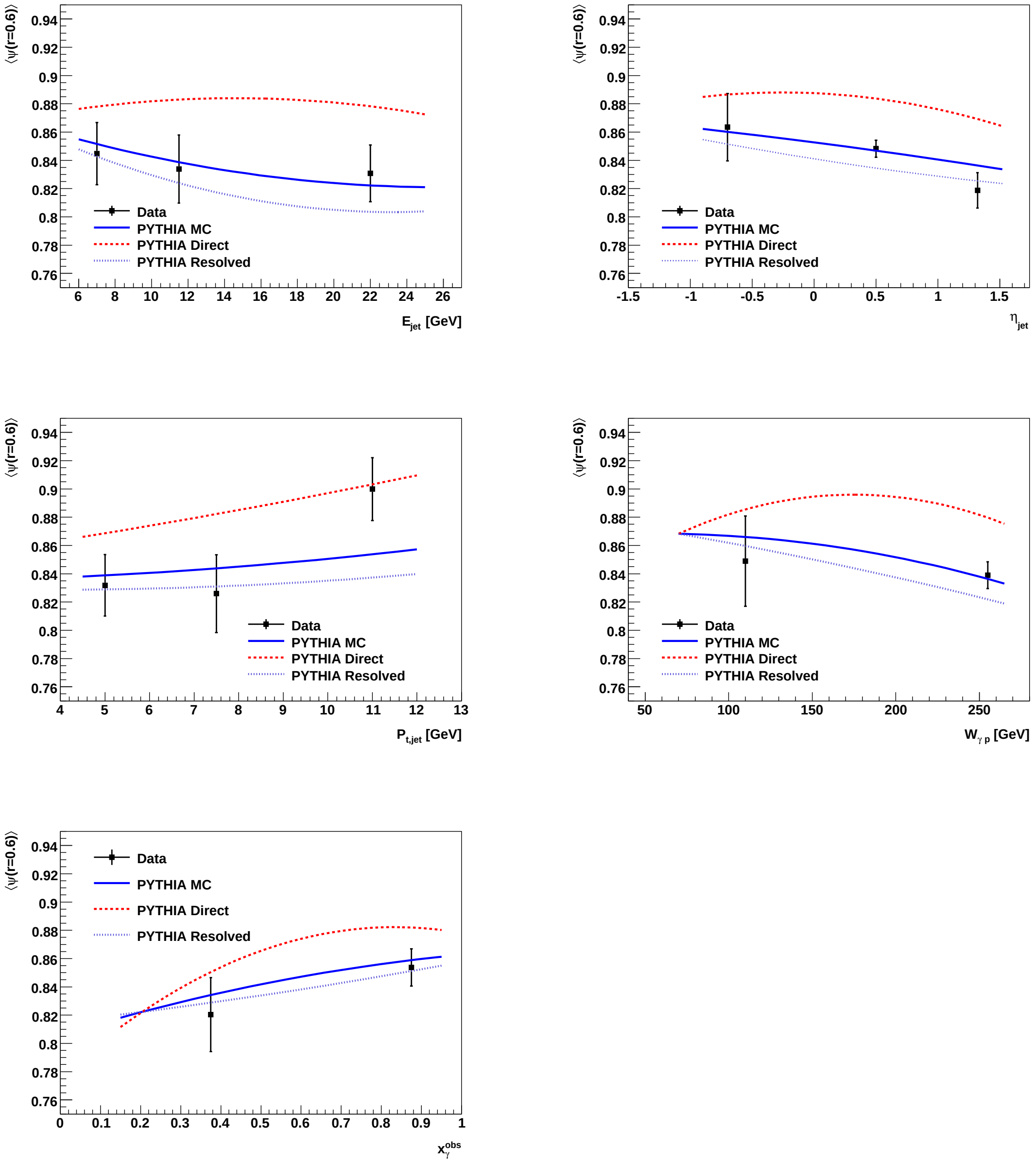

Figure 6.23: Distributions of the mean integrated jet shape at fixed value $r = 0.6$ at detector level as function of E_{jet}, η_{jet}, $P_{t,jet}$, $W_{\gamma p}$ and x_γ^{obs} in photoproduction. Pythia charm Monte Carlo prediction is shown together with separate direct and resolved expectations. Only statistical errors of the data are shown. The statistical errors of the Monte Carlo simulation are negligible.

DIS

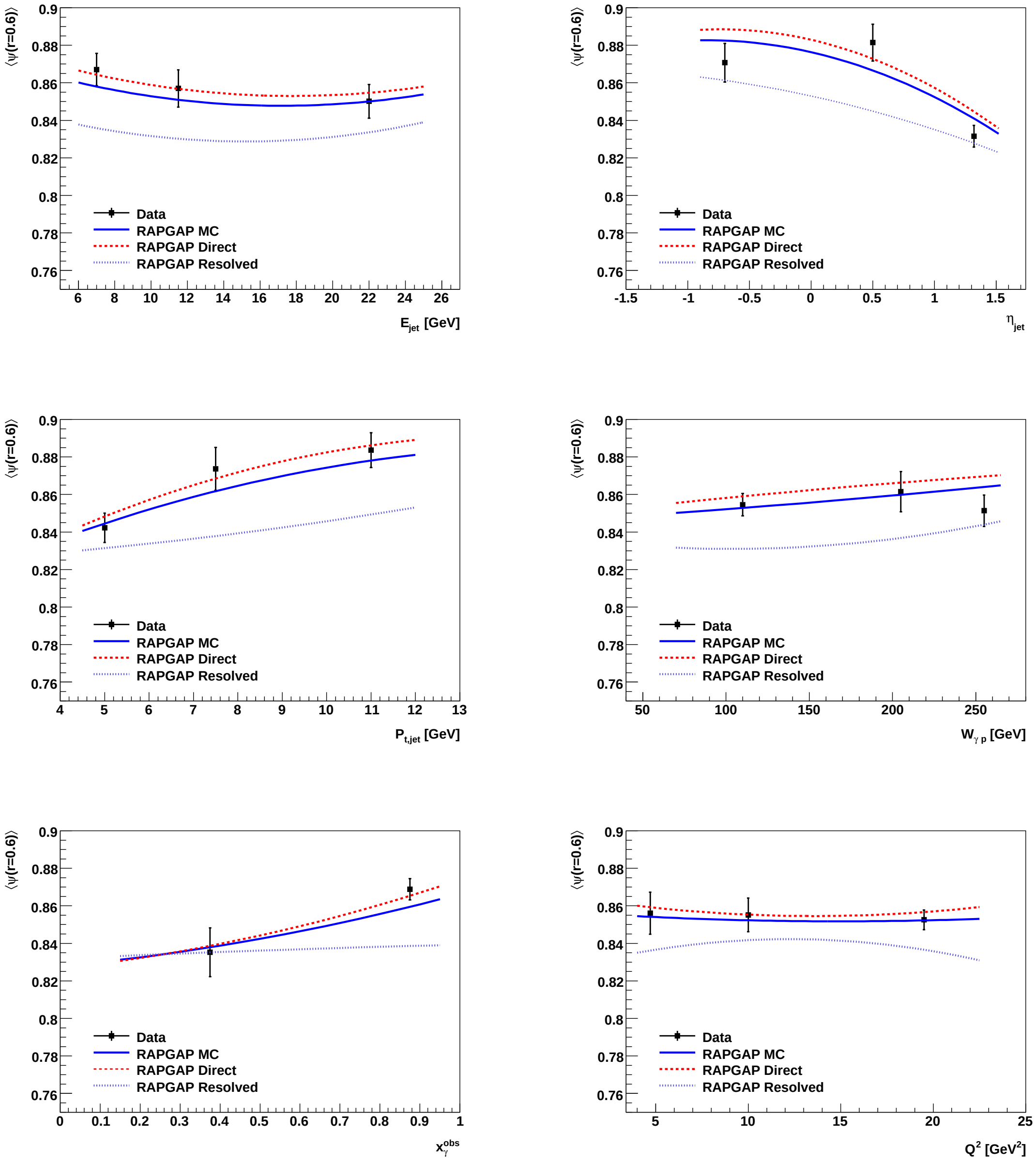

Figure 6.24: Distributions of the mean integrated jet shape at fixed value $r = 0.6$ at detector level as function of E_{jet}, η_{jet}, $P_{t,jet}$, $W_{\gamma p}$, x_γ^{obs} and Q^2 in DIS. RapGap charm Monte Carlo prediction is shown together with separate direct and resolved expectations. Only statistical errors of the data are shown. The statistical errors of the Monte Carlo simulation are negligible.

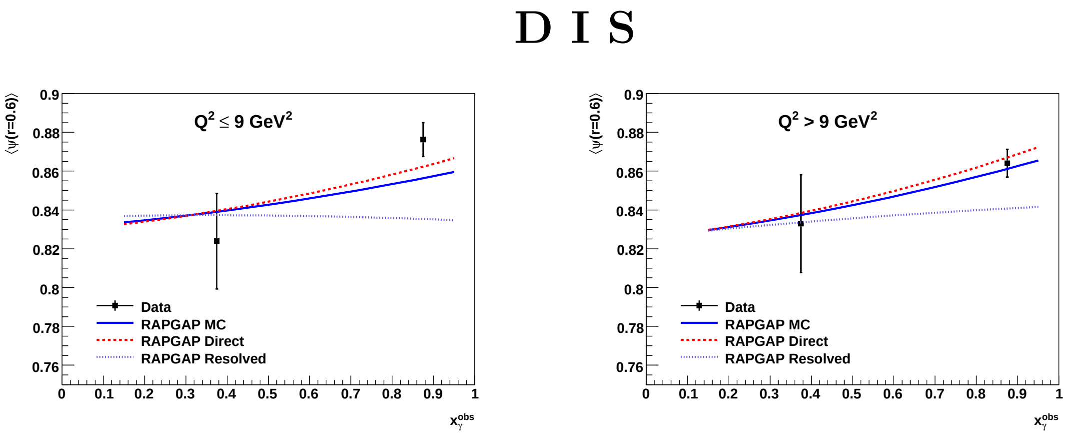

Figure 6.25: Distributions of the mean integrated jet shape at fixed value $r = 0.6$ at detector level as function of x_γ^{obs} in two regions of Q^2. RapGap charm Monte Carlo prediction is shown together with separate direct and resolved expectations. Only statistical errors of the data are shown. The statistical errors of the Monte Carlo simulation are negligible.

This choice is motivated by the maximum discrimination power found at this cone radius, i.e. the value of the difference between direct and resolved expectations divided by the statistical error of the measurement is found to reach its maximum at $r = 0.6$. The study of the optimum cone radius is performed in greater detail in appendix A. At this radius again the quantities of the jet energy E_{jet}, the energy in the photon-proton rest frame $W_{\gamma p}$ as well as x_γ^{obs} are varied. Additionally, the mean integrated jet shapes are studied under varying pseudorapidity η_{jet} and transverse momentum $P_{t,jet}$ of the analysed jet, and in the case of the DIS sample at different four momentum transfer squared Q^2. The data points are plotted in the centre of each bin and the bin boundaries are listed in appendix B.

Shown in figure 6.23 are the mean integrated jet shapes $\langle\psi(r = 0.6)\rangle$ as function of the variables named above for the photoproduction sample. The comparison with the Pythia Monte Carlo simulation as well as the separate direct and resolved prediction are also shown. Minor discrepancies occur at the high pseudorapidity bin which is better described by the resolved component alone and in the highest transverse momentum region where the direct component describes the data well. However, within the statistical errors the data is well described by the Pythia simulation.

In figure 6.24 the mean integrated jet shapes for DIS are displayed together with the RapGap Monte Carlo prediction including separate direct and resolved predictions. With the exception of minor deviations the Monte Carlo simulation is in good agreement with the data. As the fraction of resolved events is higher at lower Q^2 (cf. figure 4.9) the jet shapes in two regions of Q^2 are studied as a function of x_γ^{obs}. This can be seen in figure 6.25. At low x_γ^{obs} the difference between the direct and resolved prediction vanishes, effectively eliminating the discriminating power of the jet shape measurement in this region. This feature is independent of the chosen cone radius, as the mean integrated jet shape at low x_γ^{obs} in DIS is very similar for direct and resolved events, cf. figure 6.22. At high values of x_γ^{obs} and at high Q^2 the measured jet shape agrees with the RapGap Monte Carlo, though direct events alone are sufficient to descibe the data; in the lower Q^2 region even the direct Monte Carlo underestimates the data slightly.

6.5 Detector Correction

To correct the measured data to the hadron level, detector correction factors need to be applied. The 'hadron level' is defined as the hadronic final state consisting of all stable particles except the scattered electron and photons radiated by the electron. In this context 'stable' implies particles that are not decayed by the generators in the standard Monte Carlo event generation, i.e. particles with a lifetime of $\tau \geq 0.33 \cdot 10^{-10}$ s. Simulated particles at detector level are obtained after applying the detector simulation to the particles at hadron level. By applying the detector corrections the results become independent of the detector with which the measurement was performed. Through this step it is possible to compare the data to the results of other experiments as well as to the theoretical predictions as they are implemented in the Monte Carlo generators. In this analysis the detector corrections account for detector and trigger inefficiencies, geometrical acceptance, limited resolutions, particle interactions with the inactive material of the detector as well as the efficiency of the jet reconstruction and event selection.

To be able to use the Monte Carlo simulation to correct the data, the simulation has to describe the data distributions reasonably well. As shown earlier in section 6.3 this is the case for both the photoproduction and the DIS sample.

The corrected mean integrated jet shape in each bin i of the variables considered in this analysis and at each r is calculated in the following way:

$$\langle\psi(r)\rangle_i^{\mathrm{corr}} = C_i^{\mathrm{MC}} \times \langle\psi(r)\rangle_i^{\mathrm{meas}} \tag{6.13}$$

where $\langle\psi(r)\rangle_i^{\mathrm{meas}}$ is the measured men integrated jet shape discussed above. The correction factor is determined using the Monte Carlo simulation:

$$C_i^{\mathrm{MC}} = \frac{\langle\psi(r)\rangle_i^{\mathrm{MC_{had}}}}{\langle\psi(r)\rangle_i^{\mathrm{MC_{det}}}} \tag{6.14}$$

with the mean integrated jet shape $\langle\psi(r)\rangle_i^{\mathrm{MC_{had}}}$ at hadron level and $\langle\psi(r)\rangle_i^{\mathrm{MC_{det}}}$ at detector level, respectively.

The quantity $\langle\psi(r)\rangle^{\mathrm{MC_{had}}}$ considers jets built of the final decay products of hadrons while $\langle\psi(r)\rangle^{\mathrm{MC_{det}}}$ considers the reconstructed detector response in form of the jets of hadronic final state objects. Two Monte Carlo samples are used to determine the correction factors. One is used with the generated quantities, in the other one the detector simulation is applied additionally and the reconstructed quantities are used. At detector level the cuts listed in table 5.5 are applied. The hadron level is defined by the phase-space cuts listed in table 6.1.

In photoproduction the Pythia charm Monte Carlo simulation is chosen to calculate the correction factors, in DIS the RapGap charm Monte Carlo is used. In both cases a signal Monte Carlo is chosen as the data sample is already corrected for background and hence only represents the charm contribution.

Figures 6.26 and 6.27 show the detector correction factors for all analysis bins in photoproduction, figures 6.28 through 6.30 show the factors for DIS. In both photoproduction and DIS the factors are also shown separately for direct and resolved events.

At low values of the cone radius r the deviations of the correction factors from the value one are largest. The factors converge towards one as also the radius r increases to one. At the radius $r = 0.6$ the deviation of C^{MC} from one is usually smaller than 2%.

Photoproduction

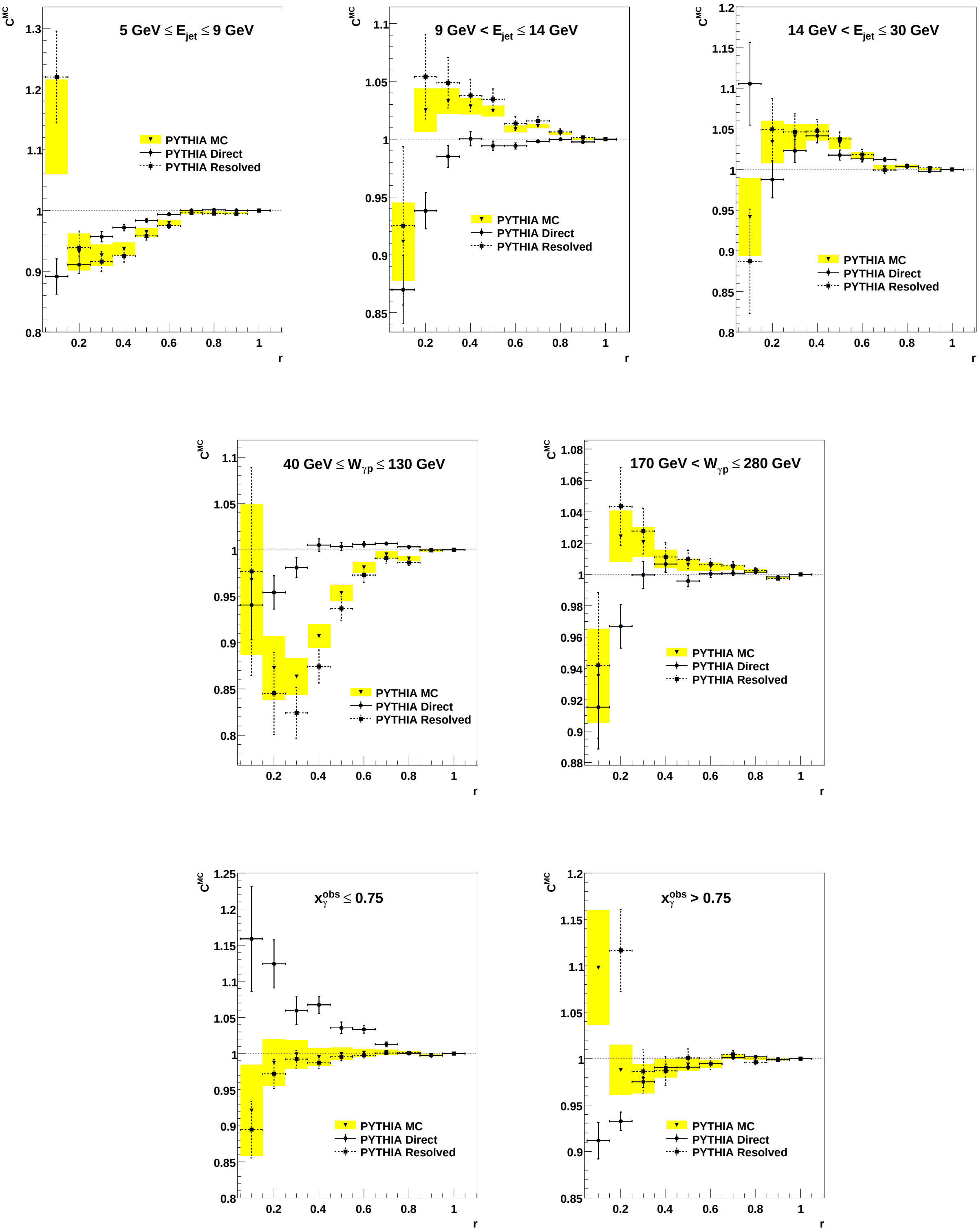

Figure 6.26: Detector correction factors for the mean integrated jet shape $\langle\psi(r)\rangle$ in photoproduction. The factors are determined separately in three regions of the jet energy E_{jet} as well as in two regions of the proton-photon reference system $W_{\gamma p}$ and x_γ^{obs},respectively, using the Pythia Monte Carlo simulation. The factors are shown for the total Monte Carlo and separately for direct and resolved processes. The error band and bars represent the statistical uncertainty of the Monte Carlo simulation.

Photoproduction

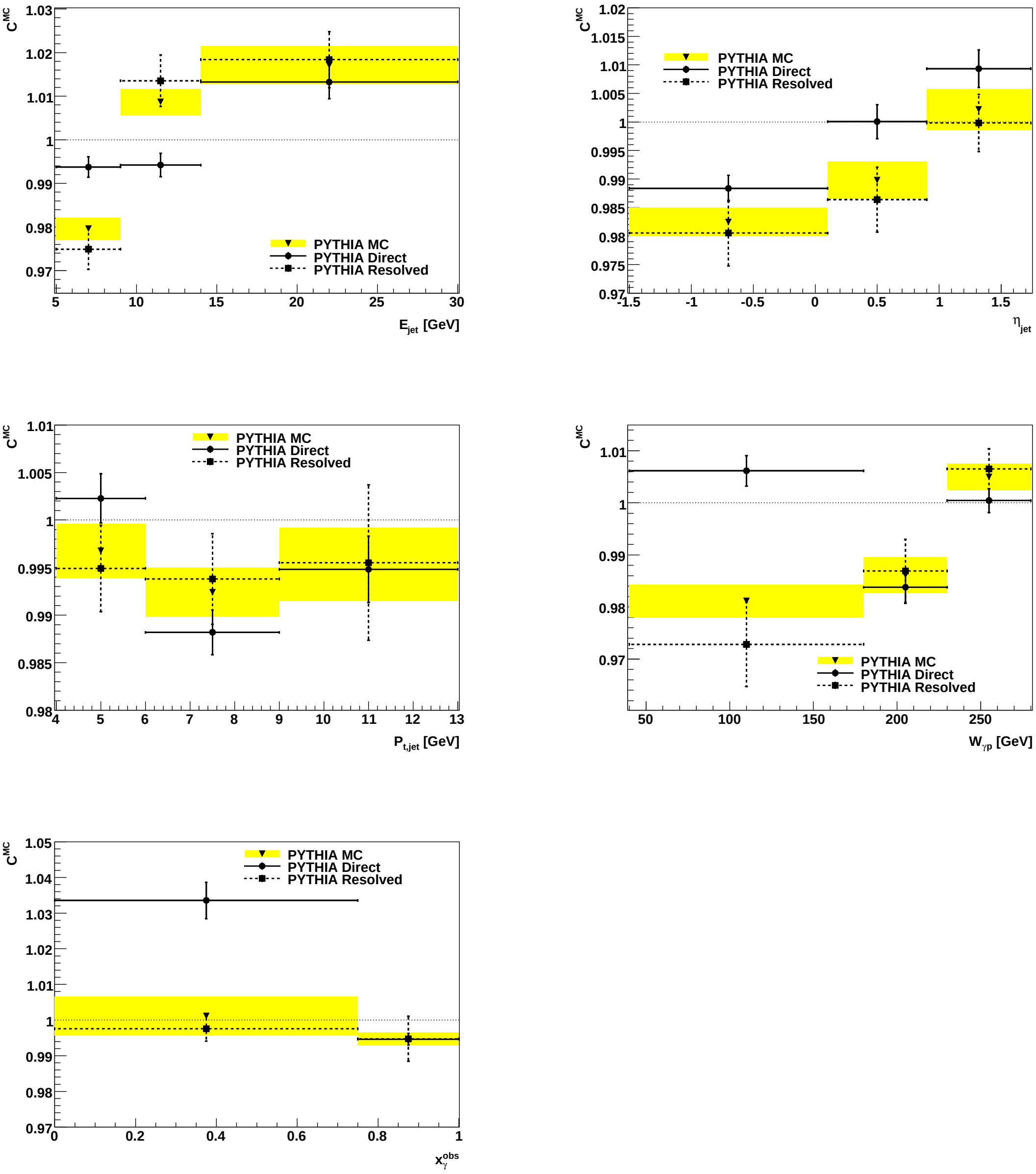

Figure 6.27: Detector correction factors for the mean integrated jet shape $\langle\psi(r = 0.6)\rangle$ in photoproduction as a function of the variables E_{jet}, η_{jet}, $P_{t,jet}$, $W_{\gamma p}$ and x_γ^{obs}, determined using the Pythia Monte Carlo simulation. The factors are shown for the total Monte Carlo and separately for direct and resolved processes. The error band and bars represent the statistical uncertainty of the Monte Carlo simulation.

DIS

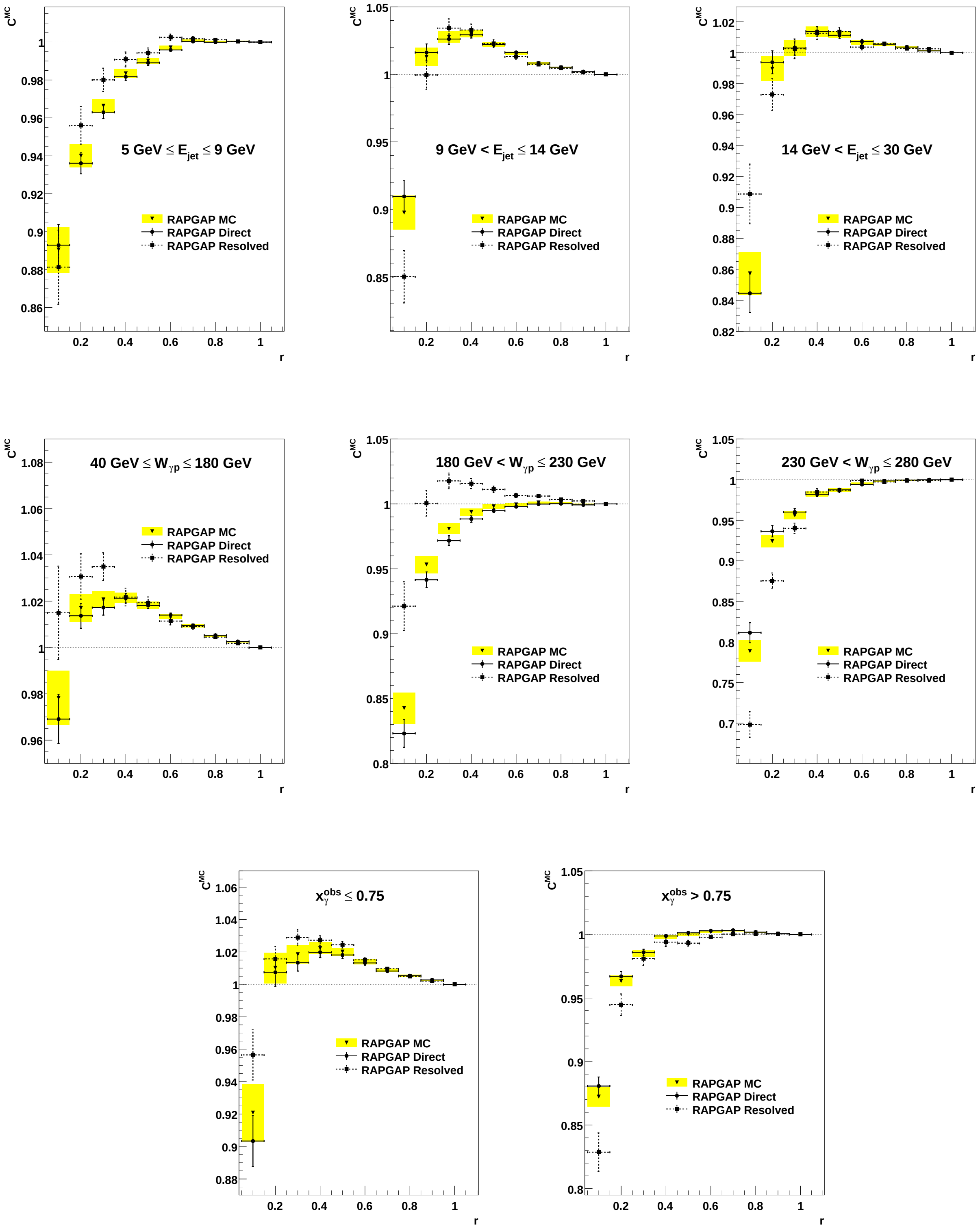

Figure 6.28: Detector correction factors for the mean integrated jet shape $\langle\psi(r)\rangle$ in DIS. The factors are determined separately in three regions of the jet energy E_{jet} and the proton-photon reference system $W_{\gamma p}$, respectively, as well as in two regions of x_γ^{obs}, using the RapGap Monte Carlo simulation. The factors are shown for the total Monte Carlo and separately for direct and resolved processes. The error band and bars represent the statistical uncertainty of the Monte Carlo simulation.

D I S

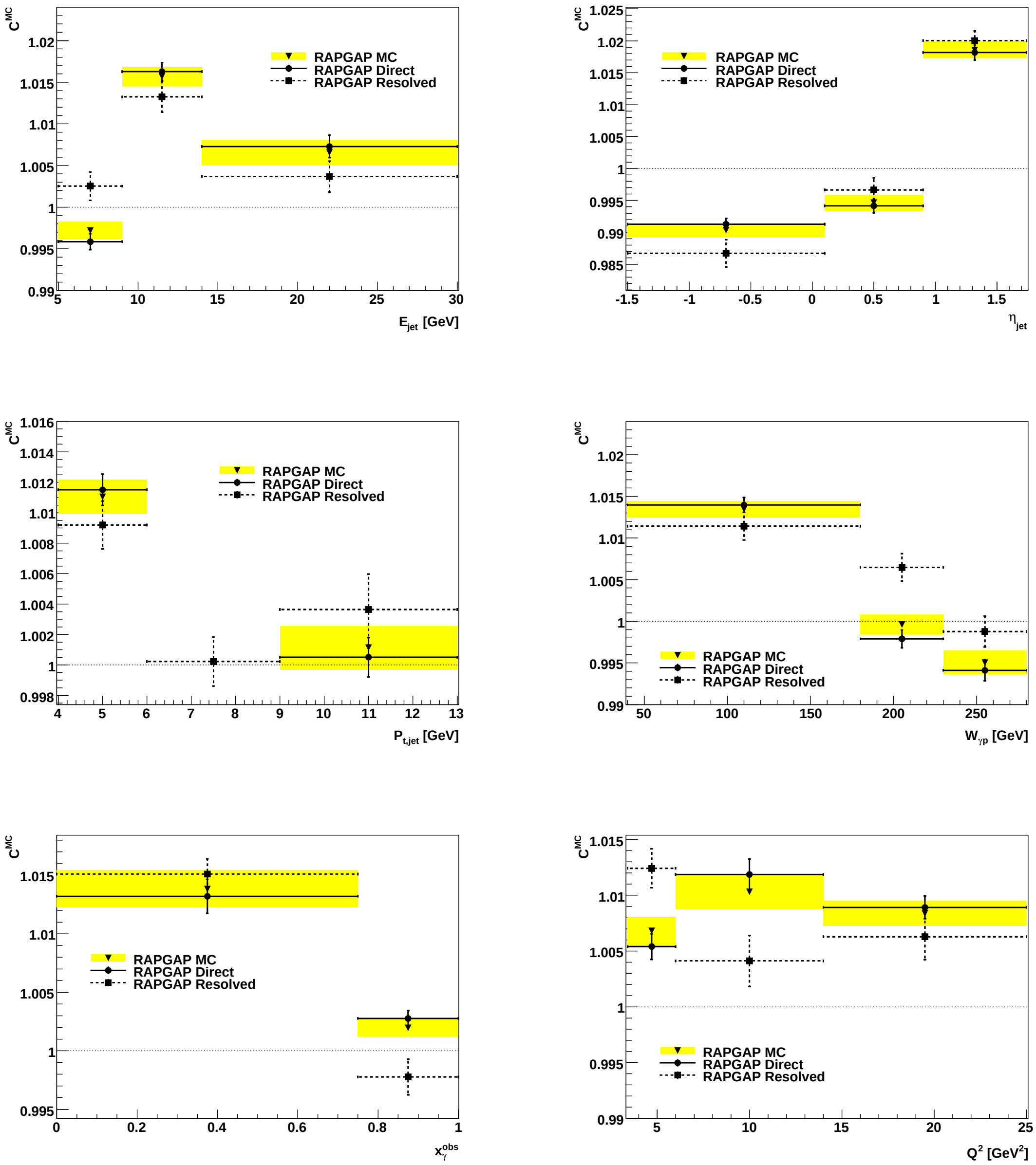

Figure 6.29: Detector correction factors for the mean integrated jet shape $\langle\psi(r = 0.6)\rangle$ in DIS as a function of the variables E_{jet}, η_{jet}, $P_{t,jet}$, $W_{\gamma p}$, x_γ^{obs} and Q^2, determined using the RapGap Monte Carlo simulation. The factors are shown for the total Monte Carlo and separately for direct and resolved processes. The error band and bars represent the statistical uncertainty of the Monte Carlo simulation.

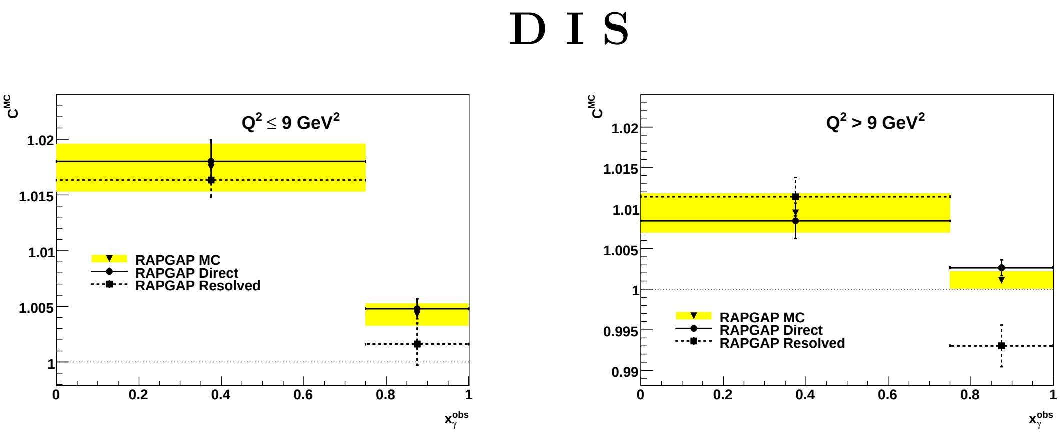

Figure 6.30: Detector correction factors for the mean integrated jet shape $\langle\psi(r = 0.6)\rangle$ in DIS as a function of the variable x_γ^{obs} in two regions of Q^2, determined using the RapGap Monte Carlo simulation. The factors are shown for the total Monte Carlo and separately for direct and resolved processes. The error band and bars represent the statistical uncertainty of the Monte Carlo simulation.

6.6 Systematic Uncertainties

The relative systematic uncertainty of the mean integrated jet shape is defined as the deviation σ_{syst}^{rel} from the central value $\langle\psi(r)\rangle^{central}$ if a given parameter of the analysis is varied

$$\sigma_{syst}^{rel} = \frac{\langle\psi\rangle^{varied} - \langle\psi\rangle^{central}}{\langle\psi\rangle^{central}}. \tag{6.15}$$

with $\langle\psi\rangle^{varied}$ as the obtained value of the mean integrated jet shape after the variation of one of the studied uncertainties. It is calculated for the variation of the hadronic energy scale and for jet axis smearing. Both calculations are performed at detector level, i.e. before the detector corrections are applied. The systematic error of the detector calculation is studied in a similar way. The estimated uncertainties are detailed below.

- **An energy scale variation** of the hadronic final state objects is performed. Here the energy of pure cluster objects is varied by ±4% and the energy of pure track objects by ±2% [68]. For combined objects consisting of clusters as well as tracks a variation of ±3% is applied. It is found that pure cluster objects as well as combined objects contribute 40% to the total jet transverse momenta while pure track objects contribute 20% [35].

  The variation is performed in all analysis bins by separately scaling the energy of all hadronic final state particles up and down. The mean integrated jet shape is found to decrease when the hadronic energy scale is varied to increasing values and vice versa. In photoproduction the maximum decrease is found to be 0.15%, the largest increase 0.07%. In DIS the maximum deviation was −0.19% and +0.08%. The highest deviation was taken to estimate the systematic uncertainty of the hadronic energy scale yielding 0.15% for photoproduction and 0.2% for DIS.

- **Jet axis smearing** is applied in the polar angle θ and the azimuthal angle ϕ. Both jet angles are convoluted with a Gaussian smearing of 2.5°. The choice of the smearing factor is motivated by the angular resolution of the jet axis in θ and ϕ as computed in the Monte Carlo simulation. This is shown in figure 6.31. The smearing results in a maximum negative deviation of the mean integrated jet shape of 0.6% in photoproduction and 0.7% in DIS.

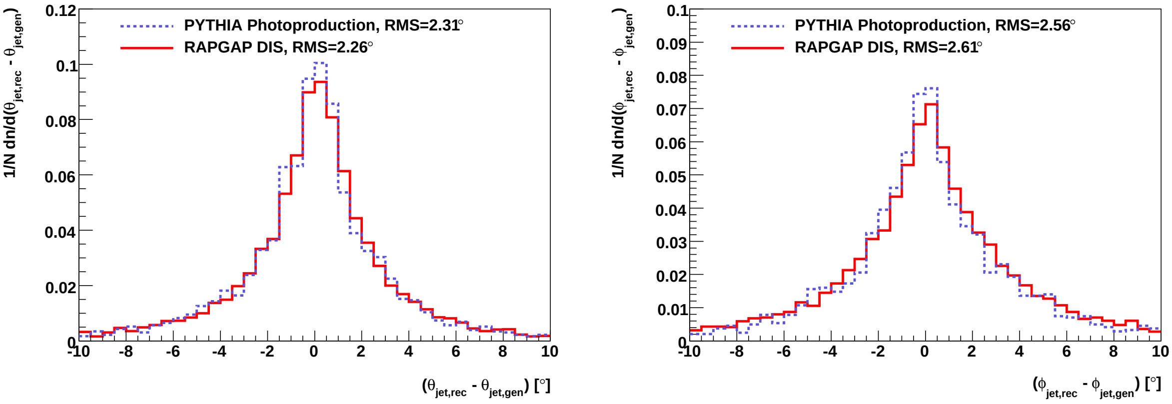

Figure 6.31: Resolutions of the polar angle θ and the azimuthal angle ϕ of the analysed jet. The resolutions are computed separately for photoproduction using the Pythia Monte Carlo and for DIS using the RapGap Monte Carlo simulation.

- **The signal extraction uncertainty** is estimated by scaling the fitting function of the D^* signal up, respectively down, by 5%. This is done while keeping the function fitted to the background constant. The magnitude of this scaling is motivated by the uncertainty of the number of D^* events obtained from the fit of the ET33 data in photoproduction, cf. figure 6.32(a).

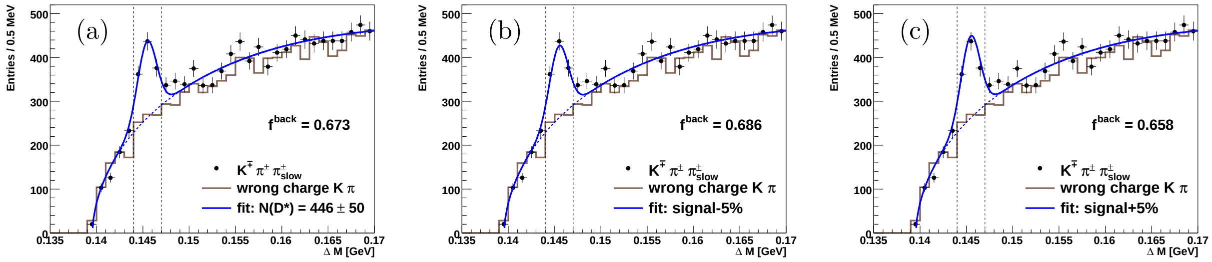

Figure 6.32: Δm distribution of the ET33 selection in photoproduction including the fit describing signal and background (a). The function describing the signal is scaled down by 5% in (b) and up by 5% in (c). Also displayed is f^{back}, the fraction of background events in the Δm signal region between the dashed lines as obtained by the fits. The function describing the background is not subject to the variation.

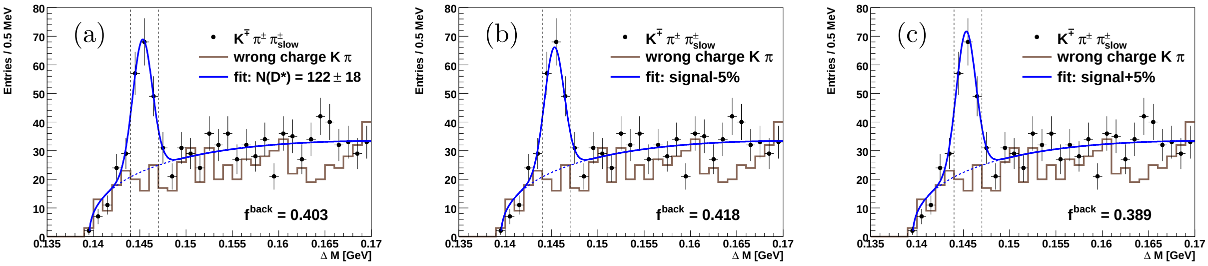

Figure 6.33: Δm distribution of the ET44 selection in photoproduction including the fit describing signal and background (a). The function describing the signal is scaled down by 5% in (b) and up by 5% in (c). Also displayed is f^{back}, the fraction of background events in the Δm signal region between the dashed lines as obtained by the fits. The function describing the background is not subject to the variation.

In DIS the same scaling is used as in photoproduction. The variation has direct impact on the determination of the background fraction f^{back} (cf. equation 6.10) detailed in section 6.2. Figures 6.32 and 6.33 show the Δm distributions in photoproduction (separately for ET33 and ET44) including the fitted functions. Next to the nominal fit the scaled versions are shown. The impact on the background fraction is indicated. The same is displayed in figure 6.34 for DIS.

The mean integrated jet shapes prove to be insensitive to the variation of the signal fit. For the photoproduction sample the largest deviation due to the fit variation is found in the medium bin of the pseudorapidity $\eta_{jet}(r = 0.6)$ of the jet and its size is 0.8%. In DIS the mean integrated jet shape changes by no more than 0.1% as a consequence of the fit variation. These values are taken as estimates of the systematic uncertainties due to the signal extraction.

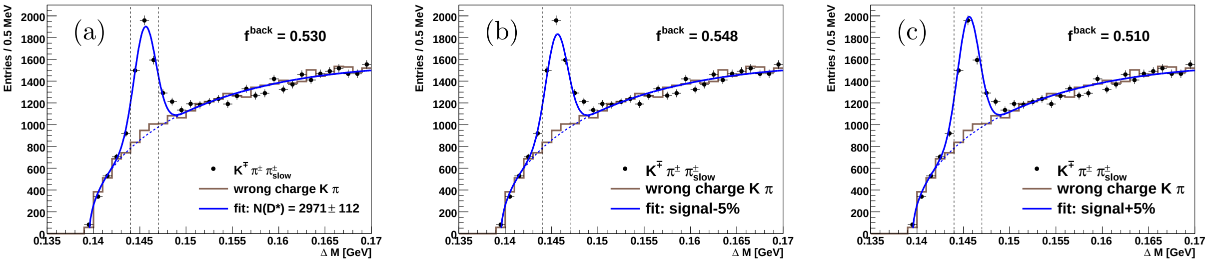

Figure 6.34: Δm distribution of the DIS selection including the fit describing signal and background (a). The function describing the signal is scaled down by 5% in (b) and up by 5% in (c). Also displayed is f^{back}, the fraction of background events in the Δm signal region between the dashed lines as obtained by the fits. The function describing the background is not subject to the variation.

Photoproduction

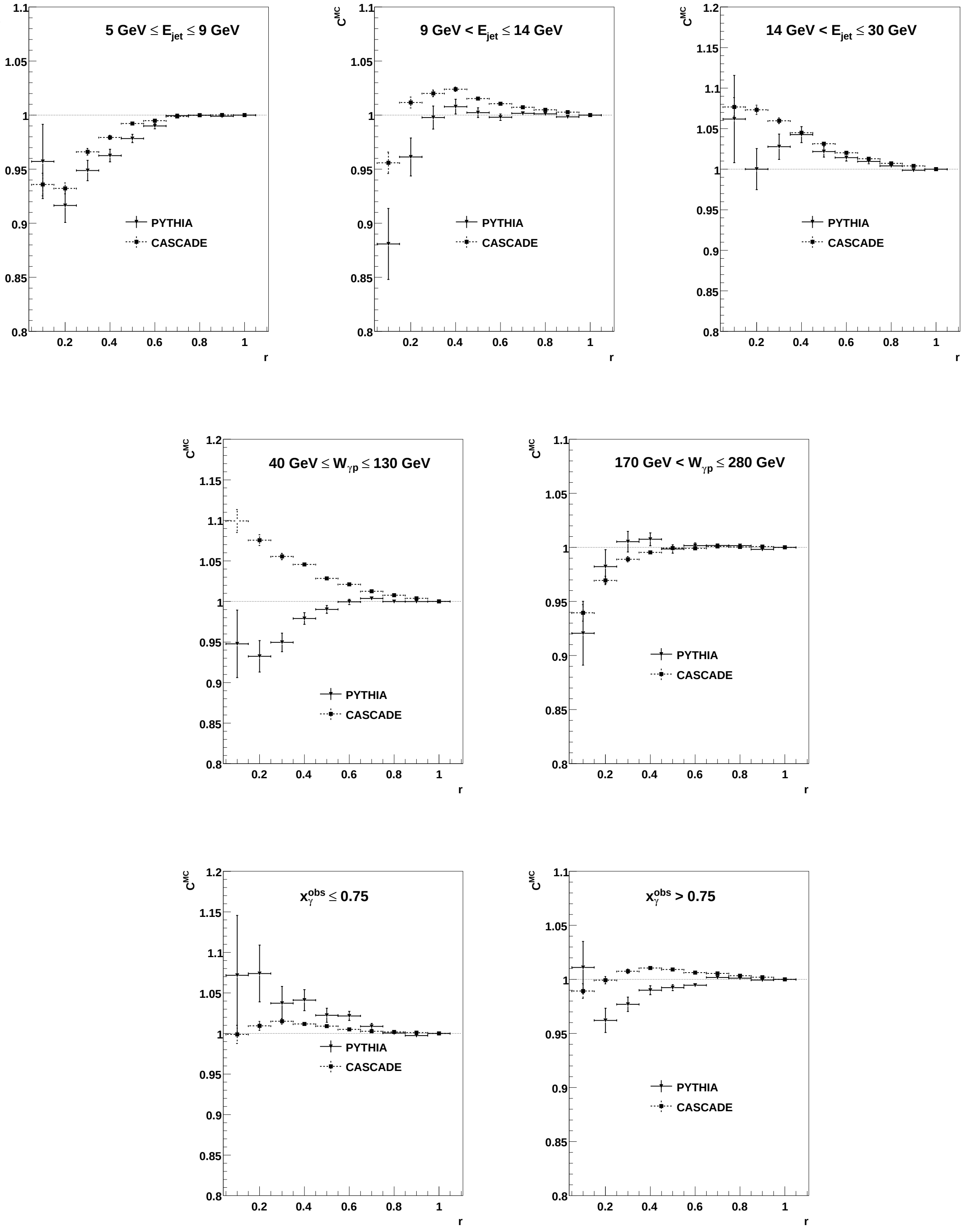

Figure 6.35: Comparison of the detector correction factors calculated by the Pythia and Cascade Monte Carlo simulations in photoproduction for the mean integrated jet shape $\langle\psi(r)\rangle$. The error bars represent the statistical uncertainty of the Monte Carlo simulation. For the determination of the systematic uncertainty the value of $\langle\psi(r = 0.6)\rangle$ has been studied.

Photoproduction

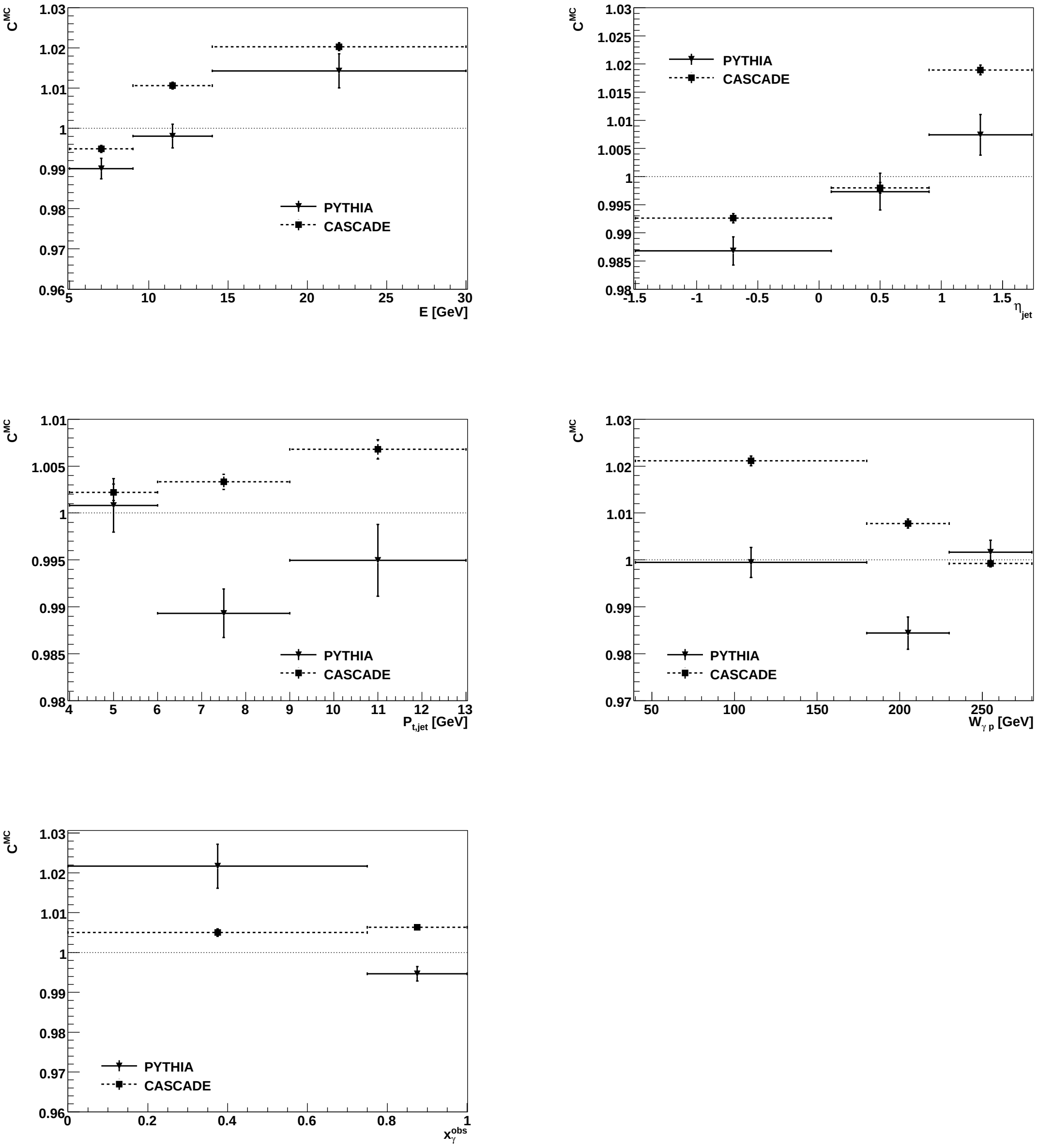

Figure 6.36: Comparison of the detector correction factors calculated by the Pythia and Cascade Monte Carlo simulations in photoproduction for the mean integrated jet shape $\langle\psi(r = 0.6)\rangle$. The comparison is performed as a function of the variables E_{jet}, η_{jet}, $P_{t,jet}$, $W_{\gamma p}$ and x_γ^{obs}. The error bars represent the statistical uncertainty of the Monte Carlo simulation.

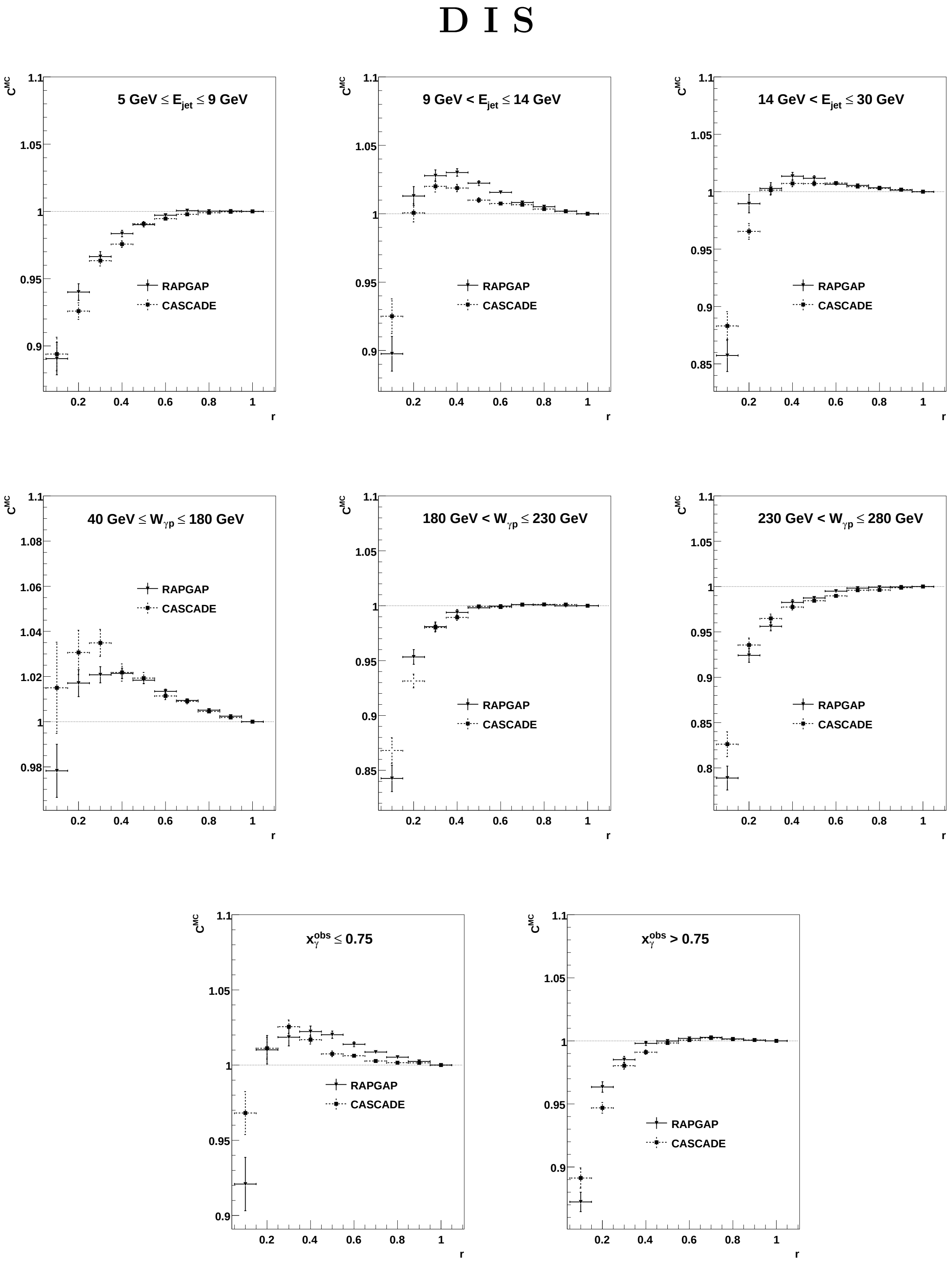

Figure 6.37: Comparison of the detector correction factors calculated by the RapGap and Cascade Monte Carlo simulations in DIS for the mean integrated jet shape $\langle\psi(r)\rangle$. The error bars represent the statistical uncertainty of the Monte Carlo simulation. For the determination of the systematic uncertainty the value of $\langle\psi(r = 0.6)\rangle$ has been studied.

DIS

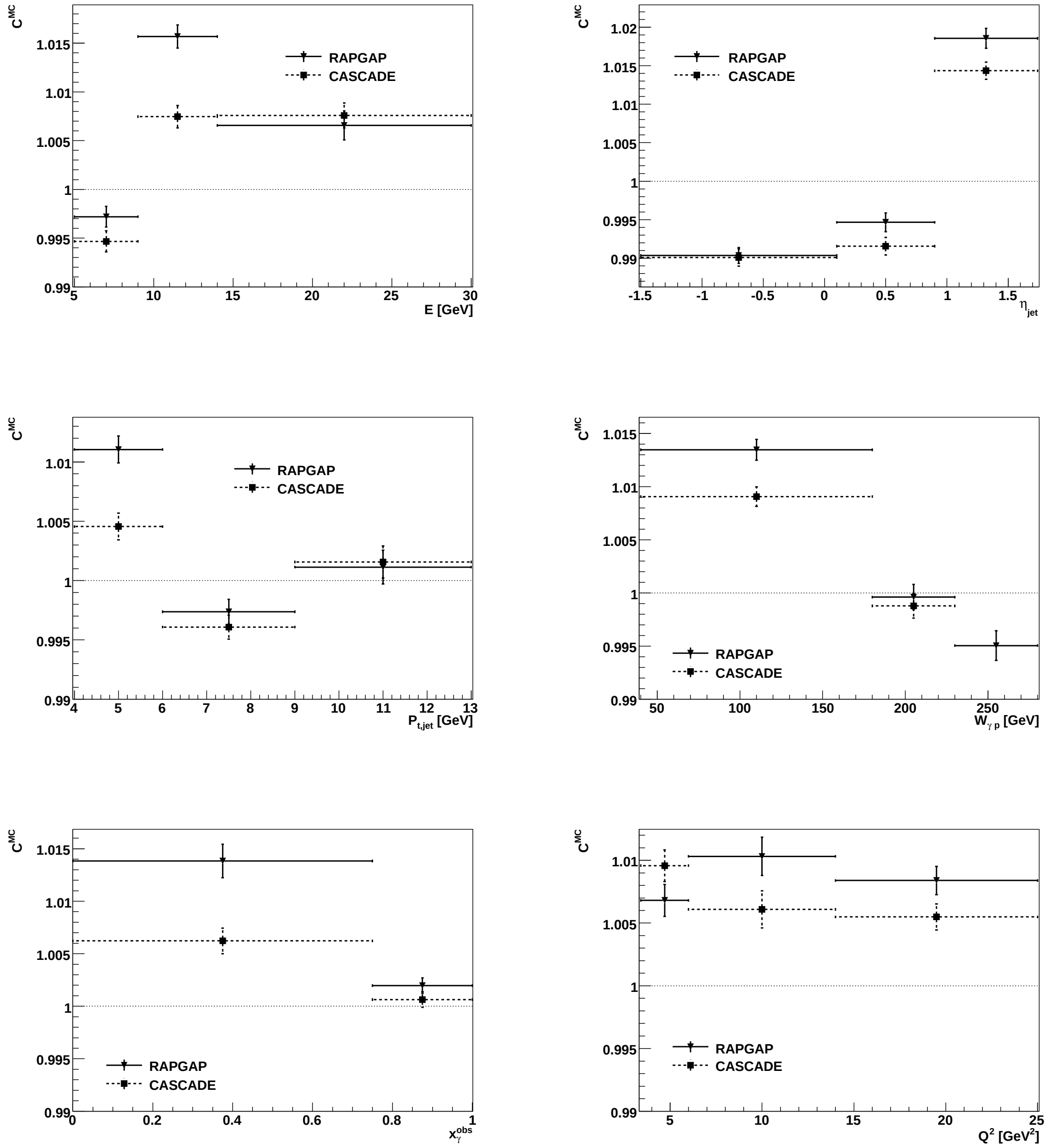

Figure 6.38: Comparison of the detector correction factors calculated by the RapGap and Cascade Monte Carlo simulations in DIS for the mean integrated jet shape $\langle\psi(r = 0.6)\rangle$. The comparison is performed as a function of the variables E_{jet}, η_{jet}, $P_{t,jet}$, $W_{\gamma p}$, x_γ^{obs} and Q^2. The error bars represent the statistical uncertainty of the Monte Carlo simulation.

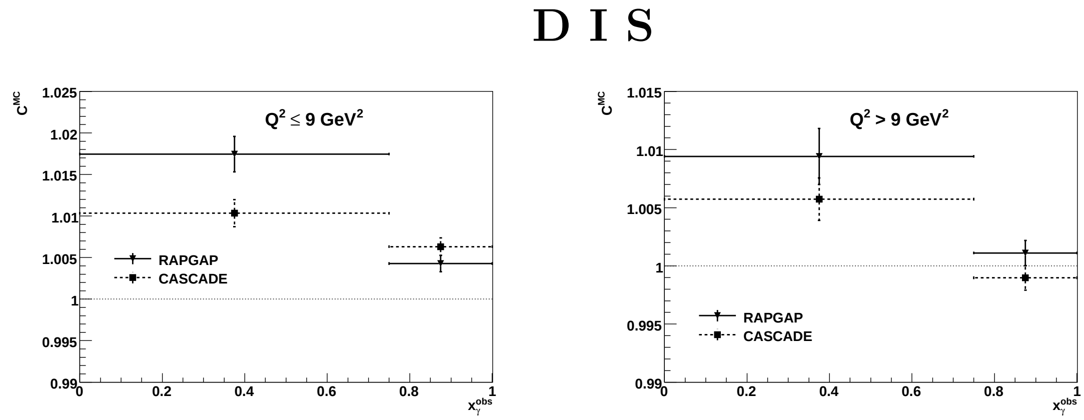

Figure 6.39: Comparison of the detector correction factors calculated by the RapGap and Cascade Monte Carlo simulations in DIS for the mean integrated jet shape $\langle\psi(r = 0.6)\rangle$. The comparison is performed as a function of the variables x_γ^{obs} in two regions of Q^2. The error bars represent the statistical uncertainty of the Monte Carlo simulation.

- **The detector correction uncertainty** is estimated by calculating the detector corrections with an alternative Monte Carlo simulation. Both the photoproduction and the DIS corrections have been performed utilising two Cascade Monte Carlo samples. These corrections have been compared to the Pythia and RapGap simulations for photoproduction and DIS, respectively. The comparison between the correction factors is shown in figures 6.35 and 6.36 for photoproduction and in figures 6.37 through 6.39 for DIS. The largest difference of the correction factors in the different Monte Carlo models at the value $\langle\psi(r = 0.6)\rangle$ is taken as the systematic error on the detector correction. The largest deviations in photoproduction between the Pythia and Cascade models are found in the lowest $W_{\gamma p}$ region and are of the order of 2%. In DIS the largest deviation between RapGap and Cascade are of the order of 1% in the medium E_{jet} bin.

For the final estimation of the systematic error the largest deviations originating from the studied uncertainty on $\langle\psi(r = 0.6)\rangle$ are a added in quadrature. It is hereby assumed that the uncertainties are independent. Table 6.2 summarises the systematic uncertainties of the analysis.

Error Source	Variation	Photoproduction δ [%]	DIS δ [%]
Hadronic Energy Scale	±4%, ±2%, ±3%	0.15	0.20
Jet Axis Smearing	$\theta \pm 2.5°$, $\phi \pm 2.5°$	0.58	0.71
Signal Extraction	signal fit ±5%	0.80	0.10
Detector Correction	Pythia, resp. RapGap vs. Cascade	2.16	0.85
Total		2.38	1.13

Table 6.2: Summary of the systematic uncertainties.

Chapter 7

Results

In the following chapter the mean integrated jet shapes corrected for detector effects are presented. In the presented distributions all systematic uncertainties determined in section 6.6 are considered. First the jet shapes as a function of the cone radius are shown in different regions of the jet energy, the energy in the photon-proton frame of reference and x_γ^{obs}. This is performed separately for photoproduction and DIS. The data distributions are compared to Pythia, respectively RapGap, as well as Cascade Monte Carlo expectations.

Next the jet shape is studied with respect to several selected variables at a fixed cone radius of $r = 0.6$ (cf. appendix A). This again is done separately for photoproduction and DIS and accompanied by Monte Carlo comparison.

Finally the jet shape as function of x_γ^{obs} is presented in increasing Q^2 regions.

7.1 Mean Integrated Jet Shape as Function of the Cone Radius

In chapter 6 the extraction of the mean integrated jet shape is discussed in detail. The visible region is defined by the phase space cuts in table 6.1. The analysed jet is always the highest-p_t jet not associated with a D^* meson. All distributions are presented at hadron level. Numerical values of the data and Monte Carlo simulation are listed in appendix B.

7.1.1 Photoprodution

For the photoproduction sample the mean integrated jet shape is shown in figure 7.1 in three different regions of the jet energy E_{jet}. Figure 7.3 shows the jet shape in two regions of $W_{\gamma p}$ and figure 7.5 in two regions of x_γ^{obs}. Also shown is the Pythia charm Monte Carlo prediction as well as the contributions from direct and resolved photon processes. In figures 7.2, 7.4 and 7.6 these same distributions are normalised to the Pythia charm Monte Carlo prediction.

The measurements at the smallest cone radii is characerised by low statistics. This is particularly visible at the lower values of E_{jet}, though the direct prediction is still within errors. Apart from this and also due to large statistical errors the data agrees well with the Monte Carlo expectation.

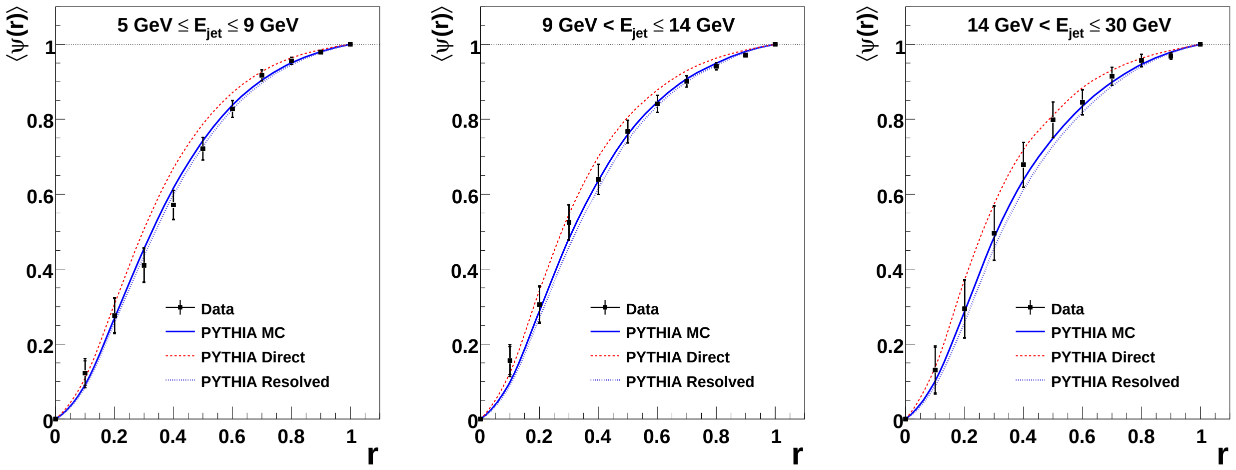

Figure 7.1: Mean integrated jet shape $\langle\psi(r)\rangle$ in photoproduction as function of the cone radius r for three different regions of E_{jet}. The data is corrected for detector effects. The Pythia charm Monte Carlo prediction is shown together with separate direct and resolved expectations, all at hadron level. The statistical errors of the Monte Carlo simulation are negligible. The inner error bars of the data points represent the statistical errors while the outer bar represents the statistical and systematic uncertainties added in quadrature.

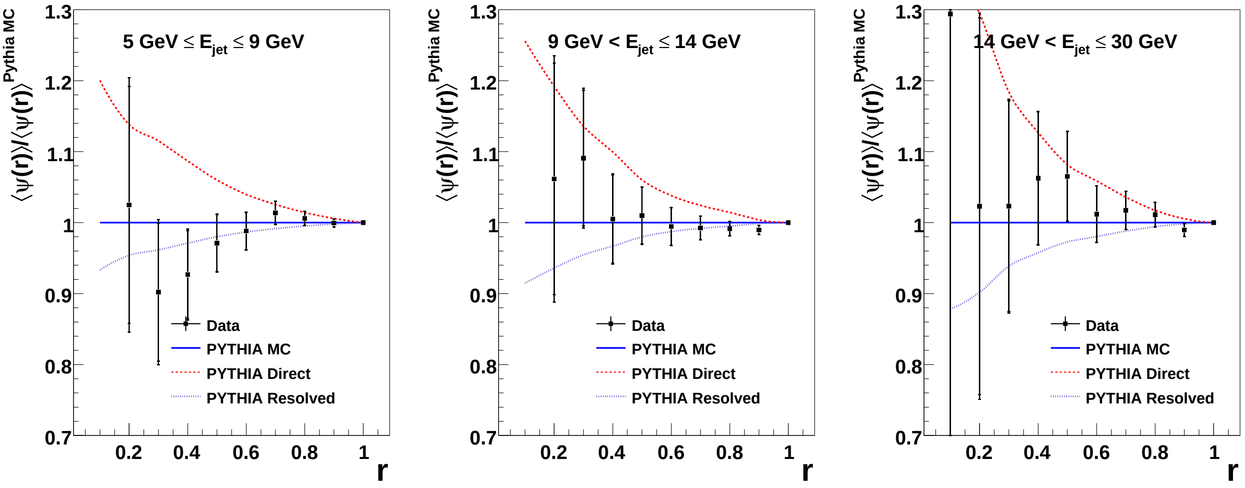

Figure 7.2: Ratio of the data points from figure 7.1 with respect to the total Pythia charm Monte Carlo prediction. Direct and resolved expectations are shown separately and also in relation to the total Pythia prediction.

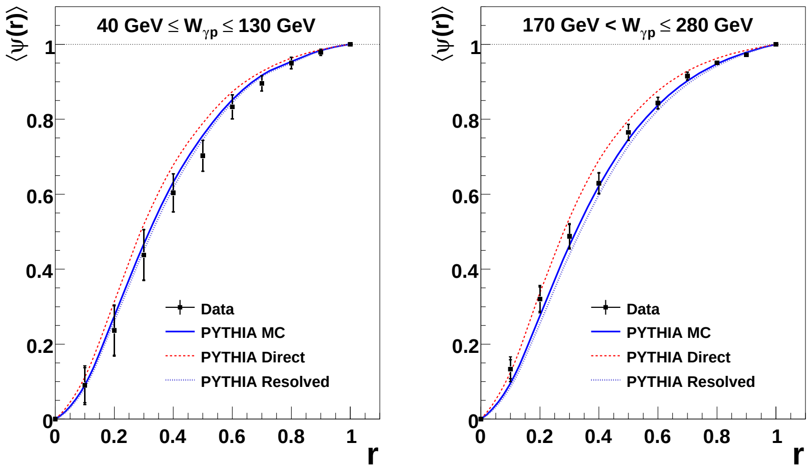

Figure 7.3: Mean integrated jet shape $\langle\psi(r)\rangle$ in photoproduction as function of the cone radius r for two different regions of $W_{\gamma p}$. The data is corrected for detector effects. ThePythia charm Monte Carlo prediction is shown together with separate direct and resolved expectations, all at hadron level. The statistical errors of the Monte Carlo simulation are negligible. The inner error bars of the data points represent the statistical errors while the outer bar represents the statistical and systematic uncertainties added in quadrature.

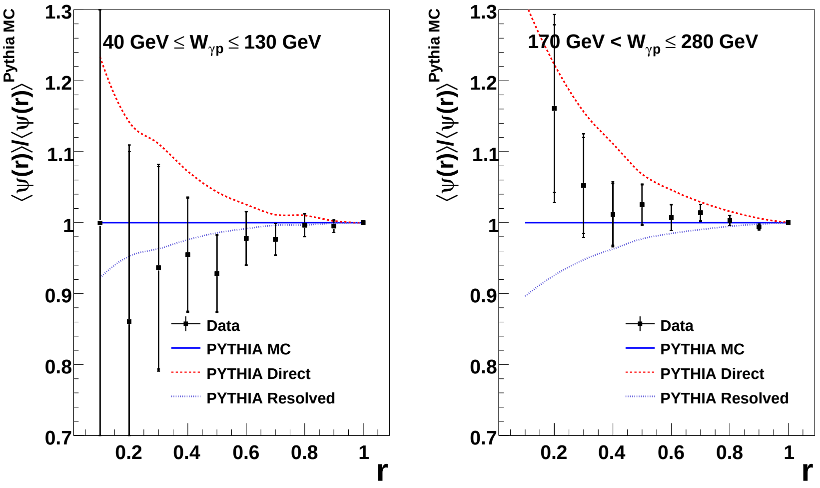

Figure 7.4: Ratio of the data points from figure 7.3 with respect to the total Pythia charm Monte Carlo prediction. Direct and resolved expectations are shown separately and also in relation to the total Pythia prediction.

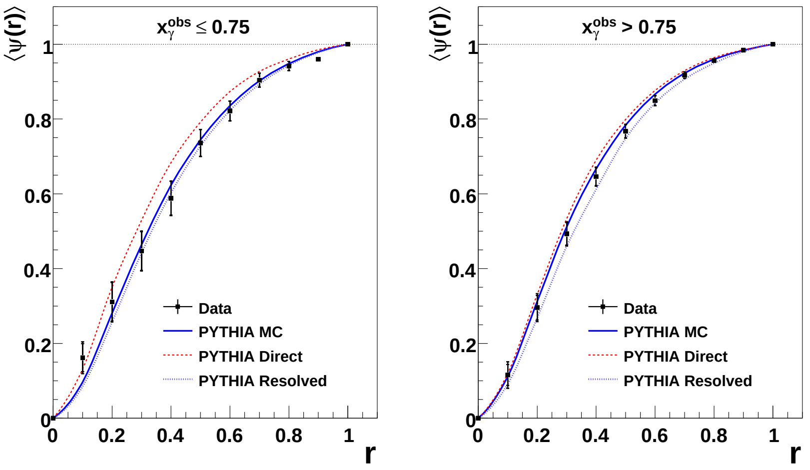

Figure 7.5: Mean integrated jet shape $\langle\psi(r)\rangle$ in photoproduction as function of the cone radius r for two different regions of x_γ^{obs}. The data is corrected for detector effects. The Pythia charm Monte Carlo prediction is shown together with separate direct and resolved expectations, all at hadron level. The statistical errors of the Monte Carlo simulation are negligible. The inner error bars of the data points represent the statistical errors while the outer bar represents the statistical and systematic uncertainties added in quadrature.

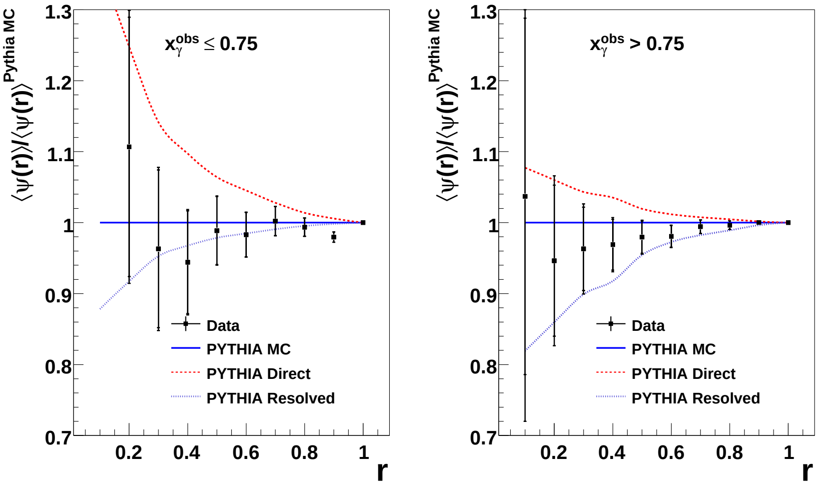

Figure 7.6: Ratio of the data points from figure 7.5 with respect to the total Pythia charm Monte Carlo prediction. Direct and resolved expectations are shown separately and also in relation to the total Pythia prediction.

Comparison with Other Monte Carlo Simulations

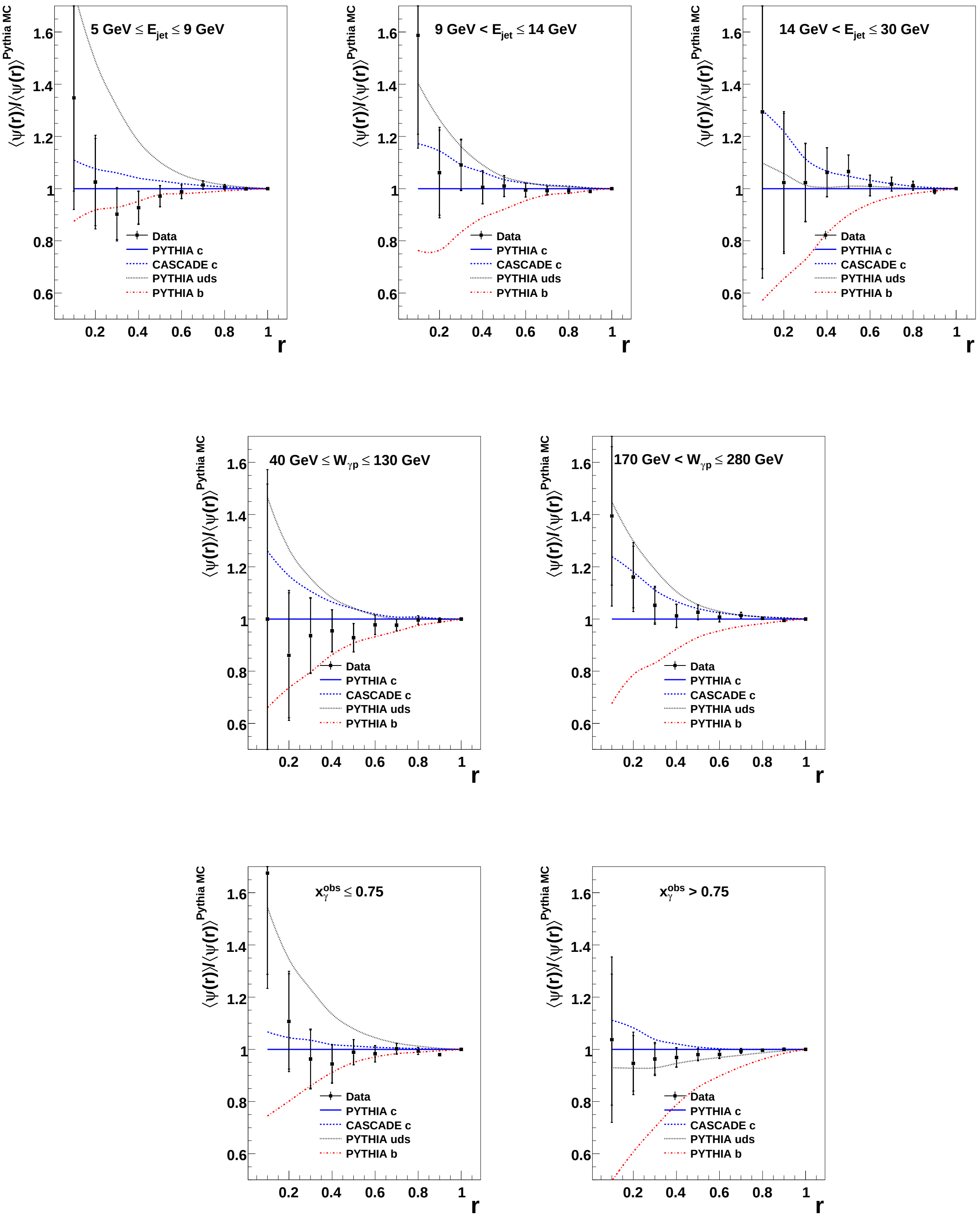

Figure 7.7: Ratio of the photoproduction data points from figures 7.1, 7.3 and 7.5 with respect to the total Pythia charm Monte Carlo prediction. Also shown is the Cascade charm Monte Carlo prediction as well as Pythia b and uds expectations.

It is apparent, however, that in the regions of low E_{jet} and $W_{\gamma p}$ the data is also well described by the resolved prediction alone. High E_{jet} and $W_{\gamma p}$ jets tend to contain less gluons as suggested by the data which in these regions behaves slightly more direct-like.

For the broader picture and to verify the degree to which charm jets can be distinguished from light quark jets as well as b jets figure 7.7 shows the normalised data and Pythia charm Monte Carlo in comparison with the b and uds jet expectations.[1] Also shown is the Cascade charm Monte Carlo simulation.

The pure b and light quark jets differ significantly in shape from the charm (and gluon) jets. The uds jet expectations are more narrow as these by construction have no contribution from gluon jets. In the region of high x_γ^{obs} though, the light quark jet prediction is slightly broader than the analysis jets (charm and gluon jets) due to the latter themselves containing less gluon jets and uds jets being broader than pure charm jets. Jets initiated by a beauty quark on the other hand exhibit a broader jet shape than the analysed jets, even in the low x_γ^{obs} regime which is strongly enriched in resolved photon events, i.e. a large fraction of these jets is initiated by a gluon.

Within the Cascade Monte Carlo model no explicit resolved component is generated. Instead a hadronic photon component is already included in the k_t factorisation. The Cascade charm simulation describes the data to a similar degree as the Pythia charm simulation, though in general the description is slightly worse. An exception is the high $W_{\gamma p}$ bin where the Cascade prediction is better.

The numerical values of the data and Pythia charm Monte Carlo prediction from the figures 7.1, 7.3 and 7.5 can be found in tables B.1, B.2 and B.3.

7.1.2 DIS

The mean integrated jet shapes for the DIS sample are shown in figures 7.8, 7.10 and 7.12 in three regions of E_{jet} and $W_{\gamma p}$ and two regions of x_γ^{obs}, respectively. These are compared to the RapGap charm Monte Carlo as well as the direct and resolved photon expectations. Figures 7.9, 7.11 and 7.13 show the data and simulation normalised to the RapGap charm prediction. The overall prediction is in good agreement with the data, though in the highest E_{jet} and $W_{\gamma p}$ regions deviations can be observed, suggesting that the contribution of gluon jets is underestimated.

The data normalised to the RapGap charm prediction is compared to the light quark and b jet expectation in figure 7.14. In DIS the fraction of resolved photon events and thus gluon initiated jets is substantially smaller than in photoproduction resulting in the analysis jets to be mainly composed of jets initiated by a charm quark. These again are more narrow. Light quark and b jets appear significantly broader.

Also shown in figure 7.14 is the Cascade charm Monte Carlo simulation, which achieves an almost equally good description of the data as the RapGap charm Monte Carlo.

The numerical values of the data and Pythia charm Monte Carlo prediction from the figures 7.8, 7.10 and 7.12 are listed in tables B.4, B.5 and B.6.

---

[1] A b and a uds one-jet Monte Carlo sample is studied where the jets are initiated by the particular parton, i.e. no resolved photon component.

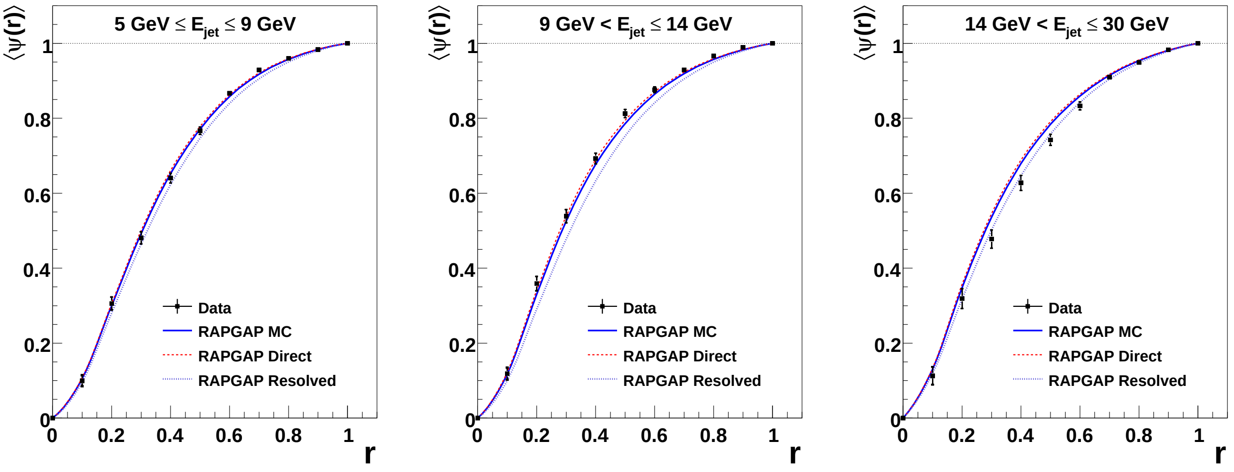

Figure 7.8: Mean integrated jet shape $\langle\psi(r)\rangle$ in DIS as function of the cone radius r for three different regions of E_{jet}. The data is corrected for detector effects. RapGap charm Monte Carlo prediction is shown together with separate direct and resolved expectations, all at hadron level. The statistical errors of the Monte Carlo simulation are negligible. The inner error bars of the data points represent the statistical errors while the outer bar represents the statistical and systematic uncertainties added in quadrature.

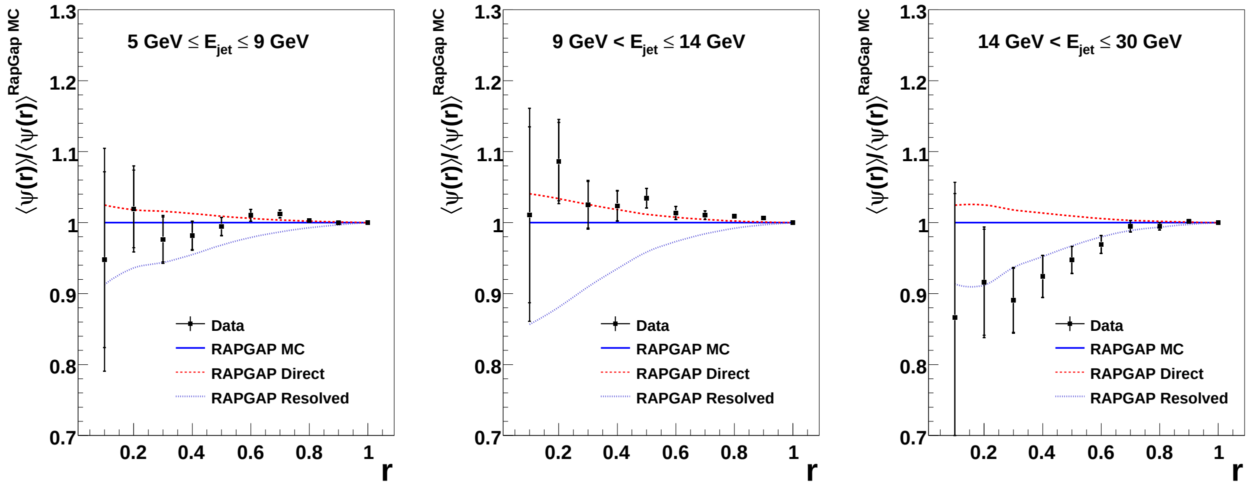

Figure 7.9: Ratio of the data points from figure 7.8 with respect to the total RapGap charm Monte Carlo prediction. Direct and resolved expectations are shown separately and also in relation to the total RapGap prediction.

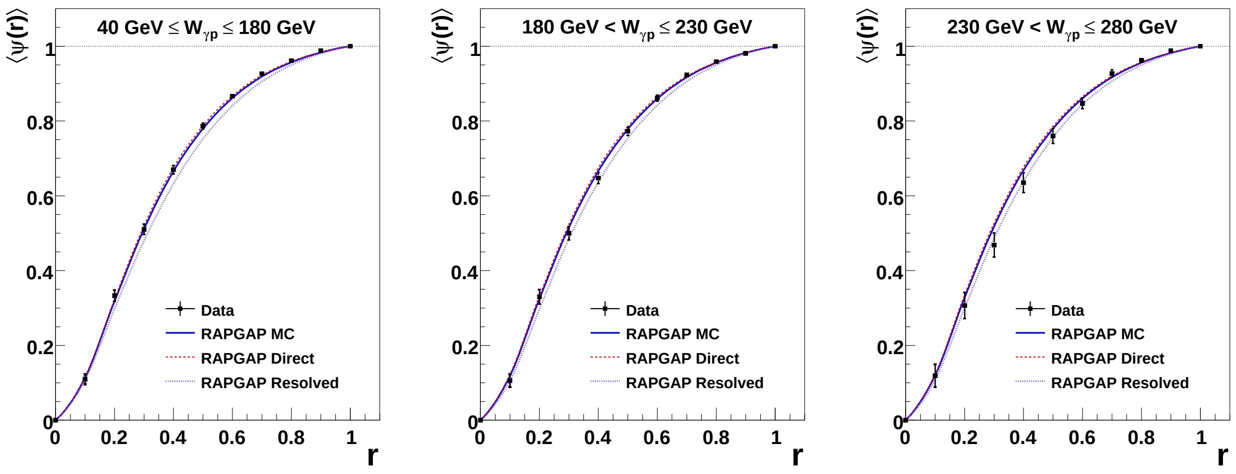

Figure 7.10: Mean integrated jet shape $\langle\psi(r)\rangle$ in DIS as function of the cone radius r for three different regions of $W_{\gamma p}$. The data is corrected for detector effects. RapGap charm Monte Carlo prediction is shown together with separate direct and resolved expectations, all at hadron level. The statistical errors of the Monte Carlo simulation are negligible. The inner error bars of the data points represent the statistical errors while the outer bar represents the statistical and systematic uncertainties added in quadrature.

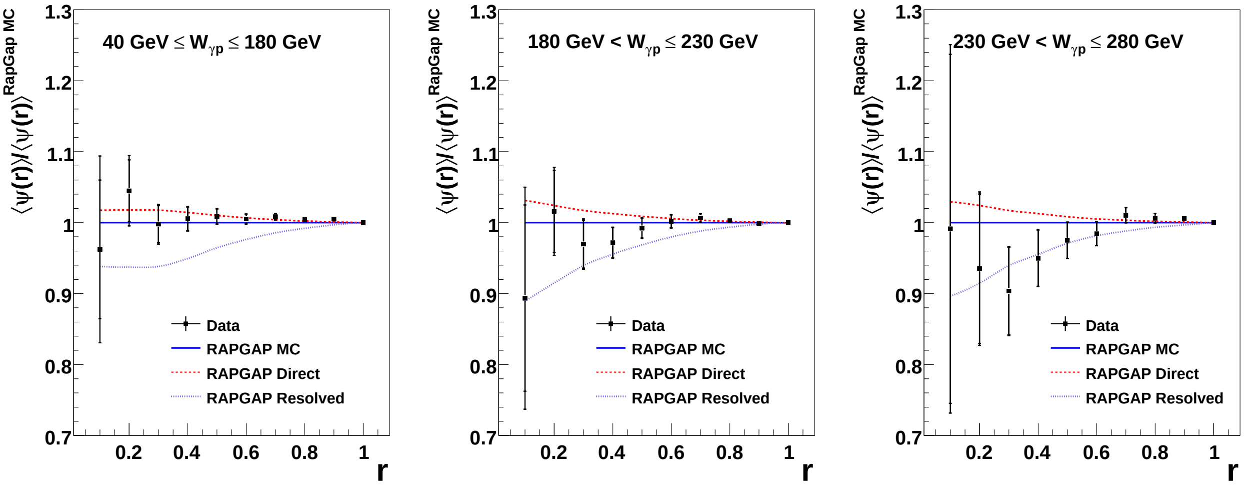

Figure 7.11: Ratio of the data points from figure 7.10 with respect to the total RapGap charm Monte Carlo prediction. Direct and resolved expectations are shown separately and also in relation to the total RapGap prediction.

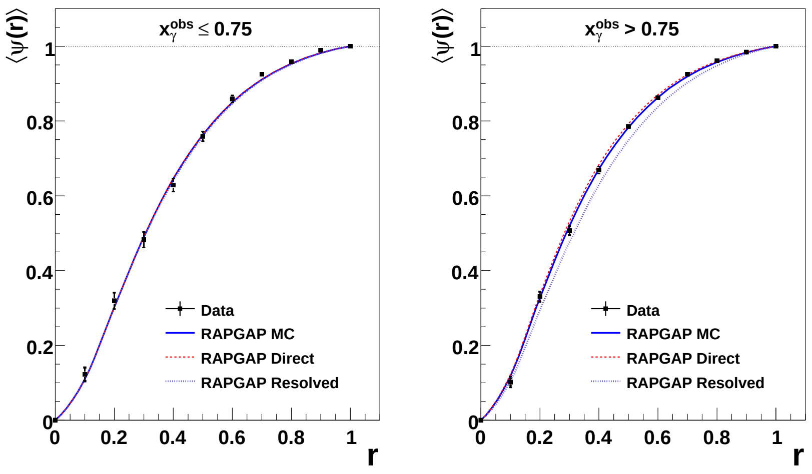

Figure 7.12: Mean integrated jet shape $\langle\psi(r)\rangle$ in DIS as function of the cone radius r for two different regions of x_γ^{obs}. The data is corrected for detector effects. RapGap charm Monte Carlo prediction is shown together with separate direct and resolved expectations, all at hadron level. The statistical errors of the Monte Carlo simulation are negligible. The inner error bars of the data points represent the statistical errors while the outer bar represents the statistical and systematic uncertainties added in quadrature.

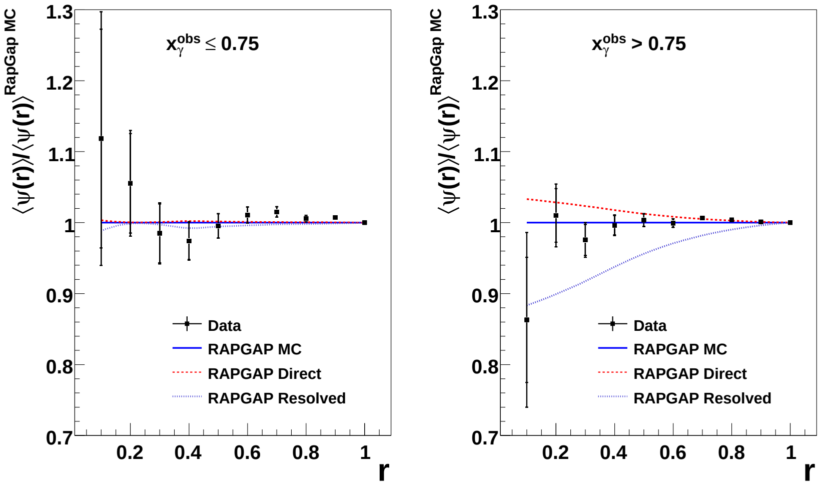

Figure 7.13: Ratio of the data points from figure 7.12 with respect to the total RapGap charm Monte Carlo prediction. Direct and resolved expectations are shown separately and also in relation to the total RapGap prediction.

Comparison with Other Monte Carlo Simulations

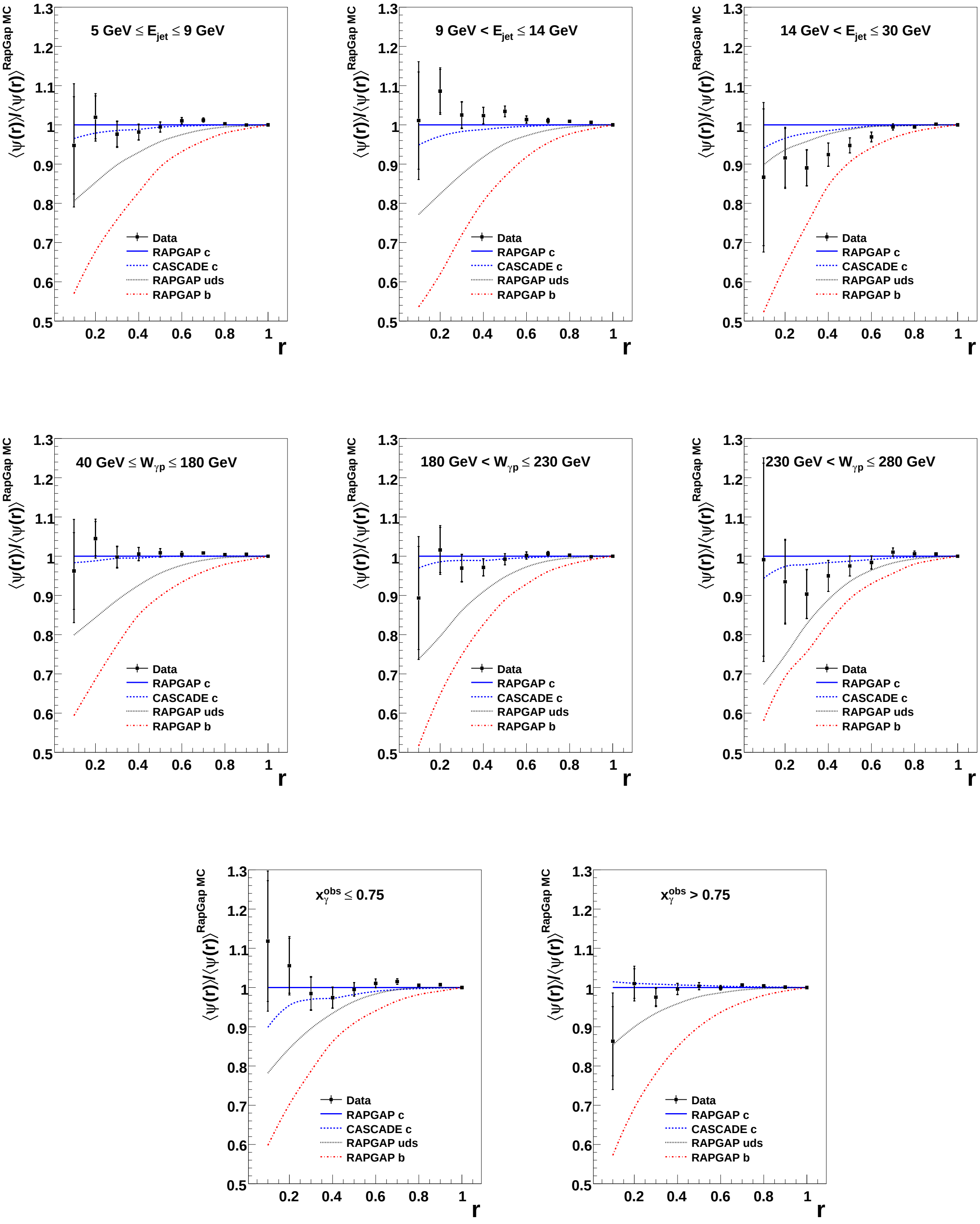

Figure 7.14: Ratio of the DIS data points from figures 7.8, 7.10 and 7.12 with respect to the total RapGap charm Monte Carlo prediction. Also shown is the Cascade charm Monte Carlo prediction as well as RapGap b and uds expectations.

7.2 Mean Integrated Jet Shape at Fixed Cone Radius

At the fixed cone radius of $r = 0.6$ the mean integrated jet shape is plotted against different kinematic and jet variables. This is done separately for photoproduction (section 7.2.1) and DIS (section 7.2.2). Of special interest is the variable x_γ^{obs} as the kinematic region of low x_γ^{obs} ($x_\gamma^{obs} < 0.75$) is enriched in resolved photon events, while direct events exhibit a distinguished peak at $x_\gamma^{obs} = 1$. The mean integrated jet shape $\langle\psi(r = 0.6)\rangle$ as function of x_γ^{obs} is thus studied in three different regions of Q^2: In photoproduction ($Q^2 < 0.01$ GeV^2) as well as for low (3.4 GeV$^2 \leq Q^2 \leq$ 9 GeV^2) and high (9 GeV$^2 < Q^2 \leq 100$ GeV^2) Q^2 in DIS. This is performed in section 7.2.3.

7.2.1 Photoproduction

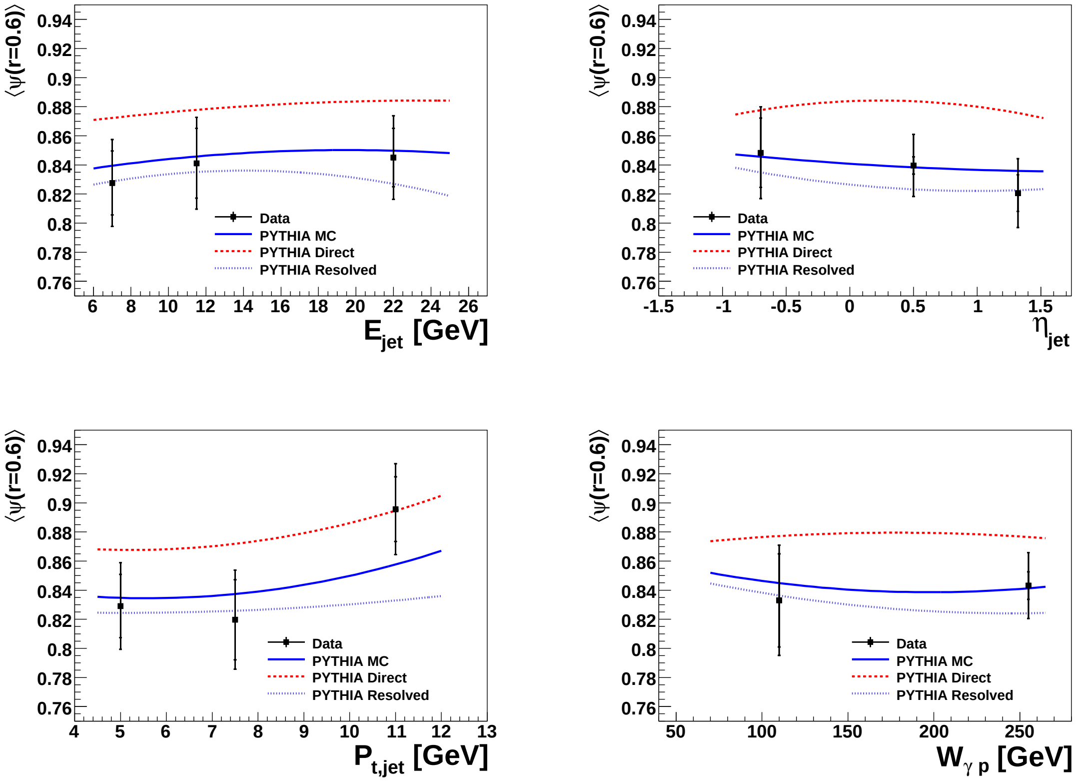

Figure 7.15: Distributions of the mean integrated jet shape in photoproduction at fixed value $r = 0.6$ at hadron level as function of the variables E_{jet}, η_{jet}, $P_{t,jet}$ and $W_{\gamma p}$. The Pythia charm Monte Carlo prediction is shown together with separate direct and resolved expectations. The statistical errors of the Monte Carlo simulation are negligible. The inner error bars of the data points represent the statistical errors while the outer bar represents the statistical and systematic uncertainties added in quadrature.

The mean integrated jet shape as a function of the energy, pseudorapidity and transverse momentum of the jet as well as the energy in the photon-proton frame of reference for the photoproduction sample is shown in figure 7.15.

The description of the data by the Pythia Monte Carlo simulation is good. Due to the large fraction of resolved photon events in the photoproduction sample a description of the data within errors is also provided by the resolved prediction alone. An exception to this behaviour is apparent in the highest bin of the transverse momentum of the jet. Here the estimate of the mean integrated jet shape by the total Pythia charm Monte Carlo falls far below the measured value, but is still in full agreement with the direct expectation, suggesting an overestimation of the fraction of gluon jets at high jet transverse momenta.

The distribution of the mean integrated jet shape as function of x_γ^{obs} is shown in context with the DIS measurement in section 7.2.3. The numerical values from the above distributions can be found in appendix B.

7.2.2 DIS

In DIS the mean integrated jet shape at fixed cone radius is measured as function of E_{jet}, η_{jet}, $P_{t,jet}$, $W_{\gamma p}$ and x_γ^{obs} as it is performed for the photoproduction sample. Additionally the dependency on the negative four momentum transfer squared Q^2 is studied. These distributions are shown in figures 7.16 and 7.17 and compared with the RapGap charm Monte Carlo prediction as well as the direct and resolved expectations. Overall the data is well described by the Monte Carlo simulation which in DIS is dominated by direct processes. In the region of the highest transverse momenta of the jet, the highest jet energies and the highest energies in the photon-proton frame of reference though, the jets are slightly broader than expected, hinting at an underestimation of the fraction of gluon jets.

The numerical values of the mean integrated jet shapes from these distributions are listed in appendix B.

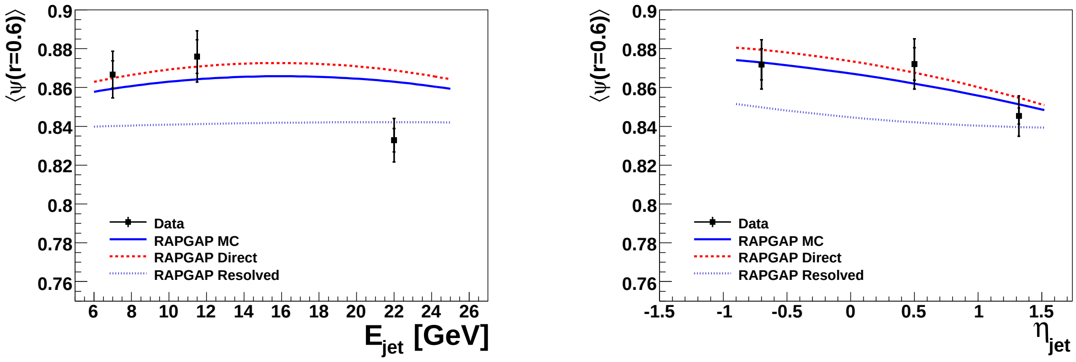

Figure 7.16: Distributions of the mean integrated jet shape in DIS at fixed value $r = 0.6$ at hadron level as function of the variables E_{jet} and η_{jet}. The RapGap charm Monte Carlo prediction is shown together with separate direct and resolved expectations. The statistical errors of the Monte Carlo simulation are negligible. The inner error bars of the data points represent the statistical errors while the outer bar represents the statistical and systematic uncertainties added in quadrature.

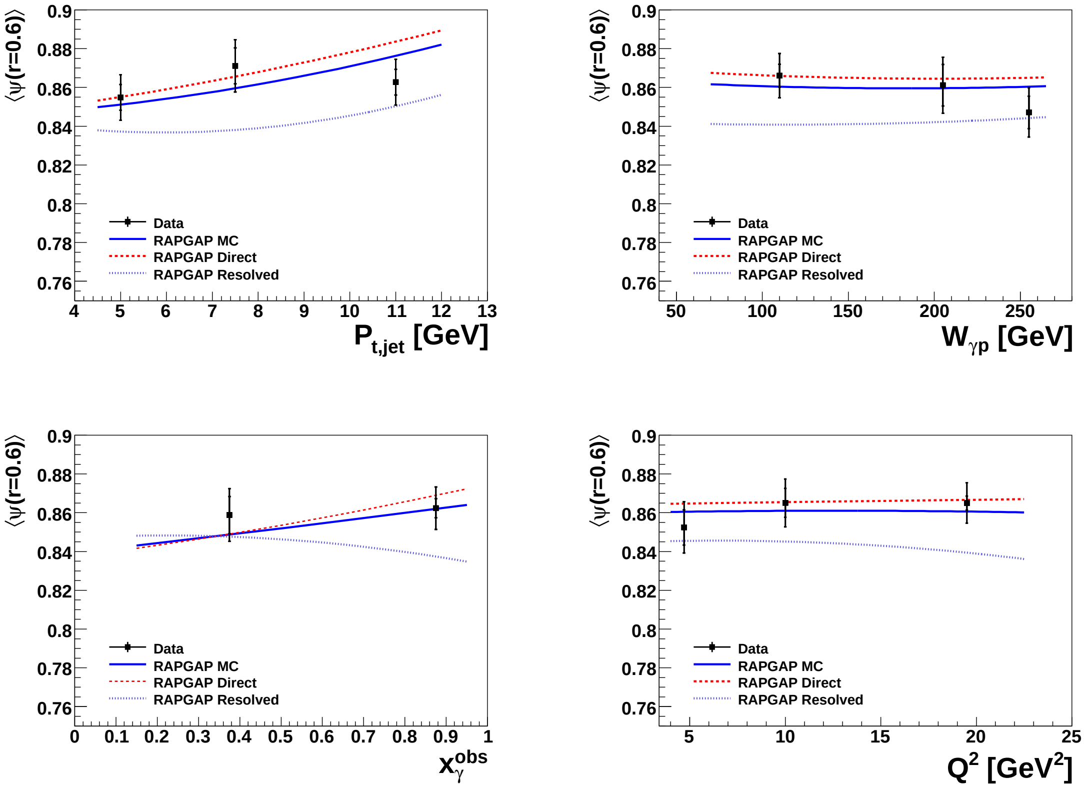

Figure 7.17: Distributions of the mean integrated jet shape in DIS at fixed value $r = 0.6$ at hadron level as function of the variables $P_{t,jet}$, $W_{\gamma p}$, x_γ^{obs} and Q^2. The RapGap charm Monte Carlo prediction is shown together with separate direct and resolved expectations. The statistical errors of the Monte Carlo simulation are negligible. The inner error bars of the data points represent the statistical errors while the outer bar represents the statistical and systematic uncertainties added in quadrature.

7.2.3 Q^2 Dependency

Direct and resolved photon processes are distinguished in the variable x_γ^{obs}. While in resolved processes only a fraction of the photon momentum participates in the hard interaction, this fraction x_γ^{obs} exhibits a clear maximum at unity for direct processes. The mean integrated jet shape as a means to differentiate between the generally broader gluon initiated jets and the spatially more confined jets initiated by the charm quark is thus studied in two regions of x_γ^{obs}.

The fraction of resolved photon events changes with increasing Q^2, as does the jet shape itself. The mean integrated jet shape at the fixed radius $r = 0.6$ as function of x_γ^{obs} is compared for three different Q^2 regions in figure 7.18.

The Pythia Monte Carlo prediction is in good agreement with the photoproduction data. The

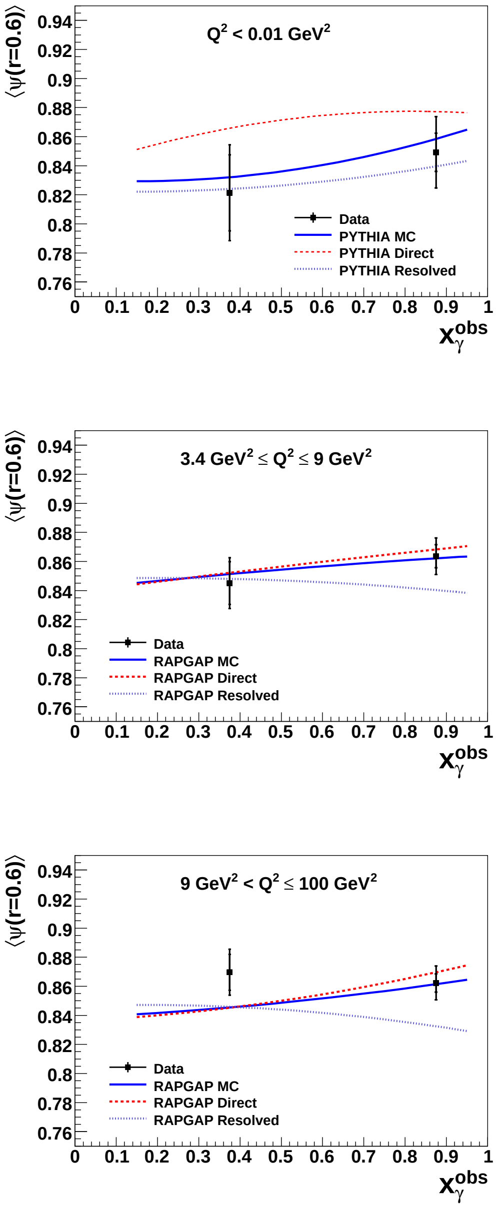

Figure 7.18: Distributions of the mean integrated jet shape in photoproduction and in two different Q^2 regions in DIS at fixed value $r = 0.6$ at hadron level as function of x_γ^{obs}. Pythia, respectively RapGap charm Monte Carlo prediction is shown together with separate direct and resolved expectations. The statistical errors of the Monte Carlo simulation are negligible. The inner error bars of the data points represent the statistical errors while the outer bar represents the statistical and systematic uncertainties added in quadrature.

difference between direct and resolved photon events though, is of the same magnitude as the error on the data.

Due to a much larger data sample and a better signal-to-background ratio the error on the DIS data is significantly smaller. Apparently though, the RapGap expectation for direct events is very similar to the resolved photon prediction at low x_γ^{obs}. Apart from the predictiction at high Q^2 and low x_γ^{obs} where the data suggests broader jets than the Monte Carlo predicts, the decription of the data by the simulation is very good. The mean integrated jet shape expectation for direct and resolved photon events in DIS at low x_γ^{obs}, however, is basically identical.

Chapter 8

Summary and Conclusion

In this analysis the mechanisms of charm production are studied in photoproduction and DIS. Production of charm in ep collisions at HERA is dominated by boson-gluon fusion (BGF). Beyond the direct photon process $\gamma g \rightarrow c\bar{c}$, resolved processes, where quarks and gluons from the photon participate in the hard interaction contribute significantly. This contribution decreases with increasing photon virtuality Q^2. While in the 'normal' resolved process, a charm quark pair is produced in the hard interaction via $gg \rightarrow c\bar{c}$, the charm excitation processes $cg \rightarrow cg$, $cq \rightarrow cq$ which represent the largest fraction of the resolved processes produce a charm quark and another parton. By studying the shapes of high p_t jets that result from the hadronisation of the outgoing BGF partons, the fraction of direct, respectively resolved processes is investigated. This is possible because the shape of the jet is strongly dependent on its initiating parton. Thus the average jet shape makes it possible to explore the relative composition of the production processes.

In this analysis photoproduction data from the years 1999 and 2000 and DIS data from the years 2004 through 2007 was used. In photoproduction the event kinematics were reconstructed by measuring the scattered electron with electron taggers 33 m, respectively 44 m from the interaction point in electron flight direction. In DIS the scattered electron was measured in the backward calorimeter. Dijet events with transverse jet momenta above 5 GeV (4 GeV for the second jet) were selected where one jet was tagged as charm jet by the reconstruction of a D^* meson. The total integrated luminosity of the photoproduction data amounts to 51.1 pb^{-1} for ET33 and 31.8 pb^{-1} for ET44. The integrated luminosity of the DIS data is 347.6 pb^{-1}.

The mean integrated jet shape $\langle\psi(r)\rangle$ was studied in different regions of the kinematic variables E_{jet}, $W_{\gamma p}$ and x_γ^{obs}. Further, the mean integrated jet shape at a fixed cone radius $\langle\psi(r = 0.6)\rangle$ was studied as a function of the jet energy E_{jet}, pseudorapidity η_{jet} and transverse momentum $p_{t,jet}$, $W_{\gamma p}$ as well as x_γ^{obs} and in DIS also as a function of Q^2. All distributions were background subtracted and corrected for detector effects.

The dependence of $\langle\psi(r)\rangle$ on the mentioned variables was compared to the Pythia Monte Carlo prediction for photoproduction and RapGap for DIS. The direct and resolved photon contributions to the total prediction were studied separately. Additionally, a comparison with the Cascade Monte Carlo simulation was performed. In this simulation no explicit differentiation between direct and resolved photon processes is made. As a cross check also light quark and beauty only Monte Carlo simulations were studied.

The data is found to be well described by the Monte Carlo prediction. In photoproduction the events are dominated by resolved photon processes. The fraction of these events decreases strongly in DIS which is dominated by direct events. In the photoproduction region of high jet transverse momenta the data suggests more narrow jets than the total Pythia Monte Carlo predicts. The data is nevertheless in full agreement with the direct prediction, hinting at an underestimation of the fraction of direct events in photoproduction at high jet transverse momenta. A further clarification requires considerably more statistics.

In several regions of phase space the resolution of the jet shape measurement is better than the difference between the direct and resolved photon Monte Carlo simulation. This allows to technically distinguish between such types of event samples. In DIS though, in the region of low x_γ^{obs} the mean integrated jet shape for direct events is basically identical to the resolved expectation, rendering an experimental distinction in this region futile. The similar shape of jets originating from direct processes and those from resolved can be explained by a hard gluon radiation prior to the BGF in low x_γ^{obs} direct events. This can result in the two highest-p_t jets being both charm initiated or initiated by a charm quark and a gluon, thus having the same signature as jets originating from resolved processes.

Appendix A

Determination of Optimum Cone Radius

In order to determine the cone radius best suited for comparison of different regions in several kinematic variables, some sort of discriminating power is to be quantified. As the goal is to distinguish direct and resolved photon processes, the difference in the mean integrated jet shape between direct and resolved events is studied with respect to the cone radius. This is performed for each analysis bin, i.e. in each kinematic region where the jet shape is computed. This is done in DIS only, as the splitting between direct and resolved events is less distinct here. To this end the Rapgap Monte Carlo simulation is used. The cone radius is varied in steps of 0.1 from 0.3 to 0.8 (the maximum of the splitting is found in this interval and approaches zero towards 0.0 and 1.0).

To allow for a graphical representation each analys bin is attached to a number. The analysis bin numbers and their associated kinematical regions are summarised in tabel A.1.

On the other hand the total error on the data points limits the possible resolution of the mean integrated jet shape. This error decreases as the radius approaches 0, respectively 1. A maximum discriminating power is expected for large direct/resolved splitting and small errors on the data points. Thus the ratio between the splitting and the error is computed.

In figure A.1 and A.2 the splitting between direct and resolved mean integrated jet shapes as expected by the Rapgap Monte Carlo is shown for cone radii between 0.3 and 0.8. Also shown is the error on the data points and the ratio between the two histograms. The mean of this ratio is indicated by a dashed line.

For the computed radii the ratio between direct/resolved splitting and the error on the data, which provides a gauge for the discriminating power, exhibits a maximum at the cone radius $r = 0.6$. When comparing the mean integrated jet shape in adjacent regions of phase space, say in different regions of x_γ^{obs}, this is thus done at this cone radius.

Analysis Bin Number	**Kinematic Region**
1	$x_\gamma^{obs} < 0.75$
2	$x_\gamma^{obs} \geq 0.75$
3	$x_\gamma^{obs} < 0.75$, $Q^2 \leq 9$ GeV^2
4	$x_\gamma^{obs} \geq 0.75$, $Q^2 \leq 9$ GeV^2
5	$x_\gamma^{obs} < 0.75$, $Q^2 > 9$ GeV^2
6	$x_\gamma^{obs} \geq 0.75$, $Q^2 > 9$ GeV^2
7	5.0 GeV $\leq E_{jet} <$ 9.0 GeV
8	9.0 GeV $\leq E_{jet} <$ 14.0 GeV
9	14.0 GeV $\leq E_{jet} <$ 30.0 GeV
10	$-1.9 \leq \eta_{jet} < 0.1$
11	$0.1 \leq \eta_{jet} < 0.9$
12	$0.9 \leq \eta_{jet} < 1.9$
13	4.0 GeV $\leq P_{t,jet} <$ 6.0 GeV
14	6.0 GeV $\leq P_{t,jet} <$ 9.0 GeV
15	9.0 GeV $\leq P_{t,jet} <$ 13.0 GeV
16	40 GeV $\leq W_{\gamma p} <$ 180 GeV
17	180 GeV $\leq W_{\gamma p} <$ 230 GeV
18	230 GeV $\leq W_{\gamma p} <$ 280 GeV
19	3.4 GeV$^2 \leq Q^2 <$ 6.0 GeV^2
20	6.0 GeV$^2 \leq Q^2 <$ 14.0 GeV^2
21	14.0 GeV$^2 \leq Q^2 <$ 25.0 GeV^2

Table A.1: Assocation of each kinematic region in the analysis to a number. The numerical representaion of the analysis bins is used on the x-axis in the histograms in figures A.1 and A.2.

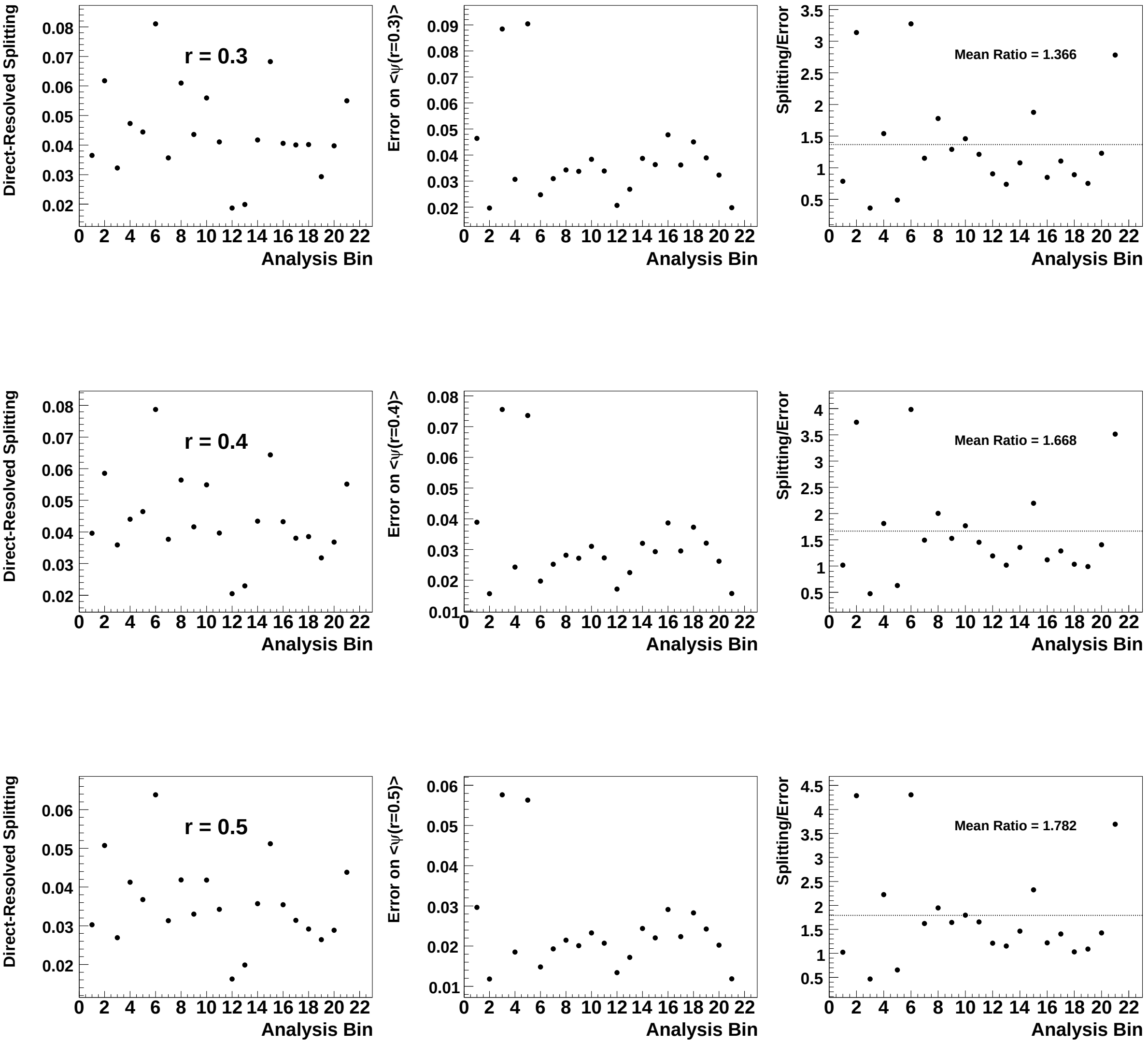

Figure A.1: Splitting between direct and resolved Monte Carlo predictions at the respective cone radius from 0.3 to 0.5 for the kinematic bins used in the analysis (left), the error on the data in the same bins (middle) and ratio of the two histograms (right). The dashed lines in the right histograms show the mean ratio, a larger ratio indicates a larger discriminating power.

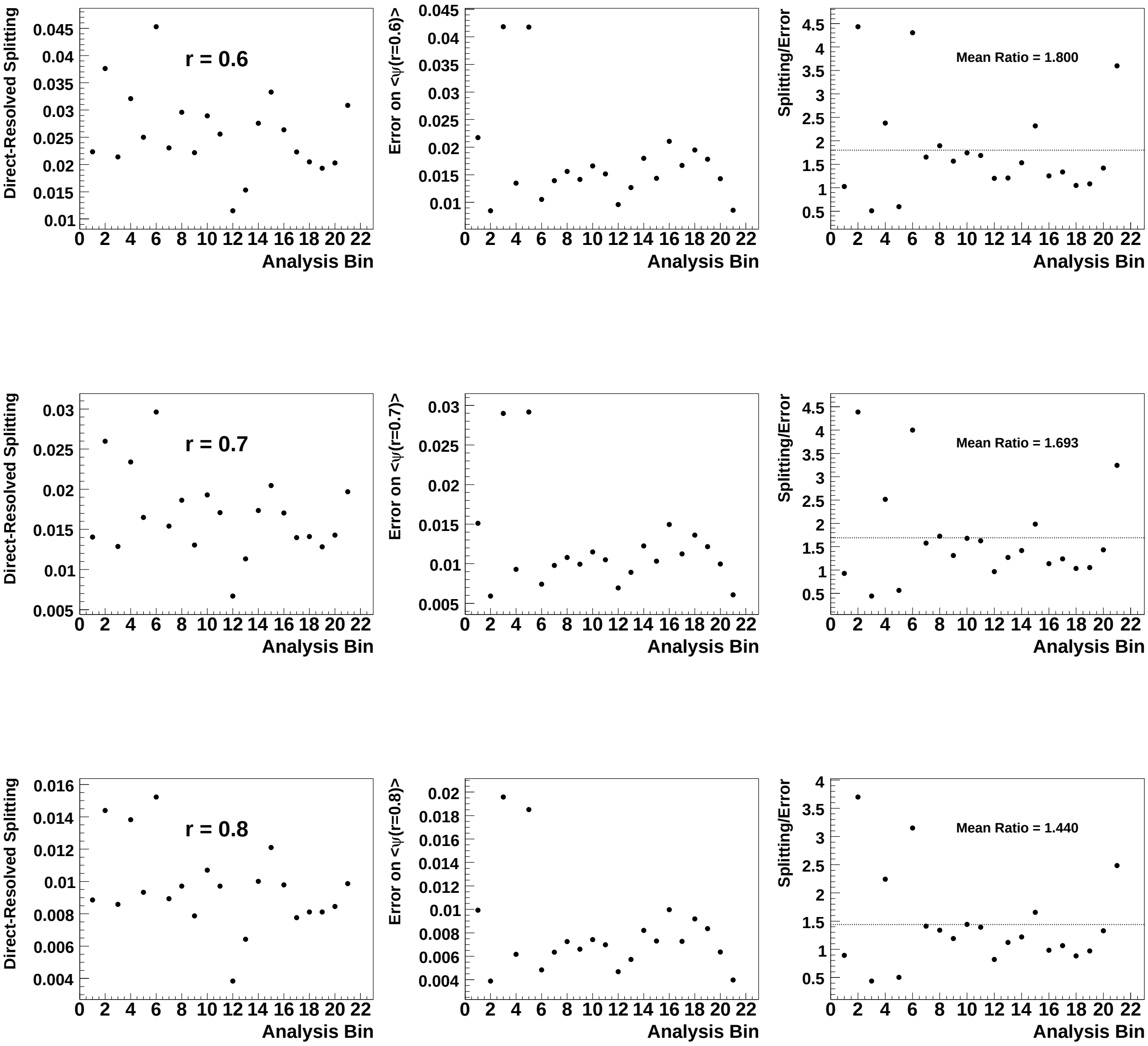

Figure A.2: Splitting between direct and resolved Monte Carlo predictions at the respective cone radius from 0.6 to 0.8 for the kinematic bins used in the analysis (left), the error on the data in the same bins (middle) and ratio of the two histograms (right). The dashed lines in the right histograms show the mean ratio, a larger ratio indicates a larger discriminating power.

Appendix B

Data Tables

40 GeV $\leq W_{\gamma p} \leq$ 130 GeV					
r	$\langle\psi(r)\rangle^{data}$	$\langle\psi(r)\rangle^{MC}$	$\langle\psi(r)\rangle^{MC}_{dir}$	$\langle\psi(r)\rangle^{MC}_{res}$	$\frac{\langle\psi(r)\rangle^{data}}{\langle\psi(r)\rangle^{MC}}$
0.1	0.0904828	0.0905177	0.111653	0.0834726	0.999614
0.2	0.236391	0.274695	0.313637	0.261715	0.860558
0.3	0.437977	0.467748	0.519758	0.450411	0.936352
0.4	0.603553	0.632093	0.67779	0.61686	0.954849
0.5	0.702422	0.756695	0.789396	0.745794	0.928277
0.6	0.832957	0.8519	0.873621	0.844659	0.977764
0.7	0.895662	0.917183	0.92746	0.913758	0.976536
0.8	0.950094	0.953543	0.963195	0.950326	0.996382
0.9	0.978644	0.983503	0.985718	0.982765	0.995059
1.0	1.00000	1.00000	1.00000	1.00000	1.00000

170 GeV $< W_{\gamma p} \leq$ 280 GeV					
r	$\langle\psi(r)\rangle^{data}$	$\langle\psi(r)\rangle^{MC}$	$\langle\psi(r)\rangle^{MC}_{dir}$	$\langle\psi(r)\rangle^{MC}_{res}$	$\frac{\langle\psi(r)\rangle^{data}}{\langle\psi(r)\rangle^{MC}}$
0.1	0.133194	0.0954836	0.125166	0.0855894	1.39494
0.2	0.320132	0.275796	0.337239	0.255315	1.16076
0.3	0.487825	0.463549	0.536	0.439398	1.05237
0.4	0.629004	0.621778	0.690953	0.59872	1.01162
0.5	0.764976	0.746041	0.797065	0.729033	1.02538
0.6	0.843141	0.837163	0.875707	0.824315	1.00714
0.7	0.91513	0.902549	0.928733	0.893821	1.01394
0.8	0.950581	0.947676	0.962649	0.942685	1.00307
0.9	0.972118	0.978087	0.984062	0.976096	0.993897
1.0	1.00000	1.00000	1.00000	1.00000	1.00000

Table B.1: The mean integrated jet shape $\langle\psi(r)\rangle$ at hadron level at different values of the cone radius r in two regions of $W_{\gamma p}$ for photoproduction data. Also listed are the total, direct and resolved Pythia Monte Carlo predictions. the last column shows the ratio of the mean integrated jet shape in data over the Monte Carlo values.

$5 \text{ GeV} \leq E_{jet} \leq 9 \text{ GeV}$

r	$\langle\psi(r)\rangle^{data}$	$\langle\psi(r)\rangle^{MC}$	$\langle\psi(r)\rangle^{MC}_{dir}$	$\langle\psi(r)\rangle^{MC}_{res}$	$\frac{\langle\psi(r)\rangle^{data}}{\langle\psi(r)\rangle^{MC}}$
0.1	0.122732	0.0910672	0.109329	0.08498	1.34771
0.2	0.276376	0.269646	0.306901	0.257227	1.02496
0.3	0.410211	0.454792	0.507249	0.437306	0.901975
0.4	0.571244	0.616407	0.669849	0.598592	0.926733
0.5	0.721212	0.742631	0.787191	0.727778	0.971158
0.6	0.827557	0.837578	0.870825	0.826496	0.988036
0.7	0.91688	0.904387	0.927472	0.896693	1.01381
0.8	0.955916	0.95017	0.963812	0.945623	1.00605
0.9	0.979449	0.980005	0.985735	0.978095	0.999433
1.0	1.00000	1.00000	1.00000	1.00000	1.00000

$9 \text{ GeV} < E_{jet} \leq 14 \text{ GeV}$

r	$\langle\psi(r)\rangle^{data}$	$\langle\psi(r)\rangle^{MC}$	$\langle\psi(r)\rangle^{MC}_{dir}$	$\langle\psi(r)\rangle^{MC}_{res}$	$\frac{\langle\psi(r)\rangle^{data}}{\langle\psi(r)\rangle^{MC}}$
0.1	0.15618	0.0983974	0.12355	0.0900131	1.58723
0.2	0.305744	0.288029	0.343289	0.269609	1.0615
0.3	0.524892	0.481188	0.546575	0.459392	1.09082
0.4	0.639537	0.636247	0.699551	0.615146	1.00517
0.5	0.767105	0.759632	0.805469	0.744353	1.00984
0.6	0.841128	0.845782	0.87786	0.83509	0.994496
0.7	0.900893	0.907783	0.929783	0.900449	0.992411
0.8	0.941284	0.949319	0.963145	0.944711	0.991535
0.9	0.970704	0.980897	0.984602	0.979662	0.989609
1.0	1.00000	1.00000	1.00000	1.00000	1.00000

$14 \text{ GeV} < E_{jet} \leq 30 \text{ GeV}$

r	$\langle\psi(r)\rangle^{data}$	$\langle\psi(r)\rangle^{MC}$	$\langle\psi(r)\rangle^{MC}_{dir}$	$\langle\psi(r)\rangle^{MC}_{res}$	$\frac{\langle\psi(r)\rangle^{data}}{\langle\psi(r)\rangle^{MC}}$
0.1	0.131114	0.101329	0.138429	0.0889626	1.29394
0.2	0.294329	0.287662	0.372449	0.2594	1.02317
0.3	0.495862	0.484587	0.573843	0.454835	1.02327
0.4	0.678449	0.638497	0.719415	0.611524	1.06257
0.5	0.798366	0.749448	0.810692	0.729033	1.06527
0.6	0.845045	0.835017	0.88415	0.81864	1.01201
0.7	0.914441	0.898891	0.930991	0.888191	1.0173
0.8	0.956844	0.946311	0.962686	0.940853	1.01113
0.9	0.968464	0.978573	0.9838	0.97683	0.98967
1.0	1.00000	1.00000	1.00000	1.00000	1.00000

Table B.2: The mean integrated jet shape $\langle\psi(r)\rangle$ at hadron level at different values of the cone radius r in three regions of E_{jet} for photoproduction data. Also listed are the total, direct and resolved Pythia Monte Carlo predictions. the last column shows the ratio of the mean integrated jet shape in data over the Monte Carlo values.

$x_\gamma^{obs} \leq 0.75$					
r	$\langle\psi(r)\rangle^{data}$	$\langle\psi(r)\rangle^{MC}$	$\langle\psi(r)\rangle^{MC}_{dir}$	$\langle\psi(r)\rangle^{MC}_{res}$	$\frac{\langle\psi(r)\rangle^{data}}{\langle\psi(r)\rangle^{MC}}$
0.1	0.161819	0.0965883	0.131842	0.0848372	1.67535
0.2	0.311081	0.281076	0.35078	0.257841	1.10675
0.3	0.447052	0.464236	0.529933	0.442337	0.962984
0.4	0.587913	0.622707	0.683226	0.602535	0.944124
0.5	0.735819	0.744172	0.791886	0.728268	0.988774
0.6	0.821366	0.835539	0.873421	0.822911	0.983038
0.7	0.903815	0.901897	0.927131	0.893486	1.00213
0.8	0.941715	0.9478	0.960755	0.943481	0.99358
0.9	0.959631	0.97963	0.985148	0.97779	0.979586
1.0	1.00000	1.00000	1.00000	1.00000	1.00000

$x_\gamma^{obs} > 0.75$					
r	$\langle\psi(r)\rangle^{data}$	$\langle\psi(r)\rangle^{MC}$	$\langle\psi(r)\rangle^{MC}_{dir}$	$\langle\psi(r)\rangle^{MC}_{res}$	$\frac{\langle\psi(r)\rangle^{data}}{\langle\psi(r)\rangle^{MC}}$
0.1	0.115552	0.111418	0.120049	0.0912774	1.0371
0.2	0.295659	0.312444	0.331233	0.268603	0.946278
0.3	0.492923	0.511849	0.534002	0.46016	0.963024
0.4	0.645882	0.666599	0.690122	0.611713	0.96892
0.5	0.767209	0.783254	0.79857	0.747518	0.979515
0.6	0.849221	0.866009	0.876195	0.84224	0.980614
0.7	0.917211	0.92252	0.929442	0.906368	0.994246
0.8	0.956273	0.959596	0.964066	0.949167	0.996537
0.9	0.984107	0.98371	0.985169	0.980308	1.0004
1.0	1.00000	1.00000	1.00000	1.00000	1.00000

Table B.3: The mean integrated jet shape $\langle\psi(r)\rangle$ at hadron level at different values of the cone radius r in two regions of x_γ^{obs} for photoproduction data. Also listed are the total, direct and resolved Pythia Monte Carlo predictions. the last column shows the ratio of the mean integrated jet shape in data over the Monte Carlo values.

5 GeV $\leq E_{jet} \leq$ 9 GeV					
r	$\langle\psi(r)\rangle^{data}$	$\langle\psi(r)\rangle^{MC}$	$\langle\psi(r)\rangle^{MC}_{dir}$	$\langle\psi(r)\rangle^{MC}_{res}$	$\frac{\langle\psi(r)\rangle^{data}}{\langle\psi(r)\rangle^{MC}}$
0.1	0.0997323	0.105229	0.107832	0.0960388	0.947768
0.2	0.305714	0.299956	0.305383	0.280799	1.0192
0.3	0.480977	0.492633	0.500501	0.464854	0.97634
0.4	0.640279	0.652278	0.660604	0.622886	0.981604
0.5	0.766709	0.770915	0.777828	0.746508	0.994545
0.6	0.86669	0.857818	0.862905	0.839858	1.01034
0.7	0.928673	0.917472	0.920874	0.905462	1.01221
0.8	0.959871	0.957197	0.95917	0.950233	1.00279
0.9	0.98335	0.983608	0.984441	0.980668	0.999737
1.0	1.00000	1.00000	1.00000	1.00000	1.00000

9 GeV $< E_{jet} \leq$ 14 GeV					
r	$\langle\psi(r)\rangle^{data}$	$\langle\psi(r)\rangle^{MC}$	$\langle\psi(r)\rangle^{MC}_{dir}$	$\langle\psi(r)\rangle^{MC}_{res}$	$\frac{\langle\psi(r)\rangle^{data}}{\langle\psi(r)\rangle^{MC}}$
0.1	0.118752	0.117462	0.12224	0.100595	1.01098
0.2	0.358803	0.330388	0.341543	0.291006	1.08601
0.3	0.53872	0.525525	0.538984	0.478009	1.02511
0.4	0.692572	0.676598	0.689048	0.632645	1.02361
0.5	0.812419	0.785423	0.794655	0.752829	1.03437
0.6	0.875961	0.864225	0.870754	0.841176	1.01358
0.7	0.928905	0.919125	0.923237	0.904608	1.01064
0.8	0.965882	0.957214	0.959358	0.949648	1.00906
0.9	0.989199	0.9827	0.983566	0.979645	1.00661
1.0	1.00000	1.00000	1.00000	1.00000	1.00000

14 GeV $< E_{jet} \leq$ 30 GeV					
r	$\langle\psi(r)\rangle^{data}$	$\langle\psi(r)\rangle^{MC}$	$\langle\psi(r)\rangle^{MC}_{dir}$	$\langle\psi(r)\rangle^{MC}_{res}$	$\frac{\langle\psi(r)\rangle^{data}}{\langle\psi(r)\rangle^{MC}}$
0.1	0.112941	0.130352	0.133548	0.119066	0.866436
0.2	0.318927	0.3482	0.356885	0.317538	0.915931
0.3	0.477738	0.536454	0.546071	0.502499	0.890548
0.4	0.627669	0.679187	0.688368	0.646776	0.924147
0.5	0.742551	0.783691	0.790981	0.757955	0.947505
0.6	0.83287	0.859326	0.864221	0.842046	0.969213
0.7	0.90995	0.914696	0.917574	0.904536	0.994811
0.8	0.949003	0.953844	0.955583	0.947706	0.994925
0.9	0.982871	0.981106	0.98178	0.978725	1.0018
1.0	1.00000	1.00000	1.00000	1.00000	1.00000

Table B.4: The mean integrated jet shape $\langle\psi(r)\rangle$ at hadron level at different values of the cone radius r in three regions of E_{jet} for DIS data. Also listed are the total, direct and resolved RapGap Monte Carlo predictions. the last column shows the ratio of the mean integrated jet shape in data over the Monte Carlo values.

40 GeV $\leq W_{\gamma p} \leq 180$ GeV					
r	$\langle\psi(r)\rangle^{data}$	$\langle\psi(r)\rangle^{MC}$	$\langle\psi(r)\rangle^{MC}_{dir}$	$\langle\psi(r)\rangle^{MC}_{res}$	$\frac{\langle\psi(r)\rangle^{data}}{\langle\psi(r)\rangle^{MC}}$
0.1	0.109709	0.114002	0.115995	0.106964	0.962344
0.2	0.332857	0.318564	0.324237	0.298538	1.04487
0.3	0.510446	0.511547	0.520507	0.479916	0.997847
0.4	0.669769	0.666102	0.675653	0.632383	1.0055
0.5	0.786342	0.779602	0.787422	0.751995	1.00865
0.6	0.866061	0.861643	0.86746	0.841108	1.00513
0.7	0.926471	0.918806	0.922565	0.905533	1.00834
0.8	0.961336	0.957411	0.959572	0.94978	1.0041
0.9	0.988268	0.983342	0.984231	0.980202	1.00501
1.0	1.00000	1.00000	1.00000	1.00000	1.00000

180 GeV $< W_{\gamma p} \leq 230$ GeV					
r	$\langle\psi(r)\rangle^{data}$	$\langle\psi(r)\rangle^{MC}$	$\langle\psi(r)\rangle^{MC}_{dir}$	$\langle\psi(r)\rangle^{MC}_{res}$	$\frac{\langle\psi(r)\rangle^{data}}{\langle\psi(r)\rangle^{MC}}$
0.1	0.106068	0.118698	0.122415	0.105576	0.893597
0.2	0.330119	0.324981	0.332817	0.297318	1.01581
0.3	0.499824	0.515439	0.524279	0.484231	0.969705
0.4	0.647521	0.666479	0.674875	0.636839	0.971555
0.5	0.772445	0.778407	0.785334	0.753952	0.992341
0.6	0.86113	0.859603	0.864524	0.84223	1.00178
0.7	0.922894	0.916832	0.919915	0.905947	1.00661
0.8	0.958512	0.956064	0.957777	0.950018	1.00256
0.9	0.980943	0.982472	0.983088	0.980301	0.998443
1.0	1.00000	1.00000	1.00000	1.00000	1.00000

230 GeV $< W_{\gamma p} \leq 280$ GeV					
r	$\langle\psi(r)\rangle^{data}$	$\langle\psi(r)\rangle^{MC}$	$\langle\psi(r)\rangle^{MC}_{dir}$	$\langle\psi(r)\rangle^{MC}_{res}$	$\frac{\langle\psi(r)\rangle^{data}}{\langle\psi(r)\rangle^{MC}}$
0.1	0.119135	0.120193	0.123721	0.107738	0.991191
0.2	0.306708	0.328024	0.335959	0.30001	0.935019
0.3	0.468398	0.518373	0.527239	0.487074	0.903593
0.4	0.634967	0.668465	0.676975	0.638422	0.949887
0.5	0.760087	0.779459	0.785896	0.756736	0.975147
0.6	0.847126	0.860645	0.865163	0.844694	0.984293
0.7	0.926763	0.917192	0.920304	0.906208	1.01043
0.8	0.962076	0.956114	0.957905	0.949789	1.00624
0.9	0.98798	0.982408	0.983314	0.979213	1.00567
1.0	1.00000	1.00000	1.00000	1.00000	1.00000

Table B.5: The mean integrated jet shape $\langle\psi(r)\rangle$ at hadron level at different values of the cone radius r in three regions of $W_{\gamma p}$ for DIS data. Also listed are the total, direct and resolved RapGap Monte Carlo predictions. the last column shows the ratio of the mean integrated jet shape in data over the Monte Carlo values.

$x_\gamma^{obs} \leq 0.75$					
r	$\langle\psi(r)\rangle^{data}$	$\langle\psi(r)\rangle^{MC}$	$\langle\psi(r)\rangle^{MC}_{dir}$	$\langle\psi(r)\rangle^{MC}_{res}$	$\frac{\langle\psi(r)\rangle^{data}}{\langle\psi(r)\rangle^{MC}}$
0.1	0.122758	0.109761	0.110128	0.108464	1.11842
0.2	0.319206	0.302441	0.302559	0.302025	1.05543
0.3	0.482772	0.490159	0.490554	0.488763	0.984929
0.4	0.628781	0.645382	0.646805	0.64036	0.974277
0.5	0.759165	0.762719	0.763921	0.758474	0.99534
0.6	0.858792	0.849666	0.850617	0.846309	1.01074
0.7	0.924686	0.910888	0.911555	0.908532	1.01515
0.8	0.958703	0.953242	0.953762	0.951408	1.00573
0.9	0.988916	0.981844	0.982202	0.980579	1.0072
1.0	1.00000	1.00000	1.00000	1.00000	1.00000

$x_\gamma^{obs} > 0.75$					
r	$\langle\psi(r)\rangle^{data}$	$\langle\psi(r)\rangle^{MC}$	$\langle\psi(r)\rangle^{MC}_{dir}$	$\langle\psi(r)\rangle^{MC}_{res}$	$\frac{\langle\psi(r)\rangle^{data}}{\langle\psi(r)\rangle^{MC}}$
0.1	0.102052	0.118243	0.122151	0.104446	0.86307
0.2	0.330395	0.327079	0.336428	0.294076	1.01014
0.3	0.506785	0.519437	0.531585	0.476551	0.975643
0.4	0.668837	0.671338	0.683176	0.629546	0.996275
0.5	0.785303	0.782553	0.792263	0.748273	1.00351
0.6	0.862354	0.862883	0.870036	0.83763	0.999387
0.7	0.924999	0.919062	0.923754	0.902497	1.00646
0.8	0.961092	0.957268	0.959914	0.947927	1.004
0.9	0.983998	0.982986	0.984057	0.979206	1.00103
1.0	1.00000	1.00000	1.00000	1.00000	1.00000

Table B.6: The mean integrated jet shape $\langle\psi(r)\rangle$ at hadron level at different values of the cone radius r in two regions of x_γ^{obs} for DIS data. Also listed are the total, direct and resolved RapGap Monte Carlo predictions. the last column shows the ratio of the mean integrated jet shape in data over the Monte Carlo values.

Bibliography

[1] M. E. Peskin and D.V. Schroeder, *An Introduction to Quantum Field Theory*, The Advanced Book Program, 1995.

[2] C. Glasman, *Precision Measurements of α_s at HERA*, AIP Conf. Proc. **792** (2005), 689.

[3] R.P. Feynman, *Photon-Hadron Interactions*, Benjamin, N.Y. (1972).

[4] J. D. Bjorken, *Asymptotic Sum Rules at Infinite Momentum*, Phys. Rev. **179** (1969), 1547.

[5] R. P. Feynman, *Very High-Energy Collisions of Hadrons* Phys Rev. Lett **23** (1969), 1415.

[6] J. P. Bjorken and E. A. Paschos, *Inelastic Electron Proton and Gamma Proton Scattering, and the Structure of the Nucleon*, Phys. Rev. **185** (1969), 1975.

[7] C. G. Jr. Callan, M. Cronau, A. Pais, E. A. Paschos, S. B. Treiman, *Light Cone Approach to Structure Function Inequalities*, FERMILAB-PUB-72-029-T.

[8] J. I. Friedman and H. W. Kendall, *Deep Inelastic Electron Scattering*, Ann. Rev. Nucl. Part. Sci. **22** (1972), 203.

[9] J. C. Collins, D. E. Soper, G. Sterman, *Factorization for Short Distance Hadron-Hadron Scattering*, **B261** (1985), 104.

[10] J. C. Collins and D. E. Soper, *The Theorems of Perturbative QCD*, Ann. Rev. Nucl. Part. Sci. **37** (1987), 383.

[11] R. Wallny, *A Measurement of the Gluon Distribution in the Proton and of the Strong Coupling Constant α_s from Inclusive Deep-Inelastic Scattering*, Dissertation, Universität Zürich (2001).

[12] V. N. Gribov and L. N. Lipatov, *Deep Inelastic ep Scattering in Perturbative Theory*, Sov. J. Nucl. Phys. **15** (1972), 438.

[13] L. N. Lipatov, *The Parton Model and Perturbation Theory*, Sov. J. Nucl. Phys. **20** (1975), 94.

[14] G. Altarelli and G. Parisi, *Asymptotic Freedom in Parton Language*, Nucl. Phys. **B126** (1977), 298.

[15] Y. L. Dokshitzer, *Calculation of the Structure Functions for the Deep Inealstic Scattering and e^+e^- Annihilation by the Perturbation Theory in Quantum Chromodynamics*, Sov. Phys. JETP **46** (1977), 143.

[16] E. A. Kuraev, L. N. Lipatov, V. S. Fadin, *The Pomeranchuk Singularity in Non-Abelian Gauge Theories*, Sov. Phys. JETP **45** (1977), 199.

[17] I. I. Balitsky, L. N. Lipatov, *The Pomeranchuk Singularity in Quantum Chromodynamics*, Sov. J. Nucl. Phys. **28** (1978), 822.

[18] M. Ciafaloni, *Coherence Effects in Initial Jets at Small* Q^2/s, Nucl. Phys. **B296** (1988), 49.

[19] S. Catani, F. Fiorani, G. Marchesini, *QCD Coherence in Initial State Radiation*, Phys. Lett. **B234** (1990), 339.

[20] S. Catani, F. Fiorani, G. Marchesini, *Small* x *behavior of Initial State Radiation in Perturbative QCD*, Nucl. Phys. **B336** (1990), 18.

[21] G. Marchesini, *QCD Coherence in the Structure Function and Associated Distributions at Small* x, Nucl. Phys. **B445** (1995), 49, hep-ph/9412327.

[22] C. Adloff et al. (H1 Collaboration), *Measurement and QCD Analysis of Neutral and Charged Current Cross Sections at HERA*, Eur. Phys. J. **C30** (2003), 1, hep-ex/0304003.

[23] S. Chekanov et al., ZEUS Collaboration, *High* Q^2 *Neutral Current Cross Sections in* e^+p *Deep inelastic Scattering at* $s^{1/2} = 318\ GeV$ Phys. Rev. **D70** (2004), 052001, hep-ex/0401003.

[24] C. Adloff et al., H1 Collaboration, *Measurement of Charged Particle Transverse Momentum Spectra in Deep Inelastic Scattering*, Nucl. Phys. **B485** (1997), 3, hep-ex/9610006.

[25] C. Adloff et al., H1 Collaboration, *Measurement of* D^{*+} *Meson Production and F2(c) in Deep Inelastic Scattering at HERA*, Phys. Lett. **B528** (2002), 199, hep-ex/0108039.

[26] L. M. Jones and H. W. Wyld, *Charmed Particle Production by Photon-Gluon Fusion*, Phys. Rev. **D17** (1978), 159.

[27] X. Artru and G. Mennessier, *String Model and Multiproduction*, Nucl. Phys. **B70** (1974), 93.

[28] M. G. Bowler, e^+e^- *Production of Heavy Quarks in the String Model*, Zeit. Phys. **C11** (1981), 169.

[29] B. Andersson, G. Gustafson, G. Ingelman, T. Sjostrand, *Parton Fragmentation and String Dynamics*, Phys. Rept. **97** (1983), 31.

[30] D. Amati and G. Veneziano, *Preconfinement as a Property of Perturbative QCD*, Phys. Lett. **B83** (1979), 87.

[31] C. Peterson, D. Schlatter, I. Schmitt, P. W. Zerwas, *Scaling Violations in Inclusive* e^+e^- *Annihilation Spectra*, Phys. Rev. **D27** (1983), 105.

[32] P. Nason and C. Oleari, *A Phenomenological Study of Heavy-Quark Fragmentation Functions in* e^+e^- *Annihilation*, Nucl. Phys. **B565** (2000), 245, arXiv:hep-ph/9903541.

[33] F. D. Aaron et al., H1 Collaboration, *Study of Charm Fragmentation into* $D^{*\pm}$ *Mesons in Deep-Inelastic Scattering at HERA* Eur. Phys. J. **C59** (2009), 589.

[34] C. Quigg, *Gauge Theories of the Strong, Weak and Electromagnetic Interactions*, Bejamin/Cummings, Menlo Park (1983).

[35] M. Martisikova, *Jet Shapes in Charm Photoproduction at HERA*, Dissertation, Universität Hamburg (2005).

[36] R. K. Ellis, W. J. Stirling, B. R. Webber, *QCD and Collider Physics*, Cambridge University Press (1996).

[37] P. Abreu et al., DELPHI Collaboration, *The Scale Dependence of the Hadron Multiplicity in Quark and Gluon Jets and a Precise Determination of C_A/C_F*, Phys. Lett. **B449** (1999), 383.

[38] G. Sterman and S. Weinberg, *Jets form Quantum Chromodynamics*, Phys. Rev. Lett. **39** (1977), 1436.

[39] G. Abbiendi et al., OPAL Collaboration, *Experimental Properties of Gluon and Quark Jets from a Point Source*, Eur. Phys. J. **C11** (1999), 217, arXiv:hep-ex/9903027.

[40] G. Alexander et al., OPAL Collaboration, *A Comparison of b and (uds) Quark Jets to Gluon Jets*, Z. Phys. **C69** (1996), 543.

[41] M. Derrick et al., ZEUS Collaboration, *Measurement of Multiplicity and Momentum Spectra in the Current Fragmentation Region of the Breit Frame at HERA*, Z. Phys. **C67** (1999), 93, arXiv:hep-ex/9501012.

[42] L. Lai et al., *Global QCD Analysis of Parton Structure of the Nucleon: CTEQ5 Parton Distributions*, arXiv:hep-ph/9903282.

[43] H. Jung, *The RAPGAP Monte Carlo for Deep Inealstic Scattering*, DESY, Notkestr. 85, 22603 Hamburg (2006).

[44] J. Pumplin et al., *New Generation of Parton Distributions with Uncertainties from Global QCD Analysis*, JHEP **07** (2002), 012, hep-ph/0201195.

[45] H. Jung, *CCFM Prediction on Forward Jets and F2: Parton Level Predictions and a New Hadron Level Monte Carlo Generator CASCADE*, (1998), hep-ph/9908497.

[46] M. Hansson and H. Jung, *Status of CCFM: Un-Integrated Gluon Densities*, (2003), hep-ph/0309009.

[47] S. Baird et al., *A Fast Track Trigger with High Resolution for H1* DESY-PRC-99/06 and H1-06/99-573 (H1 internal report) (1999).

[48] S. Baird et al., *Addendum to the proposal: A Fast Track Trigger with High Resolution for H1* H1-09/99-576 (H1 internal report) (1999).

[49] I. Abt et al. (H1 Collaboration), *The H1 Detector at HERA*, Nucl. Instrum. Met. **A386** (1997), 310.

[50] D. Pitzl et al., *The H1 Silicon Vertex Detector*, Nucl. Instrum. Meth. **A454** (2000), 334, hep-ex/0002044.

[51] M. Cuje et al., *H1 High Luminosity Upgrade 2000 CIP and Level 1 Vertex Trigger*, DESY-PRC 98/02 and H1 internal note H1-01/98-535 (1998).

[52] M. Urban, *The new CIP2k z Vertex Trigger for the H1 Experiment at HERA*, Dissertation, Zurich University (2004).

[53] A. Aktas et al. (H1 Collaboration), *Tests of QCD Factorisation in the Diffractive Production of Dijets in Deep Inelastic Scattering and Photoproduction at HERA*, (2007), hep-ex/0703022.

[54] I. Abt et al. (H1 Collaboration), *The Tracking, Calorimeter and Muon Detectors of the H1 Experiment at HERA*, Nucl. Instrum. Met. **A386** (1997), 348.

[55] M. Boenig, *Messund des D^*-Meson-Produktionsquerschnitts in tiefinelastischer Streuung mit dem H1-Experiment*, Dissertation, Universität Dortmund (2007).

[56] V. Blobel, *Central Track Finding and Reconstruction in the H1 Detector* (http://www.desy.de/blobel/phystat.html), H1 talk (2003).

[57] V. Blobel, *Central Track Reconstruction*, Tracking group meeting (https://www-h1.desy.de/idet/itracker/TrackingGroup/AgnMin/-Meet041103/blobel041103.pdf) (2004).

[58] B. Andrieu et al.(H1 Calorimeter Group Kollaboration), *The H1 Liquid Argon Calorimeter System*, Nucl. Instum. Meth. **A336** (1993),460.

[59] R. D. Appuhn et al. (H1 SpaCal Group Collaboration), *Th H1 Lead/Scintillating-Fibre Calorimeter*, Nucl. Instrum. Meth. **A386** (1997), 397.

[60] J. Janoth et al., *Response of mesh type photomultiplier tubes in strong magnetic fields*, Nucl. Instrum. Meth. **A350** (1994), 221.

[61] T. Nicholls et al. (H1 SPACAL Group Collaboration), *Performance of an electromagnetic lead/ scintilating fiber calorimeter for the H1 detector*, Nucl. Instrum. Meth. **A374** (1996), 149.

[62] D. Reyna, *Modifications to SpaCal for H1 High Luminosity Operation and the Effect on Acceptance*, h1-11/98-555 (H1 internal report) (1998).

[63] H. Bethe and W. Heitler, *On the Stopping of Fast Particles and on the Creation of Positive Electrons*, Proc. Roy. Soc. Lond. **A146** (1934), 83.

[64] H1 Collaboration, *Contributed Paper to the 28^{th} International Conference on High Energy Physics*, paper pal17-026 (1996).

[65] V. Andreev et al., *The New H1 Luminosity System for HERA II*, Proceedings to 8th International Conference on Instrumentation for Colliding Beam Physics (2002).

[66] D. Wegener and H. C. Schultz-Coulon, *Teilchendetektoren*, lecture notes (2003).

[67] E. Elsen, *Aspects of the H1 Trigger and Data Acquisition System*, 2nd Annual Conference on Electronics for Future Colliders (1992).

[68] B. Reisert, *Elektron-Proton-Streuung bei hohen Impulsüberträgen am H1-Experiment*, Dissertation, Universität München (2000).

[69] S. Chekanov et al., ZEUS Collaboration, *Dijet Angular Distributions in Photoproduction of Charm at HERA*, Phys. Lett. **B565** (2003) 87, hep-ex/0302025.

[70] F. Abe et al., CDF Collaboration *A Measurement of Jet Shapes in $p\bar{p}$ Collisions at $\sqrt{s} = 1.8$ TeV*, Phys. Rev. Lett. **70** (1993) 713.

[71] C. Adloff et al. (H1 Collaboration), *Measurement of Internal Jet Structure in Dijet Production In Deep Inelastic Scattering at HERA* (1999), arXiv:hep-ex/9901010.

[72] S. Chekanov et al. (ZEUS Collaboration), *Substructure Dependence of Jet Cross Sections at HERA and Determination of α_s*, (2004), arXiv:hep-ex/0407050.

[73] M. Milite, *The Internal Structure of Charmed Jets in Photoproduction at HERA*, Dissertation, Universität Hamburg (2001).

[74] M. Milite (ZEUS Collaboration), *Measurement of Jet Substructure in Inclusive and Charm-Induced Dijet Photoproduction at HERA*, Proceedings of the EPS 2001, Budapest (2001).

[75] M. Martisikova (H1 Collaboration), *Study of Jet Shapes in Charm Photoproduction at HERA*, DIS 2005 Conference (2005).

[76] M. Peez, B. Portheault, E. Sauvan, *An Energy Flow Algoritm for Hadronic Reconstruction in OO: Hadroo2*, H1-01/05-616 (H1 internal note) (2005).

[77] S. Catani, Y. L. Dokshitzer, M. H. Seymor and B. R. Webber, *Longitudinally Invariant $K(t)$ Clustering Algorithms for Hadron Hadron Collisions*, Nucl. Pys. B **406** (1993) 187.

[78] M. H. Seymor, *Jets in QCD*, CERN-TH/95-176, talk given at the 10^{th} Topical Workshop on Proton-Antiproton Collider Physics, Batavia, IL, May 9-13, (1995).

[79] S. Catani, Y. L. Dokshitzer and B. R. Webber, Phys Lett. **B285** (1992) 291.

[80] S. Osman and D. Salek, *The Low Pt HFS and Jet Energy Calibration*, H1-02/09-631 (H1 internal note) (2009).

[81] S. Eidelman et al. (Particle Data Group), Phys Lett. **B592**, (2007) 1.

[82] L. Gladilin, *Charm Hadron Production Fractions*, (1999), hep-ex/9912064.

[83] F. Sefkow et al., IEEE Trans. Nucl.Sci., **42**, 1995 900.

[84] H. Beck, *Principles and Operation of the z-Vertex Trigger*, H1 internal note (1996) H1-05/96-479.

[85] T. Wolff et al., *A Driftchamber Track Finder for the First Level Trigger of H1*, H1 internal note (1992) H1-02/92-213.

[86] J. Reidberger, *The H1 Trigger with Emphasis on Tracking Triggers*, H1 internal note (1995) H1-01/95-419.

[87] S. Aid et al. (H1), Z. Phys., **C69**, (1995) 27 hep-ex/9509001.

[88] Bassler, U. and Bernardi, G., *On the kinematic reconstruction of deep inelastic scattering at HERA: The Sigma Method* Nucl. Instrum. Meth. **A361** (1995), 197, hep-ex/9412004.

[89] F. Jacquet and A. Blondel, *Report from the study group on detectors for charged current events*, In U. Amaldi et al., editors, Proceedings, Study of an e-p Facility for Europe, 377. DESY-Report 79-048, 1979.

[90] A. W. Jung, *Measurement of the D^* Meson Cross Section and Extraction of the Charm Contribution F_2^c to the Proton Structure in Deep Inelastic ep Scattering with the H1 Detector at HERA*, Dissertation, Universität Heidelberg (2009).

[91] K. Lohwasser, *Optimisation of the Selection Capability of the H1 Fast Track Trigger*, Diploma thesis, Universität Dortmund (2006).

[92] G. Flucke, *Photoproduction of D^* Mesons and D^* Mesons Associated with Jets at HERA*, Dissertation, Universität Hamburg (2005).

Danksagung

Bedanken möchte ich mich als erstes bei allen, die mich während meiner Zeit bei H1 unterstützt haben. Mein besonderer Dank gilt Frau Prof. Dr. Beate Naroska, die den Abschluss dieser Arbeit zu meinem tiefen Bedauern nicht mehr erleben kann. Ich danke ihr für die freundliche Aufnahme in ihre Arbeitsgruppe und das entgegengebrachte Vertrauen, um meine Promotion am H1-Experiment durchzuführen. Mit ihrer ansteckenden Begeisterung für die Teilchenphysik wird sie mir immer als Vorbild in Erinnerung bleiben.

Bei Herrn Prof. Dr. Robert Klanner bedanke ich mich sehr für das schnelle Korrekturlesen dieser Arbeit, die hilfreichen Korrekturvorschläge und die Übernahme des Erstgutachtens.

Herrn Dr. Benno List danke ich sehr für die Übernahme der Betreuung meiner Analyse, das gründliche Korrekturlesen sowie der Erstellung des Gutachtens der Dissertation. Ich bin ihm vor allem sehr dankbar für seine Geduld und dafür, dass er meine Analyse mit wertvollen Anregungen vorangebracht hat.

Herrn Prof. Dr. Dieter Horns danke ich sehr dafür, dass er sich für die Begutachtung der Disputation bereit erklärt hat.

Mein Dank gilt außerdem allen Mitgliedern der H1-Kollaboration für die angenehme und wertvolle Zusammenarbeit. Dies gilt ganz besonders für die Mitglieder der Heavy Flavour Gruppe.

Bei Dr. Mira Krämer und Dr. Martin Brinkmann bedanke ich mich für die gute Zusammenarbeit und die angenhme Büroatmosphäre, bei Martin dabei besonders für die vielen Unternehmungen. Bedanken möchte ich mich auch bei Alexander Grünwald für den regen Austausch von Erfahrungen und die vielen Diskussionen.

Ausserdem gilt mein Dank meiner Familie, besonders meinen Eltern, die mir immer Rückhalt gegeben haben. Schließlich gilt mein besonderer Dank Eva, die mit ihrer ausdauernden und liebevollen Unterstützung sehr zur Entstehung dieser Arbeit beigetragen hat.